

Numerical Study of the Characteristics of CNG, LPG and Hydrogen Turbulent Premixed Flames

By

Mohamed Aly Abdel-Raheem

A Doctoral Thesis

Submitted in partial fulfillment of the requirements for the award of Doctor of
Philosophy of Loughborough University



August 2015

Wolfson School of Mechanical and Manufacturing Engineering
Loughborough University

© by M.A. Abdel-Raheem (2015)

Abstract

Numerical simulations have proven itself as a significant and powerful tool for accurate prediction of turbulent premixed flames in practical engineering devices. The work presented in this thesis concerns the development of simulation techniques for premixed turbulent combustion of three different fuels, namely, CNG, LPG and Hydrogen air mixtures. The numerical results are validated against published experimental data from the newly built Sydney combustion chamber.

In this work a newly developed Large Eddy Simulation (LES) CFD model is applied to the new Sydney combustion chamber of size 50 x 50 x 250 mm (0.625 litre volume). Turbulence is generated in the chamber by introducing series of baffle plates and a solid square obstacle at various axial locations. These baffles can be added or removed from the chamber to adapt various experimental configurations for studies. This is essential to understand the flame behaviour and the structure. The LES numerical simulations are conducted using the Smagorinsky eddy viscosity model with standard dynamic procedures for sub-grid scale turbulence. Combustion is modelled by using a newly developed dynamic flame surface density (DFSD) model based on the flamelet assumption.

Various numerical tests are carried out to establish the confidence in the LES based combustion modelling technique. A detailed analysis has been carried out to determine the regimes of combustion at different stages of flame propagation inside the chamber. The predictions using the DFSD combustion model are evaluated and validated against experimental measurements for various flow configurations. In addition, the in-house code capability is extended by implementing the Lewis number effects. The LES predictions are identified to be in a very good agreement with the experimental measurements for cases with high turbulence levels. However, some disagreement were observed with the quasi-laminar case. In addition a data analysis for experimental data, regarding the overpressure, flame position and the flame speed is carried out for the high and low turbulence cases. Moreover, an image processing procedure is used to extract the flame rate of stretch from both the experimental and numerical flame images that are used as a further method to validate the numerical results.

For the grids under investigation, it is concluded that the employed grid is independent of the filter width and grid resolution. The applicability of the DFSD model using grid-independent results for turbulent premixed propagating flames was examined by validating the generated pressure and other flame characteristics, such as flame position and speed against experimental data. This study concludes that the predictions using DFSD model provide reasonably good results.

It is found that LES predictions were slightly improved in predicting overpressure, flame position and speed by incorporating the Lewis number effect in the model. Also, the investigation demonstrates the effects of placing multiple obstacles at various locations in the path of the turbulent propagating premixed flames. It is concluded that the pressure generated in any individual configuration is directly proportional to the number of baffles plates. The flame position and speed are clearly dependent on the number of obstacles used and their blockage ratio.

The flame stretch extracted from both the experimental and numerical images shows that hydrogen has the highest stretch values over CNG and LPG. Finally, the regime of combustion identified for the three fuels in the present combustion chamber is found to lie within the thin reaction zone. This finding supports the use of the laminar flamelet modelling concept that has been in use for the modelling of turbulent premixed flames in practical applications.

Acknowledgment

It is with immense gratitude that, I acknowledge the support and help given by many individuals around me. This thesis would not have been possible without them.

First and foremost I am deeply thankful to my supervisors Dr Salah Ibrahim and Professor Weeratunge Malalasekera for their strong interest, continuous encouragement, and helpful discussions and suggestions during the course of my research at Loughborough University. I am very grateful to Professor Assaad Masri for providing the experimental data used for model validation and for his invaluable advices on the progress of work. Special thanks to Dr Ahmed Alharbi for supplying the experimental data. Also, I am grateful to Dr Sreenivasa Rao Gubba, Dr Maxim Bragin, and Dr Yinqing Wang for their useful discussions and help during the progress of this work.

I would like to acknowledge the Wolfson School of Mechanical and Manufacturing Engineering and Department of Aeronautical and Automotive Engineering, Loughborough University for awarding me a valuable scholarship to undertake this research.

I would like to thank my wife, for her continuous support and encouragement, without which this work is impossible. Finally, I would like to thank my parents, my brother and sister, and my friends for motivating me through their help and support in achieving this great success in my life.

Publications

1. **Abdel-Raheem, M.A.**, Ibrahim, S.S., Malalasekera, W. and Masri, A.R. (2015). Large Eddy simulation of hydrogen–air premixed flames in a small scale combustion chamber. *International Journal of Hydrogen Energy*, 40 (7), 3098-3109. <http://dx.doi.org/10.1016/j.ijhydene.2014.12.042>.
2. Bragin, M., Ibrahim, S.S. and Malalasekera, W. and **Abdel-Raheem, M.A.**, (2015). Determination of the stretch rates of LPG, CNG and H₂ turbulent deflagrating flames. To be submitted at *Journal of Loss Prevention in the Process Industries*.
3. **Abdel-Raheem, M.A.**, Ibrahim, S.S., Malalasekera, W. and Bragin, M. (2015). Numerical Simulations of CNG, LPG & H₂ Lean Premixed Deflagrating Flames. 25th *International Colloquium on the Dynamics of Explosions and Reactive Systems (ICDERS)*. University of Leeds, UK.
4. **Abdel-Raheem, M.A.**, Ibrahim, S.S. and Malalasekera, W. (2014). Numerical Experiments of Hydrogen-Air Premixed Flames. *International Journal of Research in Engineering and Science*, 2 (2), 48-55.
5. **Abdel-Raheem, M.A.**, Ibrahim, S.S. and Malalasekera, W. (2014). Numerical Modelling of Hydrogen Premixed Combustion. *Proceedings of 16th International Conference on Applied Mechanics and Mechanical Engineering (AMME-16)*. Cairo, Egypt.
6. **Abdel-Raheem, M.A.**, Ibrahim, S.S., Malalasekera, W. and Masri, A.R. (2013). Large Eddy Simulation of Hydrogen-Air Propagating Flames. *Proceedings of 8th Mediterranean Combustion Symposium (MCS)*, Izmir, Turkey.
7. **Abdel-Raheem, M.A.**, Ibrahim, S.S., Malalasekera, W. and Masri, A.R. (2013). Dynamic Flame Surface Density Model for Turbulent Premixed Flame. The Combustion Institute Summer School, Lund University, Lund, Sweden.

Contents

Abstract.....	ii
Acknowledgment.....	iv
Publications	v
Contents	vi
Nomenclature	x
List of Figures.....	xiii
List of Tables	xxi
Chapter 1	1
Introduction.....	1
1.1 Background.....	1
1.2 Turbulent Premixed Combustion.....	4
1.3 Combustion Modelling	5
1.4 Motivation.....	7
1.5 Objective of the Present Research	8
1.6 Thesis Outline	8
Chapter 2	11
Literature Review	11
2.1 Introduction.....	11
2.2 Regimes of Turbulent Premixed combustion	17
2.3 Modelling of Turbulent Premixed Combustion.....	22
2.3.1 Flamelet Modelling.....	23
2.3.2 Turbulent Flame Speed Closure	26
2.3.3 The Eddy-Break-Up Model	27
2.3.4 Artificially Thickened Flame Approach	28
2.3.5 Probability Density Function (PDF) Model.....	29
2.3.6 Flame Tracking Approach (G-equation).....	30
2.3.7 Marker Field Approach.....	32
2.3.8 Other Modelling Techniques	33
2.4 Fuel Characteristics.....	34
2.4.1 Physical and Chemical Characteristics	35

2.4.1.1 Ignition.....	36
2.4.2 Combustion Properties.....	37
2.4.3 Laminar burning velocity.....	38
2.4 Summary.....	41
Chapter 3	43
Large Eddy Simulation of Reacting Flows	43
3.1 Background.....	43
3.2 Conservation Equations	46
3.2.1 Conservation of Mass	46
3.2.2 Conservation of Momentum	47
3.2.3 Conservation of Energy	47
3.2.4 The Reaction Progress Variable Equation	48
3.2.5 The Equation of State	48
3.2 Spatial Filtering Functions.....	49
3.3 Favre Filtering (Averaging)	53
3.3.1 Filtered Governing Equations.....	54
3.4 Modelling of SGS Residual Stresses	56
3.4.1 Residual Stress Decomposition	56
3.4.2 The Smagorinsky Model.....	57
3.4.3 The Dynamic SGS Flow Model.....	59
3.4.4 Scale Similarity Models.....	61
3.5 Modelling of SGS Scalar Fluxes	62
3.6 Summary.....	63
Chapter 4	64
The Combustion Model	64
4.1 Introduction.....	64
4.2 Algebraic Expression for Flame Surface Density (AFSD) Model	67
4.3 The Dynamic Flame Surface Density (DFSD) Model.....	69
4.4 Modelling of the Fractal Dimension	72
4.4.1 Dynamic Fractal Model (DFM).....	74
4.5 Lewis Number Effect.....	76
4.6 Ignition Model	78
4.7 Summary.....	79

Chapter 5	80
Numerical Methodology	80
5.1 Finite Volume Method.....	80
5.2 Discretization of the Conservation Equations	82
5.2.1 The Unsteady Term	83
5.2.2 The Convection Term	84
5.2.3 The Diffusion Term	87
5.2.4 The Source Term	88
5.2.5 The Complete Discretized Conservation Equation.....	89
5.3 Time Advancement Scheme	90
5.3.1 Time Integration of Scalar Equation.....	90
5.3.2 Time Integration of Momentum Equations	91
5.3.3 The Pressure Correction Equation	93
5.3.4 Solution of the Algebraic Equations.....	95
5.3.5 Iteration Procedure.....	96
5.4 Boundary Conditions	98
5.4.1 Initial Conditions	98
5.4.2 Outflow Boundary Conditions.....	99
5.4.3 Solid Boundary Conditions.....	100
5.4.4 Numerical Domain.....	100
5.5 Summary	102
Chapter 6	104
The Experimental Combustion Chamber	104
6.1 Design Consideration for the Combustion Chamber	104
6.2 Experimental Setup.....	106
6.2.1 Baffles and Solid Obstacle Arrangement.....	109
6.2.2 Ignition System	110
6.2.3 Pressure Transducers	111
6.2.4 High Speed Imaging System.....	112
6.2.5 Laser Induced Fluorescence of Hydroxyl Radical (LIF-OH)	113
6.3 Experimental Procedure.....	113
6.3.1 The Experimental Sequence	114
6.4 Summary.....	115

Chapter 7	116
Quantifications of Experimental Data	116
7.1 The Overpressure Time Traces	116
7.2 Flame Position and Speed	121
7.3 Flame Stretch	126
7.3.1 Methodology for Extracting Flame Stretch	128
7.4 Sources of Errors	131
7.6 Summary	132
Chapter 8	133
Results and Discussion.....	133
8.1 Grid Dependency Test	133
8.2 Sensitivity to Ignition Source	135
8.3 Effect of Fuel Type	139
8.4 Effect of Lewis number	144
8.5 Model Validation Using Flame Stretch	150
8.6 Effect of Flow Configuration.....	152
8.7 Regimes of Combustion.....	173
Chapter 9	181
Conclusions and Recommendations for Future Work.....	181
9.1 The work presented in this thesis has achieved the following objectives:	181
9.2 Conclusions.....	182
9.3 Present Contributions.....	184
9.4 Recommendations for Future Work	184
Appendix A	186
Appendix B	188
References.....	199

Nomenclature

Latin Letters

A	Area (m ²)
A_T	Turbulent flame surface area per unit volume (m ² /m ³)
A_L	Laminar flame surface area per unit volume (m ² /m ³)
C_{EBU}	EBU Model constant
C_S	Model constant used in DFSD equation
c	Reaction progress variable
c_{ss}	Speed of sound (m/s)
D	Fractal dimension
D_L	Mass diffusivity (m ² /s)
G	Convolution function or G field
h	Grid cell height
I_o	Mean stretch factor
k	Flame Stretch (1/s)
Ka	Karlovitz number
Le	Lewis number
L_I	Integral length scale (mm)
L_F	Flame thickness (mm)
Pr	Prandtl number
Pr_t	Turbulent Prandtl number
P_{sg}	Probability in PDF equation
R	Curvature of the flame surface
Re	Reynolds number
S_+	Marker field scalar
Sc	Schmidt number
Sc_t	Turbulent Schmidt number
S_{ij}	Strain rate (1/s)
t	Time (ms)
u	Velocity in x-direction (m/s)
u'	RMS fluctuations (m/s)
u_k	Flame advancement by curvature effects (m/s)

u_d	Displacement speed (m/s)
u_l	Laminar burning velocity (m/s)
u_T	Turbulent burning velocity (m/s)
V	Volume (m ³)
Y_{fu}	Fuel mass fraction
Y_{fu}^0	Fuel mass fraction in un-burnt mixture

Greek Symbols

α	Model constant in TFS equation
α_T	Thermal diffusivity (m ² /s)
β	Model coefficient in simple FSD equation
λ	Unresolved flame surface density
$\dot{\omega}_c$	Chemical reaction rate (kg/s)
k	Turbulent kinetic energy (m ² /s ²)
ε	Dissipation rate (m ² /s ³)
ρ	Fluid density (kg/m ³)
ρ_u	Unburned gas density (kg/m ³)
Φ	Equivalence ratio
$\bar{\Delta}$	Filter width (mm)
Σ	Flame surface density (m ² /m ³)
γ	Ratio of test filter to grid filter
Λ	Unresolved flame surface density at test filter (m ² /m ³)
Ξ	Flame wrinkling factor

Subscripts/Superscripts

fu	fuel
l	Laminar
o	unburned
sgs	Sub-grid scale
t	Turbulent

Operations

\sim	Favre average
\wedge	Test filter
$-$	Spatial filter
$'$	Fluctuations

Abbreviations

BiCGStab	Bi-Conjugate Gradient Stabilized
CFD	Computational Fluid Dynamics
CNG	Compressed Natural Gas
DFSD	Dynamic Flame Surface Density
DFM	Dynamic Fractal Model
DNS	Direct Numerical Simulation
EBU	Eddy-Break-Up
FSD	Flame Surface Density
F-TACLES	Filtered Tabulated Chemistry for LES
KDP	Potassium Dihydrogen Phosphate
LIF	Laser Induced Florescence
LDA	Laser Doppler Anemometry
LDV	Laser Doppler Velocimetry
LES	Large Eddy Simulation
LHS	Left Hand Side
LPG	Liquid Petroleum Gas
MSI	Modified Strongly Implicit
Nd:YAG	Neodymium-doped Yttrium Aluminium Garnet
NTP	Normal Temperature and Pressure
PDF	Probability Density Function
PRISM	Piecewise Reusable Implementation of Solution Mapping
PUFFIN	Particles IN Unsteady Fluid Flow
RANS	Reynolds Averaged Navier-Stokes
RHS	Right Hand Side
SGS	Sub-Grid Scale
TFS	Turbulent Flame Speed

List of Figures

Figure 1.1 Sequence of spark ignited combustion images (Winklhofer (2003)). Each flame image captured from consecutive cycle.....	2
Figure 1.2 Schematic diagram for a gas turbine.	3
Figure 1.3 Sequence of images for diesel engine combustion (Cronhjort (2005)).....	3
Figure 1.4 Explosions at Fukushima nuclear power plant reactor in 2011 (Courtesy of the coming crises website, http://thecomingcrisis.blogspot.co.uk/2011_03_13_archive.html)	4
Figure 1.5 Time evolutions of temperature calculated by DNS, RANS or LES in a turbulent flame brush (Poinot and Veynante (2012)).....	6
Figure 2.1 Classical Turbulent combustion regime diagram from Peters (1988).....	19
Figure 2.2 Modified turbulent combustion diagram from Peters (1999).....	19
Figure 2.3 Regimes diagram of LES for premixed turbulent combustion by Pitsch and Duchamp de Lageneste (2002).	21
Figure 2.4 Comparison of experimental and simulated pressure dynamics for the uniform 12.8% vol. hydrogen–air mixture in a 10.7 m ³ closed vessel (Makarov et al. (2010)). FZK: Forschungszentrum Karlsruhe GmbH-Germany, JRC: Joint Research Centre-Institute for Energy-The Netherlands, KI: Kurchatov Institute-Russia, UU: University of Ulster-UK.	32
Figure 2.5 Comparison of explosion pressure for various Stoichiometric fuel-air mixtures in a 10 m wedge-shaped vessel, reproduced from Bjorkhaug (1988).	35
Figure 2.6 Flammability range of hydrogen compared with different fuels reproduced from Bjerketvedt et al. (1997).....	38
Figure 2.7 Corrected and un-corrected measurements of laminar burning velocities as a function of equivalence ratio for hydrogen-air mixture at NTP (Aung et al. (1997)). ...	39
Figure 3.1 Spatial filters used in large eddy simulations. (a) Cut-Off filter (b) Gaussian filter (c) Box filter.....	51
Figure 3.2 The filtered function \tilde{u} obtained by applying a box filter. Upper: small filter width, Lower: large filter width (Fröhlich and Rodi (2002)).	52
Figure 3.3 Temporal fluctuations and time-average in a statistically non-stationary process (Warnatz et al. (2006)).....	53

Figure 3.4 Temporal fluctuations and time-average in a statistically stationary process (Warnatz et al. (2006)).	53
Figure 4.1 Instantaneous Schlieren images of a typical lean premixed flame at different pressures showing the fractal nature of the flame (Kobayashi et al., 1996).	74
Figure 4.2 Fractal nature of the flame front showing various length scales (Gouldin et al. (1989b)).	74
Figure 4.3 Schematic of thermal-diffusive instability. Flame shapes at two moments of time t_1 and t_2 are shown. Flame propagates from left to right (Ciccarelli and Dorofeev (2008)).	76
Figure 5.1 Two dimensional forward staggered grid (Gubba (2009)). Circles are scalar nodes, horizontal arrows are nodes of the u velocity component and vertical arrows the nodes of the v velocity component. Examples of a u , v and scalar cells are highlighted.	81
Figure 5.2 3-D view of a finite volume cell and its neighbours.	83
Figure 5.3 A finite volume cell in the xy -plane.	85
Figure 5.4 Illustration of the computational domain with the combustion chamber and obstacles superimposed over the grid.	101
Figure 5.5 Description for the current work.	102
Figure 6.1: Old (left) and new (right) combustion chamber showing the quartz viewing windows.	106
Figure 6.2 The combustion chamber (left) and the removable baffles (right). B1, B2, and B3 are the baffles. Dimensions in mm.	108
Figure 6.3 Internal and external structure for the combustion chamber.	108
	109
Figure 6.4 Combustion chamber configurations used by AlHarbi (2013).	109
Figure 6.5 Arrangement of the Laser assisted ignition system (AlHarbi (2013)).	111
Figure 6.6: The two imaging tiers used to capture the maximum viewable height. Left used for configuration BBBS and right for the rest of configurations.	112
Figure 6.8 The experimental rig of the turbulent premixed combustion chamber.	114

Figure 7.1 Averaged value (black colour) imposed over the raw data for overpressure-time history for CNG-air mixture ($\Phi = 0.8$) and 000S configuration after fixing the time shift.	118
Figure 7.2 Averaged value (black colour) imposed over the raw data for overpressure-time history for CNG-air mixture ($\Phi = 0.8$) and BBBS configuration after fixing the time shift.	118
Figure 7.3 Averaged value (black colour) imposed over the raw data for overpressure-time history for LPG-air mixture ($\Phi = 0.8$) and 000S configuration after fixing the time shift.	119
Figure 7.4 Averaged value (black colour) imposed over the raw data for overpressure-time history for LPG-air mixture ($\Phi = 0.8$) and BBBS configuration after fixing the time shift.	119
Figure 7.5 Averaged value (black colour) imposed over the raw data for overpressure-time history for hydrogen-air mixture ($\Phi = 0.8$) and 000S configuration after fixing the time shift.	120
Figure 7.6 Averaged value (black colour) imposed over the raw data for overpressure-time history for hydrogen-air mixture ($\Phi = 0.8$) and BBBS configuration after fixing the time shift.	120
Figure 7.7 Flame position-time traces of experimental measurements using CNG, LPG and hydrogen air-mixture ($\Phi = 0.8$) for configuration 000S.	122
Figure 7.8 Flame position-time traces of experimental measurements using CNG, LPG and hydrogen air-mixture ($\Phi = 0.8$) for configuration BBBS.	123
Figure 7.9 Flame speed-time traces of experimental measurements using CNG, LPG and hydrogen air-mixture ($\Phi = 0.8$) for configuration 000S.	123
Figure 7.10 Flame speed-time traces of experimental measurements using CNG, LPG and hydrogen air-mixture ($\Phi = 0.8$) for configuration BBBS.	124
Figure 7.11 Flame Speed vs Flame Position for configuration 000S using the experimental measurements for CNG, LPG and hydrogen air-mixture ($\Phi = 0.8$).	124
Figure 7.12 Flame Speed vs Flame Position for configuration BBBS using the experimental measurements for CNG, LPG and hydrogen air-mixture ($\Phi = 0.8$).	125
Figure 7.13 Flame position-time traces of experimental measurements using CNG, LPG and hydrogen air-mixture ($\Phi = 0.8$) for configurations 000S and BBBS.....	125

Figure 7.14 Flame speed-time traces of experimental measurements using CNG, LPG and hydrogen air-mixture ($\Phi = 0.8$) for configurations 000S and BBBS.....	126
Figure 7.15 Image processing methodology for LIF-OH images.....	128
Figure 7.16 Extracted flame stretch from experimental images for CNG-air mixture with $\Phi = 0.8$	129
Figure 7.17 Extracted flame stretch from experimental images for LPG-air mixture with $\Phi = 0.8$	130
Figure 7.18 Extracted flame stretch from experimental images for hydrogen-air mixture with $\Phi = 0.8$	130
Figure 7.19 Comparison between the extracted flame stretch from experimental images for the three fuels, CNG, LPG and hydrogen-air mixture with $\Phi = 0.8$	131
Figure 7.20 The varied contrasts of the images of each fuel. (a) CNG (b) LPG (c) Hydrogen.	132
Figure 8.1 LES predictions of overpressure-time histories using different grid resolutions detailed in Table 8.1.	134
Figure 8.2 - Effect of various ignition radii (a) overpressure (b) flame position for BBBS configuration.....	137
Figure 8.3 - Effect of ignition shape (Hemispherical and spherical) and location on overpressure-time traces for BBBS configuration using the same ignition area.	138
Figure 8.4 Overpressure-time histories for CNG-air mixture ($\Phi = 0.8$) for configuration BBBS.	139
Figure 8.5 Overpressure-time histories for LPG-air mixture ($\Phi = 0.8$) for configuration BBBS.	140
Figure 8.6 Overpressure-time histories for hydrogen-air mixture ($\Phi = 0.8$) for configuration BBBS.....	140
Figure 8.7 Flame position-time traces of LES simulation for CNG-air mixture ($\Phi = 0.8$) for configuration BBBS.	141
Figure 8.8 Flame position-time traces of LES simulation for LPG-air mixture ($\Phi = 0.8$) for configuration BBBS.	141
Figure 8.9 Flame position-time traces of LES simulation for hydrogen-air mixture ($\Phi = 0.8$) for configuration BBBS.....	142

Figure 8.10 Flame speed-time traces of LES simulation for CNG-air mixture ($\Phi = 0.8$) for configuration BBBS.....	142
Figure 8.11 Flame speed-time traces of LES simulation for LPG-air mixture ($\Phi = 0.8$) for configuration BBBS.....	143
Figure 8.12 Flame speed-time traces of LES simulation for hydrogen-air mixture ($\Phi = 0.8$) for configuration BBBS.....	143
Figure 8.13 Comparison between unity and non-unity Lewis number on overpressure-time histories for CNG-air mixture ($\Phi = 0.8$).....	145
Figure 8.14 Comparison between unity and non-unity Lewis number on overpressure-time histories for LPG-air mixture ($\Phi = 0.8$).....	145
Figure 8.15 Comparison between unity and non-unity Lewis number on overpressure-time histories for hydrogen-air mixture ($\Phi = 0.8$).....	146
Figure 8.16 Comparison between unity and non-unity Lewis number on flame position-time histories for CNG-air mixture ($\Phi = 0.8$).....	146
Figure 8.17 Comparison between unity and non-unity Lewis number on flame position-time histories for LPG-air mixture ($\Phi = 0.8$).....	147
Figure 8.18 Comparison between unity and non-unity Lewis number on flame position-time histories for hydrogen-air mixture ($\Phi = 0.8$).....	147
Figure 8.19 Comparison between unity and non-unity Lewis number on flame speed-time histories for CNG-air mixture ($\Phi = 0.8$).....	148
Figure 8.20 Comparison between unity and non-unity Lewis number on flame speed-time histories for LPG-air mixture ($\Phi = 0.8$).....	148
Figure 8.21 Comparison between unity and non-unity Lewis number on flame speed-time histories for hydrogen-air mixture ($\Phi = 0.8$).....	149
Figure 8.22 Comparison between extracted flame stretch from experimental/numerical images, and unity/non-unity Lewis number for CNG-air mixture with $\Phi = 0.8$ in configuration BBBS.....	150
Figure 8.23 Comparison between extracted flame stretch from experimental/numerical images, and unity/non-unity Lewis number for LPG-air mixture with $\Phi = 0.8$ in configuration BBBS.....	151

Figure 8.24 Comparison between extracted flame stretch from experimental/numerical images, and unity/non-unity Lewis number for hydrogen-air mixture with $\Phi = 0.8$ in configuration BBBS.....	151
Figure 8.26 Overpressure-time histories for CNG-air mixture ($\Phi = 0.8$) and configuration 000S.....	153
Figure 8.27 Overpressure-time histories for LPG-air mixture ($\Phi = 0.8$) and configuration 000S.....	153
Figure 8.28 Overpressure-time histories for hydrogen-air mixture ($\Phi = 0.8$) and configuration 000S.....	154
Figure 8.29 Flame position-time histories for CNG-air mixture ($\Phi = 0.8$) and configuration 000S.....	154
Figure 8.30 Flame position-time histories for LPG-air mixture ($\Phi = 0.8$) and configuration 000S.....	155
Figure 8.31 Flame position-time histories for hydrogen-air mixture ($\Phi = 0.8$) and configuration 000S.....	155
Figure 8.32 Flame speed-time histories for CNG-air mixture ($\Phi = 0.8$) and configuration 000S.....	156
Figure 8.33 Flame speed-time histories for LPG-air mixture ($\Phi = 0.8$) and configuration 000S.....	156
Figure 8.34 Flame speed-time histories for hydrogen-air mixture ($\Phi = 0.8$) and configuration 000S.....	157
Figure 8.35 Overpressure-time histories for CNG-air mixture ($\Phi = 0.8$) and configuration B00S.....	158
Figure 8.36 Overpressure-time histories for LPG-air mixture ($\Phi = 0.8$) and configuration B00S.....	158
Figure 8.37 Overpressure-time histories for hydrogen-air mixture ($\Phi = 0.8$) and configuration B00S.....	159
Figure 8.38 Flame position-time histories for CNG-air mixture ($\Phi = 0.8$) and configuration B00S.....	159
Figure 8.39 Flame position-time histories for LPG-air mixture ($\Phi = 0.8$) and configuration B00S.....	160

Figure 8.40 Flame position-time histories for hydrogen-air mixture ($\Phi = 0.8$) and configuration B00S.....	160
Figure 8.41 Flame speed-time histories for CNG-air mixture ($\Phi = 0.8$) and configuration B00S.....	161
Figure 8.42 Flame speed-time histories for LPG-air mixture ($\Phi = 0.8$) and configuration B00S.....	161
Figure 8.43 Flame speed-time histories for hydrogen-air mixture ($\Phi = 0.8$) and configuration B00S.....	162
Figure 8.44 Overpressure-time histories for CNG-air mixture ($\Phi = 0.8$) and configuration BB0S.....	163
Figure 8.45 Overpressure-time histories for LPG-air mixture ($\Phi = 0.8$) and configuration BB0S.....	163
Figure 8.46 Overpressure-time histories for hydrogen-air mixture ($\Phi = 0.8$) and configuration BB0S.....	164
Figure 8.47 Flame position-time histories for CNG-air mixture ($\Phi = 0.8$) and configuration BB0S.....	164
Figure 8.48 Flame position-time histories for LPG-air mixture ($\Phi = 0.8$) and configuration BB0S.....	165
Figure 8.49 Flame position-time histories for hydrogen-air mixture ($\Phi = 0.8$) and configuration BB0S.....	165
Figure 8.50 Flame speed-time histories for CNG-air mixture ($\Phi = 0.8$) and configuration BB0S.....	166
Figure 8.51 Flame speed-time histories for LPG-air mixture ($\Phi = 0.8$) and configuration BB0S.....	166
Figure 8.52 Flame speed-time histories for hydrogen-air mixture ($\Phi = 0.8$) and configuration BB0S.....	167
Figure 8.53 Overpressure-time histories for CNG-air mixture ($\Phi = 0.8$) and configuration BBBS.....	168
Figure 8.54 Overpressure-time histories for LPG-air mixture ($\Phi = 0.8$) and configuration BBBS.....	168

Figure 8.55 Overpressure-time histories for hydrogen-air mixture ($\Phi = 0.8$) and configuration BBBS.....	169
Figure 8.56 Flame position-time histories for CNG-air mixture ($\Phi = 0.8$) and configuration BBBS.....	169
Figure 8.57 Flame position-time histories for LPG-air mixture ($\Phi = 0.8$) and configuration BBBS.....	170
Figure 8.58 Flame position-time histories for hydrogen-air mixture ($\Phi = 0.8$) and configuration BBBS.....	170
Figure 8.59 Flame speed-time histories for CNG-air mixture ($\Phi = 0.8$) and configuration BBBS.....	171
Figure 8.60 Flame speed-time histories for LPG-air mixture ($\Phi = 0.8$) and configuration BBBS.....	171
Figure 8.61 Flame speed-time histories for hydrogen-air mixture ($\Phi = 0.8$) and configuration BBBS.....	172
Figure 8.62 Regions used to identify regimes of combustion for the BBBS configurations	173
Figure 8.64 Estimates from the three fuels in Tables 8.3-8.5 are fitted into the regimes of turbulent premixed combustion diagram reported by Peters (2004). CNG (\square), LPG (O) and Hydrogen (Δ).	179
Figure 8.65 Estimates for the three fuels presented in Tables 8.3-8.5 are fitted into the regimes of LES turbulent premixed combustion diagram reported by Pitsch and Duchamp de Lageneste (2002). CNG (\square), LPG (O) and Hydrogen (Δ).	180
Figure B.1 Time sequences for the three fuels (CNG, LPG and Hydrogen) with time step $t = 0.2$ ms through configurations 000S and BBBS at equivalence ratio $\Phi = 0.8$ (AlHarbi (2013)).	198

List of Tables

Table 4.1 Fuel properties used to account for non-unity Lewis number effect.....	78
Table 7.1 Number of experimental overpressure readings for each fuel/configuration	117
Table 7.2 Summary of mean values for the first peak pressure and time of incidence measured at the base of the chamber for configurations (000S and BBBS) and three fuels LPG, CNG and hydrogen with equivalence ratio $\Phi = 0.8$..	117
Table 7.3 Number of images for each fuel/configuration.....	121
Table 8.1 Details of the numerical parameters	134
Table 8.2 Details of ignition sources, shapes and location.....	136
Table 8.3 Different scale estimates from LES predictions for CNG with equivalence ratio $\Phi = 0.8$, case BBBS. These estimates are plotted in combustion regime diagrams in Figures 8.64 & 8.65.	178
Table 8.4 Different scale estimates from LES predictions for LPG with equivalence ratio $\Phi = 0.8$, case BBBS. These estimates are plotted in combustion regime diagrams in Figures 8.64 & 8.65.	178
Table 8.5 Different scale estimates from LES predictions for hydrogen with equivalence ratio $\Phi = 0.8$, case BBBS. These estimates are plotted in combustion regime diagrams in Figures 8.64 & 8.65.	179

Chapter 1

Introduction

1.1 Background

Combustion remains the main source of energy for domestic heating, power generation, and transportation. Other energy sources such as solar and wind energy or nuclear energy still account for less than 20% of total energy consumption. It is well known that combustion not only generates heat, which can be converted into power, but also produces pollutants such as oxides of nitrogen, soot, and un-burnt hydrocarbons. In addition, unavoidable emissions of CO₂ are believed to contribute to global warming. These emissions could be reduced by improving the efficiency of the combustion process.

To achieve that, the physics of combustion with decades of research is continued, with many open questions to be answered such as combustion instabilities, extinction, re-ignition, flame-flow interactions, and the safety matters related to the use of different fuels. Combustion being a complex thermo-chemical process, understanding the presence of unsteadiness and turbulence, formulate a multifaceted problem.

In technical processes, combustion nearly always takes place within a turbulent rather than a laminar flow field. The reason for this is twofold: first, turbulence increases the mixing processes and thereby enhances combustion. Second, combustion releases heat and thereby generates flow instability by buoyancy and gas expansion, which then enhances the transition to turbulence. Technical processes in gaseous turbulent combustion can be subdivided in terms of mixing: premixed, non-premixed, or partially premixed turbulent combustion. For example, combustion in homogeneous charge spark-ignition engines as shown in Figure 1.1 (Winklhofer (2003)) or in gas turbines as shown in Figure 1.2, occurs under premixed conditions. In contrast, combustion in a diesel engine as shown in Figure 1.3 (Cronhjort (2005)) or in furnaces essentially takes place under non-premixed or partially premixed conditions.

The science of combustion involves complex interactions between many constituent disciplines, including; thermodynamics, chemical kinetics, fluid mechanics, heat and mass transfer, turbulence, and materials structure and behaviour. Hence, the optimal design of combustion systems demands rigorous experimental investigations, which require expensive experimental setups, where combustor designs are very complex. For instance, a typical gas turbine combustion chamber is not realistic for detailed experimental investigation due to the harsh internal flow and combustion characteristics. These internal conditions raise unclosed questions, which are predominant to understand in order to improve the combustor performance, which demands alternative methods of investigations. As a result, computational/numerical modelling provides a potential alternative to difficult experimental investigations.

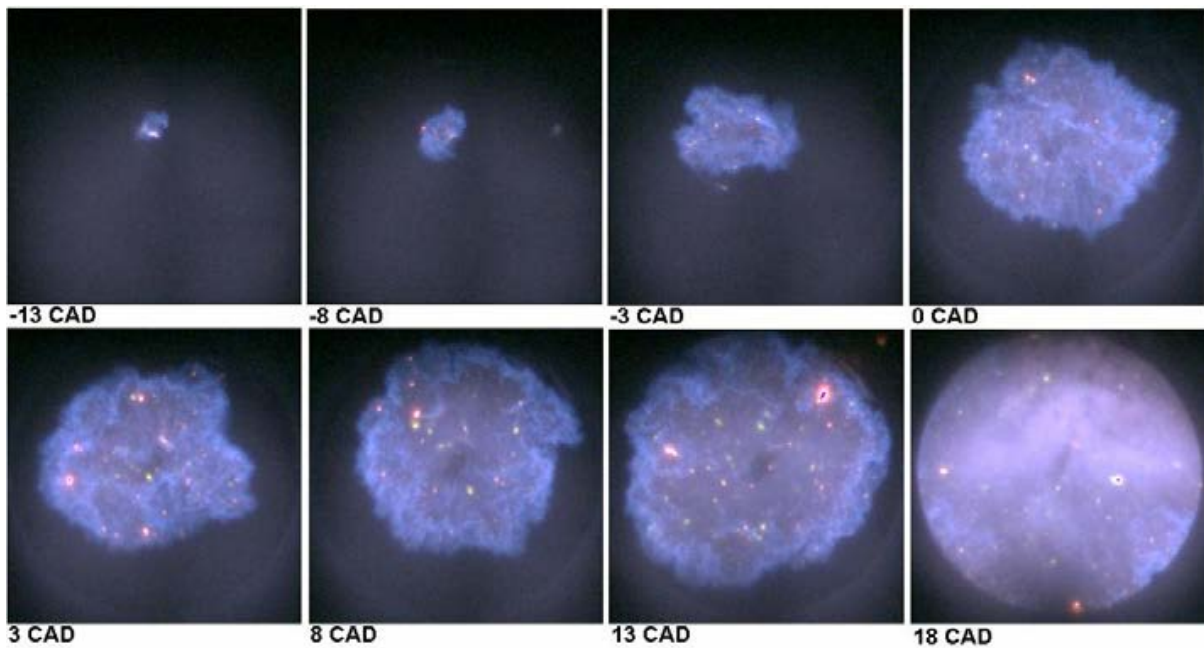


Figure 1.1 Sequence of spark ignited combustion images (Winklhofer (2003)). Each flame image captured from consecutive cycle.

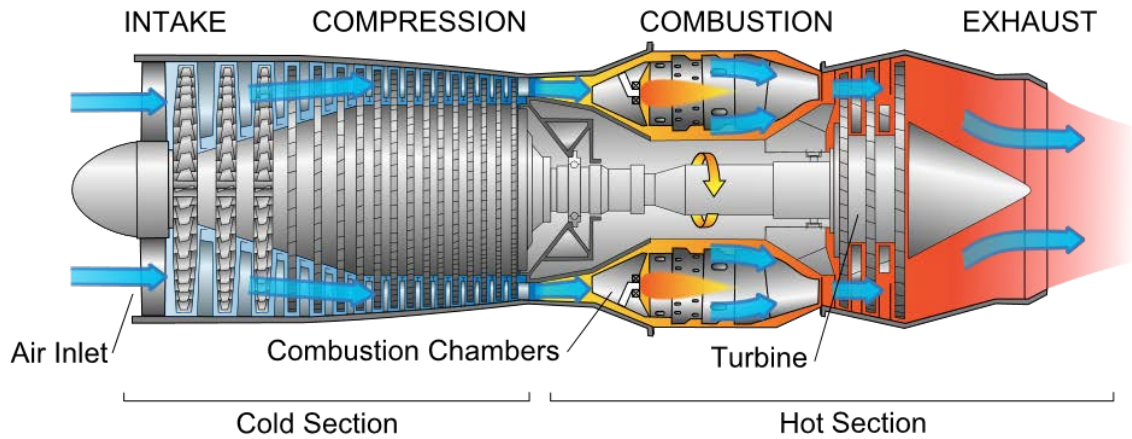


Figure 1.2 Schematic diagram for a gas turbine.

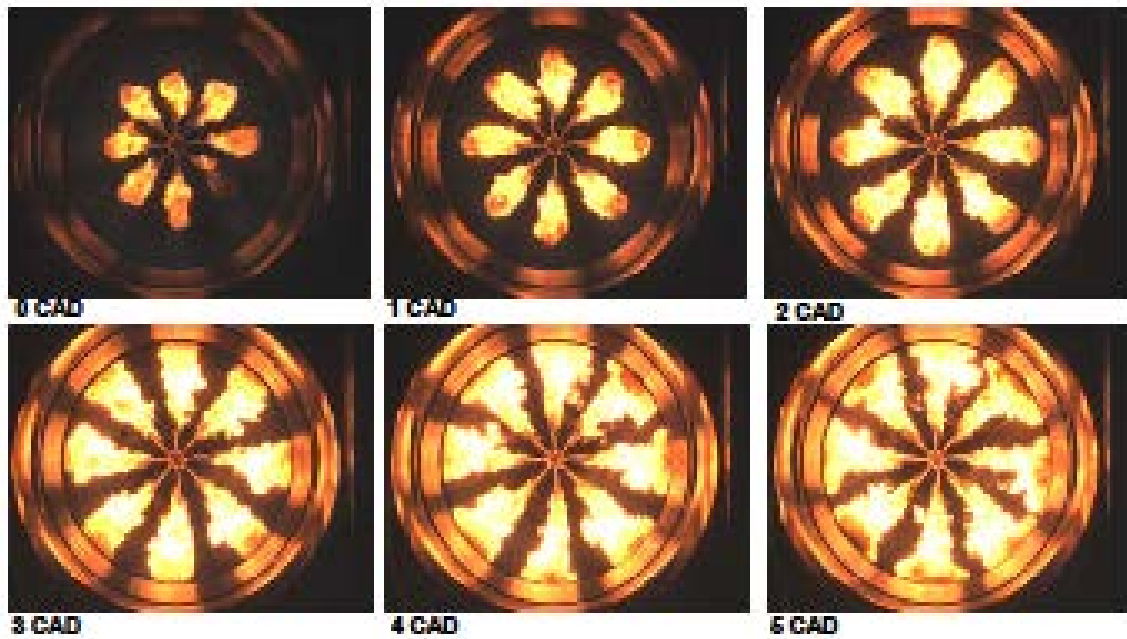


Figure 1.3 Sequence of images for diesel engine combustion (Cronhjort (2005)).

Apart from above-mentioned applications, numerical modelling plays pivotal role in the safe design of on- and off-shore chemical/fuel processing/storage plants. For example, the explosion occurred at the quake-hit Fukushima (No. 1) nuclear power plant's reactor in 2011, Japan (Figure 1.4), the damage caused by the explosion generated overpressure due to flame acceleration and its interactions with the presented equipment/solid obstacles was enormous and highly hazardous, prompted the

authorities there, to urge residents within a 20-kilometer radius to take shelter inside buildings. Investigating such large scale explosion experiments in industrial scale vessels are very expensive and risk taking, while yielding limited data.



Figure 1.4 Explosions at Fukushima nuclear power plant reactor in 2011 (Courtesy of the coming crises website, http://thecomingcrisis.blogspot.co.uk/2011_03_13_archive.html)

1.2 Turbulent Premixed Combustion

Turbulent premixed reacting flows have been very interesting and challenging problems for researchers for quite a long time. These flows are of great practical importance, being encountered in many engineering devices. Turbulent premixed combustion involves very complex thermo-chemical process which is usually coupled with combustion instabilities, extinction, re-ignition and flame-flow interactions. Fuel and oxidizer are perfectly mixed before entering the combustion zone. This situation is favourable in terms of burning efficiency but when the flame starts to propagate in the mixture of reactants this is a totally different situation which could lead to safety problems. Hence, extensive amount of research is carried out in this area and still there is more to investigate on turbulent premixed propagating flames.

The turbulent flame, unlike the laminar one, is often accompanied by noise and rapid fluctuations of the flame structure. For a laminar flame, it is possible to define a flame velocity that, within reasonable limits, is independent of the experimental apparatus (Peters (2004)). On the other hand, to define a propagation velocity for turbulent flames that would be independent of the experimental apparatus and depend only on the fuel-air ratio and some transport properties (e.g. viscosity, thermal and mass diffusivity...etc.) is not possible, because the transport properties of turbulent flame are function of the flow rather than the fluid. For example, at some stoichiometric ratios the effective thermal diffusivity can be several times larger than the molecular-thermal diffusivity in the laminar case. Thus, the theoretical concepts for turbulent flames are not so well described as laminar flames (Warnatz et al. (2006)).

The influence of turbulence in premixed combustion results from the two-way interaction of chemistry and turbulence. When the flame interacts with the turbulent flow, turbulence is modified by the combustion because of strong flow accelerations through the flame front induced by heat release, and large changes in viscosity associated with temperature changes. This mechanism may generate turbulence, called flame generated turbulence. On the other hand, turbulence alters the flame structure, may enhance chemical reaction but also could hinder it completely, leading to flame quenching.

Turbulent premixed combustion can be treated as a fluid mechanics problem as it involves the influence of turbulence in enhancing the mass consumption rate and chemical kinetics of the combustion process. Compressible flow with the premixed combustion is governed by the equations of conservation of mass, momentum, energy, and a transport equation for reaction progress variable coupled with the thermodynamic equation of state. As this type of flow involves large changes in density, high velocities and significant dilatation, all terms in the equation must be retained.

1.3 Combustion Modelling

Computational modelling tools have been proved as an excellent alternative for experiments and the methods are adequately developed in the field of aerospace, fluid dynamics, metrology and health engineering even for complex non-reacting flow

problems. However, in the case of reacting flow problems, where turbulence is involved, the progress made is less satisfactory with many outstanding research issues. With successful prediction of non-reacting flow applications, industrial usage of computational modelling for turbulent combustion is ever growing. Generally, there are three computational modelling techniques (Figure 1.5) available for current use, mainly

- Direct Numerical Simulations (DNS).
- Large Eddy Simulations (LES).
- Reynolds Averaged Navier Stokes (RANS).

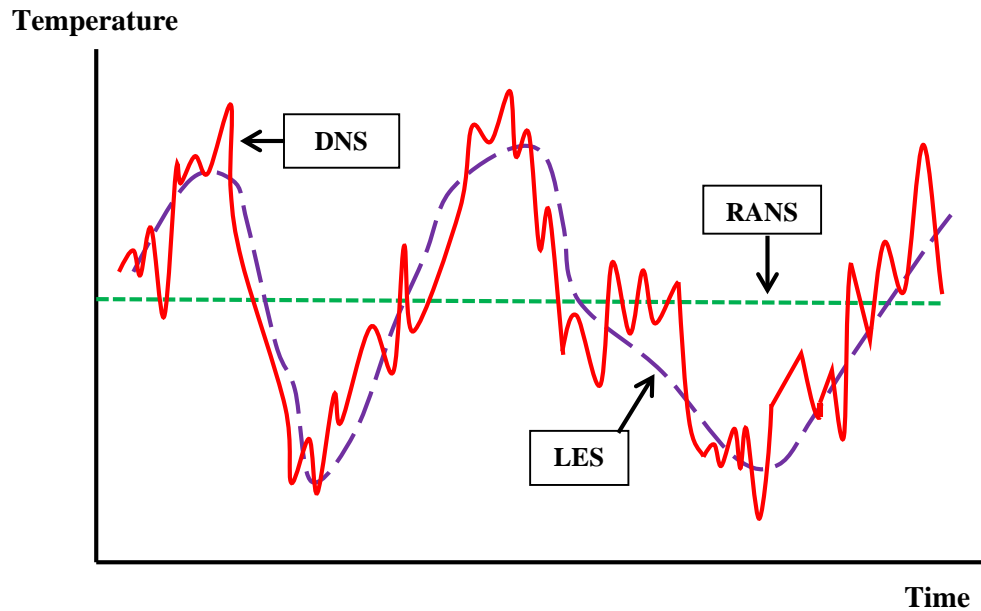


Figure 1.5 Time evolutions of temperature calculated by DNS, RANS or LES in a turbulent flame brush (Poinsot and Veynante (2012)).

Among the above-mentioned numerical techniques, DNS offers the ultimate accuracy as all the physical scales involved in a flow problem are completely resolved without modelling. However, despite significant improvements in computational resources, application of DNS is limited to low Reynolds number flows due to the cost and computational resources involved. Hence, the application of DNS to real combustion systems, where the flows are complex and involve higher Reynolds number is impractical in the foreseeable future. For instance, Moin and Kim (1997) estimated that it will take several thousands of CPU years of the fastest available supercomputer

during 1997, to compute the flow around an aircraft for one second of flight time, in order to understand the turbulence with reasonable details using 10^{16} grid nodes. This estimate limits the use of DNS for practical applications. However, DNS can still be efficiently utilised to develop and evaluate simple computational sub-models.

On the other hand, Large Eddy Simulation (LES) is now accepted as a feasible computational tool despite added computational cost, as compared with the RANS technique. Several recent works by Charlette et al. (2002), Knikker et al. (2004), Fureby (2005), Masri et al. (2006), Pitsch (2006), Gubba et al. (2011), and Abdel-Raheem et al. (2015) confirmed the high fidelity of LES in predicting key characteristics of turbulent combustion. LES has a clear advantage over classical Reynolds averaged based methods in the capability of accounting for time-varying nature of the flow and this is particularly important in transient processes such as swirling flows or transient propagating premixed flames. Also, LES allows for detailed description of turbulence/combustion interactions, which is a common failure in RANS, because in LES, large structures are explicitly determined, and instantaneous fresh and burnt gases zones, where turbulence characteristics are quite different, are clearly identified. The ever increasing speed of computers is supporting the high computational requirement of LES and shifting the focus towards developing adequate sub-grid-scale (SGS) models for combustion. The development of such SGS models is vital in modelling of combustion.

1.4 Motivation

Inspired by the need to develop and validate numerical models to account for different combustion scenarios, e.g. internal combustion engines, gas turbines, industrial burners...etc. The dynamic flame surface density (DFSD) model is considered in the present study to simulate turbulent premixed flames propagating over repeated solid obstacles. This model was originally developed by Knikker et al. (2004) and further extended by Gubba et al. (2007). In this work this concept is developed further and numerically implemented in an existing LES code PUFFIN (Kirkpatrick, 2002). This DFSD model is evaluated for three different fuel-air mixture; compressed natural gas (CNG), liquefied petroleum gas (LPG), and hydrogen (H_2) in a laboratory scale

premixed combustion chamber with a specific emphasis to predict the deflagrating premixed flame characteristics and their interactions with repeated solid obstacles.

1.5 Objective of the Present Research

In this study, the LES modelling technique is used to study turbulent deflagrating flames in the recently developed, small scale combustion chamber of AlHarbi (2013). The specific objectives of this research are to:

- Conduct transient LES simulations for turbulent premixed flames, using three different fuels; CNG, LPG and hydrogen air mixture at lean condition. The simulations use the dynamic flame surface density (DFSD) model to account for the chemical reaction rate.
- Develop the dynamic flame surface density model (DFSD) to account for Lewis number effect. The developed model has been incorporated in the in-house LES code and validated against the experimental results for different flow configurations.
- Establish an analytical method to extract stretch rate values from experimental images. These values are used to further validate the numerical results.
- Examine the influence of the number and position of obstacles inside the chamber on the generated overpressure, flame position and speed, which will help to understand different combustion scenarios. Subsequently the developed DFSD model is expected to contribute towards the advancement of the LES prediction capabilities of turbulent premixed combustion.

1.6 Thesis Outline

This chapter describes the motivation and objectives defined in modelling dynamic sub grid scales (SGS) for LES simulations of chemical reaction rate and flow in combustion systems. The number of numerical approaches and their capabilities for predicting turbulent reacting flows are briefly described. The rest of the thesis is defined as follows.

Chapter 2 - Literature Review

Outlines the latest efforts in modelling premixed combustion and highlights the various

combustion models available to account for the reaction rate. The recent research in laboratory scale combustion chambers is presented. A brief discussion is provided to review the characteristics of combustion through various regimes. Finally, an overview for the three fuels (CNG, LPG and Hydrogen) used in the present study is given.

Chapter 3 – Large Eddy Simulation of Reacting Flows

An overview of the LES approach for modelling turbulent flows, various types of filtering techniques and available filters are presented and discussed. The governing equations for turbulent premixed combustion and Favre filtering technique are briefly explained. The LES methodology has been described with details of the closing strategies employed for sub-grid scale stresses and scalar fluxes.

Chapter 4 – The Combustion Model

This describes the premixed combustion model used in this study. The dynamic flame surface density (DFSD) model and its incorporation in the in house LES code are presented. The development of the combustion model to account for the Lewis number effect is also discussed. Details of the dynamic fractal model employed to calculate the fractal dimension are outlined. The ignition model used is also presented.

Chapter 5 – Numerical Methodology

This chapter explains the Numerical implementation of the filtered governing equations outlined in Chapter 3. The implementation of the spatial discretisation and time advancement schemes through finite volume methodology are discussed. A detailed description of the initial and boundary conditions and the working procedure are also presented.

Chapter 6 – Experimental Combustion Chamber

This chapter describes the test cases used for the purpose of model validation. A complete description of the influencing factors in designing this test chamber and the novelty of the chamber are detailed. An overview for the experimental ignition system and the utilised measurement techniques are introduced. Classification of the various test case configurations in terms of the number of obstacles and their position in the

chamber are explained. A typical experimental sequence is detailed to outline the procedure followed.

Chapter 7 – Quantification of Experimental Data

This chapter analyse the experimental results to extract the data required for the numerical validation. An image processing technique is proposed to extract the stretch values is also presented.

Chapter 8 – Results and Discussion

In this chapter, the LES results obtained using the dynamic flame surface density model for reaction rate are presented for the three fuels, CNG, LPG and Hydrogen. Firstly, the LES results obtained using dynamic formulation for the model controlling parameters are presented. These include the grid dependency test and the effect of the ignition source. Secondly, the effect of fuel type on the generated overpressure, flame position and flame speed is discussed. Also, the effect of Lewis number is presented for the three fuels. Moreover, the effect of various complex flow configurations on the overpressure, flame position and speed is discussed. The extracted flame stretch from both the experimental data and LES results, is used as a further method for model validation, will be also shown. Finally, flame characteristics from LES results are calculated, analysed and plotted in two different turbulent premixed combustion regime diagrams.

Chapter 9 – Conclusions and Recommendations for Future Work

This summarises the conclusions from this research work with its key contributions towards improved prediction capabilities. It also suggests directions for further improvement.

Chapter 2

Literature Review

In this chapter, review of recent research efforts for investigating turbulent premixed flames is presented and discussed. A brief discussion is, also, provided for the characterisation of premixed flames through various turbulent combustion regime diagrams. In the final section, various RANS and LES models available to account for the chemical reaction rate in computational modelling are discussed in details.

2.1 Introduction

Turbulent premixed flames are often characterised by their ability to propagate towards the fresh gases. As the flame is initiated by an ignition source, the reaction advances through the gas with relatively thin flame front until all the fuel is consumed (Poinsot and Veynante (2012)). In turbulent flames the flame propagation speed is not equal to the incoming gas velocity, unlike laminar flames. The turbulent burning velocity has been identified to depend on many parameters such as turbulence levels, mixture reactivity, surface area of the flame and flame stretch etc. (Bray (1990), Catlin et al. (1995) and Bradley et al. (2003)). On the other hand, if the flame propagation is due to thermal conduction i.e. transporting energy from hot burnt gases to cold fuel mixture, it is known as deflagration (Gubba (2009)). If the flame propagates due to shock wave i.e. increasing the temperature as a result of compressing the fuel mixture, it is known as detonation (Oran and Boris. (2000)). Ciccarelli and Dorofeev (2008) showed that the deflagration may transform into detonation depending on boundary conditions, length and width of the chamber and the generated overpressure etc. Alternatively, the presence of solid obstructions in combustion environment eventually leads to higher flame speed/acceleration with high overpressure, which has severe consequences in many engineering applications (Bradley et al. (2008), AlHarbi et al. (2014) and Abdel-Raheem et al. (2015)). As mentioned previously, modelling of combustion systems using numerical techniques would help in designing and developing these systems. However, success of any numerical combustion model depends mainly on its capability to account for the chemical reaction rate. Hence, improvement of combustion models is

very important with the increasing industrial demands for more efficient and effective combustion systems.

Investigations of premixed flame/obstacle interactions started in the 1980's when Moen et al. (1980) and Hjertager et al. (1988) performed large scale experiments. These studies concluded that obstacle size and premixed fuel/air concentration have an influence on pressure and flame speed. Moen et al. (1980) used a cylindrical chamber with a radius of 30.5 cm, filled with a stoichiometric methane/air mixture in the presence of different obstacle configurations. The study showed that the flame speed increased by 24 times in the presence of obstacles and also the need of obstacles to maintain continuous turbulence. Later on, Hjertager et al. (1988) were more concerned with the pressure inside the chamber. The experimental set-up consisted of a tube with a length of 10 m and a diameter of 2.5 m with five equally spaced obstacles with blocking ratios of 30% and mixtures of methane/air and propane/air were used. For concentrations varying from 5.5% to 15% by volume with increment of 0.5% for methane-air mixtures; and from 2% to 9% by volume with increment of 0.25% for the propane-air mixtures the study revealed that the maximum pressures occur in fuel rich mixtures even for methane/air or propane/air mixtures. Also, the study found that the peak pressure in propane/air is twice that of the pressure in methane/air over the entire examined concentrations.

Understanding the details and the nature for flame/flow interactions is vital for the development of reliable analytical tools able to compute the structure of flames under different circumstances. Such a purpose is increasingly being approached due to the advancement in modelling capabilities and the detailed results in well-defined laboratory flames (Fairweather et al. (1999b), Kent et al. (2005) and Starke and Roth (1989)). Earlier experimental studies in flame propagation focused on large scale experiments (Moen et al. (1982), Hjertager et al. (1988), Starke and Roth (1989) and Masri et al. (2000)) where the application of advanced diagnostics was impractical and rather inadequate to measure pressure/time relationship. Later on, laboratory scale experiments became the chosen technique of investigation, using simple geometrical configurations that are fit for complex diagnostics and validation of numerical models (Masri et al. (2000), Patel et al. (2002), AlHarbi et al. (2012) and Kent et al. (2005)).

Since the earlier work of Moen et al. (1980) and Hjertager et al. (1988), researchers have become more concerned about the interaction between fuel/air and obstacles. To understand flame propagation in enclosed vessels, it is essential to test a variety of chamber configurations. Previous researchers experimented by adding obstacles, e.g. Starke and Roth (1989 & 1986), cylindrical vessels with turbulence inducing rings like Fairweather et al. (1996) and Fairweather et al. (1999b) or circular plate obstructions as Phylaktou and Andrews (1991). Other researchers re-designed the vessels, creating complex chambers with rectangular cross-sections and a single plate as an internal baffle, e.g. Lindstedt and Sakthitharan (1998) or square cross-sections and multiple baffles lining the walls as Johansen and Ciccarelli (2009).

Starke and Roth (1986) studied flame propagation inside a closed cylindrical chamber without obstacles. The study revealed the general behaviour of the flame after ignition, as the flame initially has a hemispherical shape and, after it propagates, the flame front develops sections parallel to the wall. The flame continues to propagate, until a tulip shaped flame forms as a result of wall quenching. Later on, Starke and Roth (1989) included different obstacles in different locations inside the chamber to study the influence on pressure and flame velocity. It was found that the location of the obstacle has a large effect on the burning rate and that putting the obstacle too close or too far from the ignition point increases the burning rate. However, the middle position results in the highest burning rate, as placing the obstacle too close to the ignition point prevents the flame from becoming turbulent.

The designs of combustion chambers in earlier studies, used the length (L) of the chamber in the direction of the propagating flame was greater than its diameter (D) or the width of the base (W). In the above-mentioned experiments, the ratios of L/D or L/W ranged from 2 in the design of Fairweather et al. (1999a) to 32 in the design of Johansen and Ciccarelli (2009). In contrast, Lohrer et al. (2008) used pipes with L/D ratios ranging from 4-143 in their studies of velocity and turbulence with and without obstacles at varying initial pressures. However, it should be pointed that detonations become more likely at high L/D ratios and that the presence of obstacles further increases the chance of transitioning to detonations. As the subject of this thesis is deflagration not detonation, this issue will not be further addressed. Park et al. (2007)

used methane-air mixture to study deflagration in chambers with L/D ratio of 0.235, where they found that obstacle geometry and blockage ratios did not have a significant effect on flame displacement speeds. Although this result is inconsistent with observations at higher L/D ratios, it can be explained by the lower and less developed turbulence levels at lower L/D values.

Ibrahim et al. (2001) designed a small scale combustion chamber made from 6 mm thick clear polycarbonate and had a cross section of $150 \times 75 \text{ mm}^2$ and length of 450 mm. They have also constructed second chamber section with the length variable from 0.5 to 1.5 m. A single rectangular obstacle used with cross section of $40 \times 12 \text{ mm}^2$ imposing an area blockage ratio of 50% ahead of the flame. The fuel mixtures were used of methane in air: lean, $\Phi = 0.8$, rich, $\Phi = 1.2$, and stoichiometric. It was found that the highest flame acceleration was with the stoichiometric mixture. The trapped unburned mixture behind the obstacles was found to be a large source of turbulence. This study showed that, variations in the rate of flame front length and propagation speed have a big influence on the generated overpressure. Three stages of flame propagation were identified: first, the flame starts to accelerate when it hits the wall; next, the flame decelerates when it reaches the wake behind the wall; finally, the flame starts to accelerate again due to the turbulent combustion with the wakes. Moreover, Patel et al. (2002) used multiple obstructions inside the combustion chamber, and these obstacles caused even more turbulence.

Also, Park et al. (2008) studied flame propagation over multiple obstacles with blockage ratios of 30% and 43%. A box shaped chamber with top venting was used. Five different L/Ds (height of the chamber/diameter of the chamber) were tested. It was found that chambers with an L/D ratio of 0.29 or 0.57 showed less sensitivity between the flame and the obstacles, while in chambers with an L/D ratio over 0.86 the flame was more sensitive to the obstacles.

Furthermore, premixed flames interaction with obstacles has also been studied at the University of Sydney for a decade. The earliest study was conducted by Masri et al. (2000) using a chamber with a square cross-section and a given volume of 20 L of stoichiometric propane/air mixture. Circular, triangular, and square obstacle geometries

were used and these obstacles covered blockage ratios from 10% to 78%. Images were taken of the flame front propagation and the volume of trapped mixture behind the obstacles. It was found that the obstacles with a square cross-section had the fastest flame acceleration, meaning that the geometry of the obstacles has a major effect on flame propagation. The amount of trapped unburned mixture was high when square obstacles were used, which explains why these had the highest peak pressure. The study also showed that the flame speed increased with the blockage ratio. Later on, Ibrahim and Masri (2001) performed further studies using the same chamber specifications. However, a greater number of obstacles were used than in the previous study with blockage ratios from 10% to over 75%. They aimed to study the influence of the blockage ratio and venting pressure on the peak pressure due to premixed flame propagation. It was found that the peak pressure increased by increasing the blockage ratio with no change in the venting pressure and that the time needed to reach the peak pressure decreased with increasing blockage ratios.

Later on, laser diagnostic techniques were used at the University of Sydney to improve the understanding of flame deflagration. Investigations of premixed flame propagation over obstacles continued by Masri et al. (2006) in which the group used LIF (Laser Induced Florescence) to investigate the burning rate and the structure of the flame front. The chamber with a 20 L volume and square cross-section from the previous study was used, but with different obstacle shapes and an array of baffle plates. It was shown that the burning rate as well as the overpressure increased with increments of the turbulence.

However, a new chamber was designed at the University of Sydney by Kent et al. (2005). The volume of the chamber was reduced from 20 L to 0.625 L. This reduction gave the advantage of a shorter simulation time and made it easier for researchers to add more baffle plates inside the chamber. Kamardin (2005) used new chamber constructed from Perspex with a propane/air fuel mixture. It was revealed that the overpressure peak presents on rich mixtures. Hall (2006) investigated the velocity inside the chamber using (LDV) and found that the peak velocity and peak pressure are related to turbulence. Afterward, Hall (2008) used a new rig with the same configuration as his previous study rig, but with a quartz window to allow laser sheets with no deformation to the chamber wall. Based on previous studies, it was clear that adding more baffle

plates inside the chamber would increase the peak pressure, but these studies mentioned a limit for this conclusion. Thus, at some stage, adding more baffles will make the pressure decrease rather than increase. Optical access in the chamber was later extended to the entire width Grant (2008) to enable OH-LIF images along the entire length of the chamber. It was revealed that, due to turbulence, the flame front stretch has an effect on the explosion overpressure.

In addition to the previous, flame propagation in an enclosure generates acoustic waves that, after reflections from walls and obstacles, can interact with the flame front and develop flame perturbations through a variety of instability mechanisms (Ciccarelli and Dorofeev (2008)). Such instabilities have been observed by Kogarko and Ryzhkov (1961) in closed spherical chambers and in closed tubes by Leyer and Manson (1971) and by Van Wingerden and Zeeuwen (1983) and Tamanini and Chaffee (1992) in vented enclosures. For rich propane-air mixtures, Van Wingerden and Zeeuwen (1983) observed that these instabilities could result in a peak pressure enhancement factor of 8. While, Kogarko and Ryzhkov (1961) observed enhancement factors of 2-9 for stoichiometric methane-air and propane-air mixtures. Detailed investigation for these mechanisms can be found at Oran and Gardner (1985), Searby and Rochwerger (1991), Jackson et al. (1993), Joulin (1994), and Al-Shahrany et al. (2006).

Flame acoustic instabilities are usually associated with relatively slow flames in enclosures that are free of obstacles (Ciccarelli and Dorofeev (2008)). Turbulence and turbulence inducing obstacles have been shown to reduce relative contribution of acoustic instabilities on flame propagation and pressure build-up (Kogarko and Ryzhkov (1961)). It has also been shown that such instabilities can be successfully eliminated by lining the enclosure walls with materials that can absorb acoustic waves. Teodorczyk and Lee (1995), used hydrogen-oxygen mixture in tubes with repeated obstacles to study flame acceleration with and without an absorbing material on the tube wall. Their results showed that the presence of an absorbing material reduced the final flame velocity from 1000 m/s to 100 m/s.

Generally, if confinement and/or obstructions are present, several powerful instabilities may strongly influence the flame propagation. These are the well-known Kelvin-

Helmholtz (K–H) and Rayleigh-Taylor (R-T) instabilities. The first one is associated with shear, and the second one is initiated when a lighter fluid is accelerated towards a heavier fluid. In compressible flows this instability is known as Richtmyer-Meshkov (R-M) instability. Both K-H and R-T instabilities are triggered when the flame is suddenly accelerated over an obstacle or through a vent. Finally, sufficiently fast flames can produce a shock wave that can reflect off a surface and interact with the flame. This was shown by Markstein and Somers (1953), this can result in severe flame distortion which can induce flame acceleration and, in severe cases, cause transition to detonation (Thomas et al. (2001)). While Landau-Darrieus (due to the discontinuity of unburned and burned gas density) and thermal-diffusive instabilities (due to unequal diffusivities of the reactants and heat) are relatively weak, K-H and R-T instabilities represent powerful mechanisms that are mainly responsible for the increase in flame surface and generation of turbulence in channels with obstacles. Landau-Darrieus and thermal-diffusive instabilities may only play a role at the initial stage of flame propagation, or in cases of unconfined flames (Ciccarelli and Dorofeev (2008)). Acoustic instabilities may be important for relatively slow flames in enclosures that are free of obstacles.

In conclusion, consistent in all of these studies, the combustion interaction between an air-fuel mixture and solid obstacles is challenging yet interesting. The challenge arises due to the complexity of the flame front's interaction with the turbulence generated ahead of it by the expanding gas. Such interactions impact strongly on the resulting overpressure, the rate of pressure rise, the burning rate of the gases, and the geometry of the accelerating flame front.

2.2 Regimes of Turbulent Premixed combustion

Effect of turbulence on combustion may be viewed as an interaction between flame fronts and turbulent eddies of various sizes. Eddies in a turbulent flow field may vary in size from Kolmogorov scale: the smallest, to the integral scale; the largest. The representative flow time scale of an eddy is defined by:

$$\tau_t = \frac{L_I}{u'} \quad (2.1)$$

where, L_I is the integral length scale and u' is the RMS velocity. How fast the chemical reactions are, compared to the turbulent mixing in a premixed reactive flow field, can be

identified by comparing the chemical and the integral turbulent time scales. Characteristic flame time or the chemical time scale can be defined using flame properties as:

$$\tau_c = \frac{L_F}{u_L} \quad (2.2)$$

where, L_F is the laminar flame thickness and u_L is the laminar flame speed. The ratio between the two time scales above represents the non-dimensional Damköhler number Da , which corresponds to the large eddies in combustion, and defined as:

$$Da = \frac{\tau_t}{\tau_c} = \frac{L_I}{L_F} \frac{u_L}{u'} \quad (2.3)$$

Another non-dimensional number, the Karlovitz number Ka , relates to the smallest eddies and is defined as the ratio of the chemical time scale to the Kolmogorov time scales τ_k as:

$$Ka = \frac{\tau_c}{\tau_k} = \frac{u'(\eta_k)/\eta_k}{u_L/L_F} = \left(\frac{L_I}{\delta_l}\right)^{-\frac{1}{2}} \left(\frac{u'}{u_L}\right)^{\frac{3}{2}} = \left(\frac{L_F}{\eta_k}\right)^2 \quad (2.4)$$

where η_k is the Kolmogorov micro scale. Figure 2.1 shows a classical combustion regime diagram of Peters (1988) based on the velocity scale $\left(\frac{u'}{u_L}\right)$ and length scale $\left(\frac{L_I}{L_F}\right)$. This diagram outlines four important regimes as shown in Figure 2.1. However, Poinot and Veynante (2012) showed that this classical diagram is not representative in many combustion situations due to the assumption of homogeneous and isotropic turbulence by neglecting heat release affects. On the other hand, Peters (1999) has adapted this classical combustion regime diagram by considering the heat release effects based on same velocity and length scales as shown in Figure 2.2. It is worth noting that, the criteria and regime limits used to distinguish different zones are based only on the order of magnitude estimations and not on precise derivations (Ranasinghe (2013)).

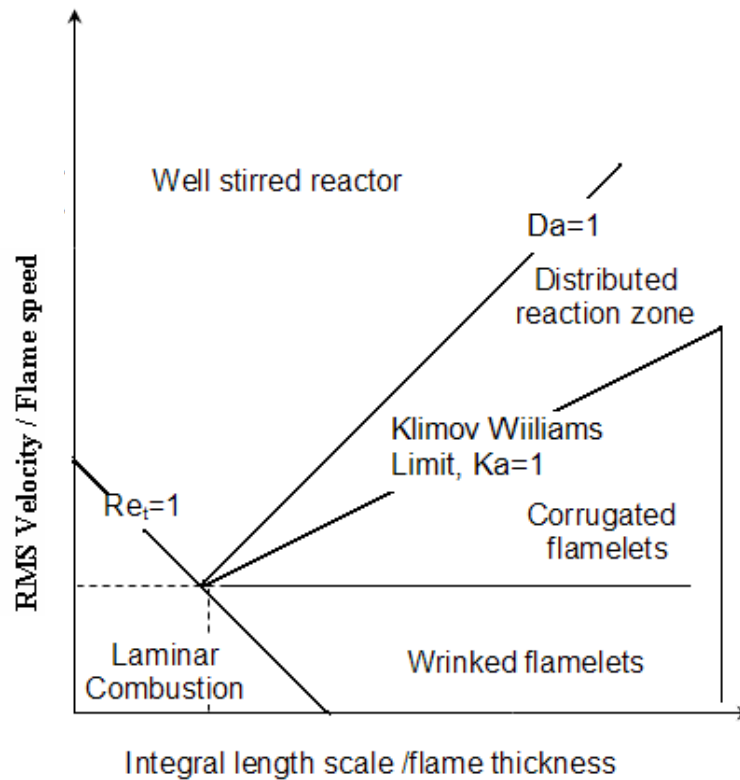


Figure 2.1 Classical Turbulent combustion regime diagram from Peters (1988).

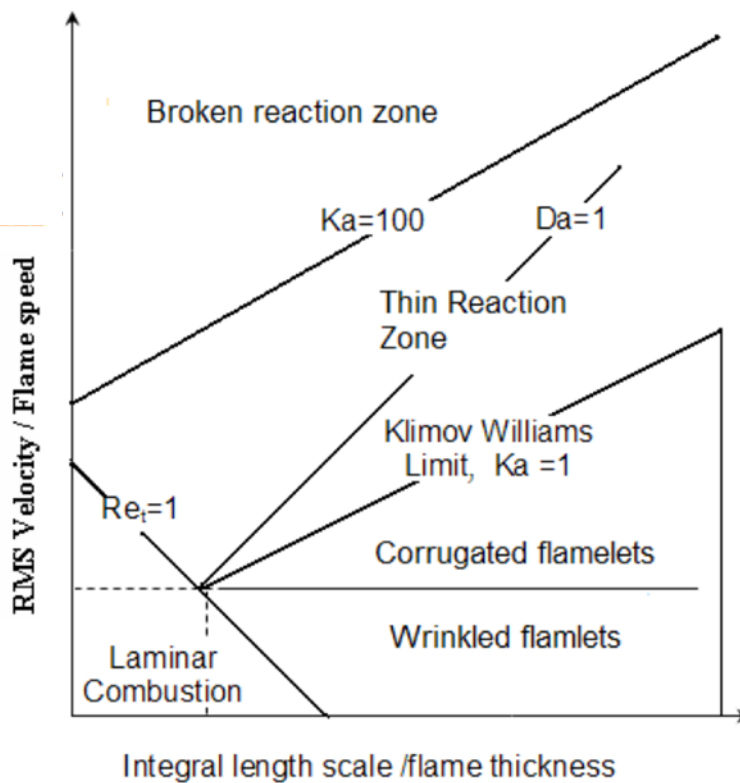


Figure 2.2 Modified turbulent combustion diagram from Peters (1999).

Three main combustion regimes are identified in Figure 2.2; corrugated/wrinkled flamelets, thin reaction zones, and broken reaction zones. The “corrugated/wrinkled flamelet” regime is characterised by the chemical time scales are shorter than any turbulent time scales i.e. $Ka < 1$. Also, the flame thickness is smaller than the smallest turbulent scale (smaller than Kolmogorov scales). This means that the flame front is not affected by turbulent motions. Moreover, the flame front in this regime is very thin and wrinkled due to turbulence motions smaller than Kolmogorov length scales, and similar to laminar flame structure.

The “thin reaction” zone, is identified where the Kolmogorov length scale becomes smaller than the flame thickness, which implies $Ka > 1$. In this regime, the order of Kolmogorov, chemical and turbulence time scales are $\tau_k < \tau_c < \tau_t$ respectively. Also, the Kolmogorov scales are smaller than the flame thickness and are able to modify the inner flame structure. It should be mentioned here, that most of the engineering combustion devices are within the thin reaction zones regime, because mixing is dominating at higher Ka numbers, which leads to higher volumetric heat release and shorter combustion times (Pitsch (2006)).

The “broken reaction” or “well-stirred reactor” regime is defined when the chemical time scale is higher than turbulent time scale, i.e. $Da \ll 1$. In this regime, turbulent motions becomes sufficiently strong to affect the whole flame structure, which means mixing is faster and the overall reaction rate is limited by chemistry. This subsequently may lead to a local extinction and can cause noise and instabilities. Excessive increase of instabilities may even lead to global extinction in premixed combustion devices (Pitsch (2006)).

However, the combustion regime diagrams discussed above are helpful in classifying the combustion phenomenon in various combustion systems, based on relevant velocity and time scales estimates (Gubba (2009)). However in case of LES, the unique parameter which distinguishes other numerical modelling approaches is the filter width ($\bar{\Delta}$), which separates large eddies from small ones in the flow field. This fact has led to the recent development of LES regime diagrams for premixed flames by Pitsch and Duchamp de Lageneste (2002). They showed that, the Karlovitz number Ka is

independent from the filter width and introduced a new regime diagram with respect to Karlovitz and Reynolds number. However, sub-grid velocity fluctuations are dependent on filter width and a change in the filter width results in a change in the sub-grid velocity fluctuations, which eventually may change the regime of combustion, provided that the solution is grid independent. This identifies that the effect of the filter width, cannot be studied independently as it has significant effect on combustion (Pitsch (2006)).

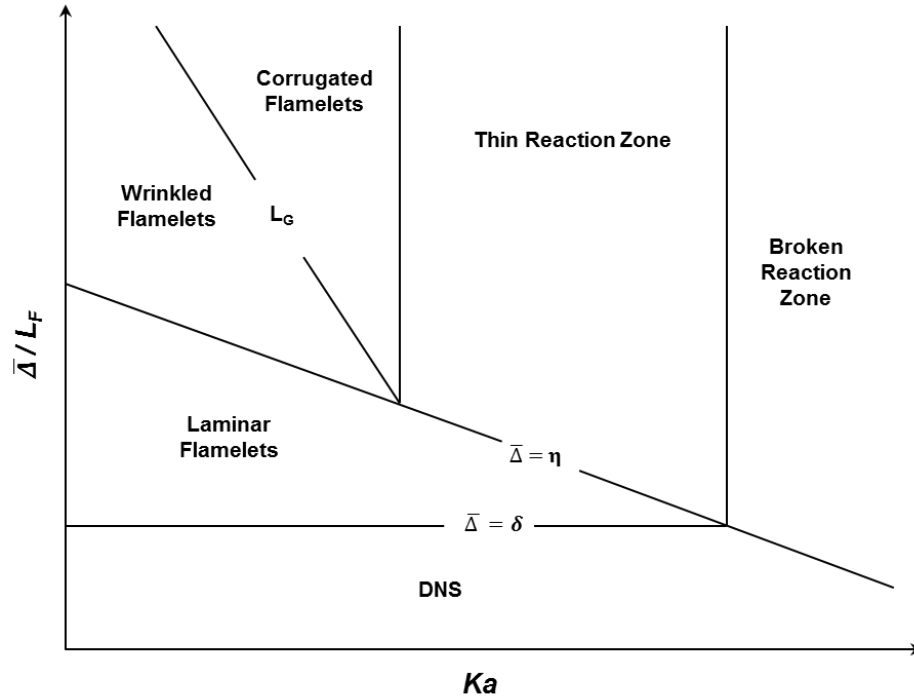


Figure 2.3 Regimes diagram of LES for premixed turbulent combustion by Pitsch and Duchamp de Lageneste (2002).

Figure 2.3 reproduces the LES regime diagram of Pitsch (2006) as a function of length scale and Karlovitz numbers. The Karlovitz number describes the physical interactions of flow and combustion at the smallest turbulent scales. Where, the Karlovitz and the sub-grid Reynolds numbers are defined as:

$$Ka_{\bar{\Delta}} = \left[\left(\frac{u'_{\Delta}}{u_L} \right)^3 \cdot \left(\frac{L_F}{\bar{\Delta}} \right) \right]^{\frac{1}{2}} \quad (2.5)$$

$$Re_{\bar{\Delta}} = \frac{u'_{\Delta} \bar{\Delta}}{u_L L_F}$$

where u'_Δ is the sub-grid scale velocity fluctuations. In LES, the Karlovitz number is a fluctuating quantity, but for a given flow field and chemistry it is fixed. The effect of changes in filter size can therefore easily be assessed at constant Ka number. An additional benefit of this regime diagram is that it can be used equally well for DNS (Pitsch (2006)) if it is associated with the mesh size.

It is worth to mention here that, the combustion regime in both figures 2.2 and 2.3 are the same but the latter is represented in terms of LES quantities. Hence, the three regimes identified and discussed in the previous section are still valid for LES. However, it should be noticed that the effect of changing the LES filter width can have an impact on the accuracy of the numerical solutions (Gubba (2009)). For example, by choosing an appropriate ratio, by decreasing the filter width, eventually leads to a smaller sub-filter Reynolds number $Re_{\bar{\Delta}}$ less than one. Hence, for a filter size smaller than the Kolmogorov micro scale, no sub-filter modelling for the turbulence is needed, which eventually reaches DNS resolution. However, the entire flame including the reaction zone can only be resolved if $\bar{\Delta} < L_F$.

2.3 Modelling of Turbulent Premixed Combustion

The utmost challenge for the modelling of the turbulent premixed flames is the modelling of the reaction rate due to its non-linear relation with chemical and thermodynamic states. This is often characterized by propagating reaction layers thinner than the smallest turbulent flow scales. The major difficulty in modelling the reaction rate is due to the variation of thermo-chemical variables through the laminar flame profile, which is typically very thin (Veynante and Poinso (1997)). This issue is strongly affected by turbulence, which causes flame wrinkling and thereby forming the most complex three way thermo-chemical-turbulence interactions. In the numerical simulation of practical transient premixed reacting flows, it is computationally expensive to resolve the flame front on the computational grid because the reaction zone “flame thickness” is very thin, normally a fraction of a millimetre (Matalon (2009) and Aung et al. (1997)). Several methods are commonly used to overcome this difficulty. In the present survey a brief discussion is presented for these methods:

➤ Flamelet Modelling

- Turbulent Flame Speed Closure
- The Eddy-Break-Up Model
- Artificially Thickened Flame Approach
- Probability Density Function Model
- Flame Tracking (G-equation) Approach
- Marker Field Approach

2.3.1 Flamelet Modelling

Flamelet modelling of turbulent deflagrating premixed flames provides a mean to introduce chemical and turbulence time scales by considering a thin laminar flame in a turbulent flow field. The key goal behind laminar flamelet modelling is to incorporate various flamelet stretching mechanisms to account for effective turbulence time scales by assuming that the heat release will only occur within the thin reaction zone. Much of the flamelet modelling literature focuses on deriving effective turbulent burning velocity (e.g. Abdel-Gayed et al. (1987)). An alternative modelling strategy has been pursued for the flamelet regime since the introduction of the Bray-Moss-Libby (BML) model (Bray et al. (1985)). This model has been extended from its preliminary form since first introduction in premixed turbulent combustion by Bray and Moss (1977), Bray et al. (1981), and Libby and Bray (1981), and subject to many interesting research later. The BML models are derived based on a combination of statistical approaches using probability density functions (PDF) and physical analysis. This combination has led to the development of both complex and simple models using probability functions. For instance, Bradley et al. (1992) used a classical presumed PDF model by assuming a weak flamelet, which considers reduced chemistry through the parameterisation of detailed chemistry. On the other hand, following BML analysis, mean chemical reaction rate can be simply modelled by analysing the flamelet and using modelling tools as Bray et al. (1985):

$$\dot{\omega}_c = \rho_u u_L^0 I_0 \Sigma \quad (2.6)$$

Where $\dot{\omega}_c$ is the chemical reaction rate, ρ_u is unburned gas density, I_0 is the mean stretch factor and Σ is the flame surface density (FSD), defined as the flame surface to volume ratio.

Modelling the chemical reaction rate, using the above approach requires models for the FSD and mean stretch factor. Several models and empirical correlations for the evaluation of flame stretch I_0 can be found in the literature. For example, Bray (1990) identified flame stretch as a function of Karlovitz number. Bradley et al. (1992) identified flame stretch as a function of Karlovitz and Lewis numbers, while Bray and Cant (1991) deduced an analytical expression from DNS data as a function of Markstein and Karlovitz numbers.

The flame surface density, Σ in equation (2.6) represents the balance between turbulence, which wrinkles the flame and the laminar flame propagation, which smoothing out the flame wrinkles (Bray and Peters (1993)). The flame surface density can be computed by either solving a transport equation (Pope (1988), Candel and Poinso (1990), and Cant et al. (1991)) or via an algebraic model (Bray (1990) and Trounev and Poinso (1994)). Various models available to compute FSD have been evaluated in the RANS (Reynolds Averaged Navier-Stokes equations) frame work (Duclos et al. (1993) and Prasad and Gore (1999)), which is a central problem in establishing a good flamelet model. Duclos et al. (1993) showed that solving a transport equation for the FSD in its exact form is highly difficult due to the excessive computational times involved. While, solving a transport equation for the flame surface density has been the subject of many works in RANS and LES (Prasad and Gore (1999), Hawkes and Cant (2001), and Patel et al. (2003)). Although solving a transport equation for the flame surface density is an attractive option, this will result in several unclosed terms which need to be closed by appropriate sub-models and restricted to handle extreme cases, where coupling between the flow-field and flame front is intense. On the other hand, algebraic models are simple, yet well established and are similar to the Bray-Moss-Libby (BML) approach in the context of RANS.

Bray et al. (1985) proposed a simple empirical model to calculate Σ as $[\bar{c}(1 - \bar{c})]/L_y$, where \bar{c} is the time averaged reaction progress variable and L_y is a length scale associated with wrinkled flame. The length scale, L_y can be modelled by assuming it is proportional to the integral length scale (Abu-Orf and Cant (2000)) or by an additional transport equation Lindstedt and Váos (1999). Gouldin et al. (1989a) and Weller et al. (1998) derived an expression for Σ based on the fractal theory by viewing the turbulent

flame as a fractal surface within the lower and outer cut-off scales and found to be in good agreement (Veynante and Vervisch (2002)) with experimental data for $\Sigma/[\bar{c}(1 - \bar{c})]$.

Pope (1988), Duclos et al. (1993), and Veynante et al. (1996), modelled the flame surface density either by balancing the production, transport and destruction terms or developing a correlation from experimental data. On the other hand, Σ can be modelled using turbulent flame speed (TFS) closure as a ratio between the turbulent flame surface area per unit volume A_T to its projection on its average surface per unit volume \bar{A} . The ratio of A_T/\bar{A} can be modelled by following the notable observation of Damköhler (1940). Recently, this approach has been used by Muppala et al. (2005) in RANS and by Aluri et al. (2006) in LES to predict various turbulent premixed flames.

Most of these flamelet models have been successfully transformed from the framework of RANS to LES and applied to a variety of practical problems such as V-flames Chan and Li (2005), SI engines (Richard et al. (2007)), gas turbines and Ramjets Menon and Jou (1991). Boger et al. (1998) deduced a simple algebraic model suitable for LES of turbulent premixed flames. This model has been used by Kirkpatrick et al. (2003) and Masri et al. (2006) to predict the turbulent deflagrating flame in an obstructed explosion chamber and found to be predicting reasonably well. However, their studies under-predicted explosion overpressures, flame position and structures. Masri et al. (2006) reported that using a complex model for the flame surface density would provide more accurate predictions for the flame characteristics.

Recently, Wang et al. (2012) mentioned that Boger et al. (1998) model may be viewed as an approximation of F-TACLES (Auzillon et al. (2010)) under the condition that the flame front is infinitely thin. Moreover, Colin et al. (2000) showed that it is less demanding in terms of mesh requirements than the thickened flame model TFLES.

2.3.1.1 The Dynamic Flame Surface Density

Gubba et al. (2007) developed the concept of the dynamic flame surface density model, which was proposed by Hawkes and Cant (2000), Knikker et al. (2002) and Knikker et al. (2004). This model follows the dynamic procedure of Germano et al. (1991) and the

similarity concept of Bardina et al. (1980). The dynamic flame surface density model, has been linked with flame wrinkling theory in order to dynamically evaluate the model coefficient. This procedure is followed to calculate the fractal dimension of the turbulent premixed flame, which has been the subject of many interesting research works (Mandelbrot (1975), Gouldin (1987), Kerstein (1988), Gouldin et al. (1989a), and Gouldin et al. (1989b)). This concept is adopted in the current study and further developed to account for the non-unity Lewis number effect and also validated using three different fuels.

2.3.2 Turbulent Flame Speed Closure

Chemical reaction rate can be simply modelled by the overall turbulent flame speed u_T as a function of the ratio of turbulent flame surface area to laminar flame surface area. Damköhler (1940) hypothesised a relation given in equation (2.7) and Abdel-Gayed et al. (1987) extended (shown in equation 2.8) this by correlating various experimental measurements of turbulent premixed flames. Since the turbulent flame speed (TFS) is not a well-defined quantity and known to be dependent on many physical and chemical parameters, use of TFS closure is quite questionable. However, (TFS) closure has been successfully used in RANS (Zimont et al. (1997), Polifke et al. (2000), and Zimont (2000)) for gas turbine combustors and in LES Flohr and Pitsch (2000) for industrial burners, with certain limitations. This simple closure has been widely used in flame tracking approach (G-equation) with various modifications. Current models calculate u_T as a function of turbulence intensity alone show significant variations (Bradley (1992)) reflecting the possible influence of other parameters, such as the scalar dissipation rates. Also, Gubba (2009) claimed that the use of TFS closure is debatable in LES as it is not well suited to close Favre averaged transport equations. However, Xu et al. (2015) used the TFS closure in the context of LES to model deflagration in a semi-confined obstructed chamber, where good results were obtained.

$$\frac{u_T}{u_L} = \frac{A_T}{A_L} \quad (2.7)$$

$$\frac{u_T}{u_L} = 1 + \alpha \left[\frac{u'}{u_L} \right]^n \quad (2.8)$$

This closure has been used in conjunction with the flame surface density model to predict turbulent premixed flames in RANS (Muppala et al. (2005)) and in LES (Aluri et al. (2006)).

2.3.3 The Eddy-Break-Up Model

The Eddy-Break-Up (EBU) model, originally developed by Spalding (1971), views the reaction zone as a collection of fresh and burnt gas pockets transported by turbulent eddies and can be modelled as:

$$\bar{\omega}_c = C_{EBU} \bar{\rho} \frac{\varepsilon}{k} \frac{\tilde{Y}_{fu}}{Y_{fu}^\circ} \left(1 - \frac{\tilde{Y}_{fu}}{Y_{fu}^\circ} \right) \quad (2.9)$$

where Y_{fu}° is the fuel mass fraction in fresh gases, k and ε are respectively the turbulent kinetic energy and its dissipation rate, C_{EBU} is a model constant. EBU models have been extensively used in RANS (Fureby and Löfström (1994) and Möller et al. (1996)) and in LES (Fureby and Löfström (1994), Möller et al. (1996) and Porumbel and Menon (2006)) for industrial applications due to its simplicity, despite over estimation of the reaction rate. In this approach, the reaction rate is assumed to be proportional to the intermittency between fresh and burnt gases and inversely proportional to the turbulence time scale. This model is attractive because the reaction rate is simply written as a function of known quantities without any additional transport equations, simply by neglecting the chemistry effects. This results in an overestimate the reaction rate, especially in highly strained flow regions (Cant and Bray (1989)).

In the context of LES, EBU models have found to predict reasonably well for bluff body stabilised flames (Fureby and Möller (1995)), without any additional sub-grid scale models. Porumbel and Menon (2006) modelled the bluff body stabilised flame using EBU model and Linear Eddy Model (LEM) in LES. They concluded that, results using EBU found to under-predict turbulent flame wrinkling, turbulent mixing rate, temperature field, and over-predict turbulent flame thickness. Kim et al. (2006) have reported results by using EBU model for gas turbine flame holder stabilised flames for various equivalence ratios, with an additional transport equation for turbulent kinetic energy and an algebraic equation for dissipation rate. Their studies found to predict stabilised flame very well except few deviations from experimental data at

stoichiometric condition. Hence, it can be concluded that the success of EBU models with or without sub-models or additional transport equations is variable.

2.3.4 Artificially Thickened Flame Approach

As mentioned earlier in this chapter, that the premixed flame is very thin i.e. about 0.1 to 1 mm (Colin et al. (2000)) and cannot be resolved on a LES numerical grid. This difficulty in resolving flame on a numerical grid, associated with the stiffness of the progress variable has led to the development of an alternative approach of — thickened flame modelling by Butler and O'Rourke (1977) originally for laminar flame calculations. This method has been extended to LES by Veynante and Poinso (1997) and Thibaut and Candel (1998) for turbulent premixed flames.

The basic idea of this approach is thickening of the flame brush by a factor F to include several computational cells, where the diffusivity is multiplied by a factor F and the reaction rate is divided by the same factor, while keeping the laminar flame speed constant, so that its structure is resolved by LES. The flame thickening is accomplished by a modification of the scalar transport equations, following the simple theories of laminar premixed flames (Kuo (2005)), such that the flame speed $u_L \propto \sqrt{\alpha_T \dot{\omega}}$, and the flame thickness $\delta_L \propto \alpha_T / u_L$. Where $\dot{\omega}$ is the reaction rate and α_T is the thermal diffusivity. This results in a flame of thickness ($F\delta_L$) that propagates at a speed u_L . The advantages of the approach are that it is simple to implement and, due to the Arrhenius law, it can handle some effects associated with ignition and flame-wall interaction processes (Colin et al. (2000)). This approach models both the reaction rate and sub-grid transport terms simultaneously.

Xiao et al. (2012) showed that a combination of thickening flame approach with the seven-step chemistry scheme is quite reliable for predicting the transient premixed hydrogen/air combustion in a closed duct. This combination reproduced the four stages of the flame dynamics well (i.e. spherical flame, finger-shape flame, flame with the skirt touching the side walls and tulip flame) with reasonably predicted pressure dynamics, but their model did not account for the wrinkling of the flame front as it remains unresolved.

The flame thickening approach seems to be very attractive for flows in which the turbulence-flame interactions are governed mainly by very large scale flow structures. However, there are several drawbacks when applied to many common scenarios. Firstly, this approach assumes implicitly that the reaction rate is controlled by chemistry rather than diffusive processes and hence the use of detailed chemical kinetics is recommended for better accuracy (Poinsot et al. (1991)). This is numerically unattractive compared to the laminar flamelet approach where fast chemistry is considered and reaction is assumed to be controlled by transport processes. Secondly, the thickening of the flame decreases the sensitivity towards turbulent motions. Therefore the turbulent and chemical time scales are altered, which need to be accounted separately. The turbulent eddies smaller than the size of thickened flame are found to have no significant effect in stretching the flame (Poinsot et al. (1991)). This effect was observed for the thickened flame model in comparison with DNS results by Veynante and Poinsot (1997). Thirdly, the sensitivity of the laminar flame velocity to stretch and curvature is increased by the transformation since the Markstein length is proportional to the flame thickness. The thickened flame will react to a stretch of k/F , as the actual flame would react to a stretch of k . This may influence flame quenching and may be prone to quench thickened flame much easily.

To overcome problem of that technique with the flame stretch, an efficiency function E relating the actual flame stretch to the stretch felt by the thickened flame has been proposed by Meneveau and Poinsot (1991) based on DNS results. Similarly, Charlette et al. (2002) developed a dynamic model based on local flame conditions to overcome the over-response of the flame stretch in thickened flame modelling.

2.3.5 Probability Density Function (PDF) Model

Probability density function (PDF) methods have been used in turbulent reacting flows for over 60 years (Kollmann and Schmitt (1981)), and are quite established, especially in turbulent non-premixed combustion (Cook and Riley (1994)). In PDF methodology, the flame front/flow field is described based on statistical properties and probability theories. These methods have close tie-ups in deriving sub-models in flame tracking and flame surface density approaches. There are several methods to describe flow/flame probability functions such as presumed PDF, where a shape is assumed by solving a

PDF balance equation, joint PDF, where probability of a set of variables are either solved using a transport equation or modelled and finally, conditional PDF, where PDF is used based on certain local conditions.

Several studies (Pope (1985), Givi (1989), Gao and O'Brien (1993), Madina and Givi (1993), Möller et al. (1996), Cook et al. (1997), and Cook and Riley (1998)) discussed the development and application of PDF methods for turbulent reacting flames in RANS and LES. The fundamental idea of the PDF method is based on describing the statistical property of thermo-chemical variables. The advantage of the PDF approach is that the reaction rate term can be closed exactly through the simple relation as:

$$\overline{\dot{\omega}_c} = \int \dot{\omega}(\varphi) P_{sg}(\varphi, x, t) d\varphi \quad (2.10)$$

where $\dot{\omega}_c$ is the reaction rate, P_{sg} is the probability density in φ -space, x is the position and t for time.

Using PDF models have produced good results in comparison with DNS data for non-premixed combustion (Möller et al. (1996), Reveillon and Vervisch (1997), Colucci et al. (1998) and Cook and Riley (1998)) successfully predicted premixed combustion using presumed PDF approach, assuming a multidimensional normal distribution for the scalar variables. With this success, PDF of turbulent premixed flames has become an alternative method to predict flames in various combustion regimes. However, the shape of initial PDF may need to be obtained either from experimental data or DNS data.

2.3.6 Flame Tracking Approach (G-equation)

The flame tracking approach or G-equation, originally introduced by Williams (1985b) is based on the flamelet assumption. In this approach the flame is assumed to be a thin surface and can be represented or tracked by the level surface of a scalar field G , which has a constant value G_o at flame surface and can be described as:

$$\frac{\partial G}{\partial t} + u \cdot \nabla G = w |\nabla G| \quad (2.11)$$

where w is the local relative propagation velocity of the flame. The equation (2.11) can be used to represent a surface of chosen variable such as temperature, reaction progress

variable or any other variable of interest. Pitsch (2006) argued that this approach is not modelling the flame front, rather a numerical method, which can resolve the flame front. Several studies reported, successful prediction of turbulent flames using G-equation in RANS and LES. Yakhot (1988) was the first to suggest this equation to be used in LES combustion. Following Yakhot (1988), several authors (Kim and Menon (2000), Pitsch and Duchamp de Lageneste (2002), and Huang (2003)) proposed LES formulation of the G-equations and applied to various combustion chambers such as ramjet (Menon and Jou (1991)), IC engines (Naitoh et al. (1992)), and Bunsen burner experiment (Pitsch and Duchamp de Lageneste (2002)).

Pitsch (2006) argued that the G-equation for the filtered flame front used in the above studies, did not consider the special character while filtering the G-equation, which has caused inconsistency with generalised scaling symmetry. Pitsch (2006) derived a new filtering technique for G-equation and reported that the filtered G-equation (equation 2.12) is valid in corrugated flamelet and the thin reaction zones.

$$\frac{\partial \tilde{G}}{\partial x} + \hat{u} \cdot \nabla \tilde{G} = -(u_L + u_k) \cdot \mathbf{n} \cdot \nabla \tilde{G} \quad (2.12)$$

where \mathbf{n} is the flame front normal vector, and u_L and u_k describe laminar flame propagation and flame advancement by curvature effects respectively, which requires sub-models to close. Pitsch (2006) proposed models for u_L and u_k based on production-dissipation balance assumption and found to fit well in LES, with certain drawbacks near the flame holder, where the flame is not fully established. Also he described that in the above equation is not the filtered G-field, but a level set representing the flame front position. This is clearing the concerns raised by Hawkes and Cant (2000) regarding this approach in tracking the level set of flame front. However, the G-equation employed in the above studies appears to still have some drawbacks.

In the study of Makarov et al. (2010) to compare between different combustion models used to study lean hydrogen mixture explosions, mainly (eddy dissipation, customized RNG model and flame tracking model), showed that the flame tracking model used by (Efimenko and Dorofeev (2001) - KI) gives the best results when compared to other models as shown in (Figure 2.4). Also the study points-out is that the mesh resolution could be a more relevant parameter than the complexity of the model.

Modelling the flame structure is a major challenge in G-equation, as the flame surface can only be tracked and not resolved in numerical space. This can be achieved by the sub-models derived either from experiments or DNS data. Filtered G-equation (2.7) does not include any diffusion terms, which may lead to numerical difficulties. Finally, there is no theoretical lower limit for the radius of the flame front curvature. As the flame front propagates, cusps can form with zero radius of curvature (Pope (1988)), which cannot be resolved on the computational mesh. Cusps are not expected for the filtered LES field since these would be smeared out by the filtering process. This problem is usually overcome by the introduction of artificial diffusion (Piana et al. (1997)).

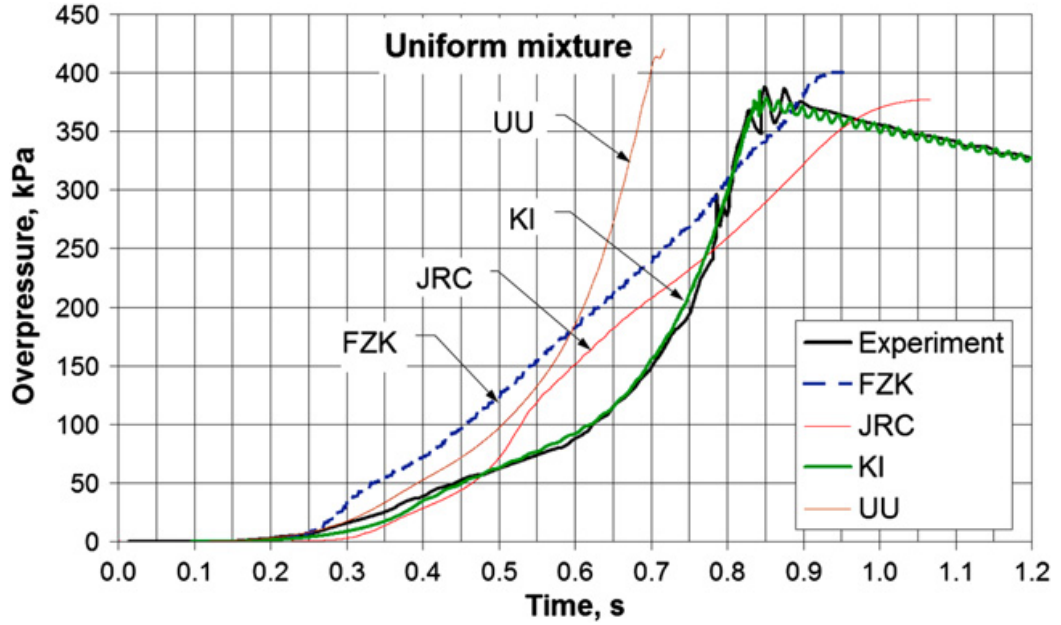


Figure 2.4 Comparison of experimental and simulated pressure dynamics for the uniform 12.8% vol. hydrogen–air mixture in a 10.7 m³ closed vessel (Makarov et al. (2010)). FZK: Forschungszentrum Karlsruhe GmbH-Germany, JRC: Joint Research Centre-Institute for Energy-The Netherlands, KI: Kurchatov Institute-Russia, UU: University of Ulster-UK.

2.3.7 Marker Field Approach

The S^+ marker field model in LES is relatively a new derivative of above discussed laminar flamelet models, which captures flame propagation by balancing reactive,

diffusive fluxes in combustion space. Originally, the concept of the marker field was introduced by Bilger (2004) in DNS and extended to RANS by Bilger et al. (2004). Recently, this model has been extended in the frame work of LES by Christophe and Laszlo (2007) to predict stabilised turbulent premixed flame behind a back-facing step.

2.3.8 Other Modelling Techniques

As mentioned above, modelling the reaction rate is a critical task in LES of premixed turbulent combustion, due to the complex thermo-chemical-turbulence interactions. One major difficulty is to predict the random, non-linear behaviour of chemical reaction rate as a function of available scalar variables. Also, in LES especially, the laminar flame thickness which is typically thinner than the characteristic flow turbulence length scale and smaller than a typical LES filter width ($\bar{\Delta}$). Hence it is a requirement of any SGS combustion model in LES, to address the above issue with an accurate, yet computationally efficient model. One way of modelling the filtered mean reaction rate term is either by solving transport equations of the detailed or reduced chemical kinetic mechanism of the fuel. This generally includes tens of species and several hundreds of elementary reactions. Solving these transport equations directly in RANS itself are quite complex and solving them in LES is almost impossible. However, several alternative approaches are available to implement detailed chemistry effects. These include techniques such as, the “skeletal mechanism” obtained due to the elimination of insignificant species from detailed chemical mechanism, “dimension reduction techniques” due to low-dimensional manifold systems such as quasi-steady state assumption (Tomlin et al. (1992) and Lu and Law (2008)), Flamelet Generated Manifolds (Oijen and Goey (2000), and Vreman et al. (2008)), flame prolongation of intrinsic low-dimensional manifold (Gicquel et al. (2000) and Fiorina et al. (2003)), and rate-controlled constrained equilibrium (Hamiroune et al. (1998), and Janbozorgi et al. (2009)). Where, it should be noticed that all the above techniques require massive computational resources.

Finally, from the previous discussions, the flame surface density concept is used in the current study, due to the simplicity and less computational time/cost required, yet effective in modelling the reaction rate with a very good accuracy.

2.4 Fuel Characteristics

This section gives an overview for the three fuels used in the current work, CNG, LPG, and hydrogen with focus on the later as it is considered as the future fuel. The possibility of using hydrogen as an energy carrier has increasingly attract the interest of both public and government policy makers in recent times due to increasing concerns about the possible impact of greenhouse gases and the finite nature of fossil fuel reserves (Middha (2010)). The expected shortage of fossil fuels and the fear of carbon induced climate changes make the deployment of hydrogen in combination with renewable energy sources and possibly nuclear energy an interesting alternative (Winter (2009)). Hydrogen combustion does not produce any greenhouse gases that are responsible for local and global environmental concerns compared to CNG and LPG.

It is worth to mention that, the majority of hydrogen research is motivated by the enhancement of its economy, i.e. developing production and storage techniques, the issues related to the safety of hydrogen during production and subsequent large-scale usage remains a significant concern (e.g. Astbury (2008)) which needs more attention. The nuclear industry has also been particularly interested in evaluating hydrogen safety, especially due to accidents like Three Mile Island (USA, 1979), Chernobyl (USSR, 1986), and Fukushima Daiichi (Japan, 2011) and the potential increase in use of nuclear power. Compared to offshore oil exploration accidents, where consequences will be mainly local, the consequences from nuclear accidents can be more global.

The risks from hydrogen primarily stem from its wide flammability range, extremely fast burning rate (order of magnitude larger compared to other fuels), and the considerable amount of energy released when it burns or explodes (Astbury (2008)). This leads to consequences that are much more severe as compared to hydrocarbons. This is clearly shown by experiments carried out by Bjorkhaug (1988) in a wedge shaped vessel (Figure 2.5), which showed that the overpressures generated in combustion of a fuel-air mixture for various gases. It is obvious from that the overpressure generated from hydrogen explosion is about four times that of ethylene and almost eight times when compared with the other hydrocarbon fuels. On the other hand, hydrogen is also quite different from natural gas in certain other ways, some of which actually help to reduce the risk of using the gas. Hydrogen is much lighter than air and therefore, has very strong buoyancy that will quickly remove the gas in an

unconfined situation. However, any leakage of hydrogen in a confined space, such as parking garages and tunnels poses a significant hazard. Further, much lower energies are needed to ignite hydrogen and mitigation methods traditionally used for other fuels rarely work in case of hydrogen (Middha (2010)). The safety issue is further worsened by the wide detonability limits and the tendency of the flames to accelerate rapidly due to the very high laminar burning velocity of hydrogen (Masri et al. (2011)). Clearly, hydrogen has many characteristics that are significantly different from conventional gaseous fuels such as methane, propane, butane...etc. These must be accounted for before designing and installing any systems such as fuel cells, engines, etc. that will form a part and parcel of any future society that uses hydrogen as an energy carrier. These are described in some details below.

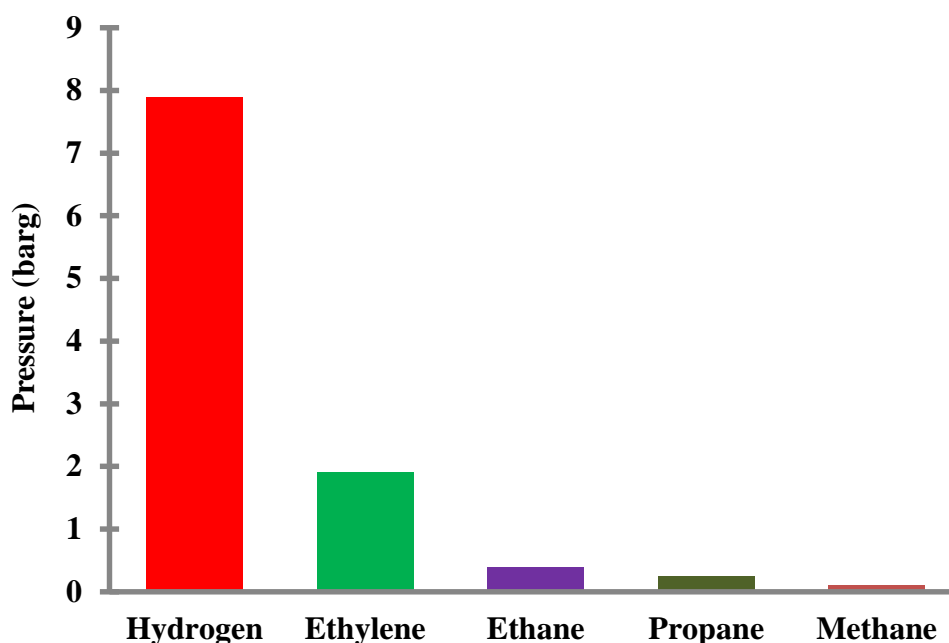


Figure 2.5 Comparison of explosion pressure for various Stoichiometric fuel-air mixtures in a 10 m wedge-shaped vessel, reproduced from Bjorkhaug (1988).

2.4.1 Physical and Chemical Characteristics

At atmospheric temperature and pressure, hydrogen is colourless, odourless, non-toxic and non-corrosive, which is physiologically not dangerous in principle. One of its most important and positive characteristics is its low density (it is the lightest of all elements).

It is positively buoyant above a temperature of (-251°C). Hydrogen gas has a very high diffusivity and a high buoyant velocity. Therefore, it mixes rapidly with ambient air upon release. As mentioned earlier, this is a favourable safety effect in unconfined and well-ventilated areas where it helps to reduce the possibility of forming a flammable mixture in the vicinity of a release. However, if leaks occur in (partially) confined or poorly ventilated spaces, the concentration of hydrogen can reach dangerous levels in higher regions, for example, underneath a roof. The risk of explosion can then be considerable if ignition sources are present. Hydrogen molecules have a small size, small molecular weight, and a low viscosity. As a result, hydrogen can permeate through materials and pass through smaller leak paths as compared to other gases. This increases the risk of the formation of a flammable gas cloud. Hydrogen gas does not have a flash point as it is already a gas at ambient conditions. Therefore, cryogenic hydrogen will flash at all temperatures above its boiling point of (-253°C).

2.4.1.1 Ignition

The auto-ignition temperature for hydrogen, which is the minimum temperature of a hot surface that can ignite a flammable mixture, is 520°C (Bjerketvedt et al. (1997)). Over the flammable range of hydrogen-air mixtures, the minimum ignition energy varies by almost three orders of magnitude and can be as low as 0.02 mJ (Cadwallader and Herring (1999)), a value that is an order of magnitude lower than that of hydrocarbon-air mixtures. The minimum ignition energy for hydrogen-air mixtures occurs around stoichiometric composition (i.e. 30 % by volume for hydrogen). At lower flammability Limits, the ignition energy for hydrogen is similar to that of methane. In addition, many of the weak ignition sources such as electrical equipment sparks, electrostatic sparks or sparks from striking objects involve more energy than what is required to ignite a hydrogen-air mixture.

Spontaneous ignition is much more commonly observed with hydrogen. There have been several explanation advocated to explain this effect. One of these is that hydrogen exhibits a positive “Joule-Thomson” effect at temperatures above (-80°C), i.e. the inversion temperature. This means that the temperature of hydrogen gas increases upon de-pressurisation, which in turn may lead to ignition. This makes hydrogen more vulnerable to ignition after sudden release from high pressure containment. Another

explanation is “diffusion ignition” whereby a shock wave from expansion of high-pressure gas into air is postulated to cause local auto-ignition.

2.4.2 Combustion Properties

Hydrogen burns in a non-luminous, almost invisible pale blue, hot flame to form water vapour (and there is no release of CO₂ or soot). A hydrogen fire is almost impossible to detect with the eye and there is very limited radiation due to the absence of soot. The low emissivity of a hydrogen flame reduces the heat transfer by radiation to objects near the flame. Thus, a hydrogen fire is potentially less dangerous than a CNG and LPG fire.

The flammability range of hydrogen compared with other fuels as shown in Figure 2.6, is between (4 - 75 % volume) in air (Coward and Jones (1952)). In comparison, the flammability range of methane (CNG) is between (5.3 - 15 % volume) and propane (LPG) is between (2.2 – 9.6% volume). It should be mentioned that the flammability range increase with the increase in the initial temperature and pressure (Liu and Zhang (2014)). For the maximum flame temperature of a burning (premixed stoichiometric) hydrogen-air mixture is 2130 °C (Glassman (1987)).

As will be discussed later in this chapter, the burning velocity of hydrogen in air at stoichiometric ambient conditions is around 2.0 m/s reaching a maximum of approximately 3 m/s at a concentration of 40.1 %, which would even increase to 11.75 m/s in pure oxygen. In comparison, the value for natural gas is of the order of 0.4 m/s. These values are higher than the ones of hydrocarbon fuel-air mixtures due to the fast chemical kinetics and high diffusivity of hydrogen. This leads to consequences (upon ignition) that are much more severe compared to CNG and LPG.

The detonability limits of hydrogen lie in the range of 18 % (as low as 11 % in some experiments) to 59 % of hydrogen concentration in air by volume. There is also a high sensitivity to a transition to detonation (DDT). Detonation can potentially cause a much severe damage as compared to an ordinary explosion (deflagration). A measure of the sensitivity of a mixture is the detonation cell size, where the severity increases as the cell size decrease. The detonation cell size for a stoichiometric hydrogen-air mixture is of the order of 10 - 15 mm. In comparison, the value for a methane-air mixture is as

large as 330 mm. Thus, from this brief description of hydrogen properties, it is clear that the use of hydrogen represents many potential hazards even if it does have some favourable properties such as high buoyancy, and hence establishing viable tools to carry out the required safety and risk analyses connected with the use of hydrogen becomes more and more urgent demand.

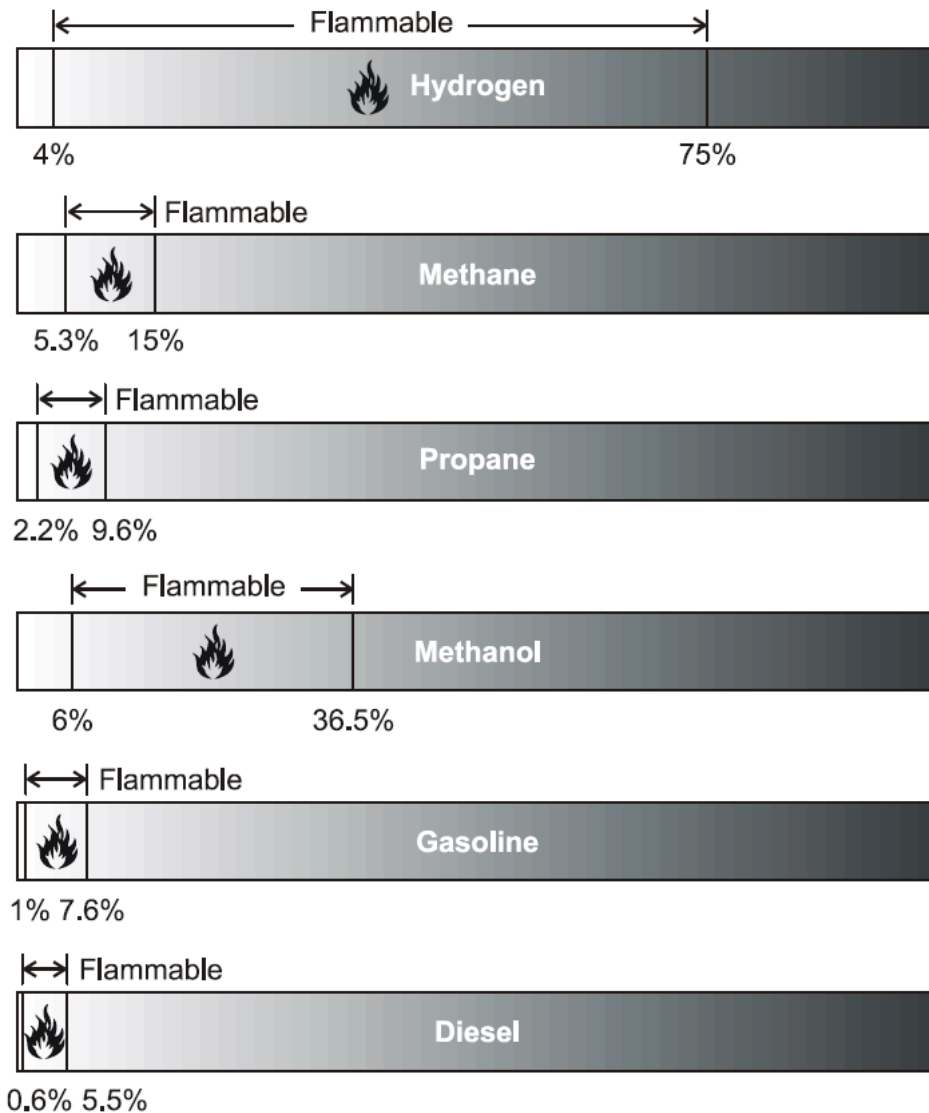


Figure 2.6 Flammability range of hydrogen compared with different fuels reproduced from Bjerketvedt et al. (1997).

2.4.3 Laminar burning velocity

The laminar burning velocity u_L plays a vital role in determining the reactivity and subsequent overpressure generation for a given mixture. Laminar burning velocities for

hydrogen-air mixtures have been determined by several researchers (Iijima and Takeno (1986), Aung et al. (1997) and Bradley et al. (2007)). Figure 2.7 presents data taken from several measurements (Aung et al. (1997)). It is evident that, as we increase the equivalence ratio Φ , the laminar burning velocity increases until we reach a maximum value around ($\Phi = 1.7$), then it starts to decrease (Iijima and Takeno (1986)). It can be seen that most of the measured values of un-stretched laminar burning velocities that have not been corrected for stretch are significantly larger than the stretch-corrected results. This behaviour is even more obvious at fuel-rich conditions where discrepancies can be as large as a factor of 2. This is due to much higher flame stretch (represented by large Markstein numbers) at these conditions.

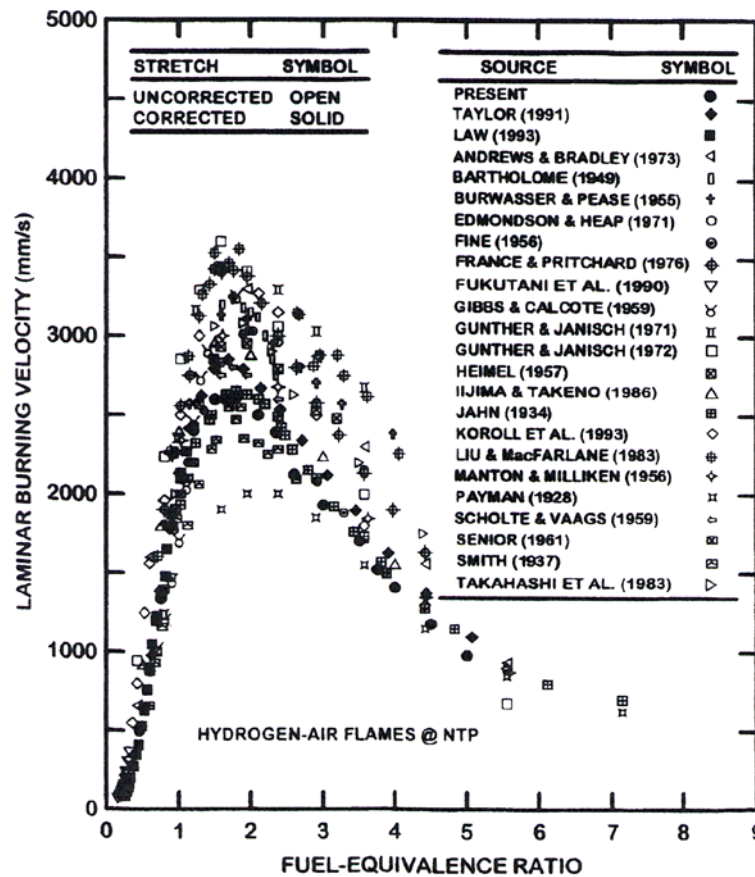


Figure 2.7 Corrected and un-corrected measurements of laminar burning velocities as a function of equivalence ratio for hydrogen-air mixture at NTP (Aung et al. (1997)).

However, in the present study, a lean fuel-air mixture is considered, so the value for the corrected and un-corrected (strained and un-strained) are almost the same (Aung et al.

(1997)) at normal temperature and pressure. It is worth to mention that, in contrast to other fuels (e.g. methane and propane) the laminar flame speed u_l increases with pressure (Iijima and Takeno (1986)) and this actually worsen the situation more in case of an explosion. Also, the laminar flame speed u_L increases as the unburned gas temperature increases as common hydrocarbon fuels (Iijima and Takeno (1986)).

The laminar burning velocity for hydrogen is calculated using the expression of Iijima and Takeno (1986), which accounts for the effects of local pressure and temperature

$$u_L = u_L^o \left\{ 1 + \beta_1 \log \left(\frac{P}{P_o} \right) \right\} \left(\frac{T}{T_o} \right)^{\alpha_1} \quad (2.13)$$

where u_L^o is the is the laminar burning velocity at reference temperature and pressure, T_o and P_o are reference temperature and pressure 298.15 K and 1.01 bar respectively, T is the un-burnt gas temperature, α_1 and β_1 are constants that depends on the equivalence ratio Φ and calculated from the following expressions of Iijima and Takeno (1986).

$$\alpha_1 = 1.54 + 0.026(\Phi - 1) \quad (2.14)$$

$$\beta_1 = 0.43 + 0.003(\Phi - 1) \quad (2.15)$$

Also, Molkov et al. (2006) used a comparable power law correlation to calculate laminar flame speed which is also found to be a function of pressure and temperature as follows:

$$u_L = u_L^o \left(\frac{T}{T_u} \right)^{m_o} \left(\frac{P}{P_o} \right)^{n_o} = u_l^o \left(\frac{P}{P_o} \right)^{\varepsilon} \quad (2.16)$$

where m_o is temperature index, n_o is baric index, $\varepsilon = m_o + n_o - m_o/\gamma_u$ and it is usually in the range of 0.49-0.68 (HySafe (2007) and Babkin (2003)). However, it was demonstrated that an error of the approximation does not exceed 15%. Also, the dependence of burning velocity on hydrogen concentration was accounted for by using a linear function $f(Y_{H_2})$, equal to 1 in the stoichiometric mixture (29.7% by volume of hydrogen) and 0 at the lower flammability limit (4% by volume of hydrogen): $u_l^o = u_l^o(Stioch) \cdot f(Y_{H_2})$.

Also, Dahoe (2005) used the same power law expression as mentioned above in his model in order to determine the laminar flame speed, with the same pressure and temperature indices used by Iijima and Takeno (1986) and obtained an expression in the form of:

$$u_l = u_l^o \left(\frac{P}{P_o} \right)^{0.6} \quad (2.17)$$

However, Dahoe (2005) showed that laminar burning velocity for rich mixtures fall within the scatter of data obtained within the scatter of data obtained by more advanced methods that take the influence of flame stretch into consideration. While for lean mixtures, the laminar burning velocity is consistently higher, but at the same time close enough to the ones obtained by more advanced methods.

On the other hand the commonly used laminar burning velocity expression of Metghalchi and Keck (1980) and Metghalchi and Keck (1982) is used in this study for CNG and LPG, which accounts for the effects of local pressure and temperature, and is given as:

$$u_L = u_L^o \left(\frac{T_R}{T_o} \right)^{\alpha_1} \left(\frac{P}{P_o} \right)^{\beta_1} \quad (2.18)$$

where u_L^o is the reference or un-strained laminar burning velocity, T_o and P_o are the reference temperature and pressure of 298.15 K and 1.01 bar respectively, T_R is the reactant temperature, and α_1, β_1 are constants calculated from the following expressions of Metghalchi and Keck (1980) and Metghalchi and Keck (1982), and can be given as:

$$\alpha_1 = 2.18 - 0.8(\phi - 1.0) \quad (2.19)$$

$$\beta_1 = -0.16 + 0.22(\phi - 1.0) \quad (2.20)$$

2.4 Summary

This chapter has described some fundamentals and features of turbulent premixed flames. A wide investigation of experimental and numerical studies, which employed similar forms of the combustion chamber employed in the present study, has been presented. Various regimes of turbulent premixed combustion have been discussed in

general and in the LES context. Several reaction rate modelling approaches suitable for RANS and LES were presented and discussed. A brief history and evolution of the flamelet models, employed in this study for mean chemical reaction rate was presented. Finally, a brief overview for the three fuels used in the present study

Chapter 3

Large Eddy Simulation of Reacting Flows

This chapter reviews the modelling of turbulent flows by applying the large eddy simulation technique (LES) and discusses the main issues that have to be considered before implementation. Some fundamentals such as, spatial filtering technique, mathematical description of filters and decomposition of velocity components are briefly explained. The governing equations along with the Favre averaging and the unclosed terms are discussed. Hence, various models and methodologies available to close the sub-grid scale momentum fluxes and the choice of model considered in the present simulations are discussed. Finally, simple and widely used gradient transport model is used to account for the sub-grid scale turbulent fluxes in filtered energy and reaction progress variable equations also discussed.

3.1 Background

Large eddy simulations (LES) is an extremely powerful and highly reliable modelling technique and has been proved to be so for the last couple of decades, following the pioneering work of Smagorinsky (1963) and the first successful application to turbulent channel flows by Deardorff (1970). Since then, LES has been intensely used to develop underlined theories and to understand various flow problems ranging from simple to complex flow configurations such as fluid flow over bodies, turbulence-transition modelling, forecasting weather conditions, understanding the aerodynamics of vehicles, and combustion dynamics...etc. LES is basically a numerical technique, which separates large eddies from small eddies by the application of a low-pass filtering technique (i.e. it filters out the scales associated with high frequencies). In most turbulent flows, large eddies above certain cut-off scale are expected to be responsible for most of the transportation of mass, momentum and energy. However, the smaller eddies formed due to the interactions of these large eddies are generally expected to be isotropic in nature and eventually die out in due course, while dissipating energy fluctuations, which slightly affect the mean characteristics of the flow. This unique observation yields to resolve the separated large eddies explicitly and to model small

eddies/scales that are smaller than a chosen filter width by using a suitable sub-grid scale (SGS) model.

Numerical modelling of turbulent flows, usually involves defining the flow properties in terms of mean and fluctuations, corresponding to the instantaneous values associated with turbulence. The way these quantities are predicted or calculated will in general calibrate the accuracy of numerical approaches. LES lies between DNS, in which the whole of the turbulence spectrum is resolved, and RANS, where equations are solved in combination with a turbulence model to give a solution for the time-averaged flow-field. DNS is able to predict instantaneous and statistical flow information by resolving all flow scales ranging from the integral to Kolmogorov and provides a high degree of accuracy. However, DNS requires high computational resources and is restricted to simulate simple, low-Reynolds number flows. The use of the DNS technique is currently very limited to model development and will remain challenging in the foreseeable future to simulate real complex flow situations.

On the other hand, RANS requires only modest resources, where all flow scales are modelled and has been applied to a wide range of flow configurations with varying degrees of success. The accuracy of a RANS simulation depends on how well the model predicts the flow and generally model parameters must be ‘tuned’ in order to achieve acceptable accuracy. Modelling the whole spectrum of flow turbulence scales poses a great difficulty, which eventually led to develop the concept of LES. In LES, the large scales explicitly resolved are in fact equal to that of DNS large scales and gives both instantaneous and statistical information of the flow, while the effect of small scales are modelled. Since, only the sub-grid, dissipative scales, which are usually expected to be universal and homogeneous are modelled, the accuracy of the LES solution is less dependent on the accuracy of the model. Hence, LES demands greater computational resources than RANS, as it involves the resolving of large eddies.

Despite the advancements in available computational resources, key challenges remained in LES are sub-grid scale turbulence modelling and the scale separation. SGS or unresolved turbulence modelling in LES has matured to a greater level and usually modelled by the classical eddy viscosity model of Smagorinsky (1963). Smagorinsky

model has been widely used in many interesting works in early stages of LES (Lilly (1966), Deardorff (1970), Schumann (1975), Moin et al. (1978), and Moin and Kim (1982)) and continuing to be used with much remarkable advancements (Kirkpatrick et al. (2003) and Malalasekera et al. (2013)). Some other models are also available to account for SGS turbulence, like the model proposed by Yakhot and Orszag (1986) and Yakhot and Orszag (1987) based on the re-normalisation theory.

The classical Smagorinsky eddy viscosity model though widely used by turbulence modellers, however, it is found to fail for various reasons. The Smagorinsky model failed to predict the energy backscatter to the resolved scales and found to have improper asymptotic behaviour for the Smagorinsky model coefficient. These failures have been fixed by the development of the dynamic procedure (Germano et al. (1991)) to calculate the Smagorinsky model coefficient using local instantaneous flow conditions. The procedure typically involves the application of a test filter to the velocity field to extract information from the resolved scales based on scale similarity ideas of Bardina et al. (1980), which are then used to calculate the coefficient. Later on, Ghosal et al. (1995) and Piomelli and Liu (1995) extended this method using a localized dynamic procedure to calculate the model coefficient. Moin et al. (1991) had extended the Germano dynamic procedure for compressible flows, which has been found to be successful in predicting model coefficient and energy backscatter, and is used in the current work.

The second challenge posed by LES, is in separating the large scales from the small ones. This can be achieved by separating the scales in the exact solution by defining a cut-off length based on (Ferziger (1977) and Rogallo and Moin (1984)) in spectral space or applying a spatial filter of Leonard (1979) in physical space. The scales that are of a characteristic size greater than the chosen cut-off length are called large or resolved scales, and others are called small or sub-grid scales (SGS). But defining the cut-off length and the scale-separation mathematical operator are very difficult tasks in LES. The difficulty comes from the fact that many parameters contribute to the definition of the effective scale-separation operator. Moreover, Debliquy et al. (2004) used a novel sampling technique, replacing the traditional filtering in LES by sampling operators, which is not yet very popular, but seems to be promising in avoiding numerical errors.

However, in the context of LES for reacting flows, the governing equations are presented in the next section, so they can be easily dealt with in the later sections.

3.2 Conservation Equations

Governing equations of fluid flows can be derived by considering an infinitesimal control volume fixed in space and applying the conservation laws of physics. The derivation of equations can be found in many text books (e.g. Turns (2011) and Kuo (2005)) and are not considered here. The governing equations shown in the following sections are derived for a Cartesian coordinate system by considering the following assumptions. The use of these assumptions tends to reduce the complexity of the problem under investigation.

- Low Mach number
- Soret and Dufour effects are neglected
- Newtonian fluid
- Negligible bulk viscosity from Stokes hypothesis
- Ideal gases
- Fully premixed reactants with one-step irreversible chemistry

3.2.1 Conservation of Mass

Conservation of mass must satisfy the condition that, neither creation, nor destruction of the mass within the control volume is possible. Here, the total mass conservation equation is unchanged compared to non-reacting flows as combustion does not generate mass. Using of this principle with convective transportation of mass across the control surface, will leads to the continuity equation:

$$\frac{\partial \rho}{\partial t} + \frac{\partial(\rho u_j)}{\partial x_j} = 0 \quad (3.1)$$

where ρ is fluid density and u_j is the velocity in x_j -direction. Equation (3.1) is for unsteady, compressible and three-dimensional mass conservation, which can be simplified according to the problem.

3.2.2 Conservation of Momentum

Conservation of momentum is based on Newton's second law, which states that the rate of change of momentum of a fluid particle equals the sum of the forces on the particle and can be expressed by Navier-Stokes equation:

$$\frac{\partial \rho u_j}{\partial t} + \frac{\partial (\rho u_i u_j)}{\partial x_j} = -\frac{\partial P}{\partial x_j} + \frac{\partial}{\partial x_j} \left(2\mu \left[S_{ij} - \frac{1}{3} \delta_{ij} \frac{\partial u_k}{\partial x_k} \right] \right) + B_i \quad (3.2)$$

where P is the static pressure, μ is the dynamic viscosity, S_{ij} is the strain rate, δ_{ij} is the Kronecker delta and B_i is other body forces such as gravity, centrifugal and Coriolis forces acting on the fluid. The strain rate can be express as:

$$S_{ij} = \frac{1}{2} \left(\frac{\partial u_i}{\partial x_j} + \frac{\partial u_j}{\partial x_i} \right) \quad (3.3)$$

It is important to mention that the momentum equation given in (3.2) is balancing various forces in the fluid flow. Although this equation does not have explicit reaction rate term, the flow is modified by combustion, as the dynamic viscosity μ strongly changes because temperature varies in a ratio from 1:8 or 1:10 (Poinsot and Veynante (2012)). Also, density changes in the same ratio and dilatation through the flame front increases all speeds by the same ratio. Subsequently, the local Reynolds number varies much more than in non-reacting flow, despite the fact that the momentum equations are the same with and without combustion. Hence, the whole treatment of the governing equations is different and more details will be discussed later.

3.2.3 Conservation of Energy

Conservation of energy can be derived from the first law of thermodynamics and usually used to evaluate the temperature T and enthalpy h for a chemical reacting flow. Many forms of this equation exist, having static temperature, specific enthalpy, stagnation enthalpy or internal enthalpy as the principal variable. However, Cant and Mastorakos (2008) mentioned that, in turbulent combustion with low Mach number, it is easier to use the energy equation in terms of specific enthalpy as follows:

$$\frac{\partial \rho h}{\partial t} + \frac{\partial (\rho u_j h)}{\partial x_j} = -\frac{\partial P}{\partial t} + 2\mu \left(S_{ij} - \frac{1}{3} \delta_{ij} \frac{\partial u_k}{\partial x_k} \right) : \frac{\partial u_j}{\partial x_i} + \frac{\partial}{\partial x_j} \left[\frac{\mu}{Pr} \frac{\partial h}{\partial x_j} \right] + \dot{q}_c \quad (3.4)$$

where Pr is the mixture Prandtl number and \dot{q}_c is the chemical source term. In the previous equation, the first three terms on the right hand side are contributions due to pressure work, viscous dissipation and flow dilation. Thermal dissipation is written in terms of the fluid viscosity and Prandtl number. The last term in the RHS of equation (4.4) is the chemical source term \dot{q}_c , which represents the enthalpy added to or removed from the fluid as a result of chemical reaction and is given as:

$$\dot{q}_c = \Delta h_f^\circ \dot{\omega}_c Y_{fu}^\circ \quad (3.5)$$

where h_f° is the lower heating value, Y_{fu}° is the fuel mass fraction in unburned mixture and $\dot{\omega}_c$ is the chemical reaction rate.

3.2.4 The Reaction Progress Variable Equation

In premixed flames, the chemical status of the mixture can be typically addressed by assuming a single step irreversible reaction between reactants and products, and a progress variable c , defined such that it is zero where the mixture is unburned and unity where it is fully burned. Mathematically reaction progress variable is defined as:

$$c = 1 - \frac{Y_{fu}}{Y_{fu}^\circ} \quad (3.6)$$

where Y_{fu} is the local fuel mass fraction. The transportation equation for the reaction progress variable which balances production and destruction of the chemical reaction can be written as:

$$\frac{\partial \rho c}{\partial t} + \frac{\partial (\rho u_j c)}{\partial x_j} = \frac{\partial}{\partial x_j} \left(\frac{\mu}{Sc} \frac{\partial c}{\partial x_j} \right) + \dot{\omega}_c \quad (3.7)$$

where Sc is the Schmidt number and $\dot{\omega}_c$ is the mean chemical reaction rate, which is required to be modelled. Modelling reaction rate in turbulent premixed flames is highly challenging due to its non-linear relation with chemical and thermodynamic states.

3.2.5 The Equation of State

As a reasonable simplification, many thermodynamic problems assume a chemical and thermodynamic equilibrium state to derive the gas properties from the ideal gas state

equation. The state equation used to close the system of equations described in previous sections and relate pressure, temperature, density as:

$$P = \rho RT \quad (3.8)$$

where P is the pressure, ρ is the density, R is the gas constant, defined as R_u/M , R_u is universal gas constant and M is the molecular weight of the gas, and T is the temperature.

3.2 Spatial Filtering Functions

Scales are filtered either in physical space or spectral space by applying a scale high-pass filter, i.e. low-pass in frequency, to the exact solution. The sub-grid scale fluctuations below chosen cut-off scale are modelled by assuming isotropic. In LES a spatial filtering operations must be defined by means of $G(x, x', \bar{\Delta})$ (Versteeg and Malalasekera (2007)).

$$\bar{\phi}(x, t) = \int_{-\infty}^{\infty} \int_{-\infty}^{\infty} \int_{-\infty}^{\infty} G(x, x', \bar{\Delta}) \phi(x', t) dx' dy' dz' \quad (3.9)$$

In the above equation, G is a filter function, which is associated with the cut-off length $\bar{\Delta}$ in space, generally taken in between Kolmogorov and integral length scales. Eddies of size larger than $\bar{\Delta}$ are classified as large eddies, while those smaller than $\bar{\Delta}$ are classified as small eddies which need to be modelled. Selection of the correct spatial filter in equation (3.9) is very important in LES as it must commute with differentiation, once filtered Navier-Stokes equation are developed for the flow field. The most commonly used filter functions are the cut-off filter, the Gaussian filter and the box filter (Figure 3.1).

Cut-Off filter: is applied on spectral space by using Fourier series to describe the flow variables and generally known as ideal low-pass filter, in which flow contributions greater than cut-off wave number k_c are removed without affecting the contributions of small wave numbers. This filter reduces the number of degrees of freedom and also known as - projective filter (Carati and Wray (2000)), which is defined as:

$$G(x, x', \bar{\Delta}) = \frac{\sin(k_c(x - x'))}{k_c(x - x')} \quad (3.10)$$

$$G(k) = \begin{cases} 1 & \text{if } |k| \leq k_c = \pi/\bar{\Delta} \\ 0 & \text{otherwise} \end{cases} \quad (3.11)$$

Gaussian filter: is generally applied in physical space, and it is widely used for homogeneous and inhomogeneous turbulence in the direction of homogeneity, often with separate cut-off scales in each direction. This filter simply transforms turbulent field u_i into a new field v_i and reduces the noise. Hence, called “smooth filter” and is defined as:

$$G(x, x', \bar{\Delta}) = \left(\frac{6}{\pi\bar{\Delta}^2}\right)^{3/2} \exp\left(\frac{-6|x - x'|^2}{\bar{\Delta}^2}\right) \quad (3.12)$$

Box or Top-Hat filter: is the other most commonly used implicit spatial filter applied in physical space, with a characteristic cut-off scale of $\bar{\Delta}$, generally defined in terms of grid spacing. Since this filter wipes out the small scales by filtering operation, this is also considered as a smooth filter and typically defined as:

$$G(x, x', \bar{\Delta}) = \begin{cases} \frac{1}{\bar{\Delta}^3} & \text{if } |x - x'| \leq \frac{\bar{\Delta}}{2} \\ 0 & \text{otherwise} \end{cases} \quad (3.13)$$

The top-hat filter is adopted in the present work, as it naturally fits into the finite volume discretization. The filtered governing equations in finite volume format can be simply rewritten by the application of equivalent box filter width of:

$$\bar{\Delta} = 2(\Delta x \Delta y \Delta z)^{\frac{1}{3}} \quad (3.14)$$

where Δx , Δy and Δz denotes the width of a computational cell in the three co-ordinates.

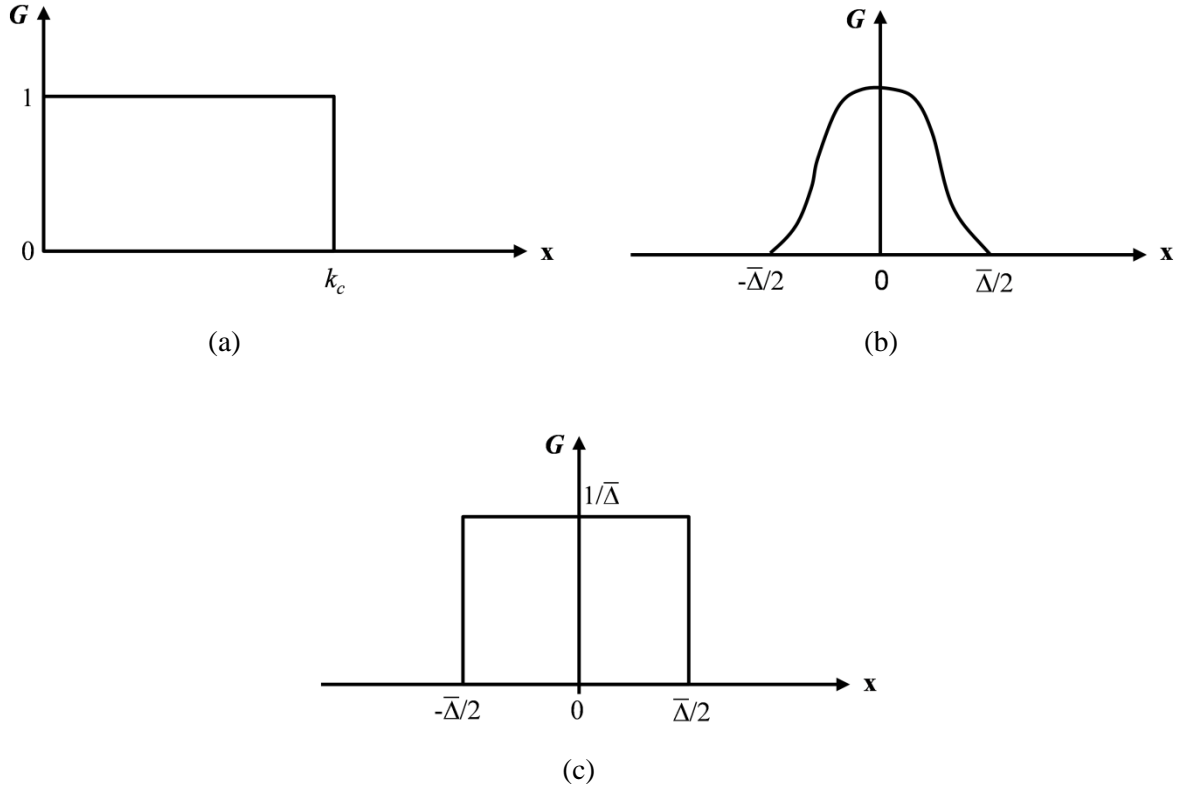


Figure 3.1 Spatial filters used in large eddy simulations. (a) Cut-Off filter (b) Gaussian filter (c) Box filter

Accuracy of LES simulations depends on many factors and filter width is one of the most important. Choice of the filter width is critical to resolve the appropriate amount of energy in the computational domain. For instance, Figure 3.2 illustrates the use of two different filter widths in obtaining the filtered velocity. It is clear that the use of larger filter width has resulted in a smoother curve compared to that of smaller filter width. However, using a large filter width may save computational time, but on the same time will led to the loss information. In a conceptual study, Pope (2004) hypothesises that the solution may reach an intermediate asymptote when the filter width lies within the inertial sub-range. However, using a box filter (3.6) simplifies the difficulty of choosing appropriate cut-off scales, yet associated with grid resolution employed.

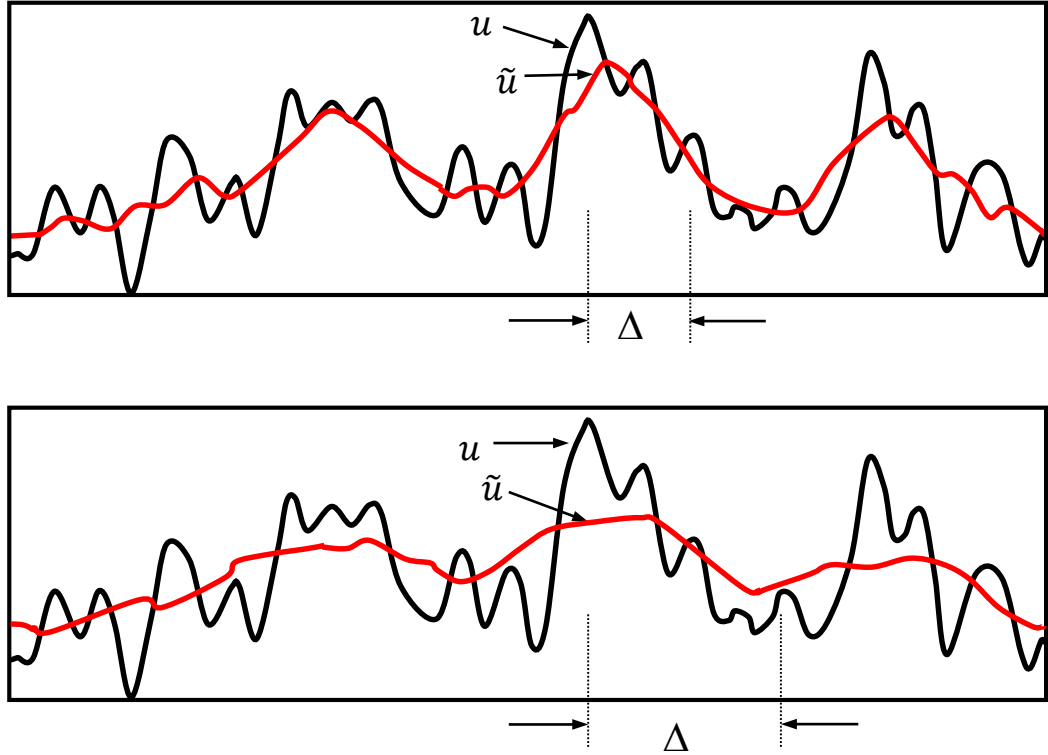


Figure 3.2 The filtered function \tilde{u} obtained by applying a box filter. Upper: small filter width, Lower: large filter width (Fröhlich and Rodi (2002)).

In general, the above filters can be classified into two categories, either implicit or explicit filters. Both filtering approaches have their own advantages and disadvantages. However, most of the LES simulations reported so far have been carried out using implicit filtering technique (e.g. Schumann (1989), Masri et al. (2006), and Gubba et al. (2011)...etc.), due to its simplicity and ability to work well into discretization schemes. Another advantage is that the definition of discrete unknown amounts to an implicit filtering i.e. any scales smaller than the grid are automatically discarded. This facilitates the implicit filter to fit naturally in the numerical discretization and the notations looks similar to that of RANS technique.

Contrary to the implicit filtering, one can change filter width and grid size independently while using explicit filtering. This explicit filtering has recently been promoted by several authors such as Moin and Kim (1997), Chow and Moin (2003), and Klein (2005), since it considerably reduces numerical discretization errors and there is a possibility to achieve a grid independent LES solution. On the other hand, it increases the modelling demands, since for the same number of grid points, more scales

of turbulent motion have to be modelled and it is not yet completely clear, which approach is more advantageous (Lund and Kaltenbach (1995)).

3.3 Favre Filtering (Averaging)

In turbulent flows, the flow consists of random fluctuations of the various flow properties such as density, temperature, velocities etc. As explained in earlier, in case of reacting flows, density is subjected to fluctuations due to heat release (Figure 3.3). In order to account for these fluctuations some sort of statistical averaging is required, where all quantities are expressed as the sum of mean and fluctuating parts. Conventional Reynolds-averaging or time averaging (Figure 3.4) will only consider velocity and pressure fluctuations in the fluid flow. This is appropriate for steady turbulence i.e. a turbulent flow that, on the average does not vary with time. Using Reynolds averaging in an unsteady, reacting problems leads to several complexities, which eventually involve the explicit modelling of velocity-density correlation due to high fluctuations, which is not recommended (Gubba (2009)).

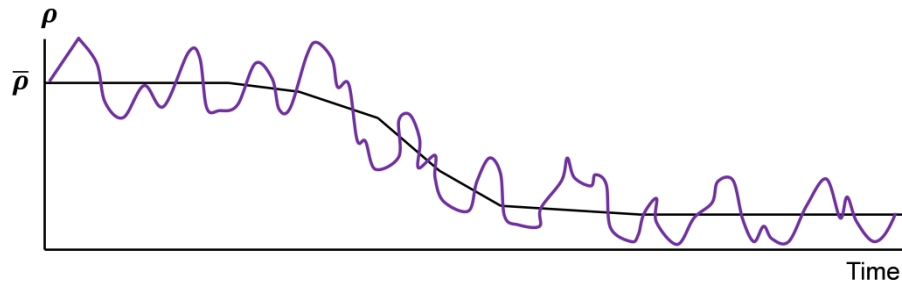


Figure 3.3 Temporal fluctuations and time-average in a statistically non-stationary process (Warnatz et al. (2006)).

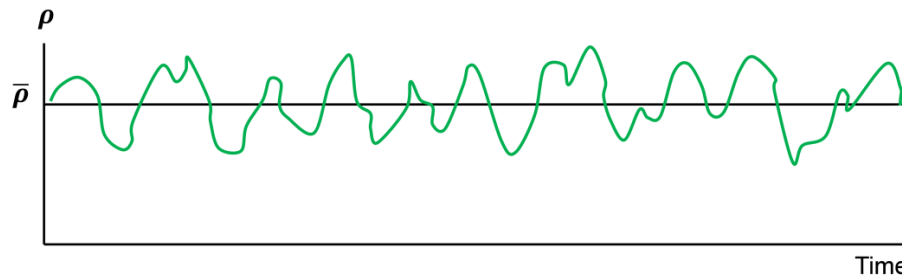


Figure 3.4 Temporal fluctuations and time-average in a statistically stationary process (Warnatz et al. (2006)).

Alternatively, Favre averaging or mass weighted averaging accounts for density and temperature fluctuations in addition to velocity and pressure fluctuations, when the medium is a compressible fluid. In Favre averaging, all the instantaneous values of velocity and scalars, except for pressure and density are decomposed into steady and fluctuating part as:

$$\phi = \tilde{\phi} + \phi'' \quad (3.15)$$

where ϕ is generic flow property, $\tilde{\phi}$ is mass-weighted mean, defined as $\tilde{\phi} = \overline{\rho\phi}/\bar{\rho}$ and ϕ'' is superimposed fluctuations. Favre mean is denoted by a tilde while the fluctuation about the Favre mean is given by double prime. Additionally, $\overline{\rho u_i''} = 0$, $\overline{\rho\phi''} = 0$ and while $\overline{\phi''} \neq 0$ and $\overline{u_i''} \neq 0$. Insertion of this decomposition into the governing equations with subsequent ensemble averaging, results in Favre averaged equations for the mean flow quantities as shown in next section.

3.3.1 Filtered Governing Equations

As described in the previous section, turbulent reacting flows are associated with large density variations, which must be properly considered. Jones (1993) argued that, considering these sub-grid density fluctuations in filtered conservation equations seems to be possible by the application of Favre-filtering. A Favre or mass-weighted spatial filter in LES is shown in equation (3.16) and similar to equation (3.9). Application of equation (3.16) to the conservation equations yields Favre-filtered conservation equations, as follows:

$$\bar{\rho}\tilde{\phi}(x, t) = \int_{-\infty}^{\infty} \int_{-\infty}^{\infty} \int_{-\infty}^{\infty} \rho G(x, x', \bar{\Delta}) \phi(x', t) dx' \quad (3.16)$$

Favre-filtered continuity equation:

$$\frac{\partial \bar{\rho}}{\partial t} + \frac{\partial(\bar{\rho}\tilde{u}_j)}{\partial x_j} = 0 \quad (3.17)$$

Favre-filtered momentum equation:

$$\frac{\partial(\bar{\rho}\tilde{u}_i)}{\partial t} + \frac{\partial(\bar{\rho}\tilde{u}_i\tilde{u}_j)}{\partial x_j} = -\frac{\partial \bar{P}}{\partial x_i} + \frac{\partial}{\partial x_j} \left(2\bar{\mu} \left[\tilde{S}_{ij} - \frac{1}{3} \delta_{ij} \tilde{S}_{kk} \right] \right) + \tilde{B}_i - \frac{\partial \tau_{ij}^{sgs}}{\partial x_j} \quad (3.18)$$

where the filtered strain rate tensor (\tilde{S}_{ij}) is defined as:

$$\tilde{S}_{ij} = \frac{1}{2} \left(\frac{\partial \tilde{u}_i}{\partial x_j} + \frac{\partial \tilde{u}_j}{\partial x_i} \right) \quad (3.19)$$

The filtered momentum equation yields an unclosed term, τ_{ij}^{sgs} due to the decomposition of nonlinear convective terms, which must be closed using models available from simple linear eddy viscosity based to complex second moment closures, where transport equations are solved (Gubba (2009)). In LES, the term τ_{ij}^{sgs} is generally referred to as residual stress and represents the impact of the unresolved velocity components on the resolved ones. Mathematically these terms arises from the non-linearity of the convection term which does not commute with the linear filtering operation. In the present work, this term is modelled by widely used, classical Smagorinsky turbulence model based on linear eddy viscosity.

$$\tau_{ij}^{sgs} = \bar{\rho} \overline{u_i'' u_j''} = \bar{\rho} (\widehat{u_i u_j} - \tilde{u}_i \tilde{u}_j) \quad (3.20)$$

- Favre-filtered energy equation:

$$\begin{aligned} \frac{\partial(\bar{\rho}\tilde{h})}{\partial t} + \frac{\partial(\bar{\rho}\tilde{u}_j\tilde{h})}{\partial x_j} + \frac{\partial(\bar{\rho}\overline{u_j''h''})}{\partial x_j} \\ = \frac{\partial\bar{P}}{\partial t} + 2\bar{\mu} \left[\tilde{S}_{ij} - \frac{1}{3}\delta_{ij}\tilde{S}_{kk} \right] : \frac{\partial\tilde{u}_j}{\partial x_i} + \frac{\partial}{\partial x_j} \left[\frac{\bar{\mu}}{Pr} \frac{\partial\tilde{h}}{\partial x_j} \right] + \bar{q}_c \end{aligned} \quad (3.21)$$

The above equation needs to be closed for SGS scalar fluxes and filtered energy source term. Modelling the scalar fluxes is quite difficult as compared to the momentum fluxes, since they are of dissipative nature (Gubba (2009)). Also, the SGS residual stresses shown in equation (3.20) are assumed to be isotropic; however, SGS scalar fluxes are anisotropic in nature and involve sharp variations due to large density variations.

- Favre-filtered reaction progress variable equation:

$$\frac{\partial\bar{\rho}\tilde{c}}{\partial t} + \frac{\partial(\bar{\rho}\tilde{u}_j\tilde{c})}{\partial x_j} + \frac{\partial(\bar{\rho}\overline{u_j''c''})}{\partial x_j} = \frac{\partial}{\partial x_j} \left(\frac{\bar{\mu}}{Sc} \frac{\partial\tilde{c}}{\partial x_j} \right) + \bar{\omega}_c \quad (3.22)$$

The above Favre-filtered reaction progress variable equation yields two unclosed terms. The last term on the LHS of equation (3.22) is due to the scalar fluxes, similar to that of momentum equation, which can be usually decomposed as $\overline{u_j''c''} = \widehat{u_j c} - \tilde{u}_j \tilde{c}$. This

term is usually modelled based on the gradient diffusion and turbulent eddy viscosity hypothesis. The second term on the RHS of equation (3.22) is the filtered reaction rate $\bar{\omega}_c$, which represents the SGS mean reaction rate. Since the turbulent flame thickness is thinner than the LES grid, most of the turbulent combustion is sub-grid phenomenon, hence, must be accounted for appropriately.

3.4 Modelling of SGS Residual Stresses

Modelling of the SGS residual stress τ_{ij}^{sgs} has gained great deal of attention by turbulence modellers and a large collection of SGS models are available in literature. The primary concern of any SGS model is to account for the local and instantaneous momentum transportation effects of small scales on large scales and vice versa (generally known as energy back-scatter in certain flows). However, it may not be always necessary for the SGS models to simulate the detailed interaction between resolved and small scales, but necessary to expect the correct representation of energy at the correct location (Gubba (2009)). A few important modelling approaches are briefly discussed in the following sections.

3.4.1 Residual Stress Decomposition

It is clear from equation (3.18) that the sub-grid stress τ_{ij}^{sgs} resulted due to the commutation of Favre filtering on convective term of momentum equation, which must be closed by modelling as a function of known resolved values. Ferziger (1982) identified that the models developed following Leonard decomposition of velocity field into mean and fluctuating quantities, are effective and efficient in accounting sub-grid scale effects. Hence, velocity component in i -direction can be decomposed as:

$$u_i = \tilde{u}_i + u_i' \quad (3.23)$$

where u_i' is the sub-grid scale component of u_i . Following the above, decomposition of the $u_i u_j$ yields:

$$u_i u_j = \tilde{u}_i \tilde{u}_j + u_i' \tilde{u}_j + \tilde{u}_i u_j' + u_i' u_j' \quad (3.24)$$

Rearranging the above equation as:

$$u_i u_j = \tilde{u}_i \tilde{u}_j + L_{ij} + C_{ij} + R_{ij} \quad (3.25)$$

where:

$$L_{ij} = \tilde{u}_i \tilde{u}_j - \tilde{u}_i \tilde{u}_j, C_{ij} = u_i' \tilde{u}_j + \tilde{u}_i u_j' \text{ and } R_{ij} = u_i' u_j' \quad (3.26)$$

where equation (3.20) can be written as:

$$\tau_{ij}^{sgs} = \bar{\rho}(\tilde{u}_i \tilde{u}_j - \tilde{u}_i \tilde{u}_j) = \bar{\rho} (L_{ij} + C_{ij} + R_{ij}) \quad (3.27)$$

In the previous equation, L_{ij} is the Leonard stresses, C_{ij} is the cross-stresses and R_{ij} is the sub-grid scale Reynolds stresses. The Leonard stresses L_{ij} are due to the effects at resolved scales. The cross-stresses C_{ij} are due to the interactions between the sub-grid scale eddies and the resolved scales. Finally, the sub-grid scale Reynolds stresses R_{ij} are caused by convective momentum transfer due to interactions of sub-grid scale eddies (Versteeg and Malalasekera (2007)). These stresses are modelled with the so-called sub-grid scale turbulence models.

Several methods have been used to model the above stress terms, based on either explicit or implicit filtered resolved values, for instance, Smagorinsky (1963), Lilly (1966), Deardorff (1970), Schumann (1975) and Bardina et al. (1980). Among the available, representation of these turbulent stresses through the use of simplified linear models based on the eddy viscosity approach are well known and widely used. The classical model of this category introduced by Smagorinsky (1963), is the most famous and subject to many developments later on. Also, the introduction of the dynamic modelling concept by Germano et al. (1991) has encouraged the progress in the sub-grid scale modelling. In dynamic modelling, model coefficients are determined as the calculation progresses, based on the energy contents of the smallest resolved scales rather than input a priori as standard Smagorinsky model.

3.4.2 The Smagorinsky Model

Representation of the turbulent stresses using scalar eddy viscosity is a well-known approach since its introduction by Boussinesq (1877). Smagorinsky (1963) was the first to propose a similar model to Boussinesq for turbulent stresses in LES, which is still widely employed in turbulence modelling. Smagorinsky model assumes that the anisotropic part of the residual stress tensor is inline and proportional to the anisotropic part of the resolved strain tensor, while the normal stresses are isotropic. This model

assumes that the scales in unresolved turbulence are approximately in equilibrium with energy cascaded down from the large scales (Gubba (2009)).

Accordingly, the SGS stress tensor τ_{ij}^{sgs} can be modelled as:

$$\tau_{ij}^{sgs} - \frac{1}{3}\delta_{ij}\tau_{kk}^{sgs} = 2\bar{\mu}_{SGS}(\tilde{S}_{ij} - \frac{1}{3}\delta_{ij}\tilde{S}_{kk}) \quad (3.28)$$

where $\bar{\mu}_{SGS}$ is the eddy viscosity, which can be expressed as a function of the filter width and the strain rate as:

$$\mu_{SGS} = \bar{\rho}C\bar{\Delta}^2|\tilde{S}| \quad (3.29)$$

where $|\tilde{S}| = \sqrt{2\tilde{S}_{ij}\tilde{S}_{ij}}$ and C is a dimensionless coefficient and often used to be specified in classical models as the Smagorinsky coefficient ($C_s = \sqrt{C}$). The isotropic part of the SGS stress tensor in equation (3.28), is modelled using the relation of Yoshizawa (1986) as:

$$\tau_{kk}^{sgs} = 2\bar{\rho}C_I\bar{\Delta}^2|\tilde{S}|^2 \quad (3.30)$$

where, C_I is the model coefficient and usually expected to be around (0.01).

The classical Smagorinsky model is quite simple and widely used, despite certain disadvantages. One of the major drawbacks is a prior requirement to specify the model coefficient, although it is dependent on local flow conditions. For instance, Lilly (1966) suggested a value of $C_s \approx 0.23$ for homogeneous isotropic turbulence, Deardorff (1970) used a value of (0.1) in turbulent channel flow simulations, whereas for the same flows Piomelli et al. (1988) found 0.0065 as an optimal value. Rogallo and Moin (1984) and Germano et al. (1991) identified that C_s value are in the ranges 0.1 and 0.25 for results through different grids and filter functions and there is no clear agreement on how it influences or depends on the flow.

Secondly, the model does not predict correct asymptotic behaviour near a wall and requires ad-hoc treatment. Simulations of transitional wall boundary flows show that the model over-damps the flow, leading to incorrect prediction of growth rates of initial

disturbance. Due to the dissipative nature of the model, Piomelli et al. (1990) identified that the model over predicts dissipation by 35% in laminar channel flows. Also, Piomelli et al. (1990) has identified that it fails to predict the energy transfer from small to large scales, which is generally known as energy back-scatter and important in certain flows. Finally, the model does not vanish in a fully resolved “laminar” flow although $\widetilde{u_i u_j} = \widetilde{u_i} \widetilde{u_j}$.

Hence, to overcome these drawbacks, several researchers employed ad-hoc procedures (Ferziger (1993), Fureby et al. (1997) and Fureby (1998)) to calculate the appropriate model coefficient and found to achieve good confidence in using Smagorinsky model. Motivated by its simplicity, Germano et al. (1991) developed a dynamic procedure to calculate the model coefficient using local instantaneous flow conditions. This procedure was found to be a great success in predicting the correct model coefficient and extended to compressible flows by Moin et al. (1991).

3.4.3 The Dynamic SGS Flow Model

For the limitations in the Smagorinsky model described in the above section, Germano et al. (1991) proposed the dynamic procedure to calculate C_s based on local flow conditions and similarity ideas of Bardina et al. (1980). Later, Moin et al. (1991) extended this procedure for compressible flows, which is used in the present simulations to calculate the model coefficient. The basic idea of the dynamic procedure is in using information from the smallest resolved scales to model the sub-grid scales effects. In order to obtain information from the smallest resolved scales, a test filter, is generally represented by $\widehat{\Delta}$, which is greater than the grid filter $\bar{\Delta}$, and is applied to velocity field. Application of the test filter to the filtered Navier-Stokes equations results in sub-test-scale stress tensor analogous to sub-grid-scale stress tensor.

$$T_{ij} = \widehat{u_i u_j} - \widehat{u_i} \widehat{u_j} \quad (3.31)$$

Applying the test filter to the equation (3.23) and rearranging will result in the resolved turbulent stress as:

$$\mathcal{L}_{ij} = \widetilde{\widehat{u_i u_j}} - \widetilde{\widehat{u_i} \widehat{u_j}} \quad (3.32)$$

The resolved turbulent stresses also known as Leonard stresses, which represent the influence of the Reynolds stresses by scales whose length is intermediate between the test and grid filter width. Identifying the relation between equations (3.27), (3.31) and (3.32) and rearranging will result in what is called Germano identity:

$$\mathcal{L}_{ij} = T_{ij} - \hat{\tau}_{ij}^{sgs} \quad (3.33)$$

The Germano identity in the above equation (3.33) can be used to compute, explicitly, the sub-grid scale stresses at the test and grid levels, T_{ij} and τ_{ij}^{sgs} .

$$T_{ij} - \frac{1}{3}\delta_{ij}T_{kk} = -2\bar{\rho}C\Delta^2|\hat{S}| \left(\hat{S}_{ij} - \frac{1}{3}\delta_{ij}\hat{S}_{kk} \right) = -C\alpha_{ij} \quad (3.34)$$

$$\tau_{ij}^{sgs} - \frac{1}{3}\delta_{ij}\tau_{kk}^{sgs} = -2\bar{\rho}C\bar{\Delta}^2|\tilde{S}| \left(\tilde{S}_{ij} - \frac{1}{3}\delta_{ij}\tilde{S}_{kk} \right) = -C\beta_{ij} \quad (3.35)$$

where the traceless tensors α_{ij} and β_{ij} are:

$$\alpha_{ij} = -2\bar{\rho}C\Delta^2|\hat{S}| \left(\hat{S}_{ij} - \frac{1}{3}\delta_{ij}\hat{S}_{kk} \right) \quad (3.36)$$

$$\beta_{ij} = -2\bar{\rho}C\bar{\Delta}^2|\tilde{S}| \left(\tilde{S}_{ij} - \frac{1}{3}\delta_{ij}\tilde{S}_{kk} \right) \quad (3.37)$$

Substituting equations (3.34) & (3.35) in the anisotropic part of equation (3.33) gives:

$$\mathcal{L}_{ij}^a = C (\hat{\beta}_{ij} - \alpha_{ij}) \quad (3.38)$$

To obtain a scalar equation for the model coefficient C , the above equation is contracted with \tilde{S}_{ij} tensor as:

$$C = \frac{\mathcal{L}_{ij}^a \tilde{S}_{ij}}{(\hat{\beta}_{ij} - \alpha_{ij}) \tilde{S}_{ij}} \quad (3.39)$$

From the above equation the value of C could be obtained, however, observing the fact that the terms within parentheses in equation (3.39), can become zero, which may cause an ill-posed problem. To improve this, C was considered to vary in only the y-direction, normal to the wall. Since, equation (3.39) is a tensor; it can only be satisfied in some average sense, which can be carried in the y-direction where the test filter is not applied. This results in an expression for C as:

$$C(y, t) = \frac{(\mathcal{L}_{ij}^a \tilde{S}_{ij})_y}{\langle \hat{\beta}_{ij} \tilde{S}_{ij} - \alpha_{ij} \tilde{S}_{ij} \rangle_y} \quad (3.40)$$

Since, equation (3.38) is a set of five independent equations, a single value of C is not often to be obtained simultaneously. To overcome this issue, Lilly (1992) proposed a tensor M_{ij} instead \tilde{S}_{ij} in equation (3.38), which locally minimizes the sum of the square of residuals as:

$$\mathcal{L}_{ij} - \frac{1}{3} \delta_{ij} \mathcal{L}_{kk} = 2 C M_{ij} \quad (3.41)$$

where $(M_{ij} = (\hat{\Delta}/\bar{\Delta})^2 \bar{\rho} |\tilde{S}| \tilde{S}_{ij} - \bar{\rho} |\tilde{S}| \tilde{S}_{ij})$, which is obtained by explicitly evaluating the stresses at test scale and comparing locally by subtracting the test-scale average of equation (3.35) from equation (3.34). Re-arranging equation (3.41) for C yields:

$$C = - \frac{\mathcal{L}_{ij} M_{ij} - \frac{1}{3} \mathcal{L}_{ll} M_{mm}}{2 \bar{\Delta}^2 (M_{ij} M_{ij} - \frac{1}{3} M_{ll} M_{mm})} \quad (3.42)$$

Hence, the Smagorinsky model coefficient can be calculated using the dynamic procedure at every spatial grid point and time by considering the localised flow conditions, which has the correct behaviour near to solid wall and in laminar flow and also allows for energy back-scatter. However, the model coefficient found to fluctuate in space and time, and some form of averaging is usually required to avoid stability problems. Typically, L_{ij} and M_{ij} are averaged in spatially homogeneous directions in space. However, this requires the flow to have at least one homogeneous direction. However, if there is no direction to perform averaging, alternative approaches may be used such as localised models of Ghosal et al. (1995) and Piomelli and Liu (1995), dynamic mixed models of Zang et al. (1993) and relaxation procedure of Breuer and Rodi (1994).

3.4.4 Scale Similarity Models

The principle of scale similarity was first proposed by Bardina et al. (1980) and expected to overcome the disadvantages of eddy viscosity models. The basic idea of scale similarity is to identify and correlate the smallest resolved scales to the sub-grid

scales of the flow. Filtering the decomposed velocity component in equation (3.23) yields:

$$\bar{u}'_i = \bar{u}_i - \bar{\bar{u}}_i \quad (3.43)$$

This can be reasonably estimated equal to the largest contributions of \bar{u}'_i and the smallest contributions of $\bar{\bar{u}}_i$. Furthermore, this equality will facilitate velocity decompositions as:

$$\overline{\bar{u}_i \bar{u}_j} \approx \bar{\bar{u}}_i \bar{\bar{u}}_j \text{ and } \overline{\bar{u}'_i \bar{u}'_j} \approx \bar{\bar{u}}_i \bar{\bar{u}}_j \quad (3.44)$$

This actually enables to model the residual stresses given in equation (3.27) as:

$$\tau_{ij}^{sgs} = \rho \left[\underbrace{\overline{\bar{u}_i \bar{u}_j} - \bar{\bar{u}}_i \bar{\bar{u}}_j}_{L_{ij}} + \underbrace{K_C [(\bar{u}_i - \bar{\bar{u}}_i) \bar{\bar{u}}_j + (\bar{u}_j - \bar{\bar{u}}_j) \bar{\bar{u}}_i]}_{C_{ij}} + \underbrace{K_R (\bar{u}_i - \bar{\bar{u}}_i) (\bar{u}_j - \bar{\bar{u}}_j)}_{R_{ij}} \right] \quad (3.45)$$

where the model coefficients K_C and K_R in the above equation should be carefully chosen such that, the expression observes Galilean invariance (Zang et al. (1993), Salvetti and Banerjee (1995) and Horiuti (1997)). The scale similarity models (SSM) allows back-scatter, i.e. transfer of energy from small to large scales and does not impose alignment between the SGS stress tensor and the strain rate. Piomelli et al. (1996) identified that the scale similarity models in conjunction with dynamic procedure perform quite well for low-order finite-difference or finite-volume methods.

3.5 Modelling of SGS Scalar Fluxes

Modelling sub-grid scalar fluxes in turbulent reacting flames is highly challenging due to their non-linear relation with chemical and thermodynamic states. The major difficulty in modelling is due to the anisotropic behaviour of scalar fluxes. This is strongly affected by the turbulent velocity fields, through the large increase in specific volume and viscosity, which causes large temperature rise in reacting flows. Modelling could be further complicated due to the large pressure gradients and density variations associated with heat release, which may cause non-gradient transport (NGT) or counter gradient diffusion.

Several models are available to account for SGS scalar fluxes, for example, simple gradient transportation assumption (Veynante et al. (1997)), scale similarity model (Fureby and Möller (1995)) and linear eddy model (LEM) (Kerstein (1991)). Also, the analysis of Boger and Veynante (2000) of DNS database, Boughanem and Trouvé (1998), revealed that the gradient or counter gradient diffusion of scalar fluxes are observed similar to RANS. However, unresolved scalar fluxes are identified to be less in LES, which supports that the use of simple model will have fewer consequences on the end solution. This is also proved by Boger and Veynante (2000), when they performed LES for turbulent premixed flames on a V-shaped flame holder using simple gradient transport assumption and able to recover counter gradient transport at resolved scales without any extra effort, which is not the situation in RANS. Hence, in the present simulations the simple gradient transport model in equations (3.21) and (3.22) for scalar fluxes is implemented.

$$\overline{\rho u_j'' h''} = - \frac{\bar{\mu}_{SGS}}{Pr_t} \frac{\partial \tilde{h}}{\partial x_j} \quad (3.46)$$

$$\overline{\rho u_j'' c''} = - \frac{\bar{\mu}_{SGS}}{Sc_t} \frac{\partial \tilde{c}}{\partial x_j} \quad (3.47)$$

where Pr_t is the turbulent flow Prandtl number, Sc_t is the turbulent flow Schmidt number, taken their values as 0.4 (Ranga Dinesh et al. (2013)) and $\bar{\mu}_{SGS}$ is the SGS eddy viscosity.

3.6 Summary

This chapter summarises use of LES concept for turbulent premixed flames. A brief history of the LES and the pioneering developments since its first use by Deardorff (1970) has been detailed. The governing equations used for turbulent premixed combustion are presented and discussed. The spatial filtering technique, which distinguishes LES from other modelling techniques, has been discussed with a variety of spatial filters. Advantages of implicit filtering over explicit filtering was briefly discussed and applied to the flow governing equations. Various modelling strategies to close the resulted unclosed terms from Favre-filtered governing equations were discussed. Suitability of the simple non-gradient transportation (NGT) strategy for SGS scalar fluxes in scalar equations has been discussed in LES.

Chapter 4

The Combustion Model

Following the work of Knikker et al. (2004) and Gubba (2009) in developing a dynamic formulation for the FSD of premixed turbulent flames, the present work is carried out by implementing the dynamic flame surface density (DFSD) model in an existing LES code PUFFIN (Kirkpatrick (2002)). The FSD models are well established in the context of LES and are the subject of many interesting developments. In this chapter, brief introduction of the flamelet and flame surface density concepts are outlined. A description of available algebraic models and the exact transport equation of FSD in LES are detailed in section 4.1. Details of a simple algebraic FSD model derived based on DNS data are explained in section 4.2. Section 4.3 presents the concept and development of the dynamic FSD (DFSD) model. Section 4.4 provides brief details of the fractal concept and the dynamic fractal model used in the present simulations to calculate the fractal dimension of turbulent premixed flames. Lewis no. effect and how it is implemented in the model is discussed in section 4.5. Finally, the ignition model used in the present work is presented in section 4.6.

4.1 Introduction

The concept of FSD in RANS is well recognized but relatively new in LES. The FSD models proposed in LES are very similar to that of RANS and can be derived from the laminar flamelet fundamentals (Poinsot and Veynante (2012)). Based on the laminar flamelet assumptions for many turbulent premixed applications, the reaction zone/flame front is viewed as a collection of asymptotically thin wrinkled, propagating layers between fresh and burnt gases. Within the limit of high Damköhler number, these layers can be assumed to propagate at local laminar flame speed. Therefore, these layers can be considered as laminar flamelets. The concept of the laminar flamelets in turbulent premixed combustion greatly reduces the complexity of the problem by decoupling turbulence from chemistry. Following the laminar flamelet concept, the wrinkling of the flame front surface by turbulence can be described by the mean flame-surface area per unit volume i.e. flame surface density, Σ . As mentioned earlier, the main advantage of

this concept is to separate complex chemistry features from turbulent/combustion interactions (Poinsot and Veynante (2012)) .

Hence, the filtered mean chemical reaction rate in equation (3.22) can be expressed as a function of the FSD, Σ as follows:

$$\bar{\omega}_c = R\bar{\Sigma} = \langle \rho_u u_d \rangle_s \bar{\Sigma} \quad (4.1)$$

In the above equation, R is the expressed as $\langle \rho_u u_d \rangle_s$, which is the surface averaged, Favre filtered displacement speed of the propagating flame into the fresh gases. Assuming that the individual flamelet is propagating with the laminar flame speed u_L into the fresh gases having density ρ_u , then R could be modelled as $\rho_u u_L$.

The filtered FSD, $\bar{\Sigma}$ is accounted for via either solving a transport equation, known as Σ -equation or by using an empirical algebraic expression (Gubba (2009)). The Σ -transport equation was first expressed by Marble and Broadwell (1977). Later on, Pope (1988) developed the transport equation by filtering the basic equation with a filter width sufficiently larger than the grid spacing such that the thin turbulent dynamic premixed flame is could be resolved on a LES grid. Also, Hawkes and Cant (2001) provided a transport equation for FSD, similar to the typical RANS equation, which includes resolved contributions neglected by the typical RANS equations. However, Pitsch (2006) shows that this equation has resulted in several unclosed terms, leading to excessive computational requirements by reaching DNS limit for fully resolved flows during computation. The exact, unclosed equation proposed by Hawkes and Cant (2001) is presented below:

$$\frac{\partial \Sigma}{\partial t} + \frac{\partial (\tilde{u}_i \Sigma)}{\partial x_i} + \frac{\partial \{((\bar{u}_i)_s - \tilde{u}_i) \Sigma\}}{\partial x_i} = \overline{(a_T)_s} \Sigma - \frac{\partial (\overline{(w N_i)_s} \Sigma)}{\partial x_i} + \left(\overline{w \frac{\partial N_k}{\partial x_k}} \right)_s \Sigma \quad (4.2)$$

where the LHS terms in the above equation represent the unsteady and diffusion of flame surface density, while the RHS represent the convection and source terms of the flame surface density.

On the other hand, flame surface density can be modelled by using an empirical algebraic model, by considering the balance between production and destruction of

flame surface density in the transport equation. The first to develop a simple algebraic model for FSD in LES was Boger et al. (1998), based on extensive DNS database of infinitely thin planar flame using a Gaussian filter. This model is given in equation (4.3), which is simple and very similar to the Bray-Moss-Libby (BML) model in the context of RANS (Bray et al. (1985)). However, several researchers used Boger's algebraic form to model turbulent premixed flames (e.g. Kirkpatrick et al. (2003), Masri et al. (2006), Di Sarli et al. (2009) and Gubba et al. (2009)).

$$\bar{\Sigma} = 4 \frac{\tilde{c}(1 - \tilde{c})}{L_{\Sigma}} \quad (4.3)$$

where \tilde{c} is the filtered reaction progress variable and L_{Σ} is the flame wrinkling scale given as $\bar{\Delta}/\beta$. The model coefficient, β in the above equation can be either considered as a constant or modelled based on a flame wrinkling factor (Gubba (2009)).

Another model similar to the BML and EBU expressions proposed by Charlette et al. (1999), including a term to account for the resolved flame surface density as:

$$\bar{\Sigma} = |\nabla \tilde{c}| + a \Gamma_k \left(\frac{\delta_L}{\bar{\Delta}}, \frac{\sqrt{2k/3}}{u_L} \right) \frac{\sqrt{k}}{u_L} \frac{\tilde{c}(1 - \tilde{c})}{L_{\Sigma}} \quad (4.4)$$

where Γ_k is the efficiency function of the Intermittent Turbulence Net Flame Stretch (ITNFS) model of Meneveau and Poinot (1991), k is the sub-grid kinetic energy and a is the model constant.

Also, Angelberger et al. (1998) proposed another model based on sub-grid RMS fluctuations which is expressed as:

$$\bar{\Sigma} = |\nabla \tilde{c}| + a \Gamma_k |\nabla \tilde{c}| \left(\frac{\delta_L}{\bar{\Delta}}, \frac{u'}{u_L} \right) \frac{u'}{u_L} \quad (4.5)$$

Weller et al. (1998) and Tabor and Weller (2004) introduced an additional equation to solve for the flame surface wrinkling factor, Ξ as:

$$\Xi = \frac{\bar{\Sigma}}{|\nabla \tilde{b}|} \quad (4.6)$$

where $|\nabla \bar{b}|$ is the area of the grid scale surface and the flame surface density is derived using the conditional filtering method.

4.2 Algebraic Expression for Flame Surface Density (AFSD) Model

As mentioned earlier, Boger et al. (1998) were the first to deduce an algebraic expression for FSD for use in LES codes. A 3-D DNS database developed by Boughanem and Trouvé (1998) has been used for decaying isotropic, homogeneous turbulence, with the assumption of an evolving thin flame front into the fresh gases. The key idea behind their expression is in identifying the sub-grid surface density, Σ (i.e. the sub-grid flame surface per unit volume) of the flame surface defined by $c = c^*$ and the conditionally averaged displacement speed of the propagating flame of the surface c^* into the fresh gases, $\langle R \rangle_s$ as:

$$\bar{\Sigma} = \int_{-\infty}^{\infty} |\nabla \bar{c}| \delta(c - c^*) G(x - x') dx' \quad (4.7)$$

$$\langle R \rangle_s = \langle \rho_u S_d \rangle \quad (4.8)$$

A generalised sub-grid flame surface density and displacement speed, which do not depend on a specific c^* isosurface, are defined as:

$$\Sigma_{gen} = \int_1^0 \bar{\Sigma} dc^* = \overline{|\nabla c|} \quad (4.9)$$

$$\langle R \rangle_s = \frac{1}{\Sigma_{gen}} \int_1^0 \langle R \rangle_s dc^* = \frac{\overline{R|\nabla c|}}{\Sigma_{gen}} \quad (4.10)$$

Following the laminar flamelet concepts, and assuming the reaction zone to be very thin, the sub-grid flame surface density Σ of $c = c^*$ isosurface is no longer dependent on the isosurface chosen and becomes equal to the generalised flame surface density Σ_{gen} . The displacement speed $\langle R \rangle_s$ can be approximated as $\rho_u u_L$ by considering that the laminar flamelets are steadily propagating. Boger et al. (1998) have validated this approximation for turbulent premixed combustion by filtering the DNS data. The laminar flame speed in the above equation is calculated using the expression presented in Chapter 2.

However, Poinso et al. (1995) identified that the process of filtering will average the effects of variations in the flame strain and the curvature on the flame speed.

To define the flame surface Boger et al. (1998) chose $c^* = 0.8$ and introduced a reduced progress variable, c_{red} which is 0 if $c \leq c^*$ otherwise it is 1. Hence, they derived a simple expression for $\bar{\Sigma}$ from DNS:

$$\bar{\Sigma} = 4\alpha_2 \frac{\tilde{c}_{red}(1 - \tilde{c}_{red})}{\bar{\Delta}} \quad (4.11)$$

where the model coefficient α_2 , analytically derived by assuming an infinitely thin flame front (i.e. $|\nabla c| = \delta(c - c^*)$):

$$\alpha_2 = \sqrt{\frac{6}{\pi}} \Xi \quad (4.12)$$

In the above expression, α_2 becomes 1.4 for a unity sub-grid scale flame wrinkling factor Ξ . Alternatively, Boger et al. (1998) proposed another expression similar to equation (4.11) by replacing c_{red} with c , which is the instantaneous value of the reaction progress variable:

$$\bar{\Sigma} = 4\beta \frac{\tilde{c}(1 - \tilde{c})}{\bar{\Delta}} \quad (4.13)$$

where β is a model coefficient which has a value equal to α_2 in equation (4.11) for sufficiently large values of $\bar{\Delta}/L_f$, i.e. infinitely thin flames compared to the grid width. The above expression has a similar format to as the Bray-Moss-Libby (BML) expression for flame surface density in RANS (Bray et al. (1989)) and only accounts for the so called resolved contributions. The ratio $\bar{\Delta}/4\beta$ represents the wrinkling length scale of the sub-grid flame surface.

Generally, the model coefficient β is not universal and is known to be dependent on many physical parameters such as grid resolution, turbulence levels and chemistry. A range of values for the model coefficient β , in RANS and LES ranging from 1.0 to 2.6 can be found in the literature.

4.3 The Dynamic Flame Surface Density (DFSD) Model

The limitation of the AFSD model, as outlined in the above section, is that it can only account for the resolved contributions, using a model constant which is not universal. To overcome this limitation, Hawkes and Cant (2000) proposed a dynamic model for the flame surface density, and Knikker et al. (2002) developed a conceptual similarity FSD model, involving a combination of the test filter application and similarity ideas (Bardina et al. (1980)) to account for the SGS reaction rate. This approach has been coupled with the fractal theory to identify the flame surface as a fractal surface and to determine the model constant, C_s , which is given in equation (4.26) below. However, this model has failed to determine the fractal dimension, D . The similarity FSD model has been tested against experimental data published by Nottin et al. (2000). The data were extracted from OH images obtained from planar laser-induced fluorescence (PLIF) measurements of propane/air turbulent premixed flames. The model was successful in predicting the specific regions where the sub-grid scale contribution to the flame surface density is high. However, this model failed to calculate the fractal dimension dynamically, which resembles the failure of the AFSD model in using the constant model coefficient.

To overcome this limitation, a DFSD model has been developed by Knikker et al. (2004). The main idea is based on modelling the unresolved FSD by applying the Germano identity (3.33) to the flame surface density, and modelling the fractal dimension dynamically. In this approach, a flame wrinkling factor, Ξ , is introduced as a ratio of the flame surface density to its projection in the normal direction of the flame propagation as:

$$\Xi = \frac{\int_v |\nabla c| G(x - x') dx'}{\mathbf{N} \cdot \int_v |\nabla c| \mathbf{n} G(x - x') dx'} = \frac{|\overline{\nabla c}|}{|\nabla \bar{c}|} = \frac{\bar{\Sigma}}{|\nabla \bar{c}|} \quad (4.14)$$

where \mathbf{n} and \mathbf{N} are the normal vectors to the instantaneous c and to the filtered \bar{c} isosurface pointing towards the unburnt gases. Knikker et al. (2004) identified that the gradient of the filtered progress variable $|\nabla \bar{c}|$ becomes zero due to the highly wrinkled nature of the flame front. To avoid this problem, they assumed the flame to be locally planar and to be an infinitely thin surface. They defined a sharp progress variable c_l using the Heaviside function and expressed $|\nabla \bar{c}|$ as $|\nabla \bar{c}_l| = \Pi(\bar{c}_l, \bar{\Delta})$, which becomes

zero only far away from the flame front. This facilitates the redefinition of the flame wrinkling factor, Ξ , as:

$$\Xi = \frac{\bar{\Sigma}}{\Pi(\bar{c}, \bar{\Delta})} \quad (4.15)$$

Knikker et al. (2004) coupled the above equation with fractal theory to identify the flame surface as a fractal surface between the inner and outer cut-off scales. In the present analysis, $\bar{\Delta}$ and δ_c are considered as the outer and inner cut-off scale respectively. Hence, the wrinkling factor at the outer cut-off scales can be presented as:

$$\Xi(\bar{\Delta}) = \left(\frac{\bar{\Delta}}{\delta_c} \right)^{D-2} \quad (4.16)$$

In this approach, the term of the mean filtered flame surface density $\bar{\Sigma} = \overline{|\nabla c|}$ (in equation 4.14), can be split into two terms as resolved and unresolved:

$$\bar{\Sigma} = \overline{|\nabla c|} = \underbrace{\Pi(\bar{c}, \bar{\Delta})}_{Resolved} + \underbrace{f(\bar{c}, \bar{\Delta}, \Pi(\bar{c}, \bar{\Delta}))}_{Unresolved} \quad (4.17)$$

In the above equation the resolved term is evaluated using the expression given by Knikker et al. (2002), and the unresolved term is calculated as:

$$\lambda = \bar{\Sigma} - \Pi(\bar{c}, \bar{\Delta}) = \overline{|\nabla c|} - \Pi(\bar{c}, \bar{\Delta}) \quad (4.18)$$

Taking γ as ratio of the test filter to the grid filter, i.e. $\hat{\Delta}/\bar{\Delta}$, such that the test filter $\hat{\Delta}$ is greater than the grid filter $\bar{\Delta}$. Applying the test filter to the flame surface density (4.17) leads to:

$$\hat{\Sigma} = \overline{|\nabla c|} = \underbrace{\Pi(\hat{c}, \hat{\Delta})}_{Resolved@testfilter} + \underbrace{[\overline{|\nabla c|} - \Pi(\hat{c}, \hat{\Delta})]}_{Unresolved@testfilter} \quad (4.19)$$

From the previous equation, the unresolved flame surface density contributions at the test filter level can be written as:

$$\Lambda = [\overline{|\nabla c|} - \Pi(\hat{c}, \hat{\Delta})] \quad (4.20)$$

Following the similarity ideas (Bardina et al. (1980)), assuming that the sub-grid scale contribution of the unresolved flame surface density at the test filter is the same as that

at the grid filter, and relating λ and Λ by using the Germano identity (Germano et al. (1991)) leads to:

$$\Lambda - \hat{\lambda} = \left[\widehat{|\nabla c|} - \Pi(\hat{c}, \hat{\Delta}) \right] - \left[\widehat{|\nabla c|} - \Pi(\bar{c}, \bar{\Delta}) \right] \quad (6.21)$$

$$\Lambda - \hat{\lambda} = \left[\Pi(\bar{c}, \bar{\Delta}) - \Pi(\hat{c}, \hat{\Delta}) \right] \quad (6.22)$$

The sub-grid scale flame surface density contributions from the above equation can be added to the resolved flame surface density (4.17) with a model coefficient C_s in order to obtain the total flame surface density. Hence the flame surface density can be expressed as:

$$\bar{\Sigma} = \Pi(\bar{c}, \bar{\Delta}) + C_s \left[\Pi(\bar{c}, \bar{\Delta}) - \Pi(\hat{c}, \hat{\Delta}) \right] \quad (4.23)$$

Using equations (4.14) & (4.15), the two terms in the unresolved equation (4.22) may be expressed as:

$$\Pi(\bar{c}, \bar{\Delta}) = \hat{\Sigma} \left(\frac{\bar{\Delta}}{\delta_c} \right)^{D-2} \quad (4.24)$$

$$\Pi(\hat{c}, \hat{\Delta}) = \hat{\Sigma} \left(\frac{\hat{\Delta}}{\delta_c} \right)^{D-2} \quad (4.25)$$

The above terms can be combined with the similarity concept in order to derive the model coefficient C_s :

$$C_s = \frac{\Pi(\bar{c}, \bar{\Delta}) - \Pi(\hat{c}, \hat{\Delta})}{\Pi(\hat{c}, \hat{\Delta}) - \Pi(\hat{c}, \hat{\Delta}) - \Pi(\bar{c}, \bar{\Delta}) + \Pi(\bar{c}, \bar{\Delta})} \quad (4.26)$$

The above equation can be simplified by using equations (4.24) and (4.25) by identifying the sub-grid scale flame surface as a fractal surface (Knikker et al. (2004)) as:

$$C_s = \frac{1}{1 - \gamma^{2-D}} \left[\left(\frac{\bar{\Delta}}{\delta_c} \right)^{D-2} - 1 \right] \quad (4.27)$$

In the above equation, δ_c is the lower cut-off scale, taken to be equal to three times of the laminar flame thickness (Knikker et al. (2004) and Gubba (2009)). The fractal dimension, D , can be calculated using either the empirical relation (North and Santavicca (1990) and Fureby (2005)) or calculated dynamically by similarity to Germano identity with the fractal theory for wrinkled flames.

The above model for C_s with the fractal model based on SGS velocity fluctuations, laminar flame speed, laminar and turbulent fractal limit, has been tested by Knikker et al. (2004) for experimentally extracted data of PLIF-OH images of Nottin et al. (2000). Where, good predictions were obtained for the global mean flame surface density together with realistic values for the fractal dimension. However, in the present study the dynamic flame surface density model is tested for the three fuels CNG, LPG, and hydrogen at lean condition and the numerical predictions are validated against some of the experimental data from a laboratory scale premixed combustion chamber of AlHarbi et al. (2013).

4.4 Modelling of the Fractal Dimension

In this section, a model based on the classical fractal theory, is presented and discussed to evaluate the fractal nature of turbulent premixed flames. Since the successful introduction of the fractal theory by Mandelbrot (1975) in homogeneous, isotropic turbulence, fractal concepts have been widely used for various diverse applications. The application of the fractal concept to turbulent premixed flames has been a subject of interest, while understanding the flame structure has been examined by many researchers such as Gouldin (1987) and Kerstein (1988). Gouldin (1987) characterized the turbulent flame surface as a passive scalar surface dominated by the fractal nature of turbulent flow field. Kerstein (1988) represented the turbulent flame structure as a fractal surface based on the dynamic similarity of the flame front. However, both studies have concluded with a value of 2.37 for the fractal dimension, D for turbulent premixed flames. Later, North and Santavicca (1990) carried out an extensive experimental study of a freely propagating turbulent premixed flame over a wide range of turbulent Reynolds and Damköhler numbers. From their experimental observations, they derived an empirical relation as a function of turbulence intensity and laminar flame speed.

The basic principle of fractal theory is to identify and characterize the flame front structure as a fractal surface, which cannot be described by conventional methods. Since turbulent flames come under the category of naturally occurring fractals as shown in Figure 4.1, there exists a wide range of self-similar shapes and forms of different scales between outer and inner cut-off scales as shown in Figure 4.2. The similarity between the different size scales implies that the dynamic processes operating at each scale of similar size is the same, and facilitates the calculation of the fractal dimension of the fractal surface. As mentioned earlier, Mandelbrot (1975) was the first to suggest a value of 2.5 to 2.67 for D in the case of isotropic, homogeneous turbulence, but subsequent experiments (Lovejoy (1982), Sreenivasan and Meneveau (1986)) and mathematical analysis (Hentschel and Procaccia (1984)) suggested a value of 2.35 to 2.41. However, Gouldin (1987) considered an intermediate value of 2.37 based on experimental studies of clouds and jet boundaries in free shear flows in his turbulent premixed modelling studies. Kerstein (1988) also suggested the same value for D , while deriving it using the dynamic similarity approach. Hence, it is evident that there exist various values for fractal dimension based on either experimental analysis or mathematical derivation in the literature.

Numerical modelling of turbulent premixed flames, based on fractal theory, generally requires a value for the fractal dimension of the fractal surface, which can be either modelled, based on local flow conditions or a prior value can be taken as an input. Nevertheless, most of the current research studies are found to follow the later approach due to either a loss of information in numerical simulations or to avoid the complexity of the whole problem. However, in the present work, the fractal dimension of the turbulent premixed flame front is modelled using the dynamic fractal model (DFM) of Knikker et al. (2004). The DFM is based on the outcome of the recent mathematical derivation of the dynamic evaluation and Germano identity of the resolved filtered flame surface density at the test and grid filter.

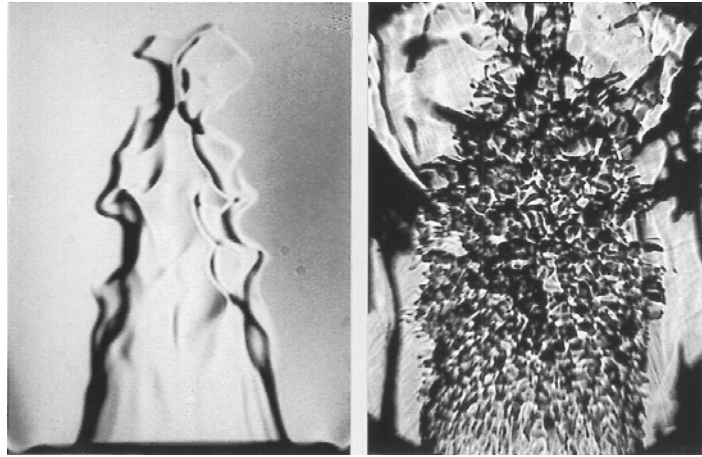


Figure 4.1 Instantaneous Schlieren images of a typical lean premixed flame at different pressures showing the fractal nature of the flame (Kobayashi et al., 1996).

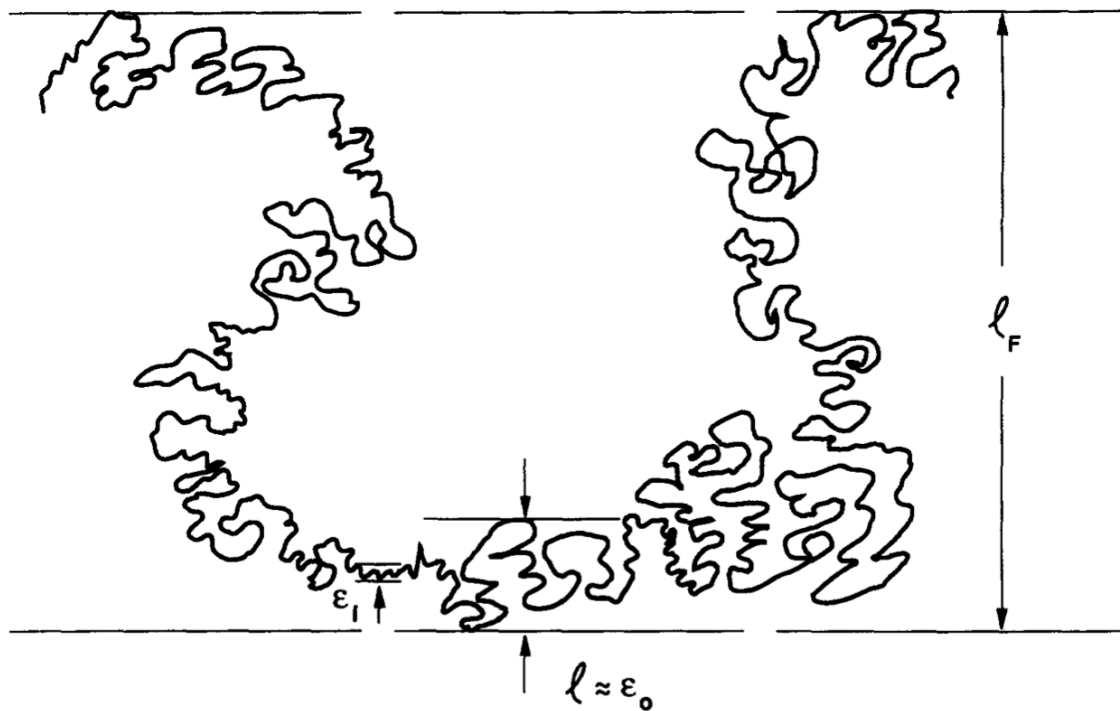


Figure 4.2 Fractal nature of the flame front showing various length scales (Gouldin et al. (1989b)).

4.4.1 Dynamic Fractal Model (DFM)

The dynamic fractal model (DFM) can be considered as a continuation of the DFSD model described in section 4.3, which identified the fractal dimension of the turbulent

premixed flame. Considering the flame kernel as a fractal surface, the fractal dimension, D , is extracted by coupling the wrinkling flame factor (equation 4.15) with the Germano identity (Germano et al. (1991)), while conserving the averaged filtered flame surface at the test and grid filter as follows:

$$\Xi(\widehat{\bar{\Delta}})\Pi(\bar{c}, \bar{\Delta}) = \Xi(\widehat{\hat{\Delta}})\Pi(\hat{c}, \hat{\Delta}) \quad (4.28)$$

Using equations (4.15), (4.24) and (4.25) the above expression can be rewritten as:

$$\left(\frac{\bar{\Delta}}{\delta_c}\right)^{D-2} \widehat{\bar{\Sigma}}\left(\frac{\bar{\Delta}}{\delta_c}\right)^{2-D} = \left(\frac{\hat{\Delta}}{\delta_c}\right)^{D-2} \widehat{\hat{\Sigma}}\left(\frac{\hat{\Delta}}{\delta_c}\right)^{2-D} \quad (4.29)$$

The above expression can be solved for the fractal dimension, D , for each time step at every grid point in the computational domain. However, some form of averaging is usually required to avoid numerical stability issues, similar to that used to dynamically evaluate the Smagorinsky constant. Hence, the volume average of equation (4.29) is carried out for every time step as follow:

$$\left\langle \left(\frac{\bar{\Delta}}{\delta_c}\right)^{D-2} \widehat{\bar{\Sigma}}\left(\frac{\bar{\Delta}}{\delta_c}\right)^{2-D} \right\rangle = \left\langle \left(\frac{\hat{\Delta}}{\delta_c}\right)^{D-2} \widehat{\hat{\Sigma}}\left(\frac{\hat{\Delta}}{\delta_c}\right)^{2-D} \right\rangle \quad (4.30)$$

Rearranging the above equation results in:

$$\left(\frac{\hat{\Delta}}{\bar{\Delta}}\right)^{D-2} = \frac{[\widehat{\Pi(\bar{c}, \bar{\Delta})}]}{[\Pi(\hat{c}, \hat{\Delta})]} \quad (4.31)$$

Applying the logarithm on both sides of the above equation and rearranging will lead to:

$$D = 2.0 + \frac{\log([\widehat{\Pi(\bar{c}, \bar{\Delta})}]/[\Pi(\hat{c}, \hat{\Delta})])}{\log(\hat{\Delta}/\bar{\Delta})} \quad (4.32)$$

The above equation can be solved at each grid point in the computational domain at every time step. To overcome the problems caused by strong local variations or to avoid irrelevant values, the maximum value of the fractal dimension is set to 2.5 in simulations (Gubba (2009)).

4.5 Lewis Number Effect

The Lewis number is defined as the ratio between thermal diffusivity α_T to mass diffusivity D_L . The Lewis number effect (also named thermo-diffusive instabilities) arises from the fact that these two diffusivities became unbalanced. This is illustrated in Figure 4.3, where diffusive fluxes of limiting component are shown with dashed lines (D_L), and diffusive fluxes of heat shown with solid lines (α_T). In cases where $Le < 1$, the local combustion temperature, T_b , is increased behind the convex part of the front, e.g., upper left part of Figure 4.3, due to the increased mass diffusion of limiting component and decreased heat loss. This results in the local increase of the burning velocity. On the other hand, the local combustion temperature is decreased behind the concave part of the front, e.g., lower left part of Figure 4.3, resulting in the local reduction of the burning velocity. All together this leads to further increase of the flame wrinkling. The opposite is true for cases where $Le > 1$, which are characterized by a tendency of smoothing out flame wrinkles, which leads to stable flames. It should be mentioned here that, the thermal-diffusion effects reveal themselves as stabilizing or destabilizing factors of the underlying hydrodynamic instability (Ciccarelli and Dorofeev (2008)). Moreover, the interaction between a laminar premixed flame and stretch depends strongly on the Lewis number of the reactant mixture.

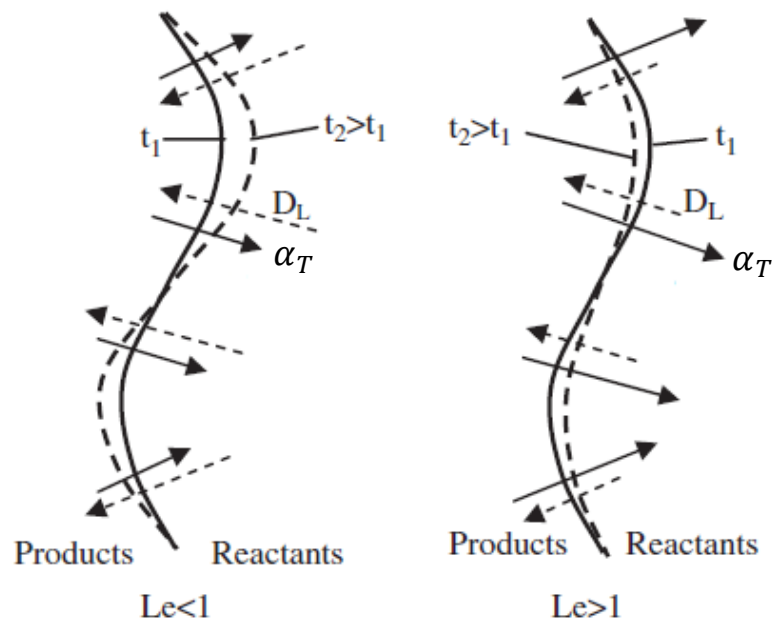


Figure 4.3 Schematic of thermal-diffusive instability. Flame shapes at two moments of time t_1 and t_2 are shown. Flame propagates from left to right (Ciccarelli and Dorofeev (2008)).

However, several methods have been used to account for the thermo-diffusive instabilities in combustion modelling. Richardson and Chen (2012) proposed a modification for two existing mixing models, i.e. interaction by exchange with the mean (IEM) and Euclidean minimum spanning tree (EMST) by adding correction terms which account for differential diffusion effects in a premixed combustion context. Recently, tabulated chemistry methods have developed lot of interest due to their simplicity and computational efficiency. Swart et al. (2010) used FGM with flamelet dimensions based on atomic mass fractions. This approach is very promising since it can account for both curvature and differential diffusion effects which is essential to capture thermo-diffusive instabilities. A more efficient two equation model combined with tabulated chemistry was proposed by Regele et al. (2013) to account for non-unity Lewis number effect in laminar premixed hydrogen flames. They used a mixture fraction definition avoiding unity Lewis number assumption to tabulate the premixed flame solutions as a function of this mixture fraction and progress variable.

On the other hand, Verbecke (2009) used the leading point concept based on Zimont and Lipatnikov (1995), where he expressed the thermos-diffusive instabilities as a function of the fuel-air mixture in terms of wrinkling factor. He applied successfully the previous concept in freely propagating large scale hydrogen explosion. However, the drawback of this method that it does not account dynamically for the flame condition until it reached the maximum value for the wrinkling factor.

However, in this study a simple method is proposed to account for the effect of non-unity Lewis number. As the combustion model is based on solving for reaction progress variable not species and originally it was original developed by Boger et al. (1998) and later by Knikker et al. (2004), for unity Lewis number by assuming equal values for both Schmidt and Prandtl numbers in the governing equations.

$$Le = \frac{\alpha_T}{D_L} = \frac{Sc}{Pr} \quad (4.33)$$

$$Sc = \frac{\nu}{D_L} \quad \text{and} \quad Pr = \frac{\nu}{\alpha_T} \quad (4.34)$$

So, to achieve that, the values of both Schmidt and Prandtl numbers in the reaction progress variable and energy equations discussed in Chapter 3 are set to account for the actual Lewis number value for each fuel-air mixture. Table 4.1 presents the actual values used in the current numerical results calculated from GASEQ program.

Table 4.1 Fuel properties used to account for non-unity Lewis number effect from GASEQ.

	CNG	LPG	Hydrogen
Equivalence Ratio (Φ)	0.8	0.8	0.8
Kinematic Viscosity (ν) (m²/s)	1.58×10^{-5}	1.49×10^{-5}	2.03×10^{-5}
Thermal Diffusivity (α_T) (m²/s)	1.98×10^{-5}	1.84×10^{-5}	3.82×10^{-5}
Mass Diffusivity (D_L) (m²/s)	2.13×10^{-5}	1.18×10^{-5}	4.60×10^{-5}
Sc	0.742	1.260	0.353
Pr	0.798	0.810	0.531
Lewis No.	0.93	1.55	0.67

4.6 Ignition Model

In setting up the numerical case under study, it is important to approximate, as closely as possible the experimental parameters and this, in some instances, may not be possible. The ignition source is one of the parameters that need to be reproduced numerically due to the fact that, experimentally, this performed with a focused laser beam. Moreover, sensitivity to the ignition energy and the location of the source has not been performed experimentally. Numerically, ignition is modelled by setting the reaction progress variable to 0.5 (Kirkpatrick (2002) and Gubba (2009)) within a certain number of cells located near the center of the base plate. It is relatively straight forward to vary the shape, size and location of the ignition source and monitor their effects on the peak overpressure, the flame structure and its propagation rates. It should be noticed that, neither, the breakdown nor complex physics in the early flame propagation is

considered in this approach, where the reaction rate is predicted using the main combustion model itself.

4.7 Summary

This chapter focuses on modelling of the reaction rate and the current challenges in accounting for it in turbulent premixed flames using the flame surface density model. One of the main challenges in LES for turbulent premixed combustion was accounting for the unresolved flame surface density, which can either be obtained by solving the exact FSD equation or by modelling using the dynamic technique. It was identified that solving the exact equation in RANS is complex, and hence solving it in LES will lead to many unclosed terms.

This study shows that algebraic FSD can be further improved by calculating the unresolved flame surface density by additional formulation. Consequently, the DFSD model (Gubba (2009)) based on the simple FSD, the Germano identity and the similarity concept has been the best available option, and a detailed derivation was provided. A dynamic model is used to calculate the fractal dimension based on experimental studies and dynamic similarity ideas.

The Lewis number and its effect on combustion modelling were discussed. Also, how it is implemented through the in-house code and parameters to be considered were presented. Finally, the ignition model and how it works was briefly presented.

Chapter 5

Numerical Methodology

The dynamic flame surface density model and other sub models used in this work are numerically implemented in an available in-house LES code PUFFIN, originally developed by Kirkpatrick (2002) and thereafter extended for compressible flows (Kirkpatrick et al. (2003)). The code was developed using sophisticated, state of the art programming techniques in FORTRAN 90, which is capable of handling 2-D and 3-D, non-reacting and reacting (specifically premixed) using LES numerical simulations of various industrial flow problems. Recently, the code has been extended to compute, non-premixed (Ranga-Dinesh (2007)) and partially premixed (Ranga-Dinesh (2007)) industrial problems as well. However, this chapter briefly describes various numerical features and solution techniques used in the LES code.

In any numerical simulation tool, the primary concern is to outline the partial differential equations, governing the fluid flow, as described in Chapter 3. The governing equations are then carefully discretized, to achieve error free/most accurate numerical results. Finally, spatially discretized equations are solved in computational space and time, which is very important to achieve results of desired and decent accuracy, within the available computational resources.

PUFFIN uses finite volume spatial discretization methodology, on a forward staggered, non-uniform, Cartesian grid, which is detailed in section 5.1. Spatial discretization of individual terms in a generic governing equation, using finite volume methodology is discussed in section 5.2. Section 5.3 describes various aspects of the code such as, time advancement scheme, pressure correction scheme, solver and typical solution iteration procedure. Section 5.4 presents the details of boundary conditions employed in the present investigation.

5.1 Finite Volume Method

In the finite volume method, the computational domain is divided into finite number of control volumes. Conservation equations described in Chapter 3 for turbulent premixed

flames are numerically integrated in each of these control volumes, that will led to a set of simultaneous algebraic equations, whose solution is an approximation to the solution of the continuous equations at a set of discrete points or nodes. Centroid of the individual control volume is generally considered as a node and the solution at this node represents the solution within the control volume. One main advantage of the finite volume methodology is that it can accommodate any type of grid, which is quite suitable for complex geometries. Also, as discussed in Chapter 3, application of box filter in LES, naturally fits into the finite volume formulation.

Hence, the work presented here uses finite volume methodology, based on a forward, staggered cartesian grid and defines the boundaries of the rectangular finite volumes as shown in Figure 5.1. Scalars such as pressure and reaction progress variable are calculated at the scalar nodes as shown in Figure 5.1. However, the velocity components are calculated at the velocity nodes i.e. centroid of scalar cell faces, forming a staggered grid, which means that the velocity cells are staggered with respect to the scalar cells. As staggering of the velocity avoids physically non-realistic predictions for oscillating pressure fields. Also, since the velocities are generated at scalar cell faces, it has the added advantage of avoiding interpolation of velocities for scalar transport computations. Extension of the grid shown in Figure 5.1 in 3-D uses the same structure in the z direction, with an addition of velocity component in z-direction i.e. w .

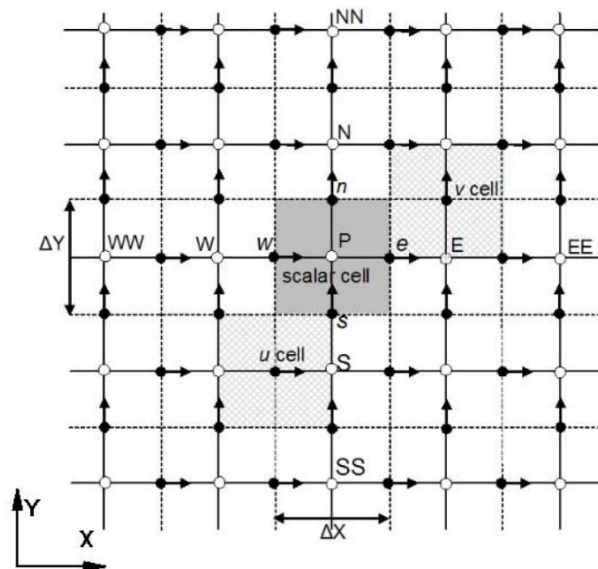


Figure 5.1 Two dimensional forward staggered grid (Gubba (2009)). Circles are scalar nodes, horizontal arrows are nodes of the u velocity component and vertical arrows the nodes of the v velocity component. Examples of a u , v and scalar cells are highlighted.

5.2 Discretization of the Conservation Equations

The conservation equations of mass, momentum, energy and reaction progress variable detailed in Chapter 3 are in similar format and therefore, can be expressed using a generic variable ϕ as:

$$\frac{\partial (\rho\phi)}{\partial t} + \frac{\partial (\rho u_j \phi)}{\partial x_j} = \frac{\partial}{\partial x_j} \left(\Gamma \frac{\partial \phi}{\partial x_j} \right) + S_\phi \quad (5.1)$$

For example, in the previous equation, equals to one represents continuity, u represents momentum in x -direction, h represents specific enthalpy (energy) and c represents reaction progress variable equation. Equation (5.1) can be rearranged as:

$$\frac{\partial (\rho\phi)}{\partial t} = - \frac{\partial (\rho u_j \phi)}{\partial x_j} + \frac{\partial}{\partial x_j} \left(\Gamma \frac{\partial \phi}{\partial x_j} \right) + S_\phi \quad (5.2)$$

In the above equation, Γ is the diffusion coefficient and S_ϕ is the source term. The equation (5.2) is integrated over a control volume V bounded by an arbitrary shape as:

$$\int_V \frac{\partial (\rho\phi)}{\partial t} dV = - \int_V \frac{\partial (\rho u_j \phi)}{\partial x_j} dV + \int_V \frac{\partial}{\partial x_j} \left(\Gamma \frac{\partial \phi}{\partial x_j} \right) dV + \int_V S_\phi dV \quad (5.3)$$

The convection and diffusion terms in the above equation can be transformed into surface integrals by using Gauss divergence theorem, which yields the integral form of the equation as:

$$\frac{\partial}{\partial t} \int_V (\rho\phi) dV = - \int_S \rho u_j \phi dS_j + \int_S \Gamma \frac{\partial \phi}{\partial x_j} dS_j + \int_V S_\phi dV \quad (5.4)$$

The differential surface area vector dS has a magnitude equal to the area of the segment of surface and direction corresponding to the direction of the outward normal to the segment. The terms in the equation (5.4) represents, unsteady term on LHS and advection, diffusion and the source terms on RHS respectively. Spatial discretization of the equation (5.4) involves approximating the volume and surface integrals within the finite volume to obtain a set of simultaneous linear algebraic equations in ϕ .

A schematic representation of 2-D forward staggered grid shown in Figure 5.1 shows the details of a scalar cell P for which the integrals are to be calculated and surrounded by its northern (N), eastern (E), southern (S), western (W) neighbours and one level away from it as north of northern (NN), east of eastern (EE), south of southern (SS), west of western (WW). Figure 5.2 extends this structure in 3-D for the same scalar and shown neighbouring cells in z -direction as up (U) and down (D), which can be extended thereafter as upper of up (UU) and down of down (DD). The surfaces separating two cells are denoted as A_n, A_e, A_s, A_w, A_u and A_d , the associated fluxes are F_n, F_e, F_s, F_w, F_u and F_d . Where, the subscripts ($n, e...$ etc.) refer to the points at the centroid of the respective cell faces. In the following section, nb is used as a generic subscript for neighbour cell and f is a generic subscript for a quantity evaluated at a cell face. To reduce the complexity of the notation, the fluxes are given for a particular face such as the east or north face. All results can be applied in a similar manner to other faces.

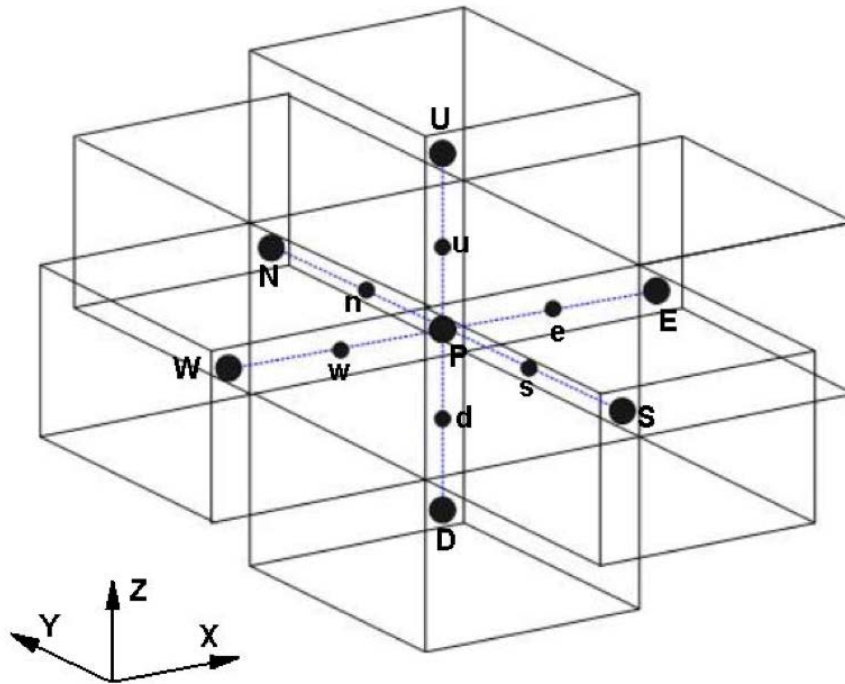


Figure 5.2 3-D view of a finite volume cell and its neighbours.

5.2.1 The Unsteady Term

The unsteady term on the left hand side of the conservation equation (5.4) can be discretized by considering the value of at the central node, which is considered to be

representing the value throughout the control volume. Using the central difference approximation for the time derivative at $n+1/2$ it can be derived as:

$$\int_V \frac{\partial (\rho\phi)}{\partial t} dV \approx \frac{(\rho\phi)^{n+1} - (\rho\phi)^n}{\Delta t} \Delta V \quad (5.5)$$

where n is the time level. The value n indicates that the values are taken at the start of the current time step, while $n + 1$ indicates the end of the time step.

5.2.2 The Convection Term

The convective fluxes are very important in any turbulent reacting flows and hence, their description is essential in numerical simulations. In order to achieve appropriate numerical stability and accuracy, a special treatment for the convective fluxes is required. Numerical discretization employed for convective fluxes is explained as follows.

Considering a control volume and representing convective fluxes as:

$$\int_S \rho u_j \phi dS_j = \sum_{n,e...} F_{conv} \quad (5.6)$$

The convection flux across a cell face is given by:

$$F_{conv} = (\rho u_{normal} \Delta A \phi)_f \quad (5.7)$$

where u_{normal} is the velocity component normal to the surface A and ΔA is the area of the face. The convection for the east face can be written as:

$$F_{conv} = (\rho u \Delta A)_e \phi_e \quad (5.8)$$

The application of weighted, linear interpolation of the neighbouring cells at the centre of the face leads to:

$$\phi_e = (1 - \theta) \phi_P + \theta \phi_E \quad (5.9)$$

Here the weighting factor for the interpolation is:

$$\theta = \frac{\Delta x_e}{\Delta x_E} \quad (5.10)$$

Δx_e and Δx_E are the distances from the node (P) to the face of the centroid (e) and the east neighbour node (E), as shown in Figure 5.3.

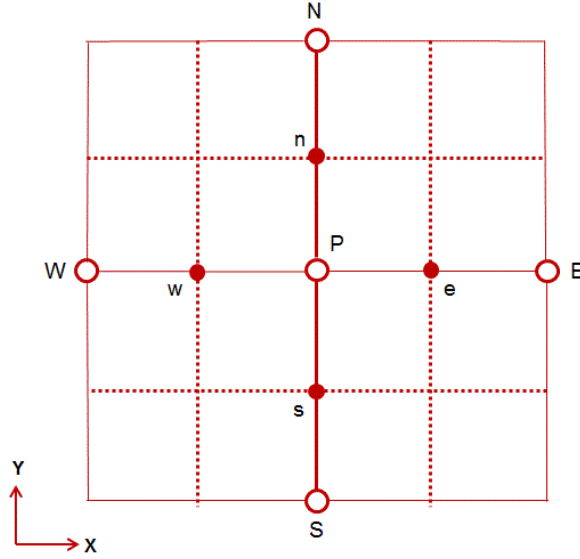


Figure 5.3 A finite volume cell in the xy-plane.

In the staggered grid it is required to find the convective velocity u_e at the face and the density ρ_e at the face depending on whether the variable is a scalar or velocity component. When ϕ is a scalar, the convective velocity is available, as u is established at the cell face. However, density must be interpolated using an equation similar to (5.9) such as:

$$\rho_e = (1 - \theta)\rho_P + \theta\rho_E \quad (5.11)$$

Contrary to that, when ϕ is a velocity component, linear interpolation is required to find the convective velocity, however, ρ is directly available. Finally the resulting formulation for the convection fluxes can be described using a second order central difference scheme as:

$$F_{conv} = (\rho u \Delta A)_e [(1 - \theta)\phi_P + \theta\phi_E] \quad (5.12)$$

This linear interpolation based numerical scheme used to calculate the variables at cell faces of the finite volumes is equivalent to a second order central difference scheme in finite difference method. This scheme is second order accurate, computationally efficient and simple to implement. This accuracy is desirable for LES since numerical damping acts as an extra un-quantified contribution to the eddy viscosity and contaminates the effects of the sub-grid scale model. However this scheme tends to give solutions containing non-physical oscillations or wiggles in areas of the field containing high gradients. The convection terms in the scalar equations are particularly problematic due to the large gradients which often occur in the scalar fields. Because scalars are often coupled with the velocity field through density, wiggles which result from use of the central difference for the scalar convection terms cause problems with the numerical stability of the overall solution. Hence this scheme is hardly suited for scalar transport, especially when they have to remain bounded. For example, reaction progress variable is limited to a range from 0 to 1. From this scheme, wiggles may lead to unphysical results such as predictions of reaction progress variable outside the range 0 and 1, which do not yield any sensible meaning. For this reason, the convection term for the scalar equation is discretized using non-centred schemes such as QUICK or SHARP for Leonard (1979).

QUICK is a third order upwind scheme and can reduce numerical oscillations by introducing fourth order dissipation. Quadratic interpolation is used to find the value ϕ at the centre of the cell faces. The formula for the east face can be written as:

$$\phi_e = [(1 - \theta)\phi_P + \theta\phi_E] - \frac{1}{8} CRV \times \Delta x_E^2 \quad (5.13)$$

Here the upwind biased curvature term define as:

$$CRV = \frac{\phi_P - 2\phi_E + \phi_{EE}}{\Delta x_E^2}, \quad u < 0 \quad (5.14)$$

$$CRV = \frac{\phi_E - 2\phi_P + \phi_w}{\Delta x_E^2}, \quad u > 0 \quad (5.15)$$

The double subscript such as EE refers to the cell east of the eastern neighbour as described in section 5.2. The weighting factor θ can be calculated from equation (5.10).

The first term in equation (5.13) is the value of ϕ at the cell face calculated using linear interpolation. The second term is an upwind biased curvature term which makes the overall interpolation quadratic.

The linear interpolation term accounts for the non-uniform grid through the weighting factor θ , while the curvature terms have no grid weighting included. Castro and Jones (1987) have shown that the uniform grid formula for QUICK gives negligible errors for grid expansion ratios ($r_x = \Delta x_{i+1}/\Delta x_i$) between 0.8 and 1.25. Substituting equation (5.13) into equation (5.5) gives the convective flux of ϕ across the east face as:

$$F_{conv} = (\rho u \Delta A)_e [((1 - \theta)\phi_P + \theta\phi_E) + S_{QUICK}] \quad (5.16)$$

where $S_{QUICK} = -1/8 CRV \times \Delta x_E^2$. The source term S_{QUICK} indicates the curvature of the field. In PUFFIN, the term S_{QUICK} is included as part of the source term S_ϕ .

However, QUICK scheme can reduce the wiggles but does not remove them completely. In this case another scheme called SHARP (Leonard (1979)), which is a modification to QUICK is used. SHARP introduces second order diffusion where local conditions are such that oscillations will not occur, thereby ensuring that the solution remains monotonic. An outline of this scheme can be found in (Leonard (1979)). Finally, summation of the convective fluxes across all faces can be added and described as:

$$\int_S \rho u_j \phi dS_j \approx \sum (\rho u \Delta A)_f [(1 - \theta_f)\phi_P + \theta_f\phi_{nb} + \sum S_{QUICK}] \quad (5.17)$$

5.2.3 The Diffusion Term

The diffusive flux is proportional to the gradient of across a cell face f and is given as:

$$F_{diff} = \left[\Gamma \Delta A \left(\frac{\partial \phi}{\partial n} \right) \right]_f \quad (5.18)$$

where n is the direction normal to the face, Γ is the kinematic diffusion coefficient and ΔA the area of the face. The flux at the centre of the east cell face is then computed from

the values at the two neighbouring points and their distance from central difference approximation as:

$$F_{diff} = (\Gamma \Delta A)_e \frac{\phi_E - \phi_P}{\Delta x_E} \quad (5.19)$$

The diffusion coefficient at the centre of the face Γ_e is calculated by linear interpolations same as density calculation in the preceding section of the convection term. Summation of the diffusive fluxes across all faces can be described as a discrete diffusion operator as:

$$\int_s \Gamma \frac{\partial \phi}{\partial x_j} dS_j \approx \sum \frac{(\Gamma \Delta A)_e}{\Delta x_E} (\phi_{nb} - \phi_P) \quad (5.20)$$

It is worth noting at this stage, that the discrete diffusion operator does not suffer from numerical instability as observed in the case of convective fluxes. Therefore, no special treatment is needed for the diffusion terms in conservation equation.

5.2.4 The Source Term

Source terms are different for each variable in individual conservation equations and dependent of the variable being transported. For instance, in case of momentum equation, source term represents the effect of the pressure gradient and the gravitational force. However, in case of energy equation, source term includes contributions due to pressure work, viscous dissipation and flow dilatation as well as a chemical source term. Chemical source term is also presented in the reaction progress variable equation.

Spatial discretization of the source term in all the transport equations is in the same manner. They are calculated by evaluating the function representing the source term S_ϕ at the node and multiplying by the volume of the cell as:

$$\int_V S_\phi dV \approx S_{\phi P} \Delta V \quad (5.21)$$

Gradients are evaluated using second order central differences, while interpolations utilize a linear profile similar to that used in evaluating convection and diffusion terms.

In general, source terms can be expressed as a combination of implicit and explicit components as:

$$S_{\phi_P} \Delta V = S_{imp} \phi_P + S_{exp} \quad (5.22)$$

The implicit component of the above equation is integrated using implicit time advancement scheme, whereas the explicit component is integrated using explicit time advancement scheme. The time advancement schemes employed in the present work are described in section 5.3.

5.2.5 The Complete Discretized Conservation Equation

It is evident from the above sections, that the complete discretized conservation equation for a generic variable can simply written by summing the individual discretized terms as:

$$\begin{aligned} & \frac{(\rho\phi)^{n+1} - (\rho\phi)^n}{\Delta t} \Delta V \\ &= \left\{ \sum (\rho u \Delta A)_f [(1 - \theta_f) \phi_P + \theta_f \phi_{nb}] \right\}^{(n-2, n-1, n, n+1)} \\ &+ \left\{ \sum \frac{(\Gamma \Delta A)_e}{\Delta x_E} (\phi_{nb} - \phi_P) \right\}^{(n-1, n, n+1)} + \{S_{imp} \phi_P\}^{(n-1, n, n+1)} \\ &+ \{S_{exp}\}^{(n-2, n-1, n, n+1)} \end{aligned} \quad (5.23)$$

Here the curly brackets ‘{ }’ with superscripts $n-2, n-1, n, n+1$ represent a weighted average of the term evaluated at the listed time intervals, which gives an estimate of the term at the $(n+1/2)$ time level, which will be discussed in next section. Collecting the coefficients and rearranging the above equation results in the final form equation as:

$$\begin{aligned} A_P^{n+1} \phi_P^{n+1} &= \sum_{nb} (A_{nb}^{n+1} \phi_{nb}^{n+1}) + S_{imp} \phi_P^{n+1} + S_{exp}^{n+1} \\ &+ \left[\sum_{nb} (A_{nb}^n \phi_{nb}^n) - A_P^n \phi_P^n + S_{imp} \phi_P^n + S_{exp}^n \right] \\ &+ \left[\sum_{nb} (A_{nb}^{n-1} \phi_{nb}^{n-1}) - A_P^{n-1} \phi_P^{n-1} + S_{imp} \phi_P^{n-1} + S_{exp}^{n-1} \right] \\ &+ \left[\sum_{nb} (A_{nb}^{n-2} \phi_{nb}^{n-2}) - A_P^{n-2} \phi_P^{n-2} + S_{exp}^{n-2} \right] \end{aligned} \quad (5.24)$$

where the coefficients corresponding to the node A_P and its neighbours A_{nb} are formed due to the contributions from convection and diffusion terms. More details of spatial discretization methods can be found in Kirkpatrick (2002) and Kirkpatrick et al. (2003)

5.3 Time Advancement Scheme

The discretized transport equation described in the above section must be solved in space and time in order to simulate reacting flows. To obtain time-accurate and unsteady simulations, time integration schemes are developed using second and third order numerical accuracy. The time integration schemes for scalar equation uses the Crank- Nicolson scheme and the momentum equations are advanced using either Crank- Nicolson or the second- and third- order hybrid Adams-Bashforth scheme.

5.3.1 Time Integration of Scalar Equation

In the present work, Crank-Nicolson scheme is employed to achieve time integration of the scalar equation. The time dependent conservation equation, integrated in time using Crank-Nicolson scheme can be written as:

$$\begin{aligned} \frac{(\rho\phi)^{n+1} - (\rho\phi)^n}{\Delta t} \Delta V = & -\frac{1}{2} [H^{n+1}(\phi_P^{n+1}) + H^n(\phi_P^n)] \\ & + \frac{1}{2} [L^{n+1}(\phi_P^{n+1}) + L^n(\phi_P^n)] \\ & + \frac{1}{2} [S_{imp}^{n+1}\phi^{n+1} + S_{imp}^n\phi^n] \\ & + \frac{1}{2} [S_{exp}^n\phi^n + S_{exp}^n\phi^n] \end{aligned} \quad (5.25)$$

where H is the discrete convection term, expressed as:

$$H(\phi) = \sum (\rho u \Delta A)_f [(1 - \theta_f)\phi_P + \theta_f\phi_{nb}] \quad (5.26)$$

and L is the discrete diffusion term, expressed as:

$$L(\phi) = \sum \frac{(\Gamma \Delta A)_e}{\Delta x_E} (\phi_{nb} - \phi_P) \quad (5.27)$$

$S_{imp}\phi$ and S_{exp} are discrete implicit and explicit source terms respectively. It is to be noted that S_{imp} is a coefficient of ϕ rather a function of ϕ .

In equation (5.25), each term is evaluated at the n and $n+1$ time levels, and employs linear interpolation to estimate their value at $n+1/2$. Therefore, this scheme is second order accurate. At least two iterations of scalar equation per time step are required due to the contributions of terms containing ϕ^{n+1} to the explicit source term which result from the use of the QUICK and SHARP spatial discretization schemes. It should be noticed at this stage that in turbulent premixed combustion, density and diffusivity vary significantly in time. Hence to maintain the stability of the solution, a number of outer iterations of the entire time advancement scheme per time step are required to ensure that the values of ρ^{n+1} and Γ^{n+1} are second order accurate. This non-oscillatory criterion for Crank-Nicolson scheme can be achieved by enforcing a condition on time as:

$$\Delta t \leq \frac{(\Delta x)^2}{\Gamma} \quad (5.28)$$

While the above criterion poses a rather stringent limitation on the improvement that could be achieved on spatial accuracy, it results from an error term in the Taylor series expansion which contains the second derivative in space ($\partial^2 \phi / \partial^2 x_i^2$). However, this term is relatively small in most flow problems and the scheme remains stable for considerably large time steps.

5.3.2 Time Integration of Momentum Equations

Time integration of the momentum equations uses either Crank-Nicolson or the second and third order hybrid Adams schemes. In the hybrid schemes, Adams-Bashforth methods are used for the advection terms and Adams-Moulton methods for the diffusive terms. The momentum equations are integrated by using Crank-Nicolson scheme can be expressed as:

$$\begin{aligned} \frac{\rho^{n+1}u^* - \rho^n u^n}{\Delta t} \Delta V &= -\frac{1}{2}[H^{n+1}(u^*) + H^n(u^n)] + \frac{1}{2}[L^{n+1}(u^*) + L^n(u^n)] \\ &+ \frac{1}{2}[S_{imp}^{n+1}u^* + S_{imp}^n u^n] + \frac{1}{2}[S_{exp}^{n+1}u^* + S_{exp}^n u^n] - Gp^{n-\frac{1}{2}} \end{aligned} \quad (5.29)$$

It is evident from the above equation, that it has similar form of the scalar equation employing Crank-Nicolson scheme (equation 5.25). However, an additional term can be

noticed, added as a pressure gradient term $G_p^{n-1/2}$, which considers $n-1/2$ time level concerning the pressure correction scheme, which will be discussed in next section. Here the approximate velocity obtained before pressure correction step at $n+1$ time level is specified with superscript u^* .

The advection terms in the momentum equations are integrated using explicit time advancement scheme, as Crank-Nicolson requires several iterations to retain second order accuracy. In PUFFIN, second and third order hybrid schemes are used such that advection terms are treated explicitly using an Adam-Bashforth scheme while diffusion term is treated implicitly using Adams-Moulton. The additional terms such as gravitational terms are treated explicitly using Adams-Bashforth.

The second order Adams-Bashforth/Adams-Moulton scheme for the momentum equations can be written as:

$$\begin{aligned} \frac{\rho^{n+1}u^* - \rho^n u^n}{\Delta t} \Delta V &= -\frac{1}{2}[3H^n(u^n) - H^{n-1}(u^{n-1})] + \frac{1}{2}[L^{n+1}(u^*) + L^n(u^n)] \\ &+ \frac{1}{2}[S_{imp}^{n+1}u^* + S_{imp}^n u^n] + \frac{1}{2}[3S_{exp}^n u^n - S_{exp}^{n-1}u^{n-1}] - Gp^{n-\frac{1}{2}} \end{aligned} \quad (5.30)$$

While the third order Adams-Bashforth/Adams-Moulton scheme can be written as:

$$\begin{aligned} \frac{\rho^{n+1}u^* - \rho^n u^n}{\Delta t} \Delta V &= -\frac{1}{12}[23H^n(u^n) - 16H^{n-1}(u^{n-1}) + 5H^{n-2}(u^{n-2})] \\ &+ \frac{1}{12}[5L^{n+1}(u^*) + 8L^n(u^n) - L^n(u^n) - L^{n-1}(u^{n-1})] \\ &+ \frac{1}{12}[5S_{imp}^{n+1}u^* + 8S_{imp}^n u^n - S_{imp}^{n-1}u^{n-1}] \\ &+ \frac{1}{12}[23S_{exp}^n u^n - 16S_{exp}^{n-1}u^{n-1} + 5S_{exp}^{n-2}u^{n-2}] - Gp^{n-\frac{1}{2}} \end{aligned} \quad (5.31)$$

The non-linear advection terms and explicit source terms in this case are calculated at previous time steps where all necessary information is known. Hence these schemes do not require any iteration procedure, as in Crank-Nicolson scheme to maintain the accuracy. However, when the density and viscosity vary significantly, as in turbulent

premixed combustion, iteration of the overall solution procedure is required to include the correct value of density in the unsteady term and viscosity in the diffusion term at the $n+1$ time step. The advection term within one time step has to be limited to at least satisfy the Courant number, $CFL = u_i \Delta t / \Delta x_i < 1.0$. Simply, this criterion requires that, within a time step, information may only travel to the neighbouring cell but no further. For advection terms, the maximum time step is proportional to the characteristic convection time $\Delta x_i / u_i$, which is usually described in terms of the Courant number. For diffusion term the maximum usable time step is proportional to the characteristic diffusion time $\Delta x_i^2 / \nu$. However, Adams methods require some treatment for the initial steps where no information about previous time step is available. Therefore, the Crank-Nicolson is used for the initial time steps to enable the calculation of the $n-1$ and $n-2$ source terms for the Adams schemes.

5.3.3 The Pressure Correction Equation

In the present study, pressure correction of unsteady compressible flow simulations have been carried out using the fractional step method based, incompressible flow pressure correction of Kan (1986) and Bell et al. (1989), which has been recently extended by Kirkpatrick (2002) for compressible flows. It is well known that in case of compressible reacting flows, pressure and density remain coupled through the state equation and large density variations exist. Hence, it is essential to correct velocity, density and pressure simultaneously by enforcing the mass conservation of the fluid flow. Since density depends on both pressure and temperature, an iterative method is required to correct it. Accordingly, considering the m^{th} iteration of the time step from $t = n$ to $t = n+1$, the transport equations of energy and reaction progress variable are solved for temperature field T^m . An approximate density field ρ^* for the m^{th} iteration is then found using the equation of the state with the temperature T^m and the pressure from the previous iteration P^{m-1} as:

$$\rho^* = \frac{RT^m}{P^{m-1}} \quad (5.32)$$

The momentum equations for three velocity components are then integrated using ρ^* and P^{m-1} to find an approximate solution for the velocity field u_i^* as:

$$\frac{(\rho^* u_i^*)^{n+1} - (\rho u_i)^n}{\Delta t} = Y(u_i^*, u_i^n) - \frac{1}{2} \left[\frac{\delta P^n}{\delta x_i} + \frac{\delta P^{m-1}}{\delta x_i} \right] \quad (5.33)$$

Where Y is an operator representing the remaining terms in the momentum equation. In order to correct u_i^* , P^{m-1} and ρ^* mass conservation is thus enforced through the obtained velocity field as:

$$\frac{(\rho^m u_i^m)^{n+1} - (\rho u_i)^n}{\Delta t} = \gamma(u_i^*, u_i^n) - \frac{1}{2} \left[\frac{\delta P^n}{\delta x_i} + \frac{\delta P^m}{\delta x_i} \right] \quad (5.34)$$

which eventually satisfies conservation of mass as:

$$\frac{\rho^m - \rho^n}{\Delta t} + \frac{\delta(\rho^m u_i^m) P^n}{\delta x_i} = 0 \quad (5.35)$$

Subtracting equation (5.33) from (5.34) gives:

$$\rho^m u_i^m - \rho^* u_i^* = - \frac{\Delta t}{2} \frac{\delta P'}{\delta x_i} \quad (5.36)$$

where the pressure correction is defined as $P' = P^m - P^{m-1}$. Taking the divergence of equation (7.36) yields:

$$\frac{\delta(\rho^m u_i^m)}{\delta x_i} - \frac{\delta(\rho^* u_i^*)}{\delta x_i} = - \frac{\Delta t}{2} \frac{\delta^2 P'}{(\delta x_i)^2} \quad (5.37)$$

Substituting equation (5.35) in the above results in:

$$\frac{\rho^m - \rho^*}{\Delta t} + \frac{\rho^* - \rho^n}{\Delta t} + \frac{\delta(\rho^* u_i^*)}{\delta x_i} - \frac{\Delta t}{2} \frac{\delta^2 P'}{(\delta x_i)^2} = 0 \quad (5.38)$$

Finally, writing the density correction in terms of the pressure correction using the state equation as:

$$\rho^m - \rho^* = \frac{P'}{RT^m} \quad (5.39)$$

Substituting equation (5.39) in (5.38) results in pressure correction equation as:

$$\frac{P'}{\Delta t RT^m} - \frac{\Delta t}{2} \frac{\delta^2 P'}{(\delta x_i)^2} = - \left[\frac{\rho^* - \rho^n}{\Delta t} + \frac{\delta(\rho^* u_i^*)}{\delta x_i} \right] \quad (5.40)$$

Once the pressure correction is evaluated, it is used to correct pressure, velocity and density as:

$$P^m = P^{m-1} + P' \quad (5.41)$$

$$\rho^m = \rho^* + \frac{P'}{RT^m} \quad (5.42)$$

$$u_i^* = \frac{1}{\rho^*} \left[\rho^m u_i^m + \frac{\Delta t}{2} \frac{\delta P'}{\delta x_i} \right] \quad (5.43)$$

Hence, the pressure correction equation is spatially discretized in the similar manner to the discretization of the generic transport equation described in the earlier sections. Integrating the equation (5.40) over a control volume and applying the Divergence theorem gives:

$$\frac{P'}{\Delta t R T^m} \Delta V - \frac{\Delta t}{2} \sum \left(\Delta A \frac{\delta P'}{\delta x_i} \right) = - \left[\frac{\rho^* - \rho^n}{\Delta t} \Delta V + \sum (\rho^* u_i^* \Delta A)_f \right] \quad (5.44)$$

where summation is performed over each of the faces of area ΔA , and ΔV is the volume of the cell. Second order central differences are used to calculate the gradients $\frac{\delta P'}{\delta x_i}$. It is important to use same discretization for the pressure gradient in momentum equation and the pressure correction in pressure correction equation (5.40). This minimizes the projection error and ensures convergence if an iterative scheme is used.

The boundary condition for pressure correction equation at solid boundaries uses zero-normal gradient condition, since the mass flux across these boundaries is constant. However, for outflow boundaries, a special treatment is required to reduce the pressure reflections as discussed in later sections of this chapter.

5.3.4 Solution of the Algebraic Equations

The system of algebraic equations, obtained through numerical discretization, is generally solved using linear equation solvers. The flow simulation code, PUFFIN has two solvers, Alternating-Direction-Implicit (ADI) solver and Bi-Conjugate Gradient Stabilized (BiCGStab) solver with a Modified Strongly Implicit (MSI) pre-conditioner. Current work has been carried out using BiCGStab to solve the momentum, scalar and

pressure correction equations, which is more efficient and requires ten times less number of iterations to achieve same level of convergence by ADI (Kirkpatrick (2002)).

Convergence of the solvers is measured using the L_2 norm of the residual, where L_2 norm is a vector norm that is commonly encountered in vector algebra and vector operations such as dot product). The residual was set to be less than 10^{-10} for the solution of the momentum and scalar equations, which typically required one or two sweeps of the solver to obtain convergence. At each time step, a number of iterations of the pressure/velocity correction steps are generally required to ensure adequate mass conservation.

Pressure correction equation is solved for all iterations with a condition, either to reduce the residual to 10% of its original value or the BiCGStab solver has performed 7 sweeps. Each sweep of the solver includes 2 sweeps of the pre-conditioner. The solution is then used to correct the pressure and velocity field and the divergence of the corrected velocity field is calculated. The process is repeated until the (L_2) norm of the divergence error is less than pre-set value. Typically, 6 to 8 projections are required to attain the minimum divergence error.

5.3.5 Iteration Procedure

In case of unsteady, compressible reacting flows, where density and pressure variations are predominant, it must be ensured that the pressure, density and velocity are corrected simultaneously by enforcing mass conservation. The overall solution procedure for each time step follows similar to that of Kirkpatrick (2002) for compressible flows and the combustion modelling capabilities in LES has been enhanced using dynamic modelling of flame surface density (DFSD). A typical iteration procedure requires information at current and previous time steps represented by superscripts (n) and ($n-1$) respectively. In the following, superscript (k) refers to the iteration cycle within the time step and the superscript (0) indicates the initial guess for the first iteration with a time step i.e. ($k = 0$).

Step 1: Predict or choose appropriate initial values for the variables at time = 0. In the present work, a straightforward choice is adopted by choosing the solution values at the current time level as:

$$u_k^0 = u_k^n, \phi_k^0 = \phi_k^n, \text{etc.}$$

Step 2: Solve scalar transport equations to obtain provisional values, which will facilitates better estimate of the density early in the iteration process.

Step 3: Calculate the fluid properties such as temperature, density, molecular viscosity according to the combustion model implemented.

Step 4: Update the scalar field information, based on the new density available from preceding step and solve for momentum equation.

Step 6: Solve the pressure correction equation.

Step 7: Correct pressure, velocity and density fields.

Step 8: Check mass conservation error and repeat steps 6 and 7 as required.

Step 9: Calculate eddy viscosity.

Step 10: Calculate dp/dt , S_{kk} , etc.

Typically 8-10 outer iterations of this procedure are required to obtain satisfactory convergence at each time step. The time step is limited to ensure that the Courant number (CFL number), CFL remains less than 0.5 by enforcing a limit on time advancement, δt as:

$$CFL = \frac{\delta t u_i}{\delta x_i} \quad (5.45)$$

However, to avoid un-realistic times an extra condition has been imposed such that the upper limit for δt is 0.3 ms. The solution for each time step requires around 8 iterations to converge, with residuals for the momentum equations less than $2.5e-5$ and scalar equations less than $2.0e-3$. The mass conservation error is less than $5.0e-8$.

5.4 Boundary Conditions

Additional to the mathematical model and the numerical scheme, suitable boundary conditions are important for successful LES predictions. Mathematically, the imposition of exact boundary and initial values are prerequisite for unique solution of the set of partial differential equations to be solved.

In the present study, the problem considered is a propagation of turbulent premixed flame, evolved from stagnant condition in a rectangular chamber having multiple solid obstacles. Solving premixed flames requires the boundary conditions for all the dependent variables such as density, velocity, pressure, temperature and reaction progress variable. Since density is dependent on the pressure and temperature, the boundary condition for density can be specified from pressure and temperature. Continuity requires that mass conservation be satisfied over the complete domain at all times, and the boundary conditions for the velocity field must therefore ensure that:

$$\int_{\Omega} \frac{\partial \rho}{\partial t} dV + \int_S \rho u_i n_i S = 0 \quad (5.46)$$

For the combustion configuration under investigation, outflow boundary conditions at outlet (top) of the chamber and solid wall boundary conditions at rest of the walls (four vertical and one bottom) and solid obstacles are used. The details of these boundary conditions are described in the following sections.

5.4.1 Initial Conditions

At the beginning of a new simulation, the energy and reaction progress variable are set to zero everywhere in the computational domain. The initial velocity field is quiescent, with random perturbation field to allow for development of turbulence. As explained in the previous chapter, to achieve the initial quasi-laminar flame phase corresponding to experiments, ignition is modelled by setting the reaction progress variable to a specific value within a certain radius (Bradley and Lung (1987)) at the bottom centre of the chamber.

5.4.2 Outflow Boundary Conditions

The outflow boundary conditions generally use either a zero normal gradient (ZNG) condition or a convective outlet boundary condition. The zero gradient condition at an outflow boundary is generally given by:

$$\frac{\partial \phi}{\partial n} = 0 \quad (5.47)$$

where $\partial/\partial n$ denotes the gradient taken normal to the outflow boundary. Alternatively, the convective boundary condition is expressed as:

$$\frac{\partial \phi}{\partial t} + U_b \frac{\partial \phi}{\partial n} = 0 \quad (5.48)$$

where U_b is the bulk velocity across the boundary. It is very important in case of compressible flow that the pressure wave generated within the chamber must be allowed to leave smoothly without reflection. Since the pressure field is dependent on the velocity field, the boundary conditions applied for velocity will determine the pressure wave behaviour. The outflow boundary conditions described in equations (5.47) and (5.48) work well when the dominant force on the fluid flow is due to advection and diffusion. However, in the present work, due to the compressible nature of the propagating flame, the dominant force is the pressure gradient resulting from pressure waves generated from the chamber. Consequently, both the above boundary conditions would result in significant pressure reflections. Hence, to overcome this problem, Kirkpatrick (2002) developed a new non-reflecting boundary condition for velocity, similar to the commonly used convective boundary condition in incompressible LES as:

$$u_i = \left(u_{i-1} - \frac{\Delta x_i}{c_{ss}} \frac{\partial u_{i-1}}{\partial t} \right) \frac{R_{i-1}^3}{R_i^3} \quad (5.49)$$

where u_i is the velocity on the boundary, u_{i-1} is the velocity in the adjacent cell within the domain, Δx_i is the distance between the two nodes, R_i and R_{i-1} are the distance from the two nodes to the centre of the open end of the chamber and c_{ss} is the speed of sound, which is convective velocity. To ensure that this boundary condition is accurate, the numerical domain has to be extended with far-field boundary conditions from the chamber outlet.

5.4.3 Solid Boundary Conditions

For solid wall boundaries, it is common to set the normal and tangential velocity components to zero at the wall. These conditions correspond to the impermeable and the no-slip conditions. At the domain boundaries overlapping with a stationary impermeable wall, the no-slip condition can be applied as:

$$u_i(x, t) = 0 \quad (5.50)$$

In turbulent reacting flows, it is important that the near wall treatment should be accurate enough to account for the boundary layer effects. In general, the flow near wall behaves differently than away from it due to shear forces within the vicinity of wall. The main structures capable to determine the flow properties within this region are of the order of boundary layer thickness. Consequently, in high Reynolds flows, it is very important to employ fine grid in the domain near wall, which eventually reaches DNS limit in order to resolve energy carrying scales. Refining grid near wall in LES is not possible due to the computational limitations and alternative methods, such as wall functions are required to mimic the overall dynamics of the near wall effects. Hence, in the present study, the $1/7^{\text{th}}$ power-law wall function of Werner and Wengle (1991) is used to calculate wall shear as:

$$\tau_w = W(\tilde{u}, y) \quad (5.51)$$

where τ_w is the wall shear stress, W is a functional dependence, y is the distance of the grid point from the wall and \tilde{u} is the tangential velocity at y . Solid boundary conditions with this wall function are applied at the bottom, vertical walls, and for solid obstacles in the chamber.

5.4.4 Numerical Domain

In order to simulate the turbulent premixed flame of the stoichiometric propane/air flame, in the combustion chamber shown in Figure 5.4, a computational domain with the applied boundary conditions is required. As described in before, in the case of compressible flows, the domain must extend in the direction normal to the outflow boundary to avoid pressure reflections. However, to avoid certain numerical instabilities, in general, the domain is extended in the other two directions as well. A typical computational domain, superimposed with the numerical combustion chamber and

obstacles is shown for clarity in Figure 5.4. The combustion chamber has dimensions of 50 x 50 x 250 mm where the flame propagates over the baffles and solid obstacle surrounded by solid wall boundary conditions. To ensure that the pressure wave leaves the chamber smoothly, without reflections, the open end of the domain is extended to 250 mm in the z-direction with far-field boundary conditions. Similarly, the domain is extended to 325 mm in the x and y directions with large expansion ratios approximately equal to 1.25 outside the combustion chamber.

The simulations are carried out for the 3-D, non-uniform, Cartesian co-ordinate system for a compressible flow, having low Mach number. In order to examine the solution dependence on the grid resolution, simulations are performed with four different grid resolutions as detailed later on in Table 8.1.

Finally, the work done and the procedure of the current thesis is explained in the chart below (Figure 5.5). Where the DFSD model is examined for the three fuels, then the Lewis number is then implemented and further validated using the extracted stretch rate and different flow configurations.

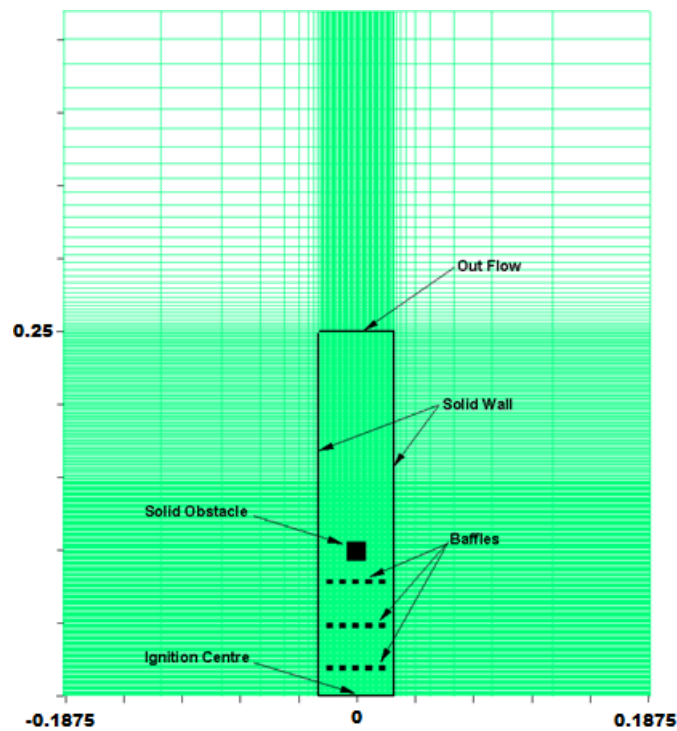


Figure 5.4 Illustration of the computational domain with the combustion chamber and obstacles superimposed over the grid.

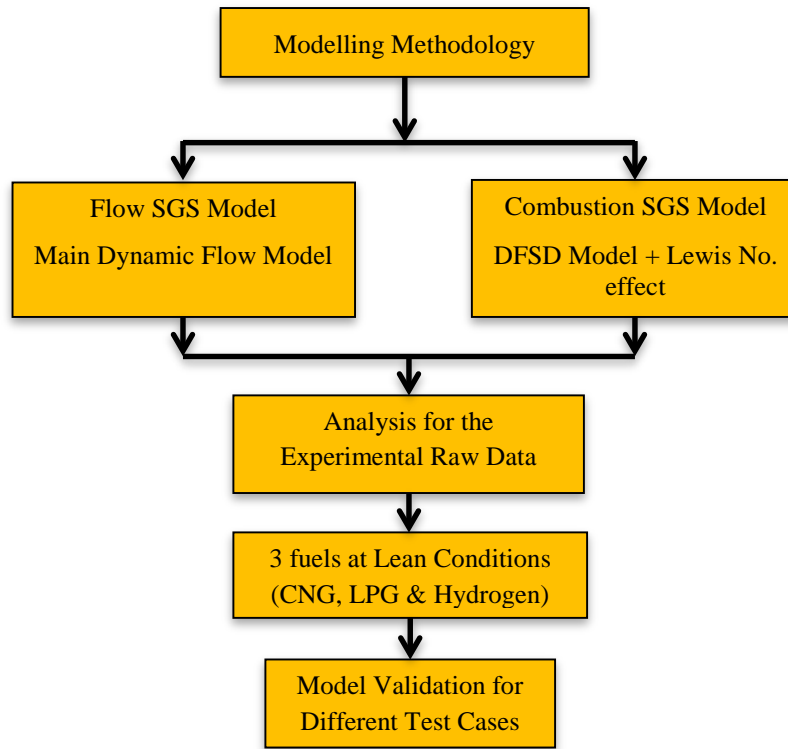


Figure 5.5 Description for the current work.

5.5 Summary

This chapter described numerical features of the in-house code PUFFIN in LES. It uses finite volume methodology, which generally allows complex geometries to form grids and solve successfully. Spatial discretization and numerical implementation of a generic transport equation of variable has been detailed. Several challenges were discussed while dealing the individual terms of the generic equation. Since the fluid flow numerically marches into time, time advancement of the spatially discretized equations are very important for accurate predictions. Mainly, Crank-Nicholson time advancement scheme was discussed as it was used for momentum and other scalar equations. Pressure correction is critical as the fluid flow involved mainly is unsteady, compressible, which generally involved in large density variations and directly coupled with pressure via state equation. Hence, the methodology developed by Kirkpatrick (2002) is used to correct the pressure, velocity and density fields simultaneously by enforcing the mass conservation.

Various linear solvers available in the present numerical in house code “PUFFIN” were briefly outlined and the choice of BiCGStab to solve system of linear equations has been explained. Typical iteration procedure used by PUFFIN was outlined with possible modifications carried out while accounting the chemical reaction rate of the propagating flame. Various boundary conditions such as solid and outflow used in the present study were also presented and discussed.

Chapter 6

The Experimental Combustion Chamber

This chapter describes the experimental combustion chamber used for model validation in the present investigation. Section 6.1 discusses the importance of the experimental turbulent flames and the design consideration for any experimental combustion configuration. Section 6.2 describes the combustion chamber established at The University of Sydney, which is a revised version and fourth inline to test turbulent premixed propagating flames. Accordingly, a brief introduction and some technical details of the various measuring techniques and laser ignition system are provided. Finally, the experimental procedure and sequence of operations are detailed in section 6.3.

6.1 Design Consideration for the Combustion Chamber

Turbulence being an unsolved problem for several decades with available analytical and experimental techniques, turbulence-flame interactions is one of the very interesting and most challenging areas of research. In this series, with the advancement of the numerical prediction tools and computational power, numerical techniques became an alternative method of solving turbulent fluid flow and combustion problems. In order to capture the correct physics and chemical properties of fluid flow problems, it is essential to validate the numerical model, method and the technique implemented against a valid experimental test case. Since the introduction of laser technology for the flow measurements into combustion studies, such as Laser Induced Florescence (LIF), Laser Doppler Velocimeter (LDV), and Particle Image Velocimetry (PIV), extracting the more accurate information regarding turbulence intensity and various other flow parameters made possible. However, the major challenge is to quantify these measurements of turbulence and its interactions with flame in a transient process.

The work presented here, mainly aims to simulate a real explosion situation, where multiple solid obstacles are presented in the path of a propagating flame, which is expected to facilitate understanding some of the remaining key challenges such as

complex feedback system formed due to flame-flow interactions and flame dynamics with respect to position and number of obstacles etc.

Since, one main objective of the current work is experimental validation of the DFSD model, it is ideal to choose a combustion chamber, which could provide sufficient optical access for measurements, affordable for computational modelling, and also to have a simplistic geometries than those encountered in practice so a generalised predictive tool could be developed. It is worth mentioning here, that the original experimental chamber used by combustion groups at both Loughborough and the University of Sydney (Masri et al. (2000), Ibrahim and Masri (2001) and Masri et al. (2006)) was a big chamber of 20 litres in volume and found to be impractical for LES modelling studies due to the long computational times. Hence, an alternative design (Kent et al. (2005)), that preserved the same physics and optical access, yet with a reduced volume of 0.625 litre (smaller by 32 times) is adopted in this study.

Essentially the present experimental combustion chamber is designed to represent many of the most realistic situations of the propagating turbulent premixed flames in a confined chamber, such as SI engines, accidental explosion situation, bluff body combustion...etc. Hence, understanding the turbulence generation, flame propagation speed, and the flame interactions will help to design a better combustion device. This allows analysis of the relationship between turbulence levels and flame surface density, and the associated influence/dependence of flame front structure on turbulent burning rates to be related to other real world applications, such as prevention of loss and damage in case of accidental explosions in industrial areas. One important factor influencing the design of any experimental chamber is applicability for model validations and numerical simulations. This requires well defined initial and boundary conditions and also the physical size must be affordable for numerical simulations in order to resolve the length scales (Masri et al. (2006)). Additionally, good optical access is required to allow the imaging experiments to be easily performed. Considering the factors stated above, the experimental chamber designed in this investigation has a simple rectangular chamber with the ability to hold a maximum of three baffle plates and a solid obstacle in the path of propagating flame.

6.2 Experimental Setup

As described in the previous section, the experimental setup adopted in this investigation is originally developed by Kent et al. (2005) at The University of Sydney. This vessel is the latest and fourth iteration of the combustion chambers used in similar experimental investigations. The main modification in the new version is the viewing window, which is rectangular (Figure 6.1). This gives the advantage for extending the optical access area to all the baffles and obstacle positions, thus making it possible for the laser sheet to cover the main area of interest. By doing so, OH-LIF imaging can include the propagation of the flame over all of the obstructions

Figures 6.2 and 6.3 illustrate the schematic representation of the vessel used in this study. The combustion chamber is constructed from a Perspex square prism, with internal dimensions of 50 x 50 mm, and an overall length of 250 mm giving an experimental volume of 0.625L. The external prism is constructed from 20 mm thick Perspex walls, is used to enclose the thinner 5 mm Perspex combustion chamber. External prism holds the inner chamber rigidly and adds additional strength to withstand the shock waves encountered during the explosion. The external and internal prisms are placed in between a Perspex base plate and an open vented aluminium top plate and the entire rig is then held firmly together using draw bolts.



Figure 6.1: Old (left) and new (right) combustion chamber showing the quartz viewing windows.

Horizontal grooves (stations) are cut into the sidewalls at locations of 20 mm (S1), 50 mm (S2) and 80 mm (S3) downstream of the ignition point in which turbulence inducing baffle plates can be placed. For this investigation, baffle plates are situated at various combinations of these locations in order to change the turbulence generating characteristics of the flame and the flow properties. The baffles are constructed from 3 mm thick aluminium sheet placed perpendicular to the propagating flame front, and consist of five, 4 mm wide strips evenly separated by six 5 mm wide spaces, rendering a blockage ratio of 40% as shown in Figure 6.2. A solid square obstacle of 12 mm in cross section with a blockage ratio of 24% is centrally located at 96 mm from the ignition point running throughout the chamber, causing significant disruption to the flow. The influence of the individual obstacle in generating turbulence and flame propagation is detailed in the following section. This chamber has reconfigurable capability, which facilitates to generate different configurations and several analysis were done by Kent et al. (2005), Hall (2006 & 2008), Masri et al. (2011), and AlHarbi (2013) based on the number and position of baffle plates as shown in Figure 6.4. However, for the purpose of comparison between the three fuels, AlHarbi (2013) used only 4 configurations, mainly 000S, B00S, BB0S and BBBS.

All experiments conducted by AlHarbi (2013) used hydrogen, liquefied petroleum gas (LPG: 95 % C_3H_8 , 4 % C_4H_{10} , and 1 % C_5+ hydrocarbons by volume), and compressed natural gas (CNG: 88.8% CH_4 , 7.8 % C_2H_4 , 1.9 % CO_2 , and 1.2 % N_2 with the remaining 0.3 % being a mixture of propane, propene, butane, and pentane) which enters through a non-return valve in the base plate at a flow rate of 26.21 litre/min. This provided seven times the volume of the chamber to purge any gases left over from the previous cycle. The flow was then stopped and the gases within the chamber were allowed to settle to ensure the mixture homogeneity before the stagnant mixture is ignited. A hinged flap closes the top of the vessel during filling. This flap was opened just before ignition to allow the exhaust gases to escape, and remains open until the completion of the combustion process. The entire experimental sequence from initial filling of the vessel to opening of the flap, ignition of the mixture and operation of the LIF components was automated using a computer.

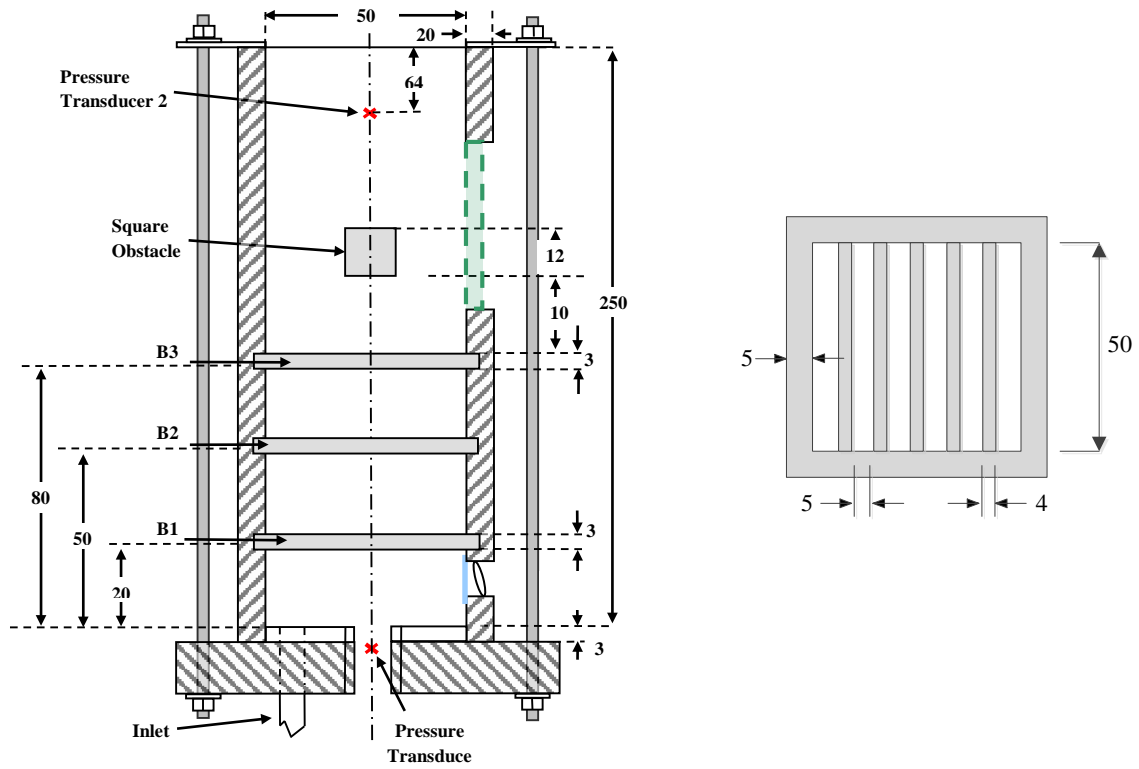


Figure 6.2 The combustion chamber (left) and the removable baffles (right). B1, B2, and B3 are the baffles. Dimensions in mm.

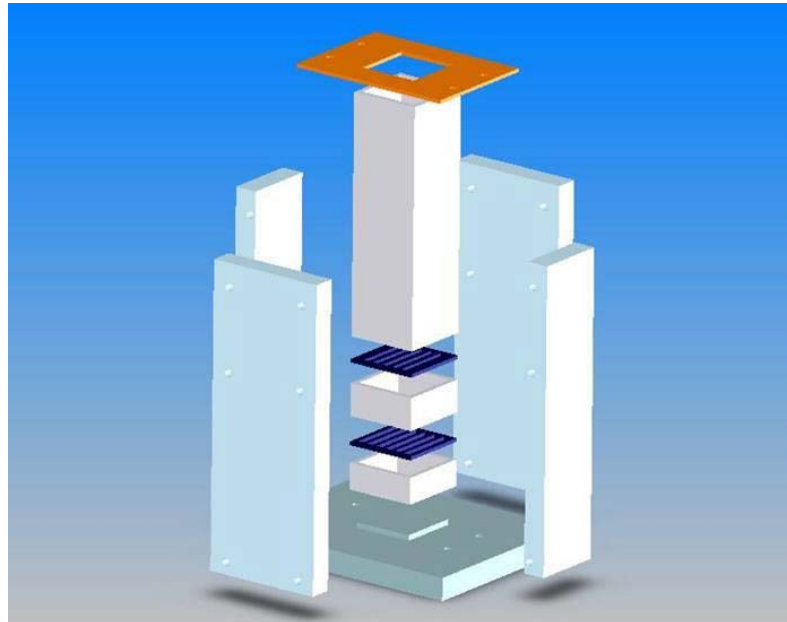


Figure 6.3 Internal and external structure for the combustion chamber.

6.2.1 Baffles and Solid Obstacle Arrangement

The presence of baffle plates and obstacles into the flow inside the combustion chamber serve to increase the turbulence level and flame propagation speed. The position and number of the baffle plates employed with respect to the square obstacle significantly alters the generated peak pressure, flame speed and structure (Kent et al. (2005), Masri et al. (2006), Masri et al. (2011) and AlHarbi (2013)). From these experimental investigations, it is found that the addition of baffle plates increases the overpressure, speeds up the flame and causes significant level of stretching in the flame front as it jets through the baffles. Higher turbulence levels increase the burning rates and hence the overpressures at an even faster rate than the flame speed. Hence, large increase in overpressure can be achieved through only a small increase in flame speed. The influence of individual baffle plates and square obstacle on the flow will be discussed in the next part. However, to simplify identification for the different configurations, baffles will be given (B), the square obstacle (S) and for no baffle in place (0).

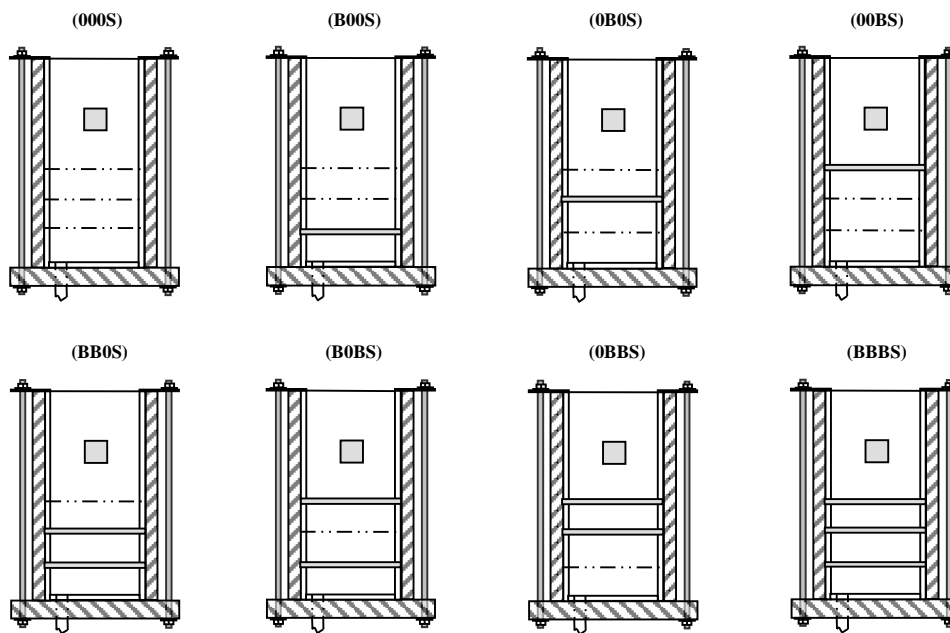


Figure 6.4 Combustion chamber configurations used by AlHarbi (2013).

Baffle Plate One (B1): This plate is located at 20 mm from the base (Figure 6.2). Due to the closeness to the ignition point the flame speed is still relatively low, thus this

obstacle only has a small effect on turbulence generation. Thus, re-laminarisation of the flame front shortly after this obstruction can be observed. The main purpose of this baffle plate is to increase the initial propagation speed of the flame front, hence leading to a faster time to peak pressure.

Baffle Plate Two (B2): This plate is located at 50 mm from the base (Figure 6.2). This serves both to increase the pressure and increase the propagation speed of the flame. In particular it affects the positioning of the flame front at peak overpressure.

Baffle Plate Three (B3): This plate is located at 80 mm from the base (Figure 6.2). It has the most influence on increasing the amount of turbulence generated within the combustion chamber. Flame accelerates at its greatest after hitting this baffle, thus increasing the amount of turbulence and flame propagation speed.

Square Obstacle: The solid square obstacle is located at 96 mm downstream from the ignition close end (Figure 6.2). This is not a turbulence-inducing device but work to increase the blockage ratio and hence alter the development of the flame front. Rapid propagation for the flame is recorded past this obstruction followed by the wrapping of the flame in the recirculation region, which enhances the mixing and distortion at the flame front.

6.2.2 Ignition System

The air/fuel mixture within the combustion chamber was ignited using a Neodymium-doped Yttrium Aluminium Garnet (Nd:YAG) laser. This is done by focusing laser pulse in order to ionize atoms in the chamber to create a spark. The use of a laser has several advantages over a normal spark plug, including that it is non-intrusive and has a higher timing accuracy. A focused laser beam with a wavelength of 1064 nm provided the spark and, for alignment purposes, a green laser beam with a wavelength of 532 nm was generated by KDP crystal, as the infrared spectrum is not visible to the naked eye. The laser has output energy of 500-600 mJ at 1064 nm (AlHarbi (2013)). A height-adjustable platform was used to move the chamber up or down and enabled images to be easily taken at different heights within the chamber. Also, the chamber could move in three directions through rails mounted on the platform (Figure 6.5). The LIF

equipment is fixed to the optical table in front of the combustion chamber. When the YAG laser sent the ignition laser beam, the beam is reflected by a fixed prism to a mirror implanted in the movable system with a focal length of 25 mm. The ignition laser is directed to the chamber and focused at a height of 2 mm above the base of the chamber. An external control unit is used to adjust the intensity and the frequency of the laser pulse. In addition, laser timing is controlled by the Q-switch of the Nd:YAG and this marks the start of the experiment, or time zero.

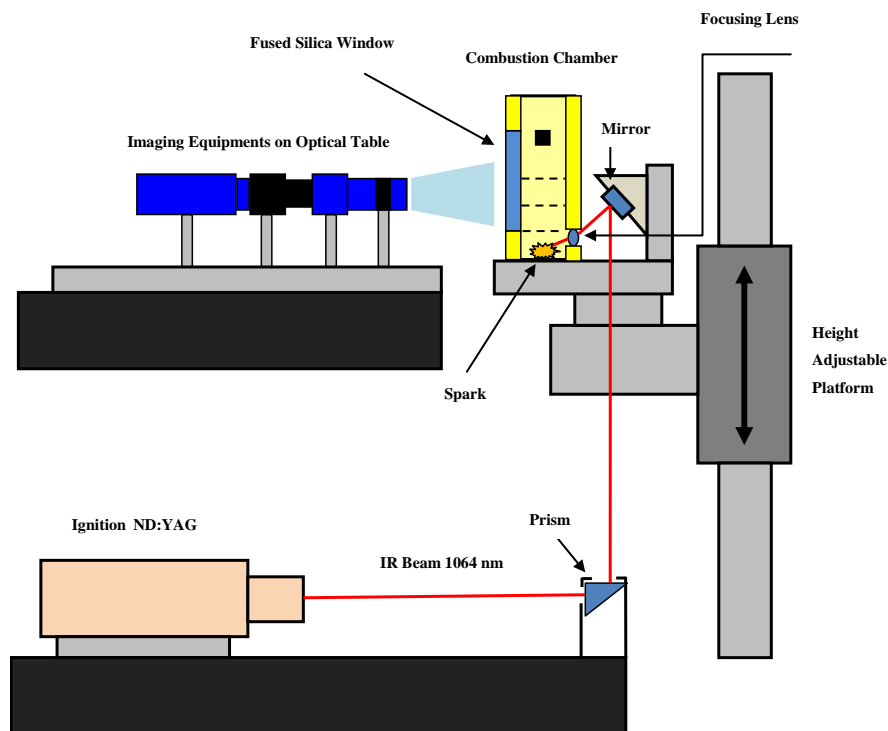


Figure 6.5 Arrangement of the Laser assisted ignition system (AlHarbi (2013)).

6.2.3 Pressure Transducers

The pressure is recorded at 25 kHz measured using piezo-electric pressure transducers with a range of 0-1 bar and a total error $< 0.5\%$. These devices utilize quartz crystals that develop a charge relative to the pressure applied. The piezo-electric sensor is particularly sensitive to rapid changes in pressure and hence makes it an ideal choice for this experiment. Two pressure transducers are employed to measure the pressure, one is

positioned at the ignition end of the vessel and other one is positioned after the square obstruction from ignition point. The pressure signals measured from both the transducers confirms to follow the same trend with slight variations. However, overpressure results from the base transducer are used in this work to validate LES simulations.

6.2.4 High Speed Imaging System

A High speed camera (LaVision - HSS6) with a lens-coupled two-stage intensifier is used to obtain images of the propagating flame. The camera was run at a repetition rate of 5 kHz with an array of 1024 x 1024 pixels. Due to the quick nature of the explosion, the camera was operated at 5000 fps, i.e. 0.2 ms between each captured image. The repetition rate was high enough to capture flame front propagation from shot-to-shot.

6.2.4.1 Imaging Tiers

The imaged area measured 50 mm × 75 mm, which covered the height of the laser sheet but not the whole chamber. The possible height of examination with the experimental setup was about 77 mm (AlHarbi (2013)). To overcome this problem, it was necessary to select two slightly overlapping imaging windows. For each case, the imaging process was repeated two times to cover each of the imaging windows, T1 and T2. As there was some difficulty during the experiment. Figure 6.6 shows the two imaging tiers used to capture the maximum viewable height.

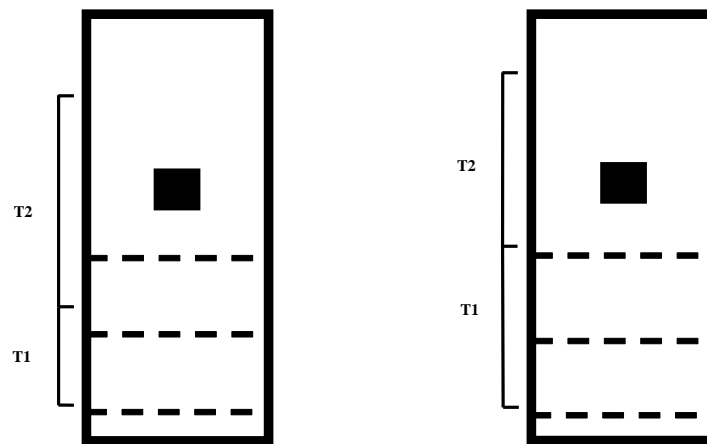


Figure 6.6: The two imaging tiers used to capture the maximum viewable height. Left used for configuration BBBS and right for the rest of configurations.

6.2.5 Laser Induced Fluorescence of Hydroxyl Radical (LIF-OH)

Laser Induced Fluorescence from the hydroxyl radical, OH (LIF-OH) is performed using a typical arrangement with a Pulsed YAG laser (Spectra-Physics DCR-2A) used to pump a Pulsed Dye Laser (Spectra-Physics PDL-2). The beam is then passed through cylindrical optics to form a thin sheet of approximately 200 μm thick which illuminates the viewing region. The laser is positioned 110 mm downstream pointing through a 1-inch diameter quartz-viewing window with the camera placed at a right angle with the lens pointing through a second quartz-viewing window.

The LIF-OH is being collected on the camera. The timing is such that the LIF measurement is made just when the flame front is crossing defined imaging tiers (Figure 6.6). Since the OH is formed in the reaction zone of the flame and is rapidly quenched by cold un-reacted gases, it is a good indicator of the flame front position in flames where the reaction zone is thin. It should be noticed here that the flame front is measured from the flame leading edge position in the LIF images to the base of the chamber.

6.3 Experimental Procedure

The entire experimental sequence is controlled by a computer, operating all equipment and solenoid valves in a predetermined sequence. The fuel/air mixture is directed to the combustion chamber either directly or bypassing via the seeding vessel and finally straight out to the exhaust. Whereas the required equivalence ratio is obtained by fuel/air controller through percentage scale. The technical issue involved in directing the fuel/air mixture through the various way points as the experiment progresses, arises due to the seeding of the fuel before it enters the chamber. This may corrupt the outcome of the experiment. Though, to avoid the risk of corruption of the results, two sets of two-way valve are used in series as shown in Figure 6.7, which are also operated by the computer. The ignition laser is controlled by a computer to enable a base timeframe for the collection of the data. However, the experimental test rig with all the attached parts can be seen in Figure 6.8.

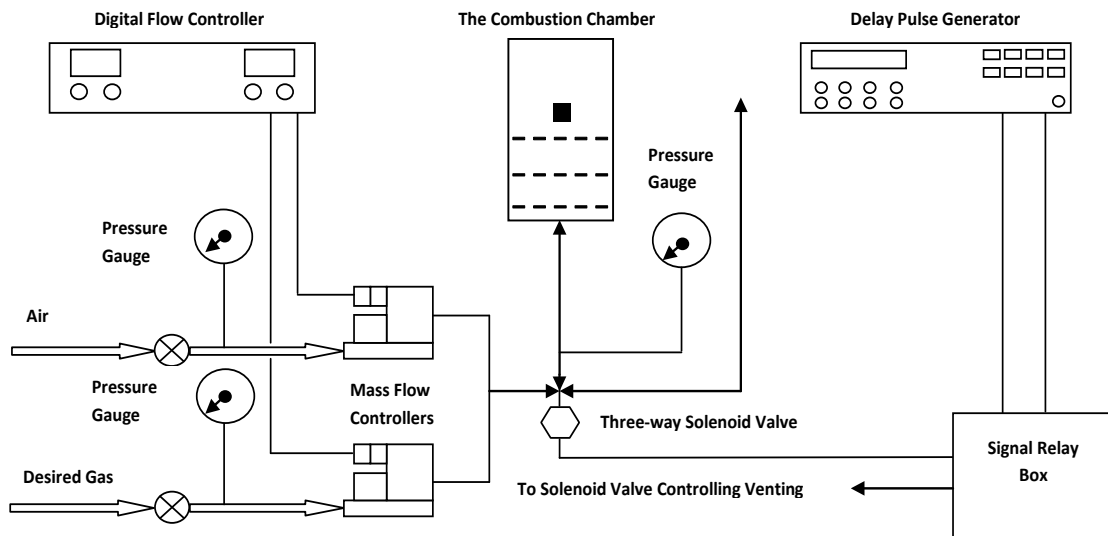


Figure 6.7 Fuel/Air direction system.



Figure 6.8 The experimental rig of the turbulent premixed combustion chamber.

6.3.1 The Experimental Sequence

As a typical experimental procedure is involved in co-ordinating several systems, such as fuel-air mixture filling into the chamber, high speed imaging system, pressure transducers and laser system for ignition, hence the entire sequence is controlled and the data is collected by a computer.

Step 1 - Fill time: With the flap closed, the fuel-air mixture is injected into the chamber. A digital flow controller controls the quantity of the fuel/air mixture entering the combustion chamber.

Step 2 - Settling time: All the mixtures required to settle for 15 (CNG), 10 (LPG), or 5 (H_2) seconds in the chamber, to keep the mixture inside the chamber homogenous and also when ignition occurs, the mixture is assumed to be quiescent. The flap remains closed.

Step 3 - Ignition: The flap is now open and the laser is triggered for ignition. This sets time zero. The laser imaging system is now triggered to start collecting image

6.4 Summary

This chapter summarizes influencing factors in designing an experimental combustion chamber and the challenges faced in the past due to large scales experimental test rigs. A novel chamber that has recently been developed by The University of Sydney Combustion group that can retain the combustion physics with good optical access has been discussed. Details of the individual obstacles used and their influence in generating turbulence and overpressure of the propagating premixed flame were discussed. Brief details of various measurement devices such as LIF-OH and techniques such as ignition control, image capturing were presented and discussed. Finally, the experimental sequence has been presented.

Chapter 7

Quantifications of Experimental Data

In this chapter the main objective is to obtain a set of data from AlHarbi (2013) experiments in-order to validate the model results as will be discussed in the next chapter. The analysis includes the overpressure, flame position, speed and flame stretch. This will be investigated for three different fuels; CNG, LPG and hydrogen with equivalence ratio 0.8 for configurations BBBS and 000S. The reason for choosing these two cases specifically, because they are considered as the high and low turbulence cases. For the flame stretch, the methodology and how the stretch is extracted are explained in this chapter.

7.1 The Overpressure Time Traces

The experimental pressure measurements of AlHarbi (2013) were done for different configurations, fuels and equivalence ratio. However, depending on the case, several readings were provided. On the other hand, for each of these cases, only one curve is required in-order to compare the numerical results with the experimental one.

For the purpose of comparison, the equivalence ratio of 0.8 will be considered for the three different fuels CNG, LPG and hydrogen. As mentioned previously, for each of the fuels, several tests were done to ensure that the repeatability of the measurements is quite good. Table 7.1 presents the number of experiments done for each fuel and with different chamber configurations. While Table 7.2 shows the averaged peak overpressure for the three fuels and the corresponding time. Where, it is clear that hydrogen has the highest value followed by LPG and CNG respectively.

However, as time shift is observed from the raw data of AlHarbi (2013), the peaks have to be aligned in-order for a proper average to be done. So, one curve could be used for comparison later on. So, a post-processing program (see Appendix A) is developed to fix the shift in all the curves and then calculate average value for all the curves. The basic idea is to find the average value for the pressure and time, then adjust all the curves according to these values. This procedure is done for all the configurations under

study as shown in Figures 7.1 – 7.6. The smoother curves for hydrogen over CNG and LPG are due to the less number of recorded data points captured by the pressure transducer due to the high reactivity, hence a faster combustion for hydrogen.

Moreover, the baffle locations are plotted on these figures, to investigate their effect on the generated overpressure. From these results, the following points are observed. First, the repeatability of the measurements is quite good showing that the peak is similar for all traces and confirming that the all conditions are well optimized. Second, the pressure oscillations after the first peak are consistent. These oscillations are thought to be for the reflected pressure waves since they occur even for 000S. Also, the subsequent burning of the gases trapped upstream and downstream the solid obstacles may contribute to such pressure fluctuations. Finally, the maximum pressure for the three fuels and configurations is noticed after the square obstacle. This is due to the trapped fuel behind this obstacle which tends to raise the pressure massively.

Table 7.1 Number of experimental overpressure tests for each fuel/configuration.

Fuel	CNG	LPG	Hydrogen
Configuration	No. of Readings for each Fuel/Configuration		
000S	20	20	20
BBBS	10	20	20

Table 7.2 Summary of mean values for the first peak pressure and time of incidence measured at the base of the chamber for configurations (000S and BBBS) and three fuels LPG, CNG and hydrogen with equivalence ratio $\Phi = 0.8$.

Fuel	CNG		LPG		Hydrogen	
Configuration	$P_{b,max}$ (mbar)	$T_{p,b}$ (ms)	$P_{b,max}$ (mbar)	$T_{p,b}$ (ms)	$P_{b,max}$ (mbar)	$T_{p,b}$ (ms)
000S	4.6	28.03	6.0	23.5	218.5	4.78
BBBS	26.4	21.99	26.9	19.74	997.1	3.33

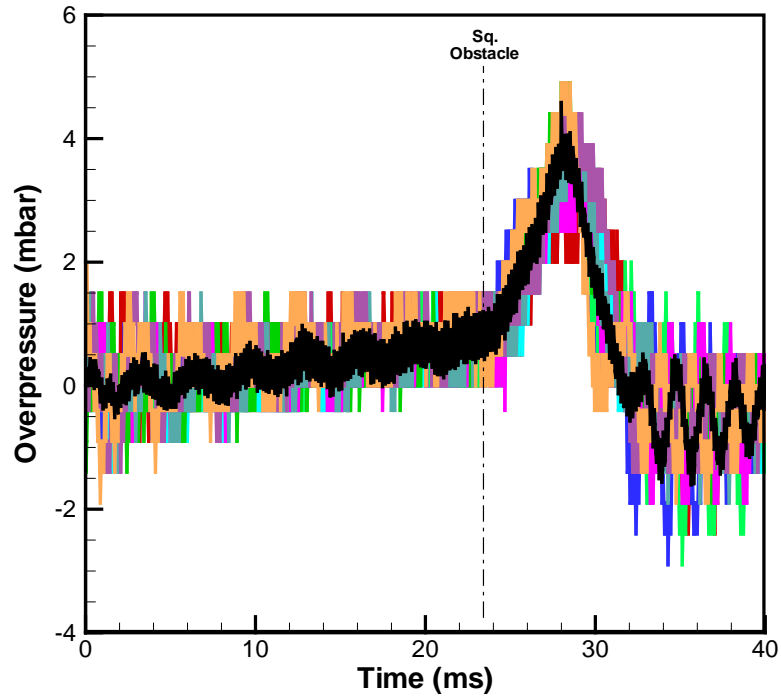


Figure 7.1 Averaged value (black colour) imposed over the raw data for overpressure-time history for CNG-air mixture ($\Phi = 0.8$) and 000S configuration after fixing the time shift.

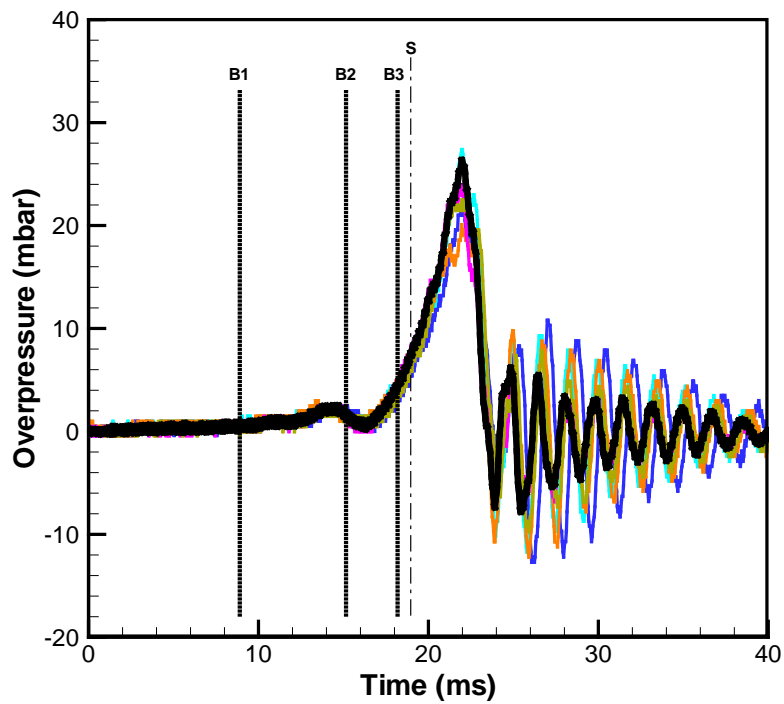


Figure 7.2 Averaged value (black colour) imposed over the raw data for overpressure-time history for CNG-air mixture ($\Phi = 0.8$) and BBBS configuration after fixing the time shift.

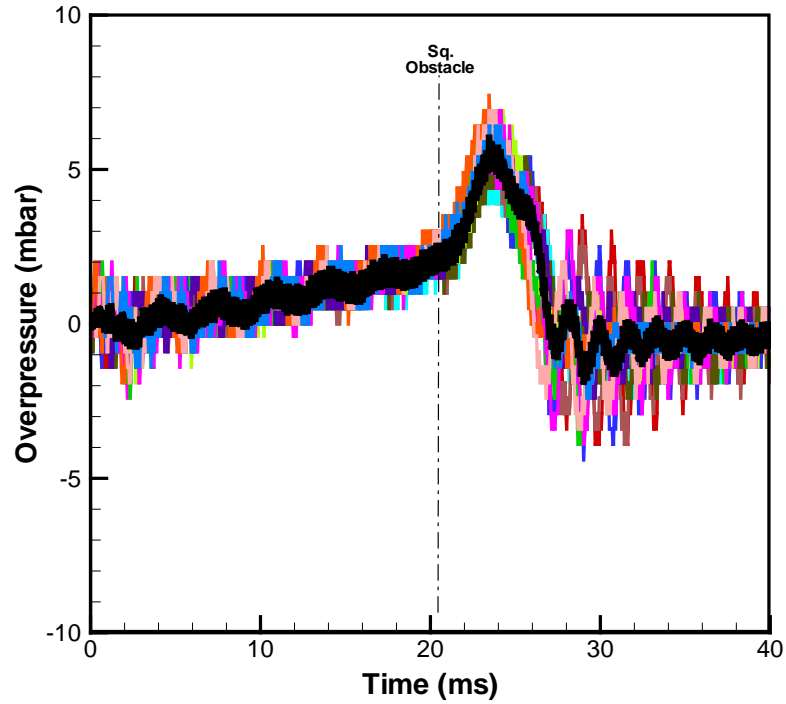


Figure 7.3 Averaged value (black colour) imposed over the raw data for overpressure-time history for LPG-air mixture ($\Phi = 0.8$) and 000S configuration after fixing the time shift.

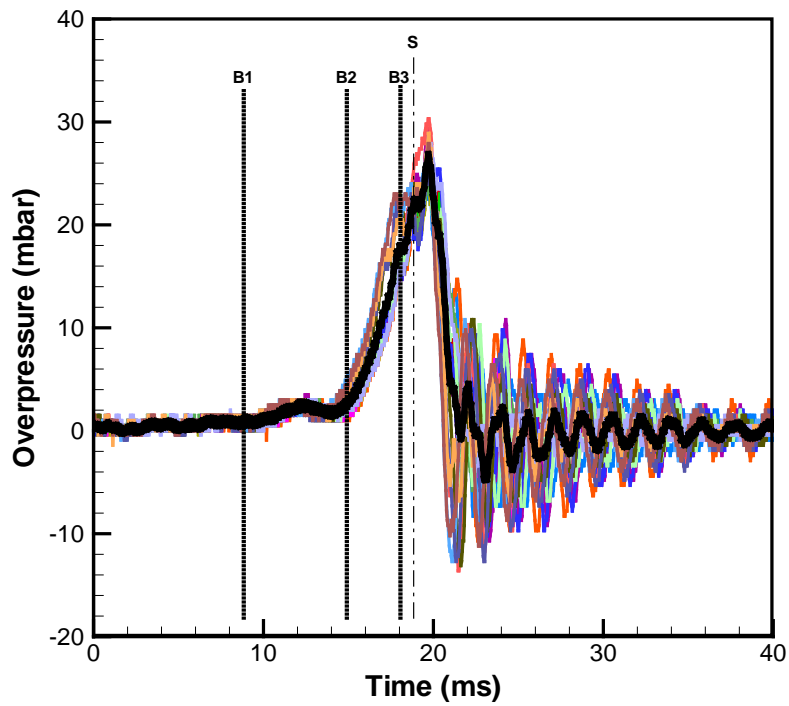


Figure 7.4 Averaged value (black colour) imposed over the raw data for overpressure-time history for LPG-air mixture ($\Phi = 0.8$) and BBBS configuration after fixing the time shift.

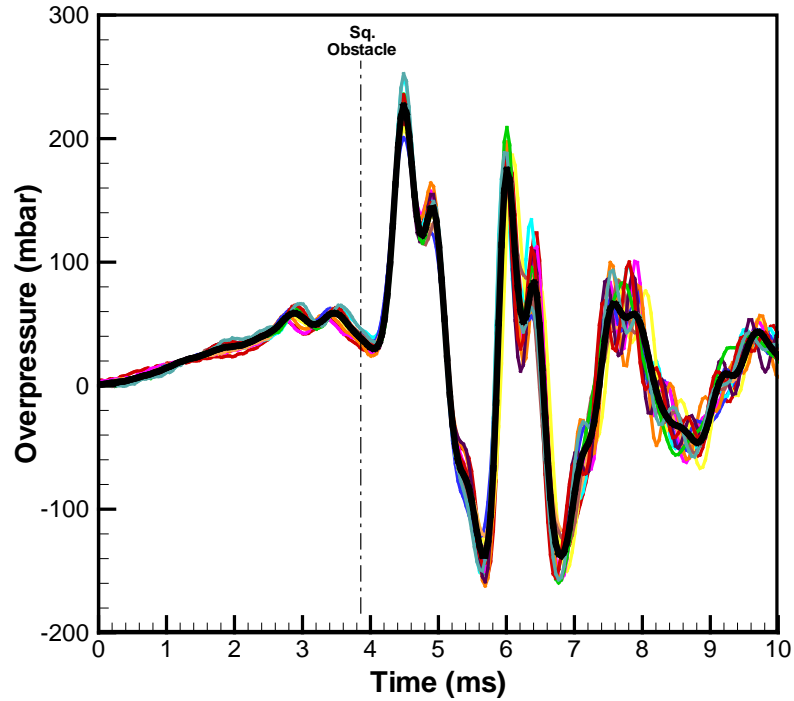


Figure 7.5 Averaged value (black colour) imposed over the raw data for overpressure-time history for hydrogen-air mixture ($\Phi = 0.8$) and 000S configuration after fixing the time shift.

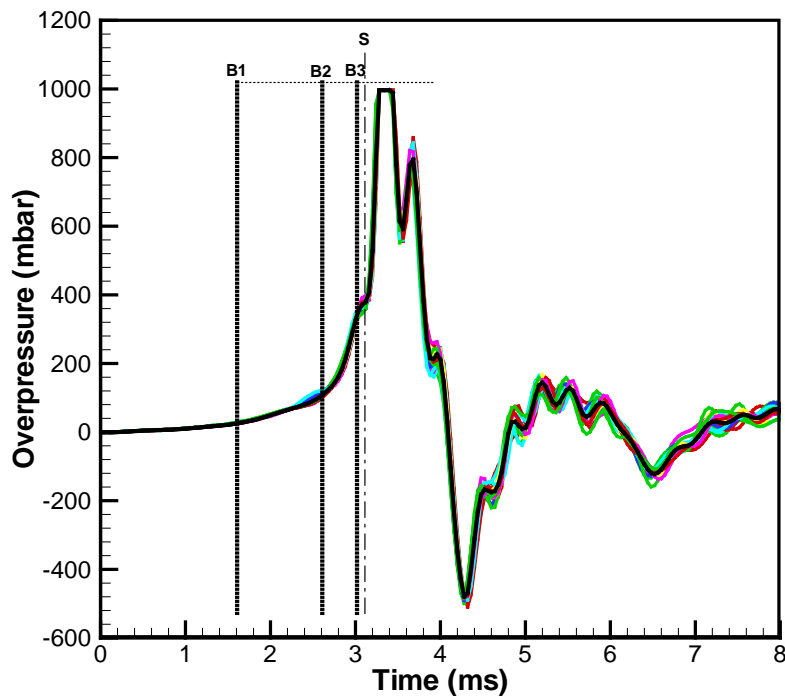


Figure 7.6 Averaged value (black colour) imposed over the raw data for overpressure-time history for hydrogen-air mixture ($\Phi = 0.8$) and BBBS configuration after fixing the time shift.

7.2 Flame Position and Speed

The flame speed was calculated by using the displacement of the leading edge flame position in the LIF images from the base of the chamber and a change in time of 0.2 ms (AlHarbi (2013)) and according to the tier system described in Chapter 6. Table 7.3 presents the available number of images for the three fuels and for both configurations. As can be seen the number of images for CNG and LPG are greater than that for hydrogen, as the former fuels are slower in propagation and the used camera could capture more images for them over hydrogen.

Table 7.3 Number of images for each fuel/configuration.

Fuel	CNG	LPG	Hydrogen
Configuration	No. of Images for each Fuel/Configuration		
000S	124	110	18
BBBS	69	61	9

Figures 7.7 and 7.8 show the flame position extracted from the images for configurations 000S and BBBS (see Appendix B). The curves are smooth for all three gases until there is a sudden change in direction as a result of hitting an obstacle/baffle at distances where the obstacle/baffle placed. Also, it is clear for both configurations that hydrogen flame propagates faster than CNG and LPG. However, for configuration 000S, LPG is faster than CNG. While for configuration BBBS almost both of them reach the square obstacle in the same time. Figures 7.9 and 7.10 show the flame speed for the three gases with the same mentioned fuel mixtures. Both figures confirm the previous note that hydrogen is faster in reacting with the obstacles more than CNG and LPG.

Figures 7.11 and 7.12 compare the flame speed against the flame position for both configurations. From Figure 7.11, the flame tends to slow down before hitting the square obstacle and this is because of the pressure accumulated/built-up ahead of the flame, just before the obstacle. However, the flame re-starts to speed-up again while passing the obstacle. This could be observed for the three fuels. This is also confirmed in Figure 7.10, for CNG and LPG but for hydrogen this is not observed. This could be

happened either because the flame becomes less sensitive to/overcome the pressure ahead, due to the very fast propagation or the amount of turbulence generated that tends to keep the increase at the flame speed. These conclusions confirm with the extracted scales in the next chapter.

Figures 7.13 and 7.14 compare the flame position and speed for both configurations and the three fuels. It is obvious that the introducing of baffles enhances the flame-flow interaction and hence faster flame is observed in configuration BBBS over configuration 000S. Also, for hydrogen in both configurations the flame position curve is almost overlapped for both configurations until reaching 60 mm and after that flame travels faster in case of BBBS. Again, this confirms the role of baffles to enhance the flame propagation. Finally, for the CNG and LPG flame speed plots show fluctuations, the hydrogen velocity plot appears more stable. This is due to the higher number of flame speed data points were collected for CNG and LPG than for hydrogen due to hydrogen's higher flame front speed which requires an advanced camera to capture.

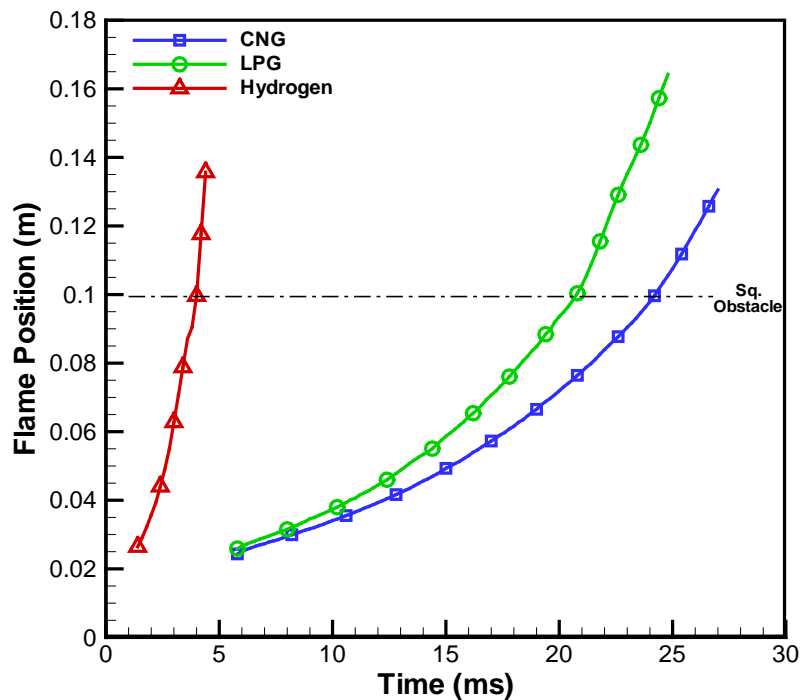


Figure 7.7 Flame position-time traces of experimental measurements using CNG, LPG and hydrogen air-mixture ($\Phi = 0.8$) for configuration 000S.

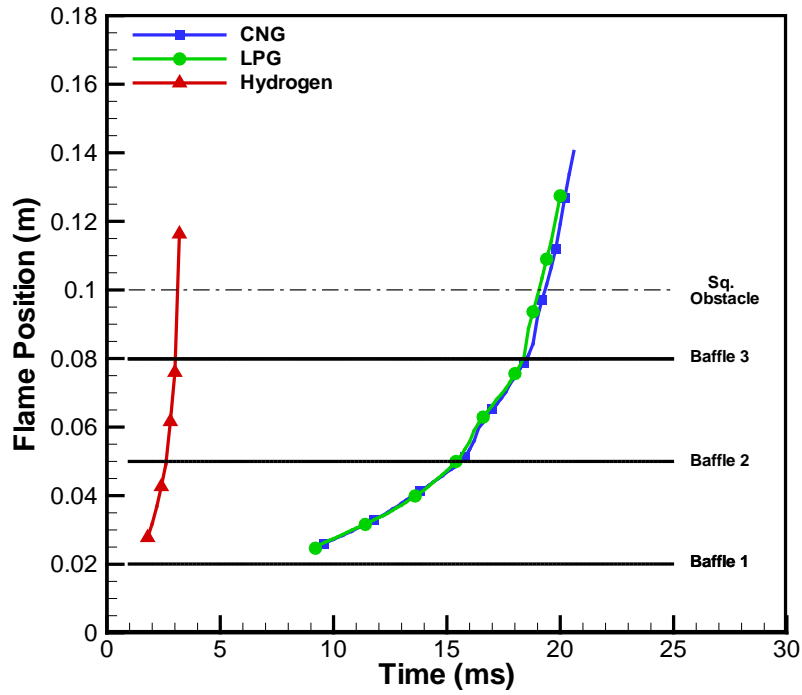


Figure 7.8 Flame position-time traces of experimental measurements using CNG, LPG and hydrogen air-mixture ($\Phi = 0.8$) for configuration BBBS.

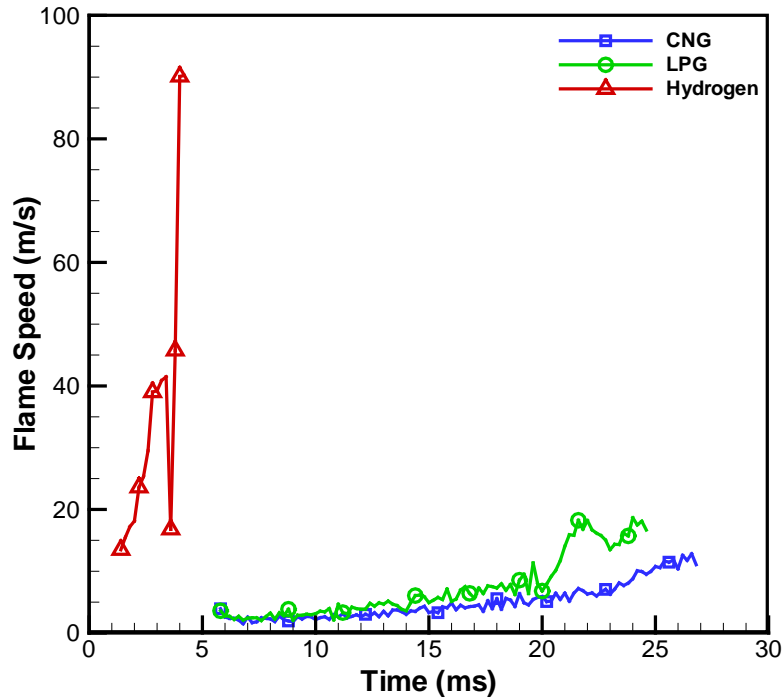


Figure 7.9 Flame speed-time traces of experimental measurements using CNG, LPG and hydrogen air-mixture ($\Phi = 0.8$) for configuration 000S.

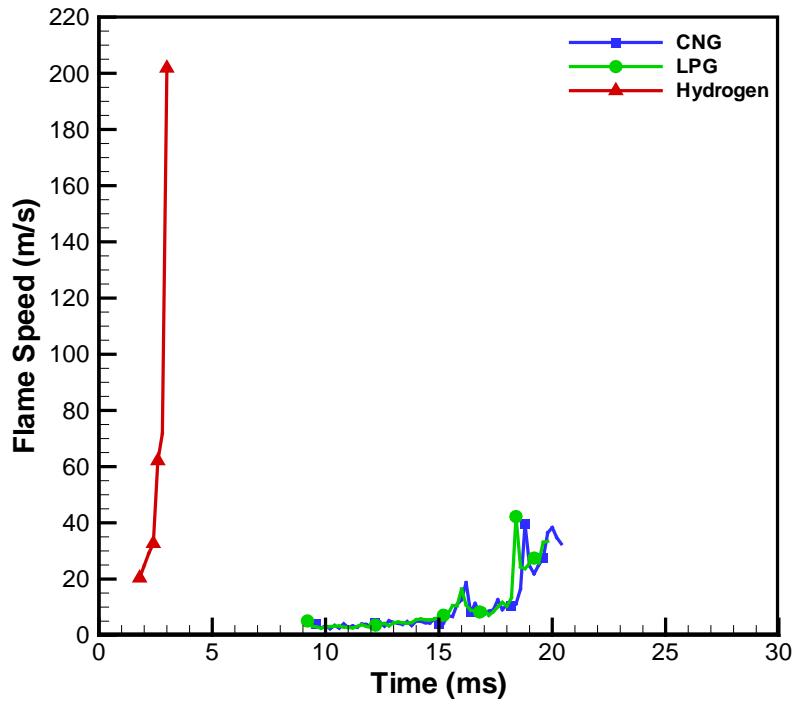


Figure 7.10 Flame speed-time traces of experimental measurements using CNG, LPG and hydrogen air-mixture ($\Phi = 0.8$) for configuration BBBS.

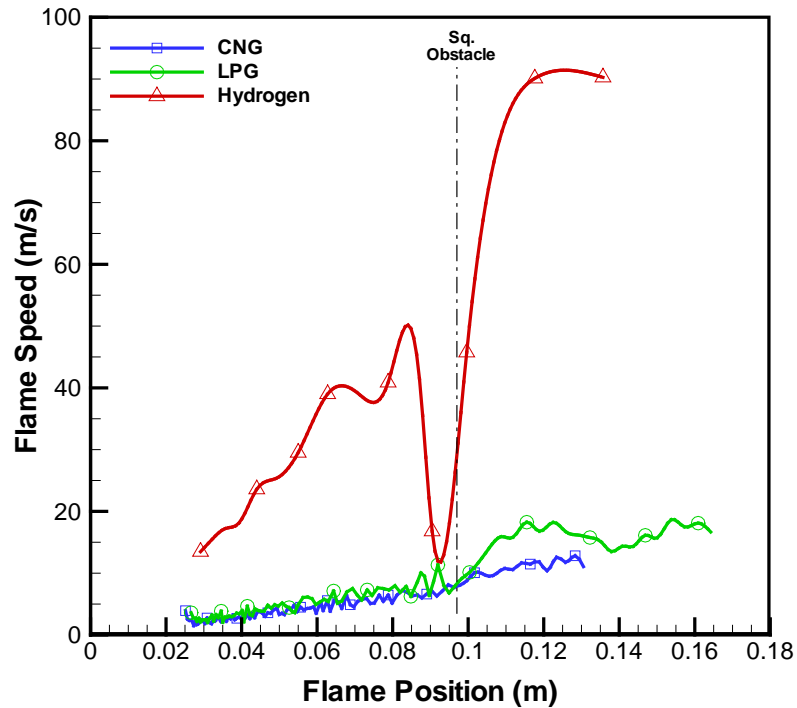


Figure 7.11 Flame Speed vs Flame Position for configuration 000S using the experimental measurements for CNG, LPG and hydrogen air-mixture ($\Phi = 0.8$).

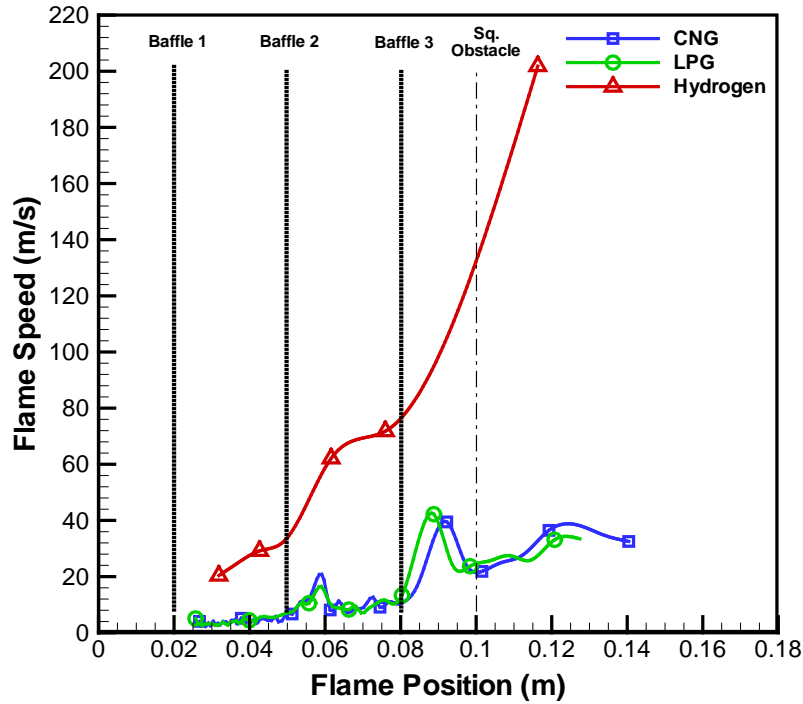


Figure 7.12 Flame Speed vs Flame Position for configuration BBBS using the experimental measurements for CNG, LPG and hydrogen air-mixture ($\Phi = 0.8$).

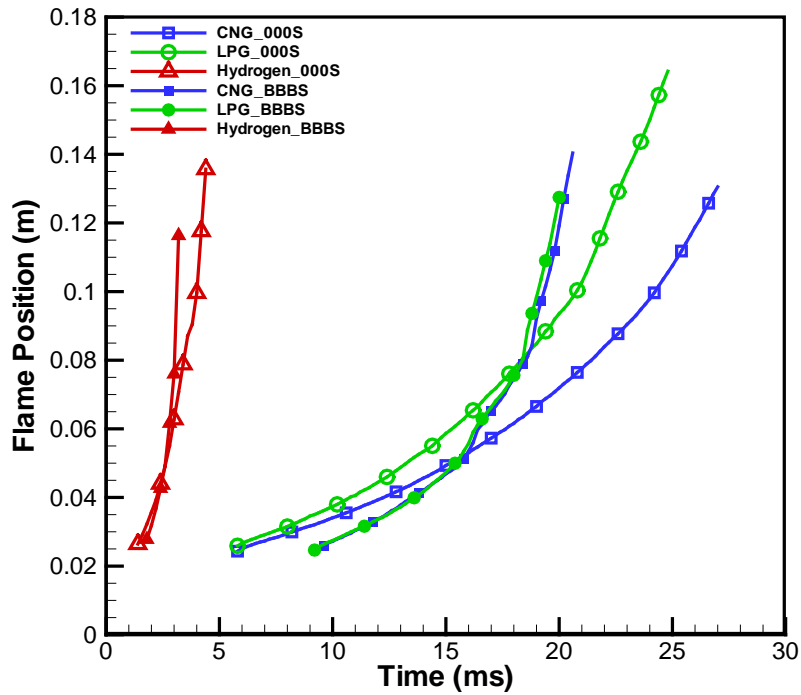


Figure 7.13 Flame position-time traces of experimental measurements using CNG, LPG and hydrogen air-mixture ($\Phi = 0.8$) for configurations 000S and BBBS.

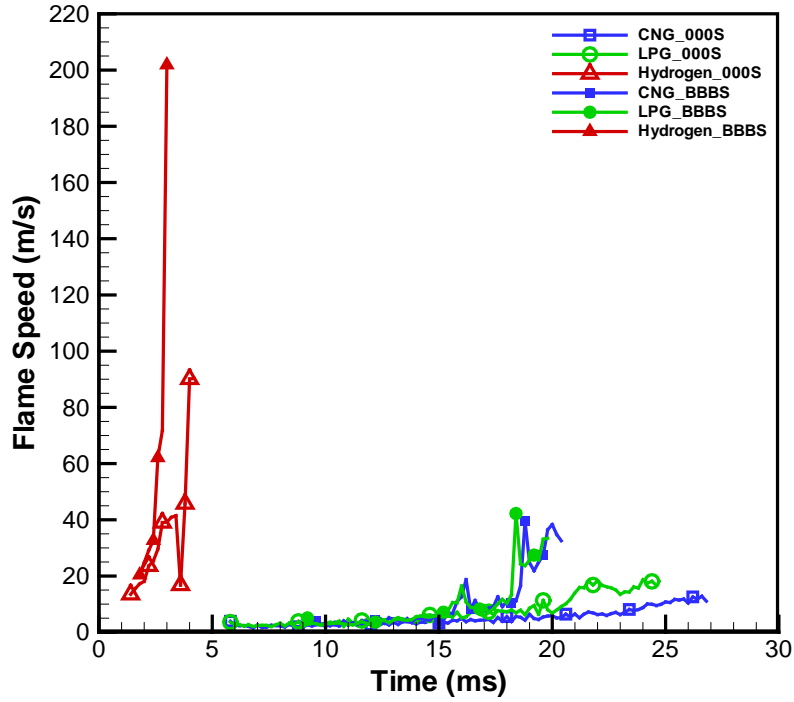


Figure 7.14 Flame speed-time traces of experimental measurements using CNG, LPG and hydrogen air-mixture ($\Phi = 0.8$) for configurations 000S and BBBS.

7.3 Flame Stretch

An important parameter in the study of premixed flames is the flame stretch. As, the stretch rate k is of great interest in understanding of flame/flow interactions. For a flame front propagating in a fresh gas mixture, it is subjected to strain and curvature effects which lead to changes in flame area (Williams (1985a)). These changes are measured by flame stretch. It is defined as the rate of change of a flame surface element as described by Matalon and Matkowsky (1982) and Candel and Poinot (1990) as:

$$k = \frac{1}{A} \frac{dA}{dt} \quad (7.1)$$

Candel and Poinot (1990) proposed for a thin flame sheet a general expression for stretch as:

$$k = -\vec{n}\vec{n} : \nabla\vec{w} + \nabla \cdot \vec{w} \quad (7.2)$$

Where \vec{n} is the unit vector normal to the flame surface pointing towards the fresh gases, \vec{w} is the flame front velocity and expressed in terms of the unburned gas velocity \vec{u} and the displacement speed u_d while $\vec{n} \cdot \nabla \vec{w}$ is the gradient operator normal to the flame surface. The flame front velocity \vec{w} could be written in terms of the unburned gas velocity \vec{u} and the displacement speed u_d (Poinsot and Veynante (2012)) as:

$$\vec{w} = \vec{u} + u_d \vec{n} \quad (7.3)$$

According to Poinsot and Veynante (2012) the difference between the flame front velocity \vec{w} and the flow velocity \vec{u} is the displacement speed $u_d \vec{n}$ which takes into consideration the effect of flow on the flame structure. However, substituting equation (7.3) in equation (7.2) leads to:

$$k = -\vec{n} \cdot \nabla \vec{u} + \nabla \cdot \vec{u} + u_d (\nabla \cdot \vec{n}) \quad (7.4)$$

where $\nabla \cdot \vec{n}$ is the curvature for the flame front and in spherical expanding flames, it is expressed as:

$$\nabla \cdot \vec{n} = \frac{-2}{R} \quad (7.5)$$

where R represents the curvature of the flame surface. The effect of $u_d (\nabla \cdot \vec{n})$ to the stretch in equation (7.4) is negative, i.e. the flame propagation works on decreasing stretch and the flame surface (Poinsot and Veynante (2012)).

However, following the analysis of Chung and Law (1984) for the flow strain, equation (9.2) could be arranged for spherical flames as:

$$k = \nabla_t \cdot \vec{u} - u_d \left(\frac{2}{R} \right) = \nabla_t \cdot \vec{u} + u_d \nabla_t \cdot \vec{n} \quad (7.6)$$

where $\nabla_t \cdot \vec{u}$ is the strain due to flow non-uniformity and $u_d \nabla_t \cdot \vec{n}$ represents the curvature of the flame front.

Generally, in turbulent flames zones of positive and negative stretch are available and the final length of a flame depends on the competition between these zones. Finally, for expanding flame, it is obviously growing since its size increases with time so that its stretch must be positive.

7.3.1 Methodology for Extracting Flame Stretch

Available methods for calculation of flame stretch rely on the flame surface area. In simplified configurations, such as spherically expanding flame, this is easily obtainable and traceable. However, when flame propagation through a set of obstacles is considered, the calculation of the flame surface area becomes very difficult. Instead, in the current work we consider the area of the flame symmetry cross-section plane. Figure 9.15 shows a typical experimentally obtained LIF-OH image. It is clear that the picture is slightly non-symmetrical, but this is attributed to the difference in luminance as the light source was directed from one side, and for the purpose of flame analysis we consider the brighter half of the image assuming that the other half is identical.

The procedure for extracting the stretch values from experimental images consisted from the following steps:

1. Calibrate the image dimensions based on the visible width of baffle (T1) or obstacle (T2)
2. Split the image in half (left part is always used for measurements)
3. For each time step follow the flame front to measure the area of the flame front cross-section
4. Calculate flame stretch using the equation 7.1

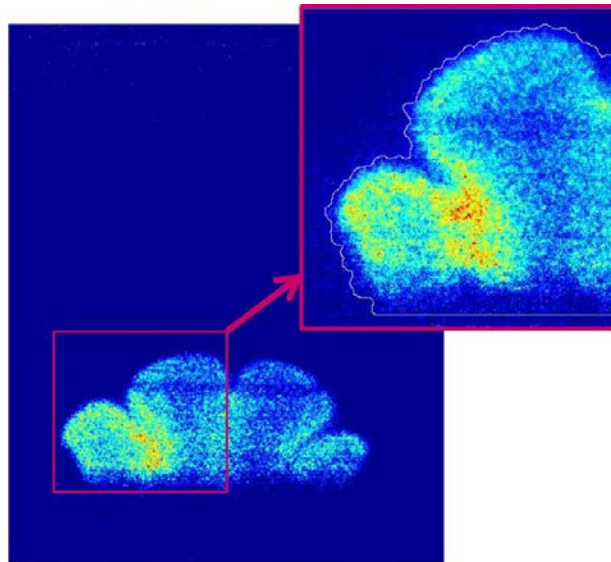


Figure 7.15 Image processing methodology for LIF-OH images

The experimental images are captured using the defined image tiers described in Chapter 6. The calculation of stretch for the flame moving into the tier two was based on the extrapolation of area increase in tier 1 plus the visible flame cross-section area in tier two.

However, from Figures 7.16-7.19, it is clear that hydrogen has the highest values of stretch compared with CNG and LPG with almost 3.5 times greater than the other fuels. This is associated with its explosion nature which enhances the flame flow interactions and hence increase the flame wrinkling. The oscillations occur for CNG and LPG but not in hydrogen due to the high number of images presented for the two fuels compared with hydrogen. Also, from Figure 7.19 a comparable behaviour could be observed between CNG and LPG, which emphasis on their close performance, similar as that for pressure, flame position and speed.

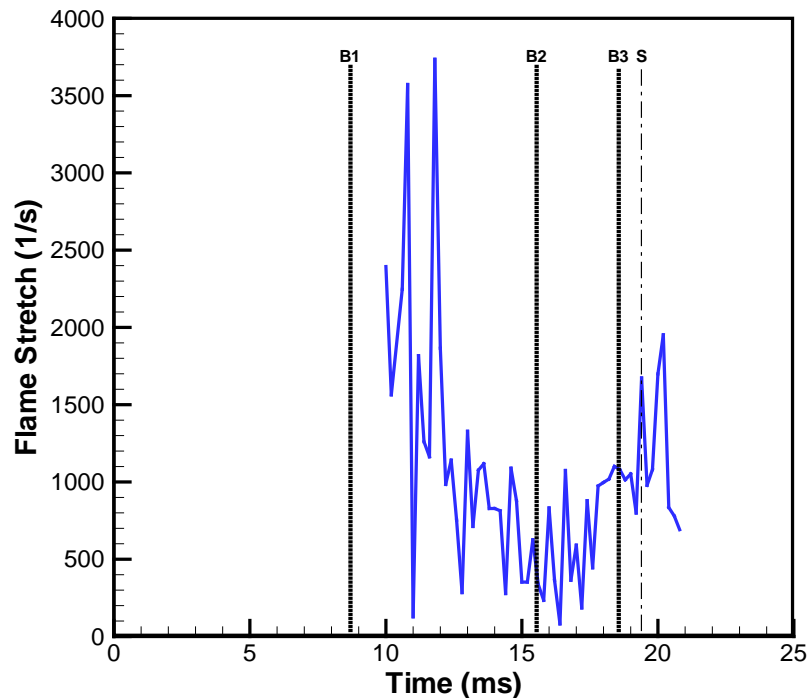


Figure 7.16 Extracted flame stretch from experimental images for CNG-air mixture with $\Phi = 0.8$

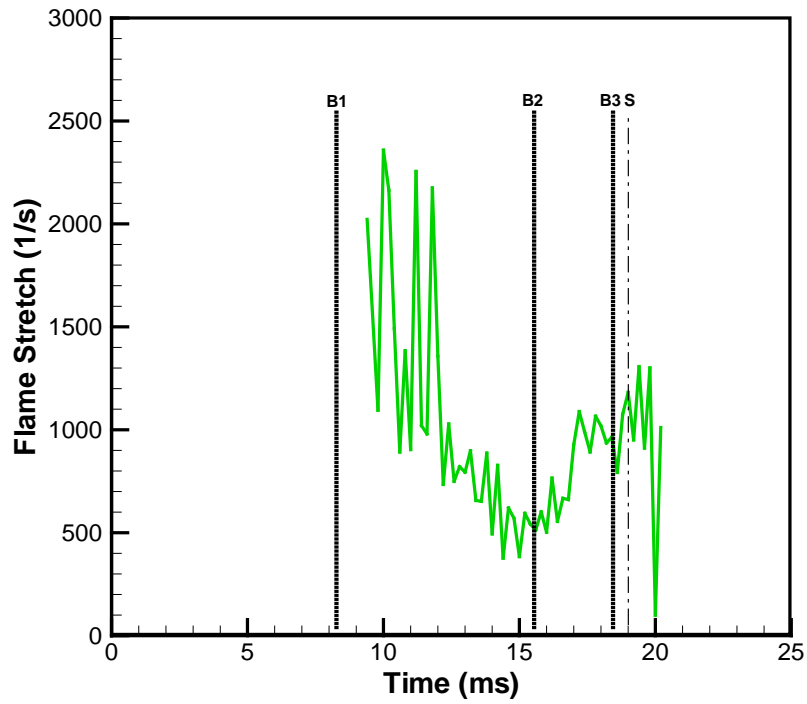


Figure 7.17 Extracted flame stretch from experimental images for LPG-air mixture with $\Phi = 0.8$.

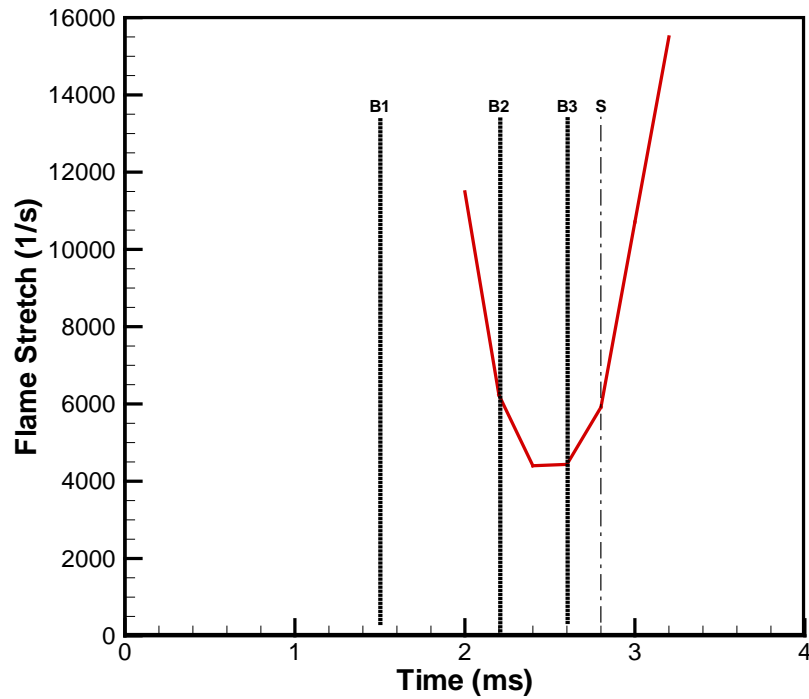


Figure 7.18 Extracted flame stretch from experimental images for hydrogen-air mixture with $\Phi = 0.8$.

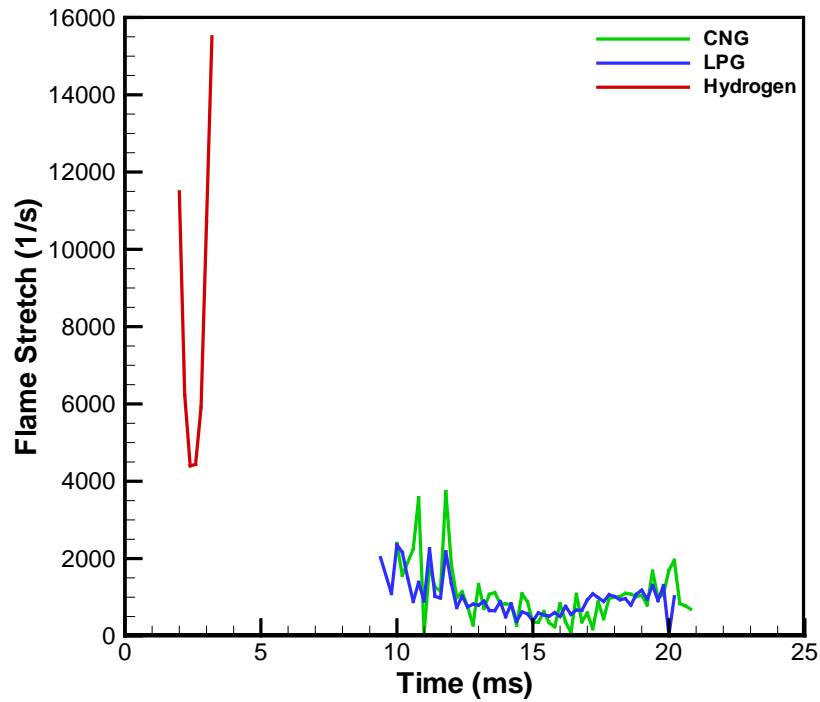


Figure 7.19 Comparison between the extracted flame stretch from experimental images for the three fuels, CNG, LPG and hydrogen-air mixture with $\Phi = 0.8$.

7.4 Sources of Errors

While repeatability of the measurements is critical in these experiments, there are many factors that could affect the results such as:

- The temperature of the ignition mixture
- The position of the laser ignition source
- Variability in the mixture composition
- Errors in the pressure transducer measurements
- Geometric factor associated with the chamber's baffles, obstacles and flap
- The power of the ignition laser is the main source affecting the repeatability of the experiments (AlHarbi (2013))
- The vibrations produced due to fuel explosions, which would affect both the chamber and surrounding equipment

On the other hand, regarding the extraction of the data from LIF-OH images, the sources of error could be a result of:

- The measuring program inaccuracy
- Human measuring error
- Visible variance seen in the LIF-OH images, which varied for the three different fuels, producing images of diverse contrast as shown in Figure 7.20. As shown, the LPG image is clearer than either of the other two fuels.

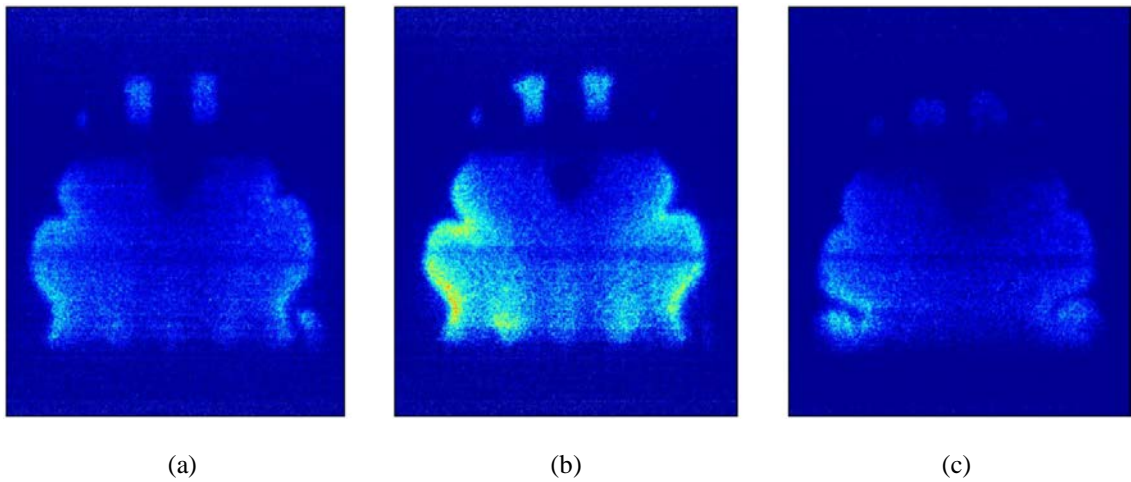


Figure 7.20 The varied contrasts of the images of each fuel. (a) CNG (b) LPG (c) Hydrogen.

7.6 Summary

This chapter explains the procedure in analysing the experimental data. LPG, CNG and hydrogen were used in preparing the discussion for this chapter. A comparison between the three fuels and were evaluated in terms of the overpressure, flame position and speed for low turbulence (000S) and high turbulence (BBBS) cases. Also, the LIF-OH images were presented in a way that facilitates the comparison between the three fuels. Moreover, the flame stretch and a proposed methodology to extract that from the images also discussed for high turbulence case (BBBS) and the three fuels. Finally, the main reasons of errors in the measured data were discussed.

Chapter 8

Results and Discussion

This chapter presents results from LES simulations of turbulent premixed combustion carried-out for three different fuels CNG, LPG and hydrogen air mixtures. As discussed in Chapter 6, model validation is made against experimental data of AlHarbi (2013), where, typical configurations are chosen to compare the numerical predications with the experimental data. In the first part, grid independency tests are carried out using the DFSD model for configuration BBBS. Moreover, other numerical aspects such as ignition radius, shape and location are studied and discussed. It should be noticed that, in sections 8.1 and 8.2, hydrogen-air mixture with equivalence ratio 0.7 is used for the setting-up of the model. However, in the following sections and for the purpose of comparison between the three fuels, equivalence ratio of 0.8 is used. In the section 8.3, the effect of fuel type is examined using configuration BBBS. Lewis number effect is discussed in section 8.4. More validation will be done in section 8.5 by extracting the flame stretch from the numerical results and compare that with experimental data. In section 8.6, the effect of various flow configurations on will be tested for the three fuels. Finally, various velocity and length scales are extracted from the LES simulations in order to identify the regimes of combustion in the current combustion chamber.

8.1 Grid Dependency Test

In numerical simulations, the grid independency is a much debatable and contentious topic as mentioned by Klein (2005), where it depends on many numerical and physical aspects, especially in LES. However, in numerical modelling, it is desirable to achieve substantial uniqueness of results, independent of the grid resolution employed. Hence, in the present investigation, LES simulations of turbulent propagating premixed flames have been carried out by refining the grid employed for configuration BBBS, as detailed in Table 8.1. Case A consists of 0.25 million, case B has 0.55 million, case C has 2.7 million, and case D has 3.6 million grid points in the computational domain shown in Figure 8.1. The pressure-time histories of the overpressure near the closed ignition end of the chamber are considered here as bench mark to assess the grid dependence of the

LES results (Gubba (2009)). Pressure-time histories for cases A, B, C and D are presented together with the experimental data of AlHarbi (2013) in Figure 8.1.

Table 8.1 Details of the numerical parameters

Parameters	A	B	C	D
Dimension	40 x 40 x 156	54 x 54 x 190	90 x 90x 336	90 x 90 x 448
Grid Size (millions)	0.25	0.55	2.70	3.62
Consumed Time (days)	1	2	10	25
Δx (mm)	2.0	1.47	0.75	0.75
Δy (mm)	2.0	1.47	0.75	0.75
Δz (mm)	1.0 – 2.0	1.0 – 1.75	0.75 - 1.0	0.48 – 0.75
$\bar{\Delta}$ (mm)	3.17 – 4.0	2.59 – 3.12	1.5 – 1.65	1.29 – 1.5
L_F (mm)	0.35	0.35	0.35	0.35
$h/\bar{\Delta}$	0.32 – 0.5	0.39 – 0.56	0.5 – 0.6	0.37 – 0.5
$\bar{\Delta}/L_F$	10.8 - 11.4	7.4 – 8.9	4.3 – 4.7	3.69 – 4.29

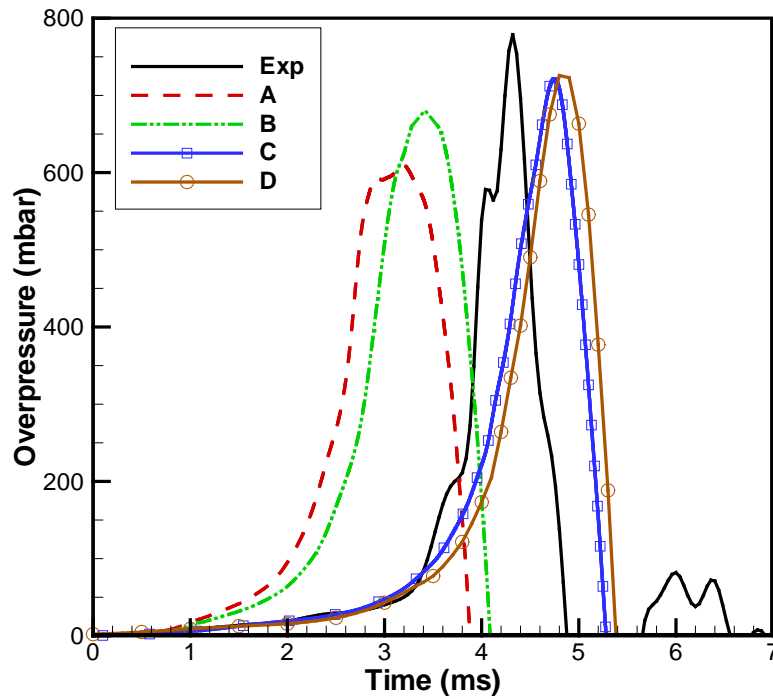


Figure 8.1 LES predictions of overpressure-time histories using different grid resolutions detailed in Table 8.1.

From Figure 8.1, it is obvious that grids A and B show an initial increase in overpressure at 1.2 ms and 1.5 ms after ignition, respectively, while this instant corresponds to 3.2 ms for grids C and D, which is in reasonable agreement with experimental measurements. This initial increase in overpressure in cases of grid C and D corresponds to the time where the flame is due to interact with the second baffle plate. Evidently, these calculations are confirming the peak overpressures of 721 and 725 mbar, occurring at 4.75 ms for grids C and 4.8 ms for D, respectively. Based on the peak overpressure, LES results can be considered grid independent, beyond the grid resolution C. However, LES calculations with grids C and D found to under-predict the experimental peak pressure of 778 mbar occurring at 4.35 ms after ignition.

8.2 Sensitivity to Ignition Source

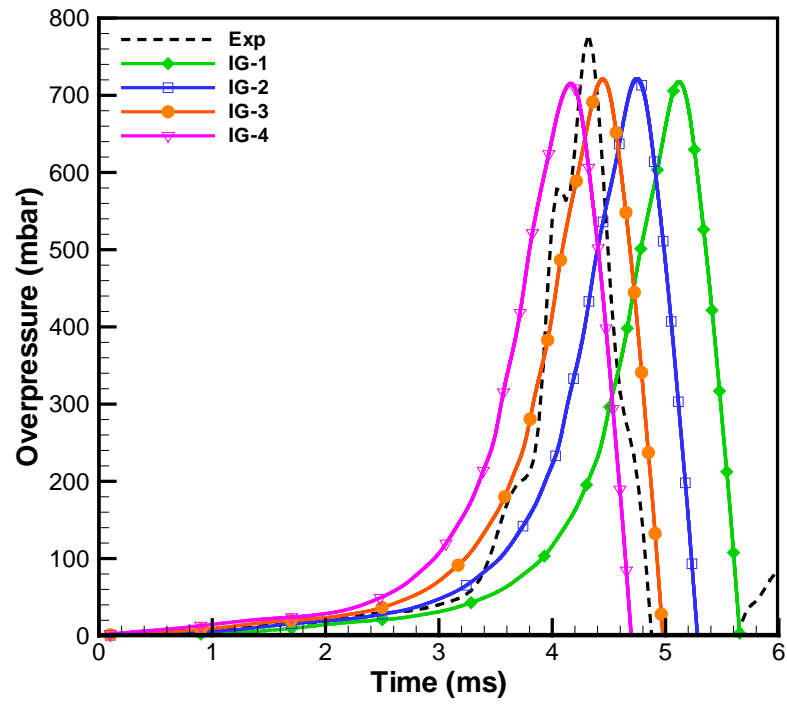
In setting up the boundary and initial conditions, it is important to make them approximate, as closely as possible to the experimental configurations and this, in some instances, may not be possible. The ignition source is one of the parameters that need to be reproduced numerically due to the fact that, experimentally, this performed with a focused laser beam. Moreover, sensitivity to the ignition energy and the location of the source has not been performed experimentally. Numerically, ignition is modelled by setting the reaction progress variable to 0.5 within a certain number of cells located near the center of the base plate. It is relatively straightforward to vary the shape, size and location of the ignition source and monitor their effects on the peak overpressure, the flame structure and its propagation rates. The results are presented here, albeit for a limited number of cases but extremely useful not only in optimizing ignition, but also in determining whether the ignition source is primary parameter in setting up the boundary conditions.

Calculations are repeated for configuration BBBS (3 baffles and square obstacle) but with a range of ignition sources (labeled IG-1 to IG-6) as shown in Table 8.2. The shape of the ignition kernel is varied from hemispherical to spherical, and its location is shifted from being flush with the base plate to 5 mm downstream (Cases IG-5, IG-6). Also, the ignition energy is varied by increasing the size from a radius of 2 mm to 5mm (Cases IG-1 to IG-4) respectively. Figure 8.3 shows the overpressure and flame position calculated for case BBBS. It is evident from these plots that the predicted peak

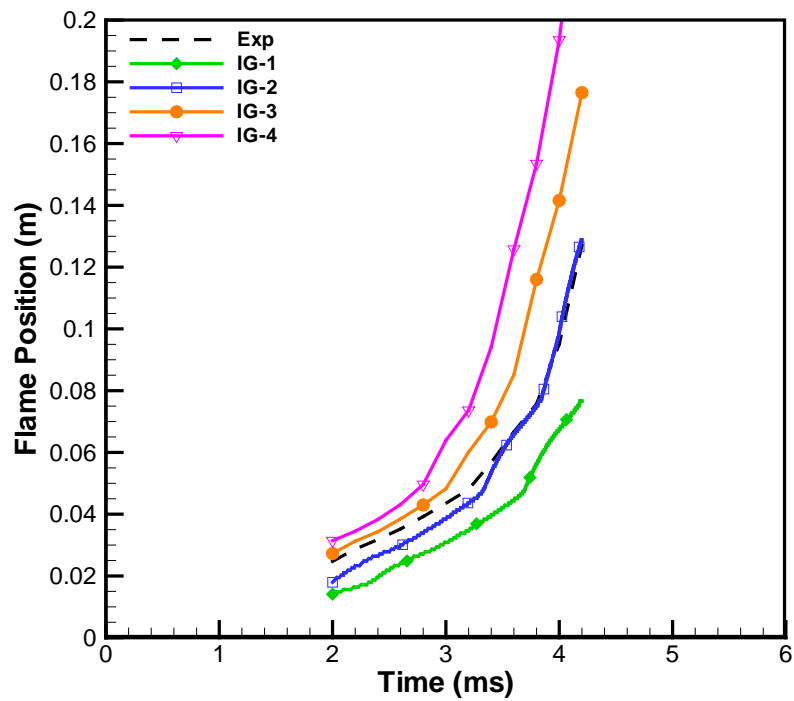
overpressure is independent of the ignition radius. It can be seen from Figure 8.2 that the only effect found is in the timing of the occurrence of the maximum pressure. Also, from Figure 8.2 the ignition radius which is found to be most appropriate to represent the early phase of flame propagation is 3 mm. on the other hand, from Figure 8.3, for the same ignition area (IG-2 and IG-5), the shape either hemispherical or spherical has almost no effect on either the overpressure or the timing of occurrence as long as the center is very close to base. However, as the location of the ignition source is set far from the base as in case (IG-6), a decrease on the peak overpressure can be noticed. This might be referred to the fact that the flame doesn't have enough time to expand/accelerate before hitting the first baffle. The same conclusion was observed by Xiao et al. (2014). However, calculations presented in the remainder of this study use the hemispherical ignition source (IG-2) with a diameter of 3 mm and located on the base plate. It should be noticed here that the ignition radius for CNG and LPG would be doubled as the energy required to ignite them is almost twice of that required for hydrogen as mentioned earlier in chapter 2.

Table 8.2 Details of ignition sources, shapes and location

Case	Shape	Radius (mm)	Distance of centre from base plate (mm)
IG-1	Hemispherical	2	0
IG-2	Hemispherical	3	0
IG-3	Hemispherical	4	0
IG-4	Hemispherical	5	0
IG-5	Spherical	2.12	2.12
IG-6	Spherical	2.12	5



(a)



(b)

Figure 8.2 - Effect of various ignition radii (a) overpressure (b) flame position for BBBS configuration.

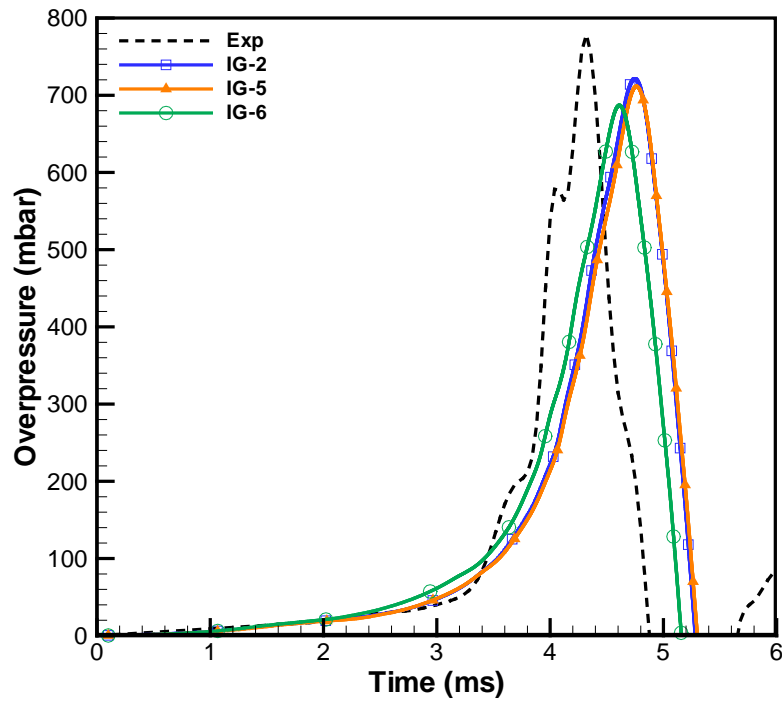


Figure 8.3 - Effect of ignition shape (Hemispherical and spherical) and location on overpressure-time traces for BBBS configuration using the same ignition area.

8.3 Effect of Fuel Type

It is clear from Figures 8.4-8.12 that hydrogen has the biggest value for overpressure, flame position and speed compared to CNG and LPG. The value of overpressure of hydrogen is almost about 38 times higher than that of CNG and LPG. Also, the flame speed is much faster for hydrogen than that for CNG and LPG. LPG is slightly higher than CNG and the flame speed is almost the same as CNG. This is due to the higher laminar flame speed and diffusivity hydrogen has over the CNG and LPG. This points-out the importance of considering safe design when using hydrogen in facilities and commercial applications.

Also, from Figures 8.4-8.6, LES simulations for CNG and hydrogen are slightly under-predicted while it is over-predicted for LPG. One of the factors for this discrepancy is the value of laminar flame speed used, as range of values for each fuel is available in the literature. This is in-addition to the model accuracy, grid...etc. The same observation for the over/under-predictions is confirmed in both the flame position and speed figures.

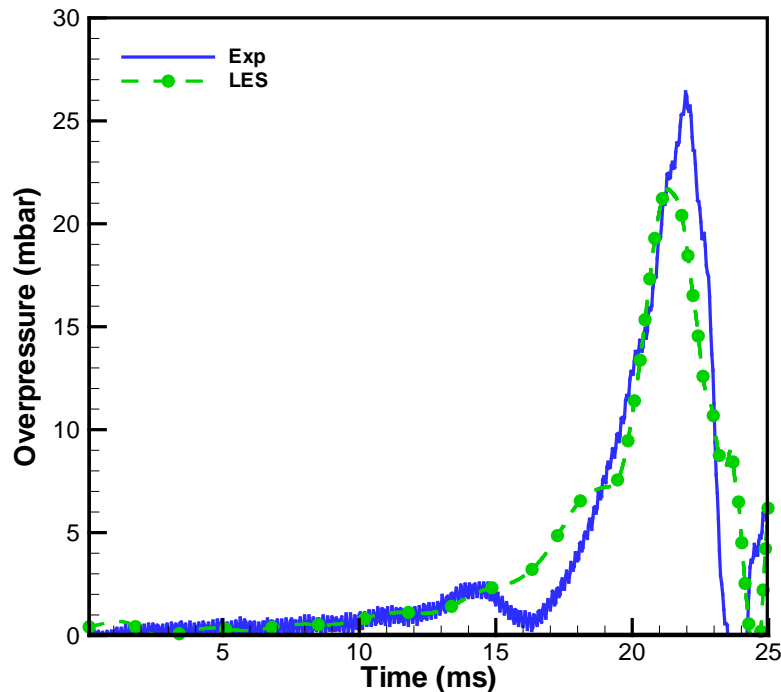


Figure 8.4 Overpressure-time histories for CNG-air mixture ($\Phi = 0.8$) for configuration BBBS.

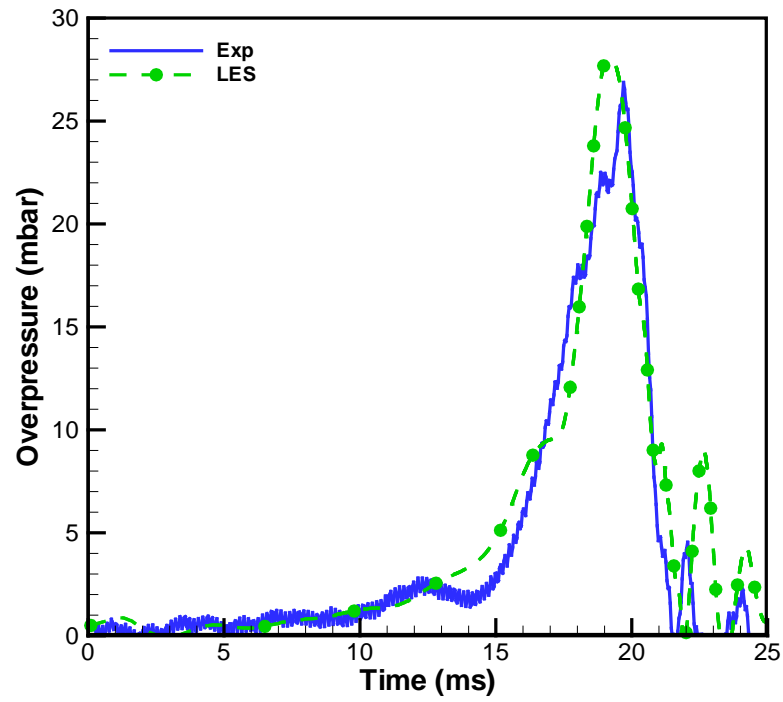


Figure 8.5 Overpressure-time histories for LPG-air mixture ($\Phi = 0.8$) for configuration BBBS.

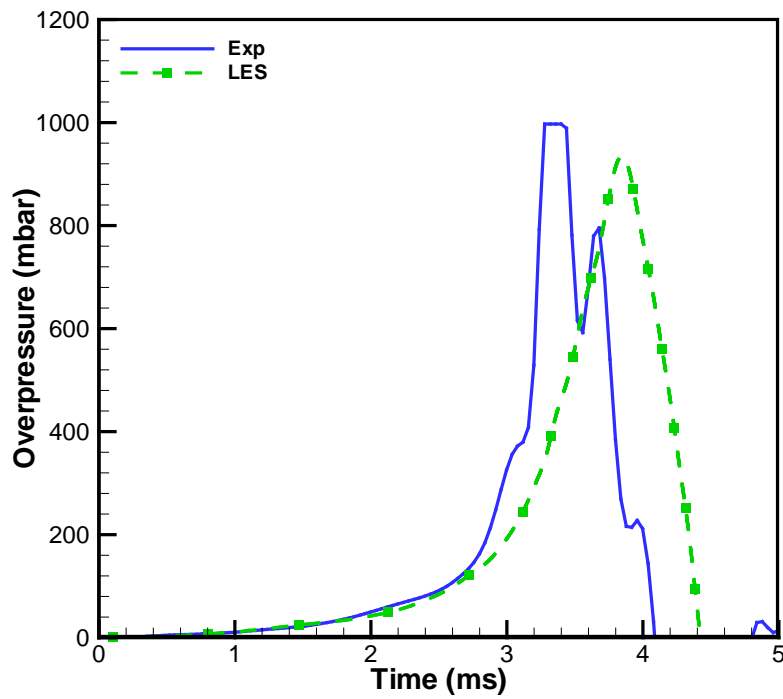


Figure 8.6 Overpressure-time histories for hydrogen-air mixture ($\Phi = 0.8$) for configuration BBBS.

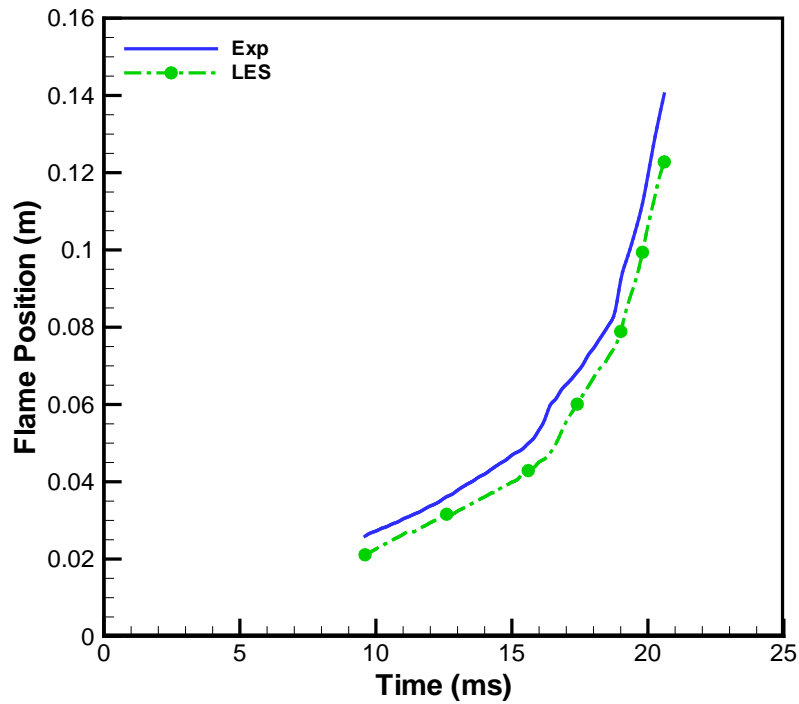


Figure 8.7 Flame position-time traces of LES simulation for CNG-air mixture ($\Phi = 0.8$) for configuration BBBS.

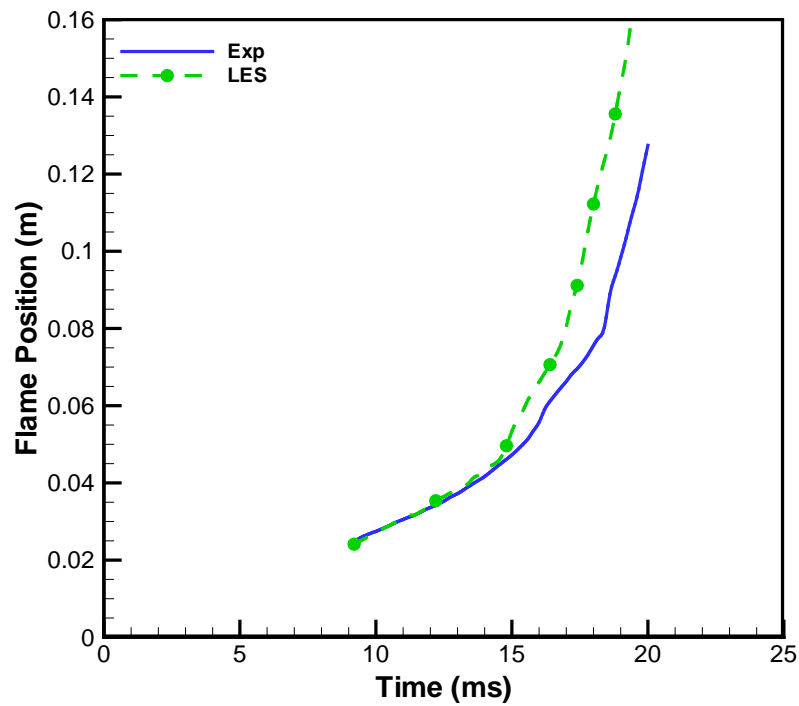


Figure 8.8 Flame position-time traces of LES simulation for LPG-air mixture ($\Phi = 0.8$) for configuration BBBS.

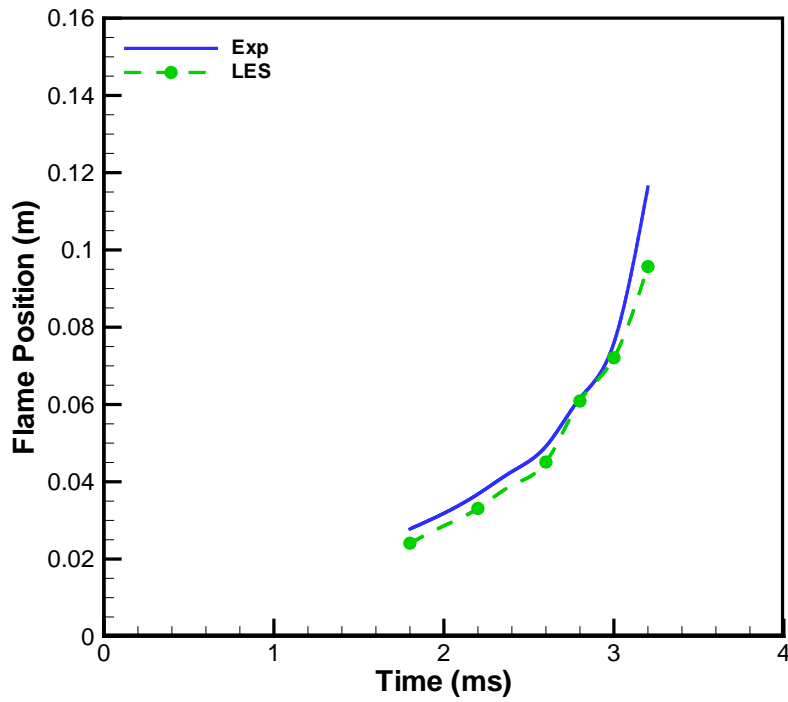


Figure 8.9 Flame position-time traces of LES simulation for hydrogen-air mixture ($\Phi = 0.8$) for configuration BBBS.

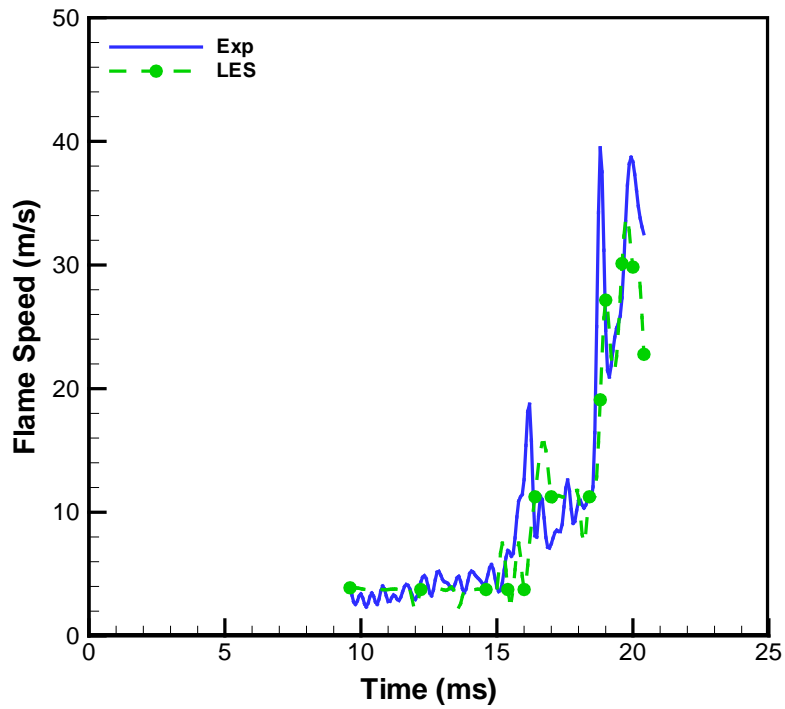


Figure 8.10 Flame speed-time traces of LES simulation for CNG-air mixture ($\Phi = 0.8$) for configuration BBBS.

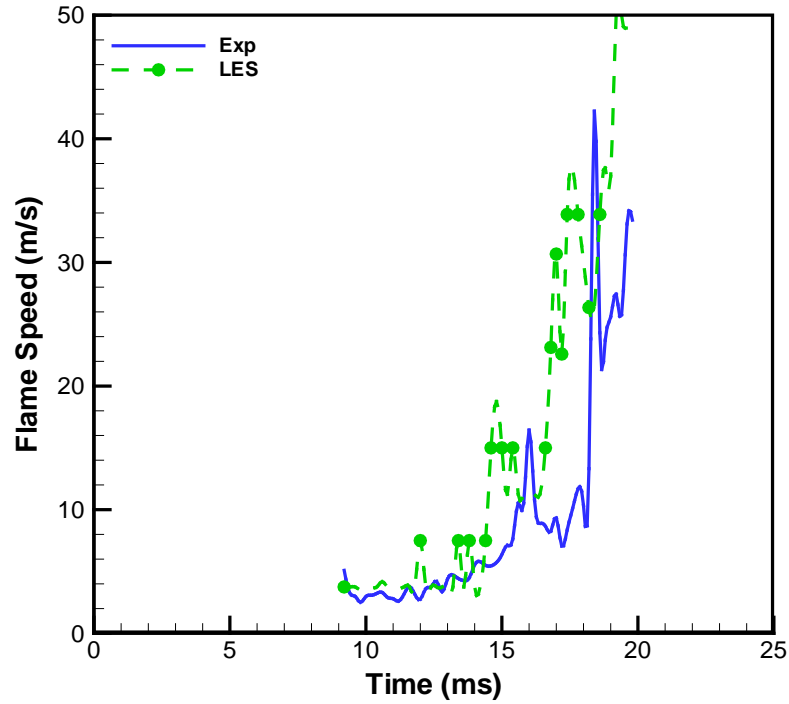


Figure 8.11 Flame speed-time traces of LES simulation for LPG-air mixture ($\Phi = 0.8$) for configuration BBBS.

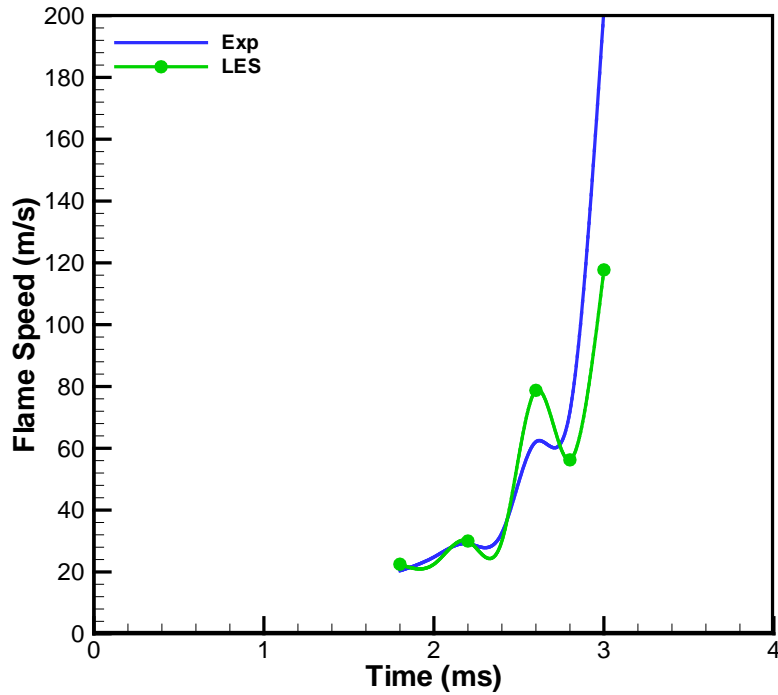


Figure 8.12 Flame speed-time traces of LES simulation for hydrogen-air mixture ($\Phi = 0.8$) for configuration BBBS.

8.4 Effect of Lewis number

In this section the effect of non-unity Lewis number is considered with the model as described earlier in Chapter 4. However, as it could be noticed from Table 4.1 that Lewis numbers vary in value for both LPG and Hydrogen and are away from unity, while for CNG its value is very close to unity. From Figure 8.13, it is clear that there is almost no change in the overpressure for CNG when using unity or non-unity Lewis number and for both cases a reasonable agreement is obtained. While from Figure 8.14 for LPG, using unity Lewis number assumption tends to over-predict the overpressure when compared with experiments. However, for the non-unity Lewis case, good agreement was achieved. For Hydrogen as shown in Figure 8.15, the unity Lewis number assumption under-predicts the pressure, while for the non-unity Lewis number better agreement was obtained with the experimental results. This is very crucial in accidental explosions as the over/under-prediction of the overpressure may lead to critical problems in designing the industrial, commercial or domestic facilities. The flame position and flame speed figures confirm also with this observation for the three fuels.

The reason for over/under-predictions is mainly due to diffusivity. In the hydrogen case, higher diffusivity exists in the non-unity Lewis number case rather than the unity one. This is led have a faster flame. An inverse effect happened for the LPG where non-unity Lewis number led to a slower flame. For CNG, a negligible effect is observed. This points-out the importance of considering non-unity Lewis number on modelling of fuel/air mixtures as they could lead to disastrous results, especially on designing hydrogen systems. Hence, in the following sections this effect is considered in the results.

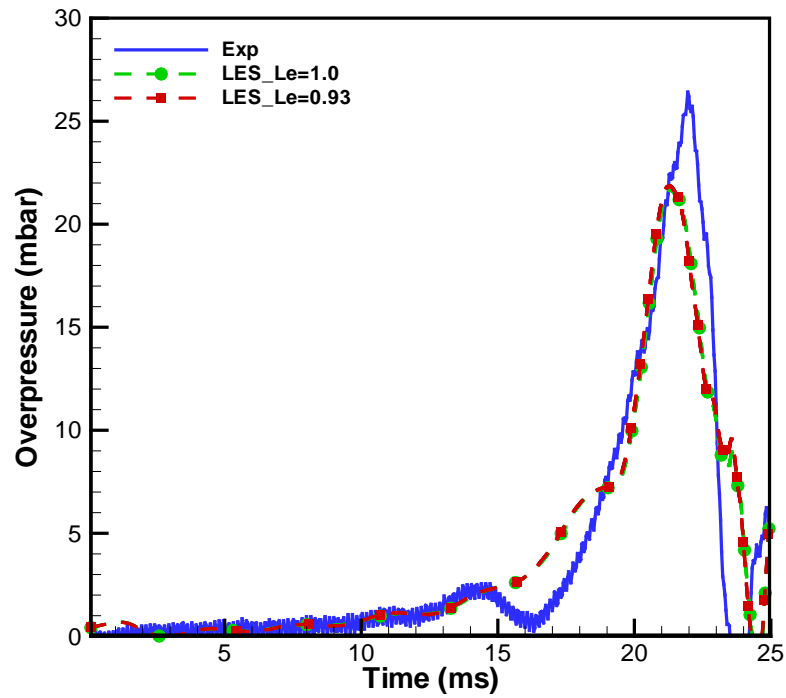


Figure 8.13 Comparison between unity and non-unity Lewis number on overpressure-time histories for CNG-air mixture ($\Phi = 0.8$).

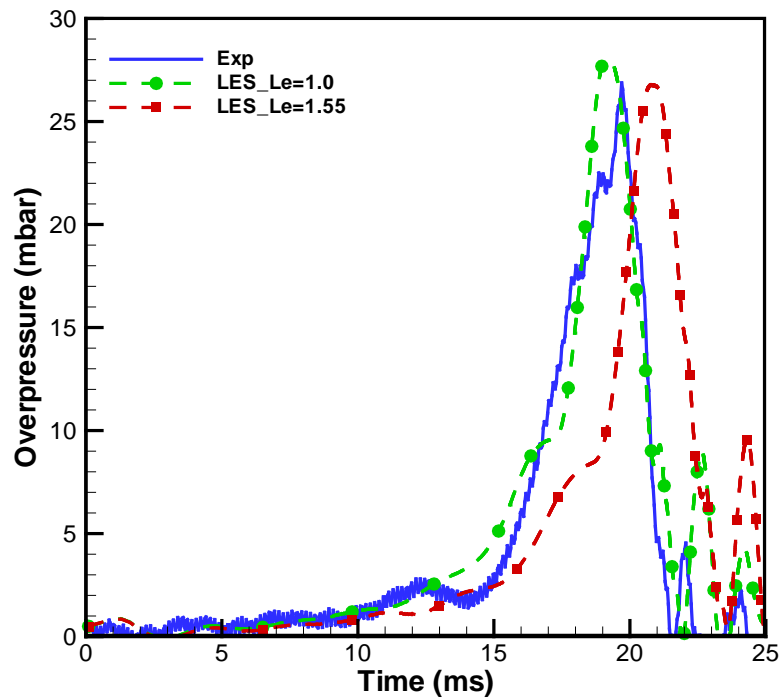


Figure 8.14 Comparison between unity and non-unity Lewis number on overpressure-time histories for LPG-air mixture ($\Phi = 0.8$).

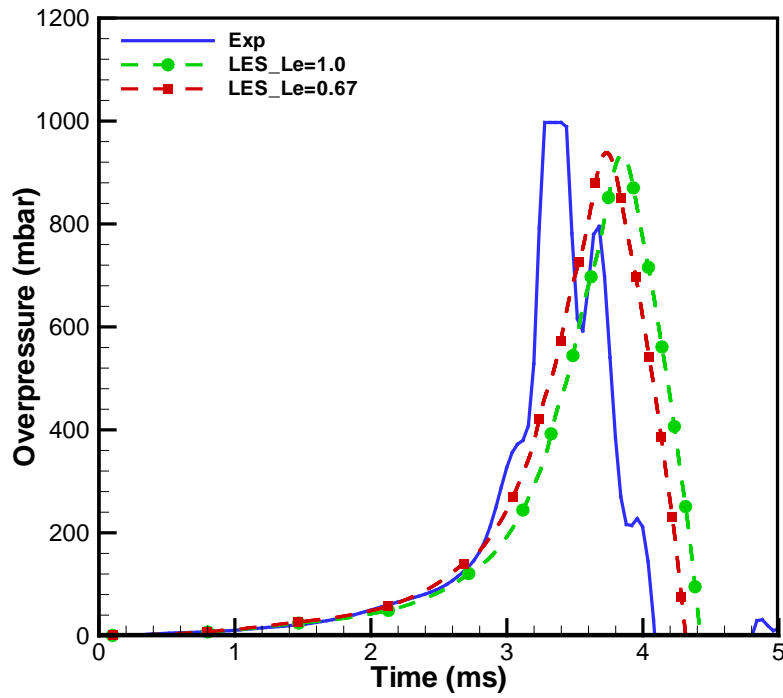


Figure 8.15 Comparison between unity and non-unity Lewis number on overpressure-time histories for hydrogen-air mixture ($\Phi = 0.8$).

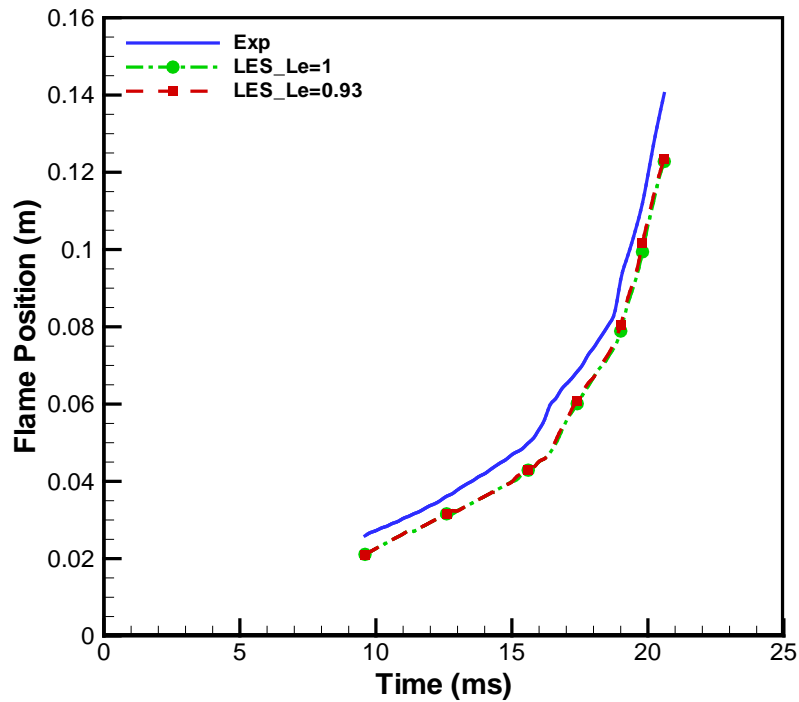


Figure 8.16 Comparison between unity and non-unity Lewis number on flame position-time histories for CNG-air mixture ($\Phi = 0.8$).

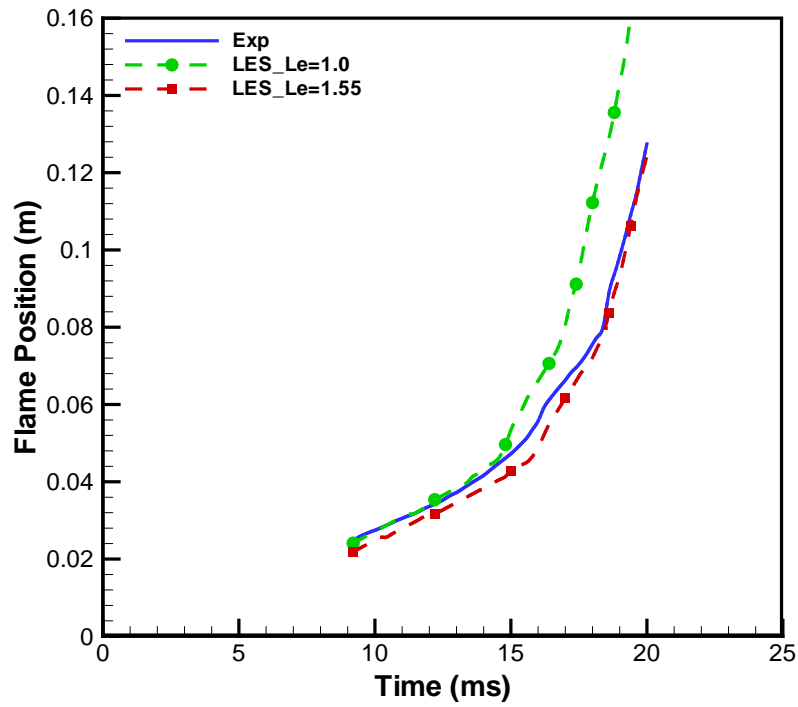


Figure 8.17 Comparison between unity and non-unity Lewis number on flame position-time histories for LPG-air mixture ($\Phi = 0.8$).

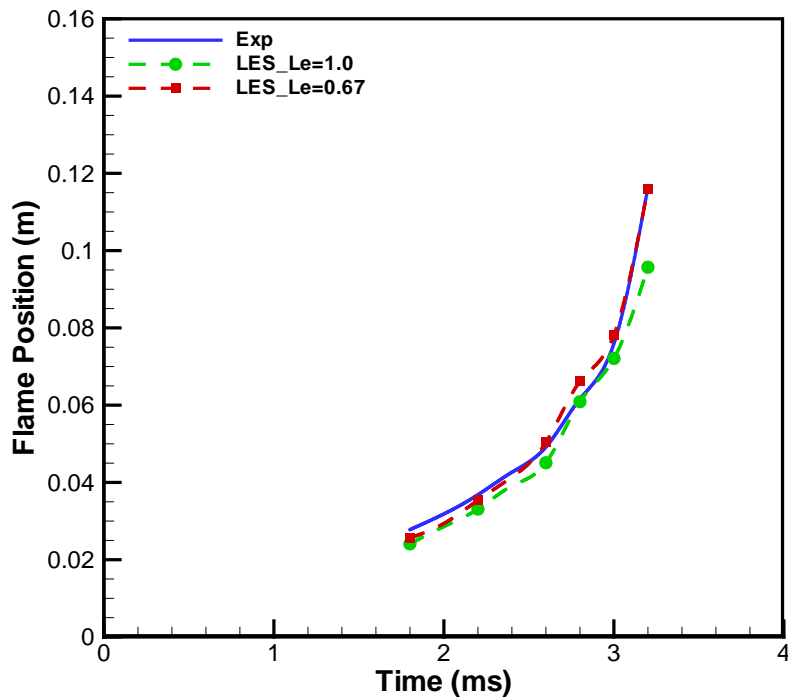


Figure 8.18 Comparison between unity and non-unity Lewis number on flame position-time histories for hydrogen-air mixture ($\Phi = 0.8$).

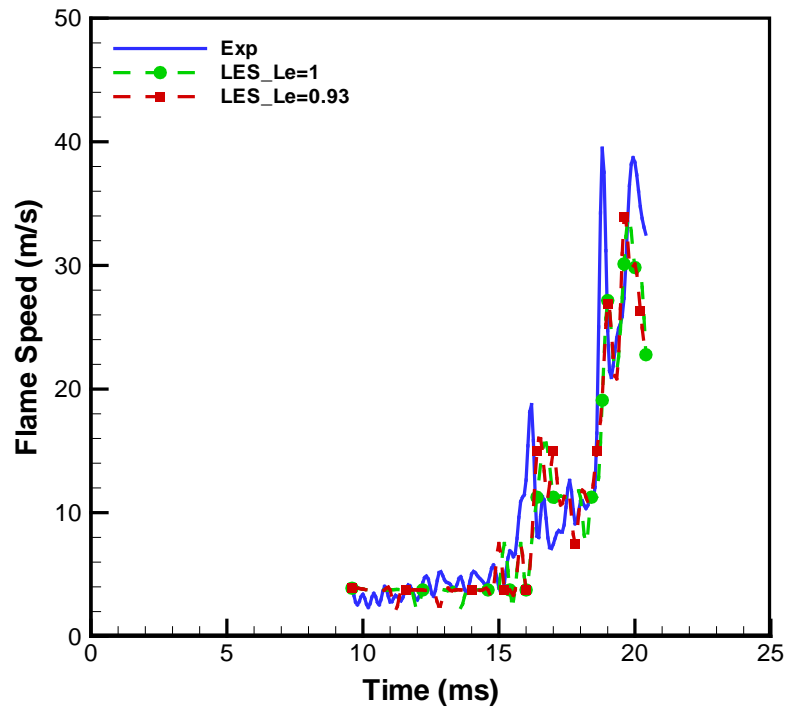


Figure 8.19 Comparison between unity and non-unity Lewis number on flame speed-time histories for CNG-air mixture ($\Phi = 0.8$).

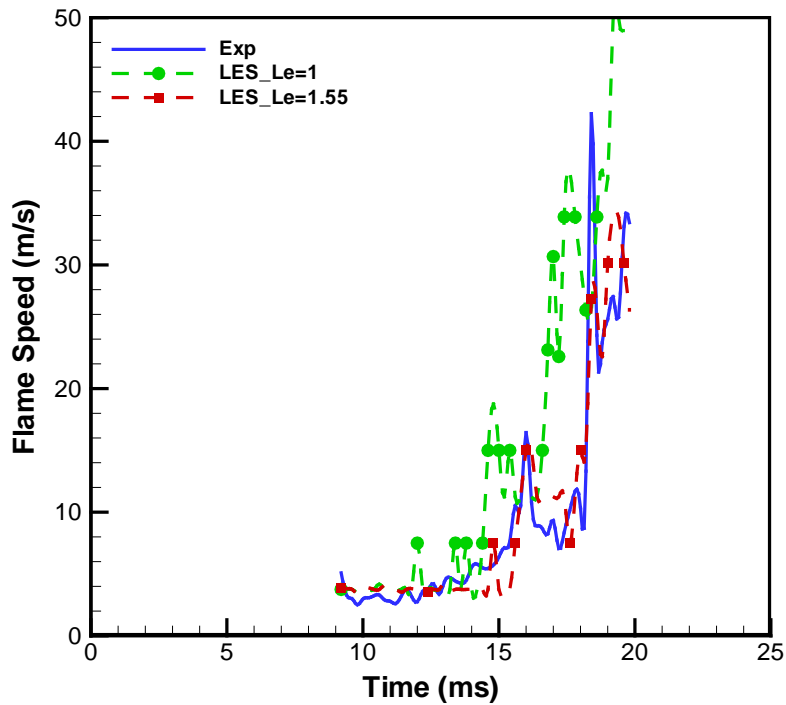


Figure 8.20 Comparison between unity and non-unity Lewis number on flame speed-time histories for LPG-air mixture ($\Phi = 0.8$).

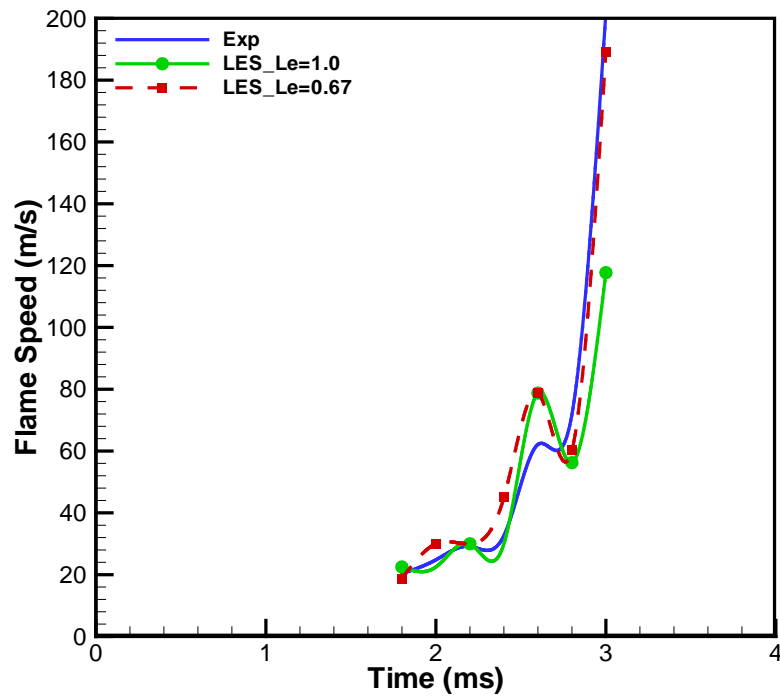


Figure 8.21 Comparison between unity and non-unity Lewis number on flame speed-time histories for hydrogen-air mixture ($\Phi = 0.8$).

8.5 Model Validation Using Flame Stretch

Figures 8.22 - 8.24 compares the extracted stretch values for the three fuels and for both unity and non-unity cases with the experimental data. The same procedure explained in the previous chapter to extract the flame stretch values is used to extract the values from the generated numerical images. However, discrepancies between the experimental and numerical values are due to many factors. For example, the resolution for the images is different which could lead to a magnification in value of error. Also, the human error is possible especially that the process is done manually. However, from qualitative point of view both results matches and the effect of the square obstacle can be seen in all the results in increasing the flame stretch, similarly with the pressure increase after the obstacle. Also, the effect of baffles on how the flame stretch oscillates can be seen in all the figures and came with the observation of Poinso and Veynante (2012) as the flame stretch tends to increase and decrease but still with positive values for propagating flames. The value of stretch for hydrogen is about three times that of CNG and LPG and this confirms with the previous that the amount of turbulence generated and flame wrinkling for hydrogen are much higher than CNG and LPG. Also, using the non-unity Lewis number cases tends to have better results rather than the unity cases.

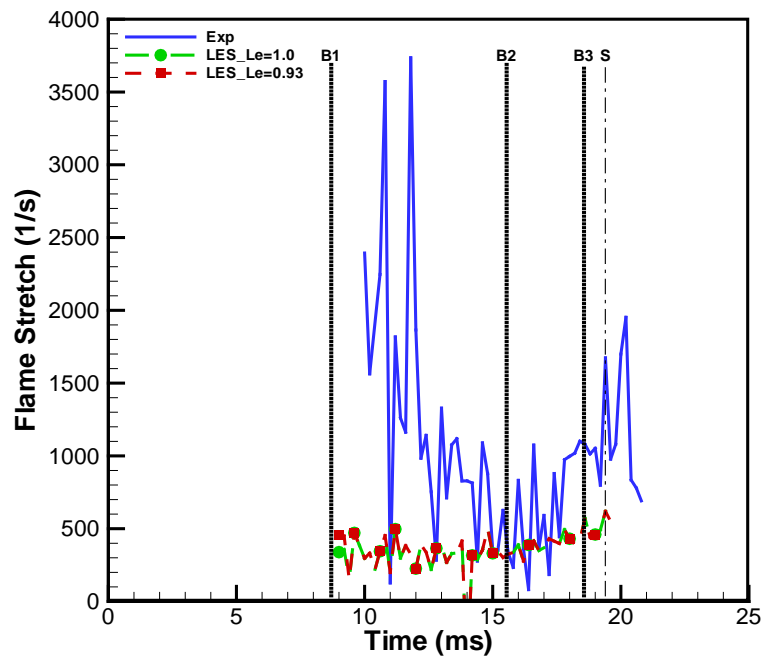


Figure 8.22 Comparison between extracted flame stretch from experimental/numerical images, and unity/non-unity Lewis number for CNG-air mixture with $\Phi = 0.8$ in configuration BBBS.

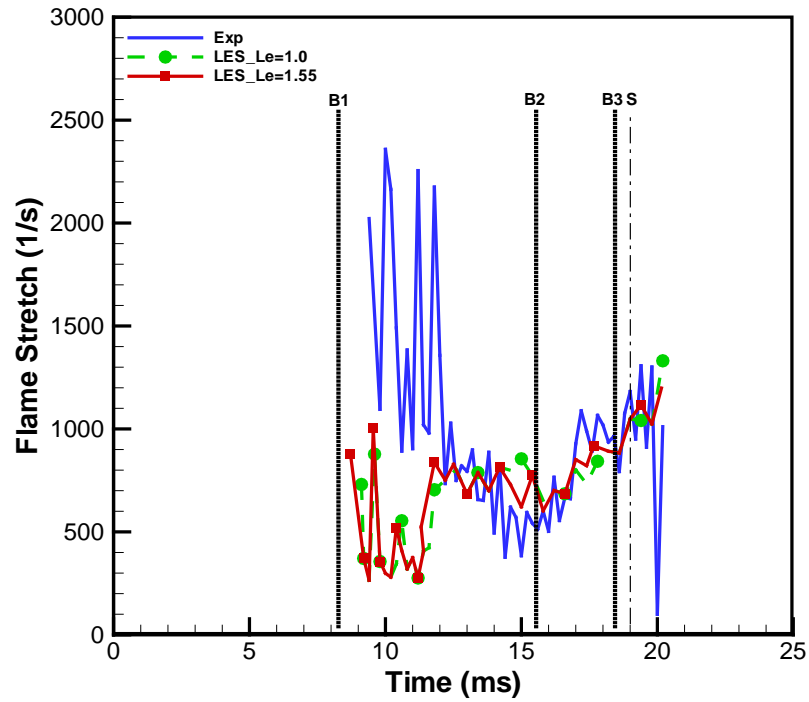


Figure 8.23 Comparison between extracted flame stretch from experimental/numerical images, and unity/non-unity Lewis number for LPG-air mixture with $\Phi = 0.8$ in configuration BBBS.

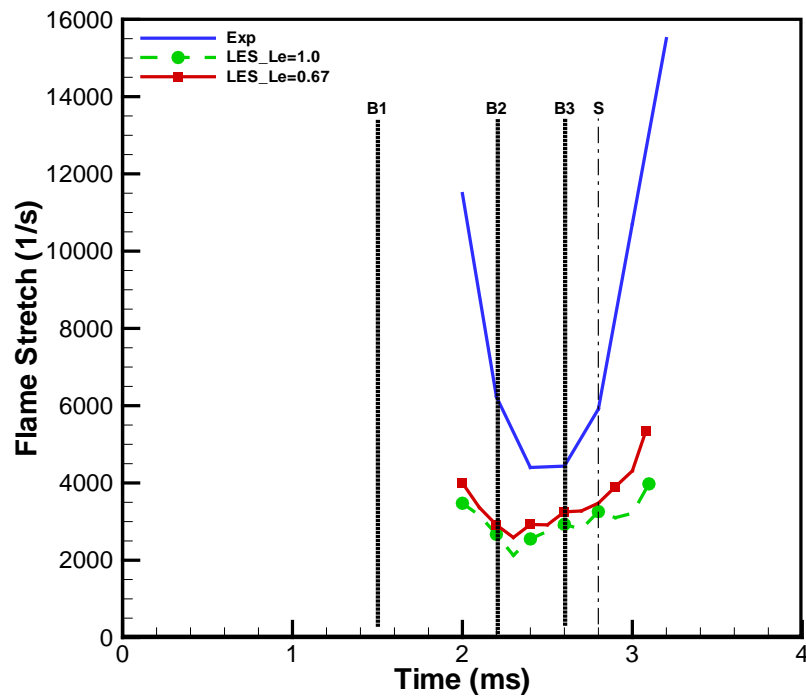


Figure 8.24 Comparison between extracted flame stretch from experimental/numerical images, and unity/non-unity Lewis number for hydrogen-air mixture with $\Phi = 0.8$ in configuration BBBS.

8.6 Effect of Flow Configuration

The baffles in these configurations are progressively increasing from no baffle to three from ignition source as shown in Figure 8.25.

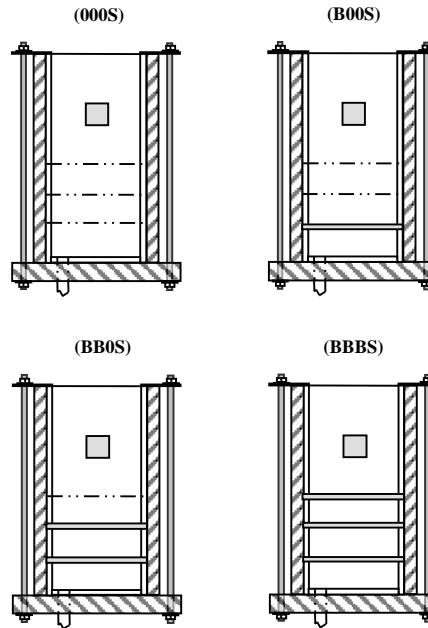


Figure 8.25 Combustion chamber configurations used in the present work.

The overpressure and flame speed shows an increase as the number of baffles used increases. This observation could be seen for the three fuels. The effect of baffles came from the fact that turbulence tends to increase as the blockage ratio increases. However, some over-prediction is observed especially in the cases of less number of baffles and this is originally due the model is basically for turbulent cases. As, the laminar phase is not modelled properly which affects later on the turbulent phase (Wang et al. (2012)). Again, hydrogen has the highest overpressure, flame position and speed for all the cases while CNG and LPG are close to each other with slightly higher values for LPG. The time shift observed is due to the ignition model as the model in the present study is artificially tuned to capture the right incident time for the overpressure, where a proper dynamic model would fix this issue (Vianna and Cant (2013)).

For the 000S configuration, the same trend for the overpressure curves is observed for the three fuels with a better agreement with hydrogen, LPG and CNG respectively.

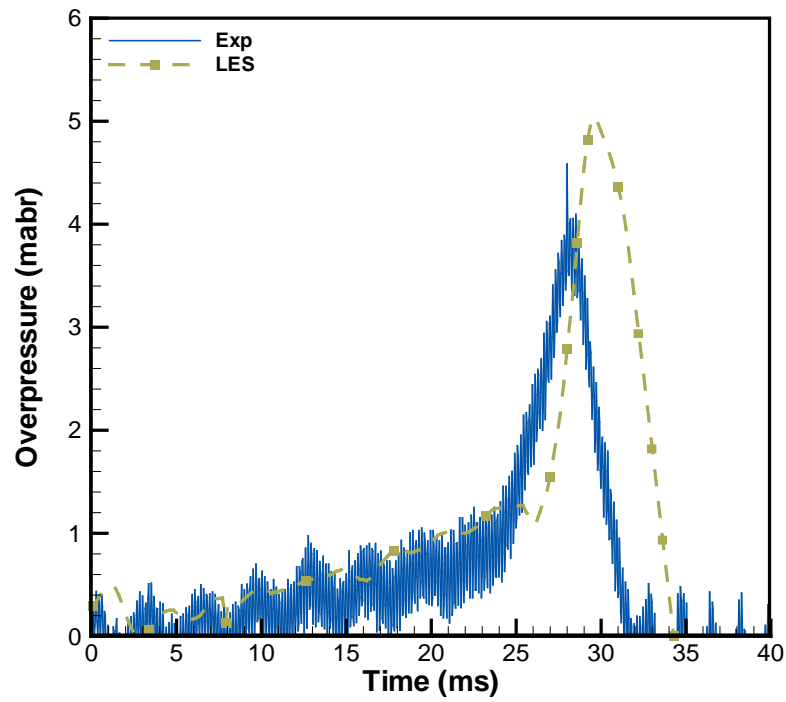


Figure 8.26 Overpressure-time histories for CNG-air mixture ($\Phi = 0.8$) and configuration 000S.

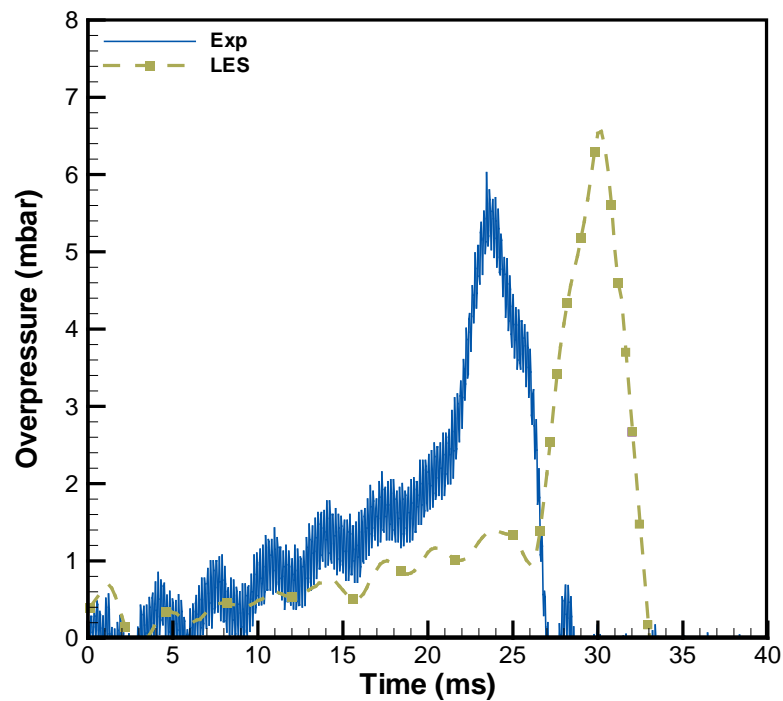


Figure 8.27 Overpressure-time histories for LPG-air mixture ($\Phi = 0.8$) and configuration 000S.

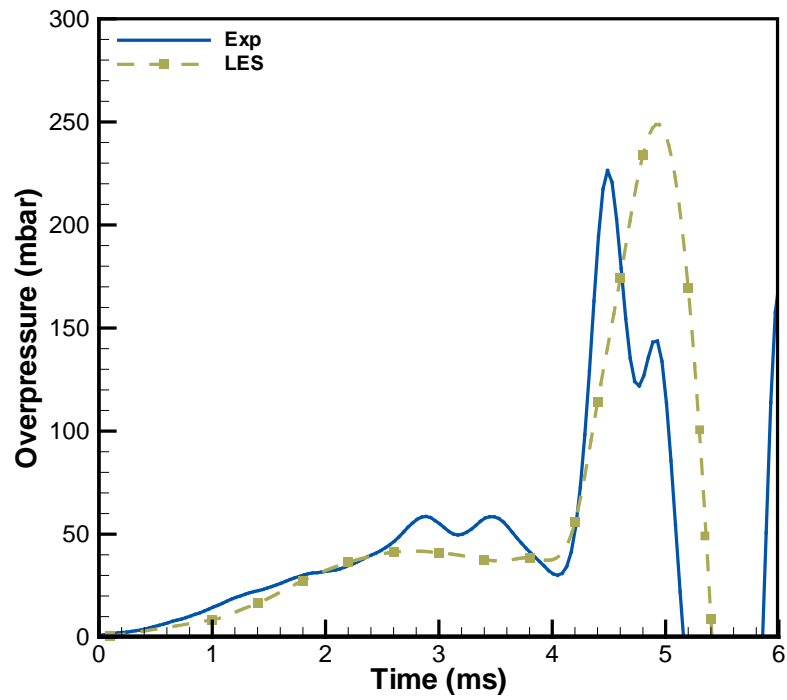


Figure 8.28 Overpressure-time histories for hydrogen-air mixture ($\Phi = 0.8$) and configuration 000S.

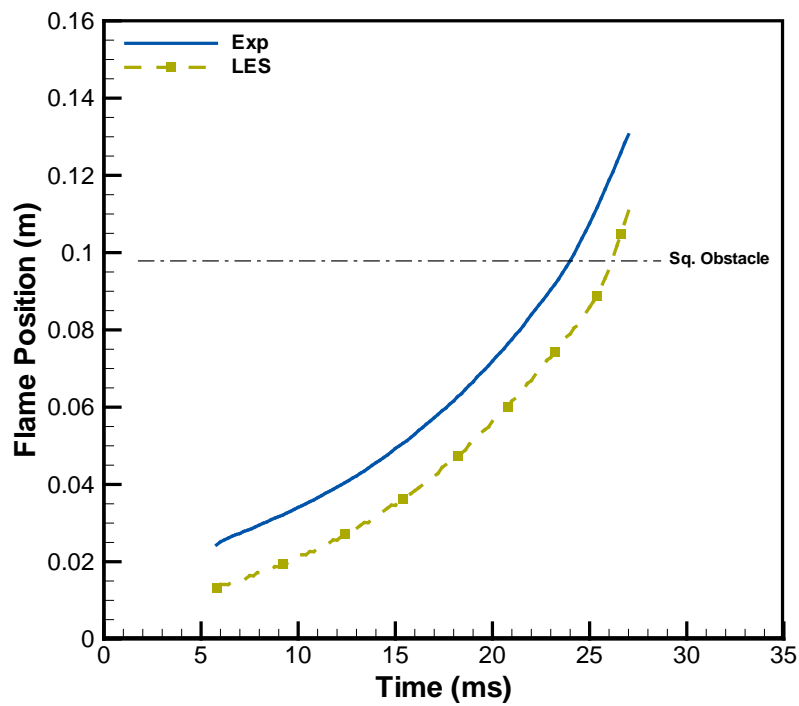


Figure 8.29 Flame position-time histories for CNG-air mixture ($\Phi = 0.8$) and configuration 000S.

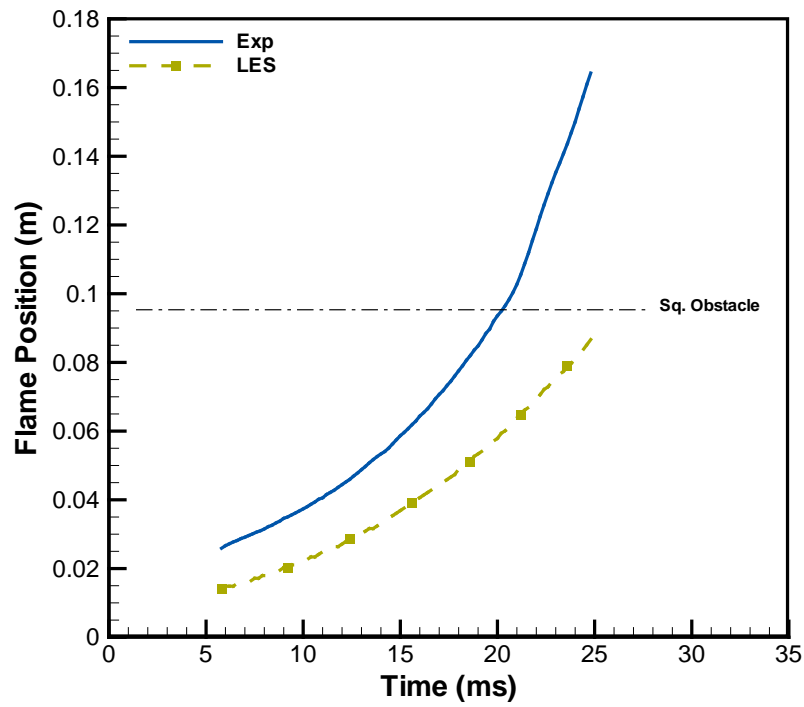


Figure 8.30 Flame position-time histories for LPG-air mixture ($\Phi = 0.8$) and configuration 000S.

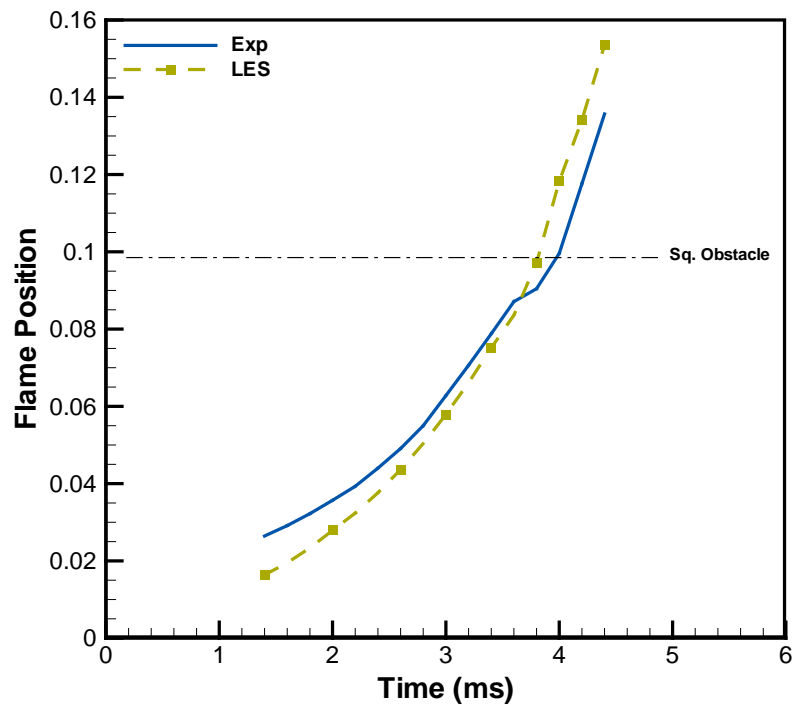


Figure 8.31 Flame position-time histories for hydrogen-air mixture ($\Phi = 0.8$) and configuration 000S.

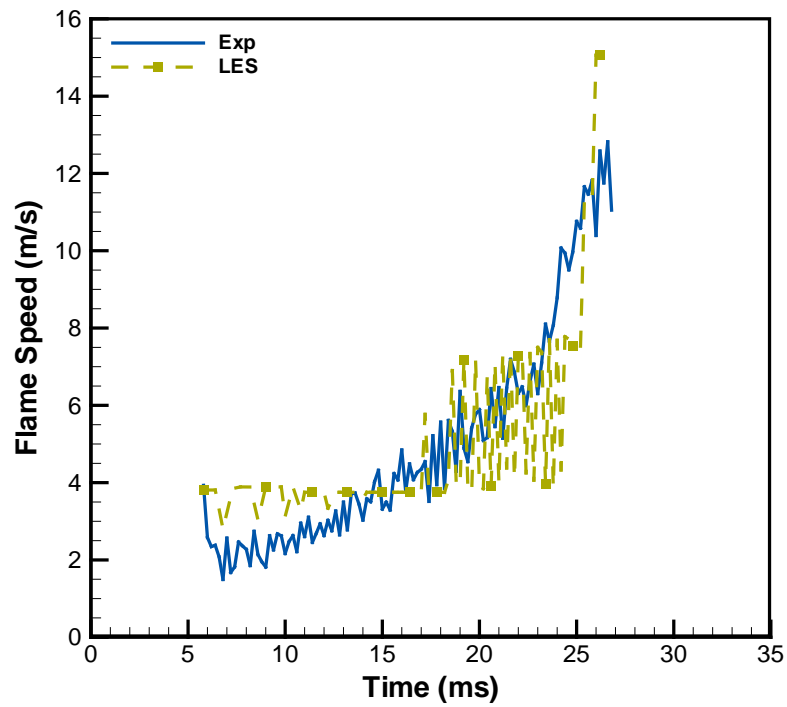


Figure 8.32 Flame speed-time histories for CNG-air mixture ($\Phi = 0.8$) and configuration 000S.

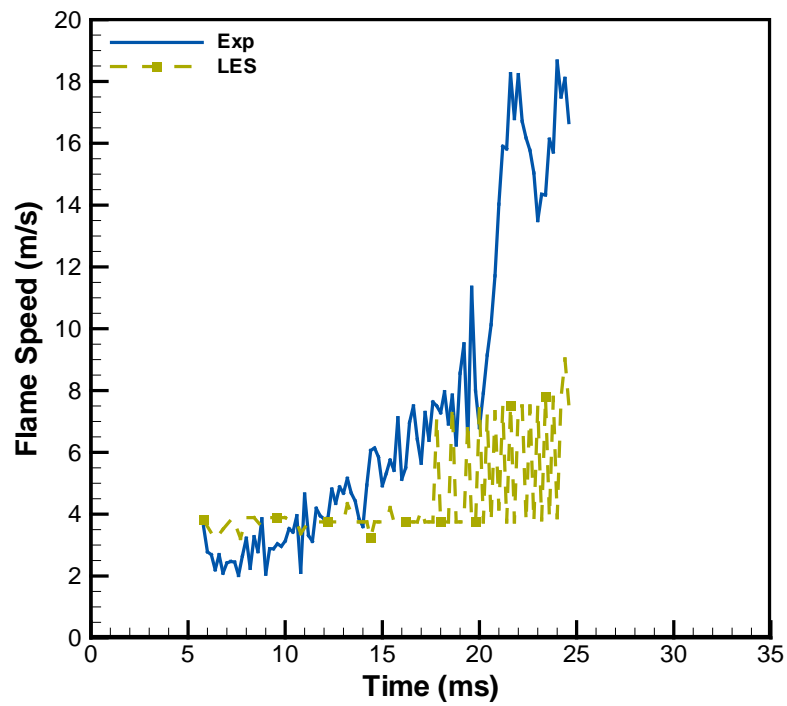


Figure 8.33 Flame speed-time histories for LPG-air mixture ($\Phi = 0.8$) and configuration 000S.

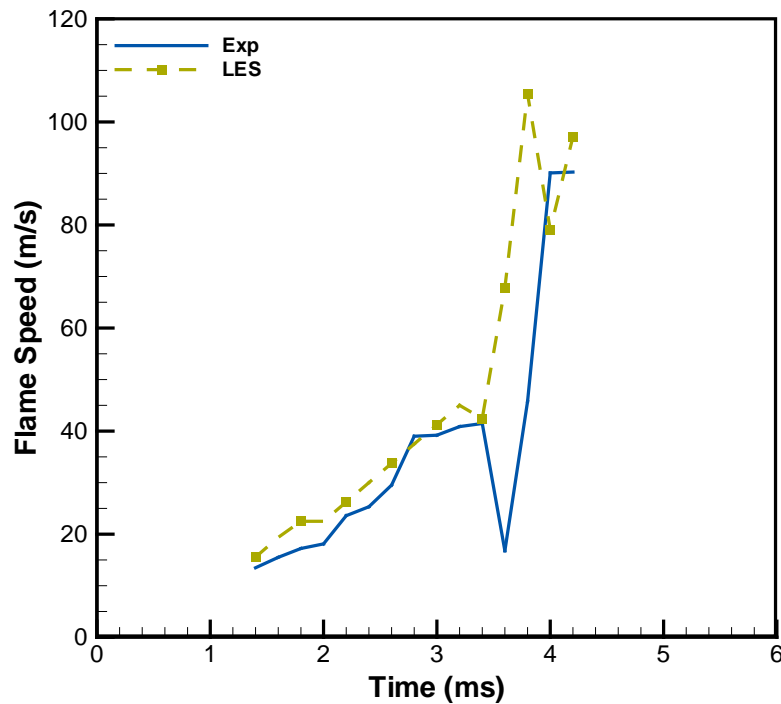


Figure 8.34 Flame speed-time histories for hydrogen-air mixture ($\Phi = 0.8$) and configuration 000S.

It should be noticed from the above figures that the over-prediction associated with CNG and LPG is more than for hydrogen in case of 000S. In addition to the previously mentioned reason, this could be also for the sensitivity of model to the values of laminar burning velocity. As, this case tends to be the most quasi-laminar one. So any small error in the value of the laminar burning velocity would cause this mismatch between the measured and predicted results.

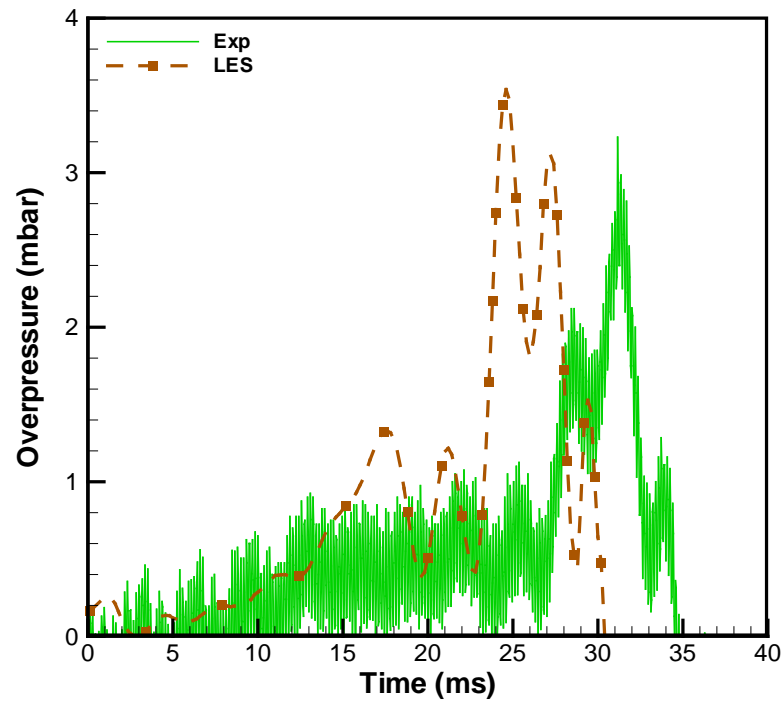


Figure 8.35 Overpressure-time histories for CNG-air mixture ($\Phi = 0.8$) and configuration B00S.

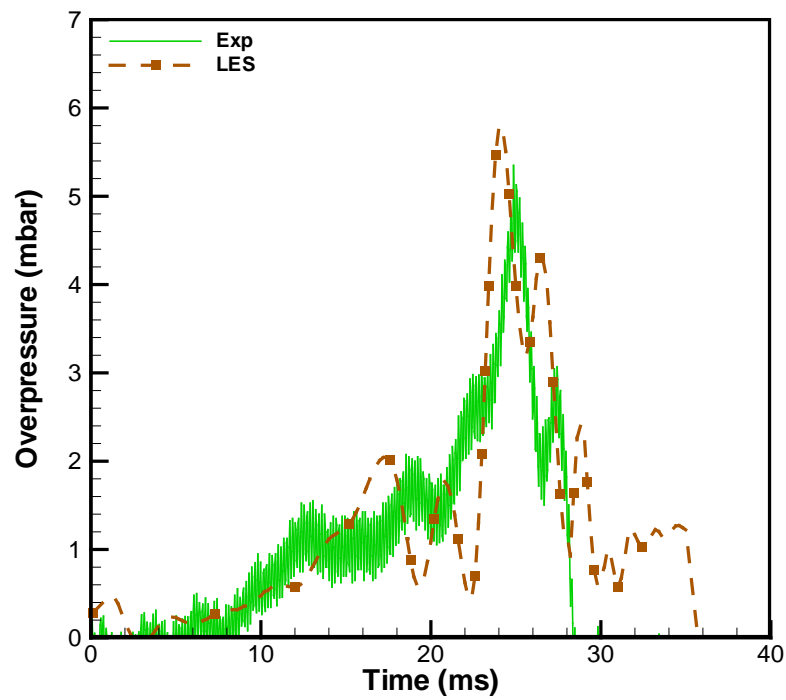


Figure 8.36 Overpressure-time histories for LPG-air mixture ($\Phi = 0.8$) and configuration B00S.

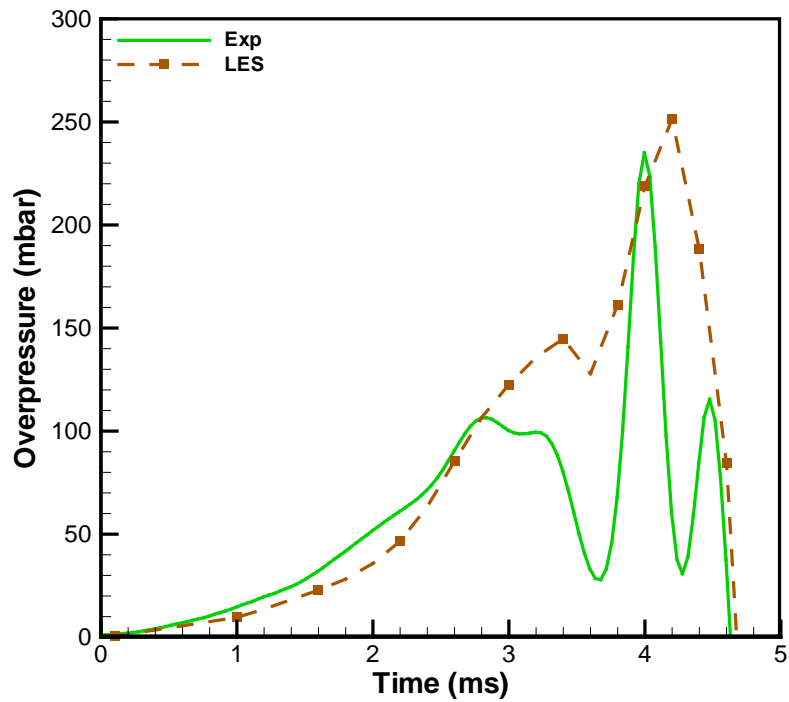


Figure 8.37 Overpressure-time histories for hydrogen-air mixture ($\Phi = 0.8$) and configuration B00S.

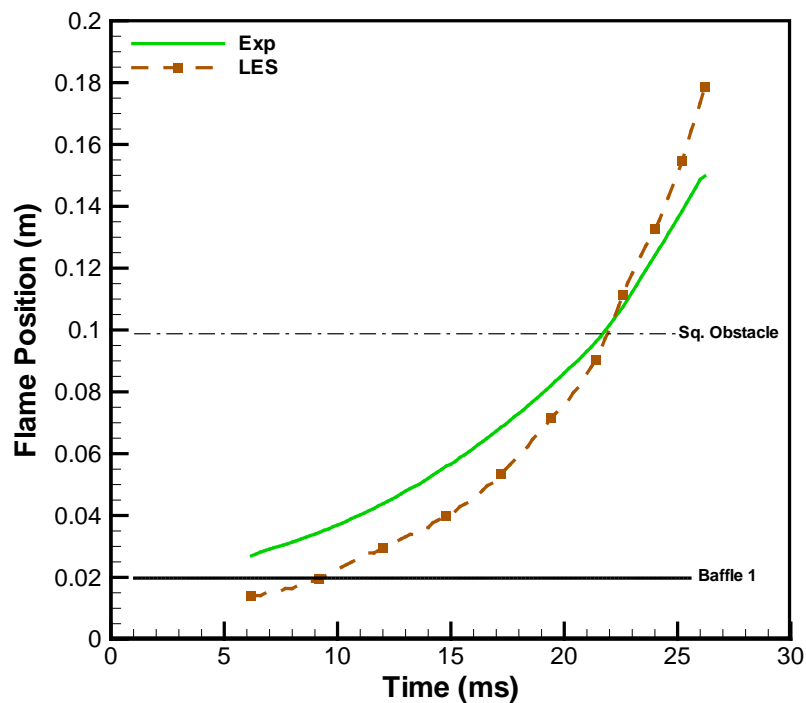


Figure 8.38 Flame position-time histories for CNG-air mixture ($\Phi = 0.8$) and configuration B00S.

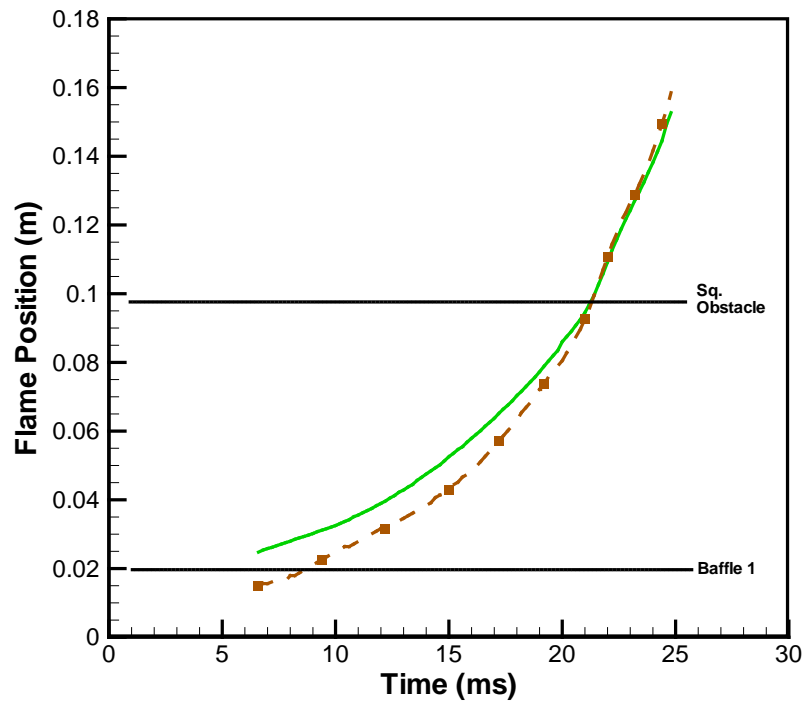


Figure 8.39 Flame position-time histories for LPG-air mixture ($\Phi = 0.8$) and configuration B00S.

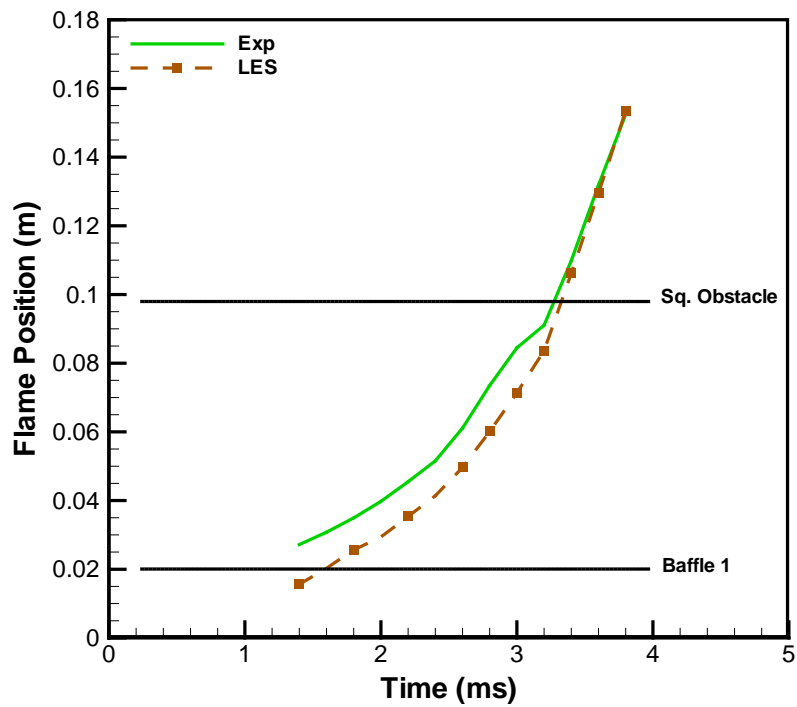


Figure 8.40 Flame position-time histories for hydrogen-air mixture ($\Phi = 0.8$) and configuration B00S.

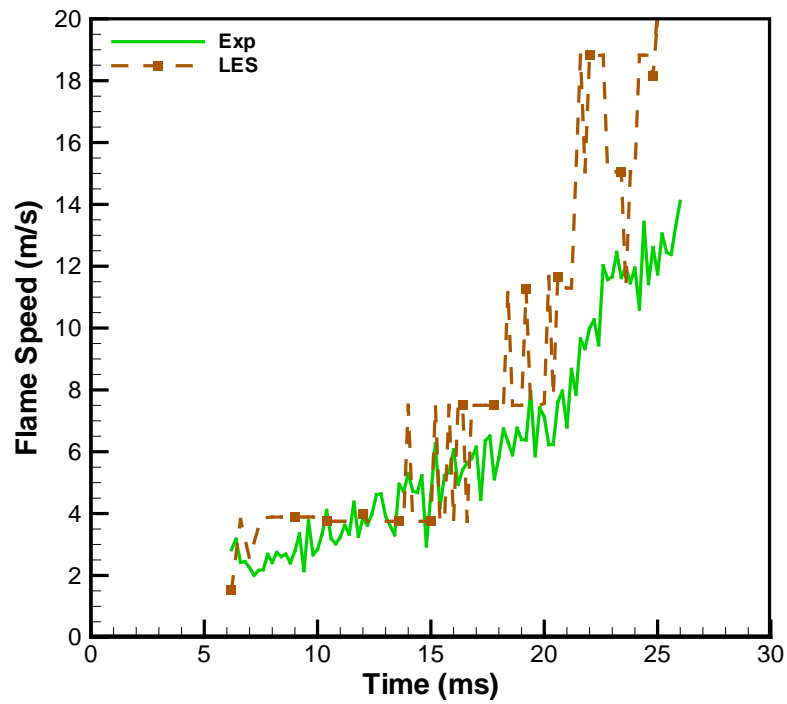


Figure 8.41 Flame speed-time histories for CNG-air mixture ($\Phi = 0.8$) and configuration B00S.

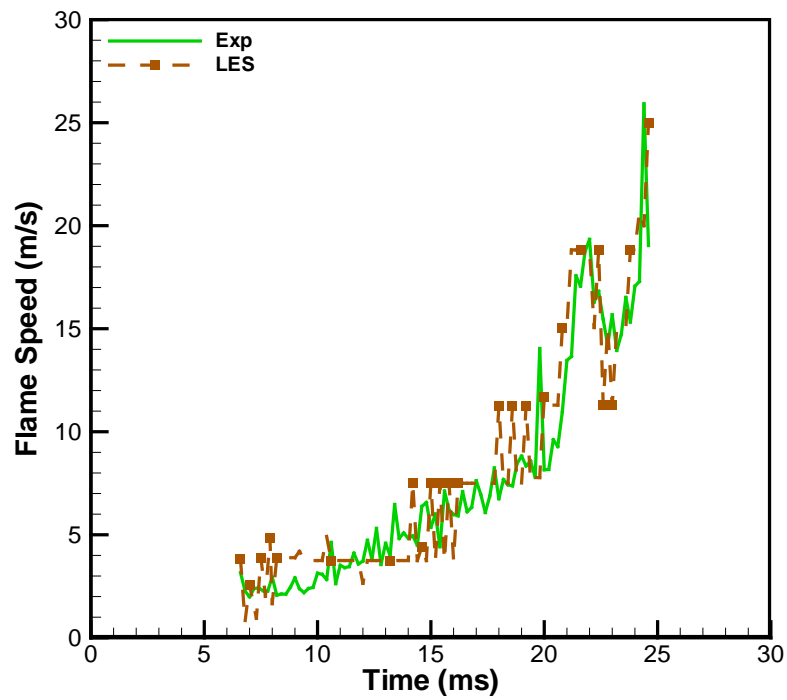


Figure 8.42 Flame speed-time histories for LPG-air mixture ($\Phi = 0.8$) and configuration B00S.

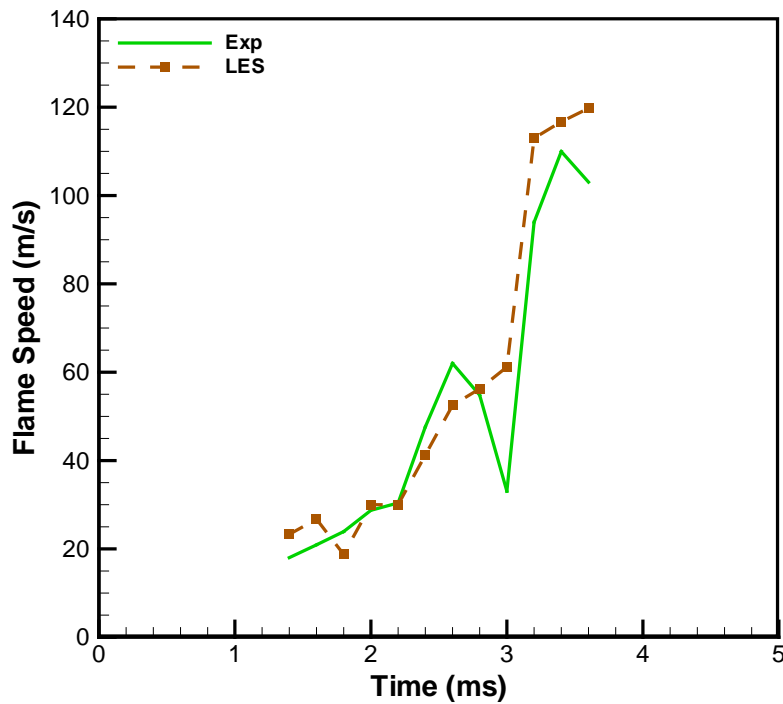


Figure 8.43 Flame speed-time histories for hydrogen-air mixture ($\Phi = 0.8$) and configuration B00S.

In configuration B00S; a better agreement is obtained for LPG, hydrogen then CNG respectively. This could be observed in the overpressure, flame position and speed. The effect of adding one baffle on these parameters, is not clear over 000S configuration but only very small increase in gradient after hitting that baffle. The re-laminarisation of the flow/flame could be observed from the flame position curves, as the increase in gradient tends to be very small.

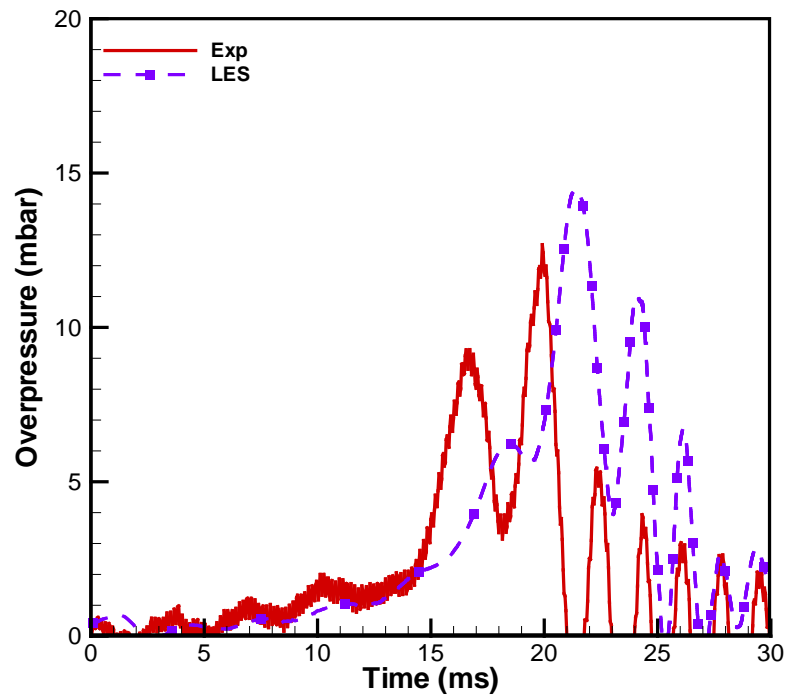


Figure 8.44 Overpressure-time histories for CNG-air mixture ($\Phi = 0.8$) and configuration BB0S.

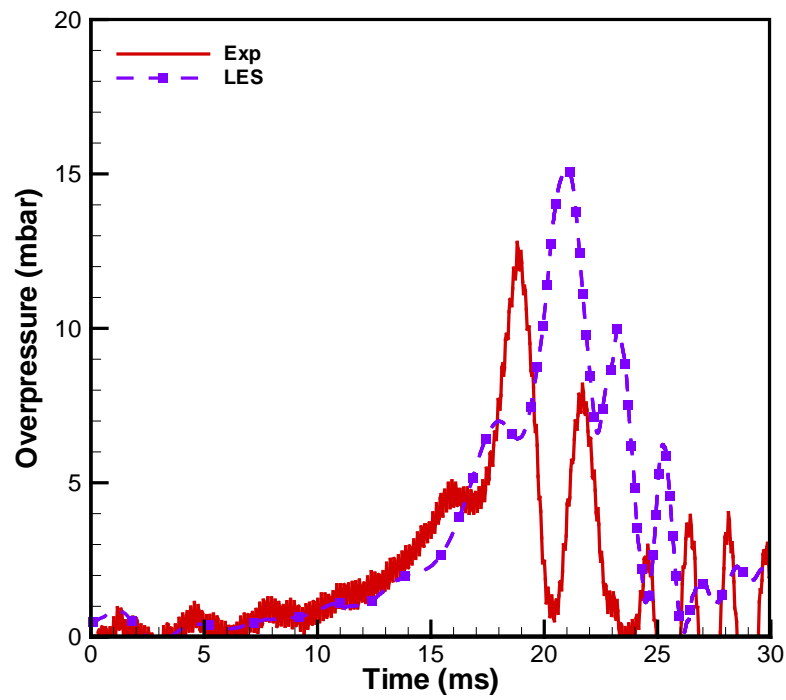


Figure 8.45 Overpressure-time histories for LPG-air mixture ($\Phi = 0.8$) and configuration BB0S.

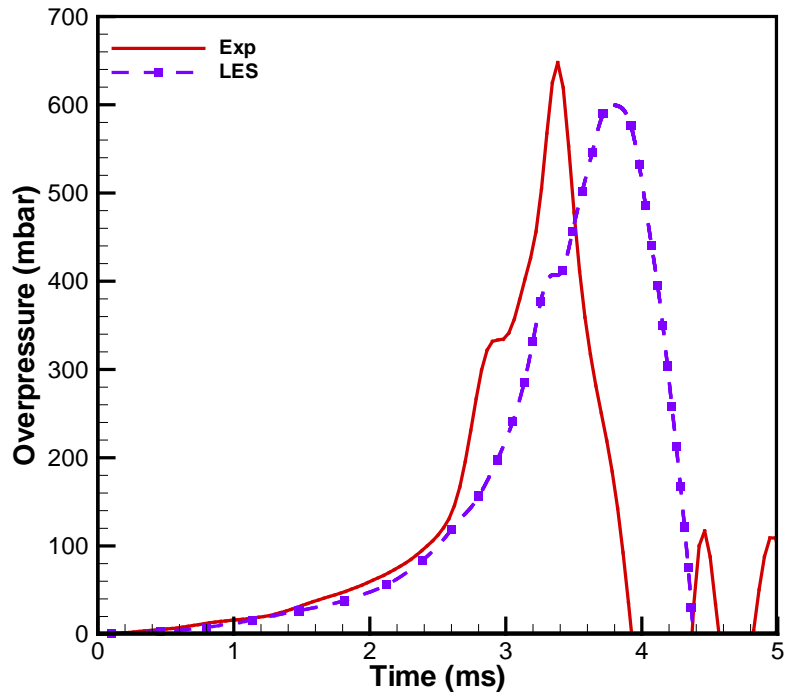


Figure 8.46 Overpressure-time histories for hydrogen-air mixture ($\Phi = 0.8$) and configuration BB0S.

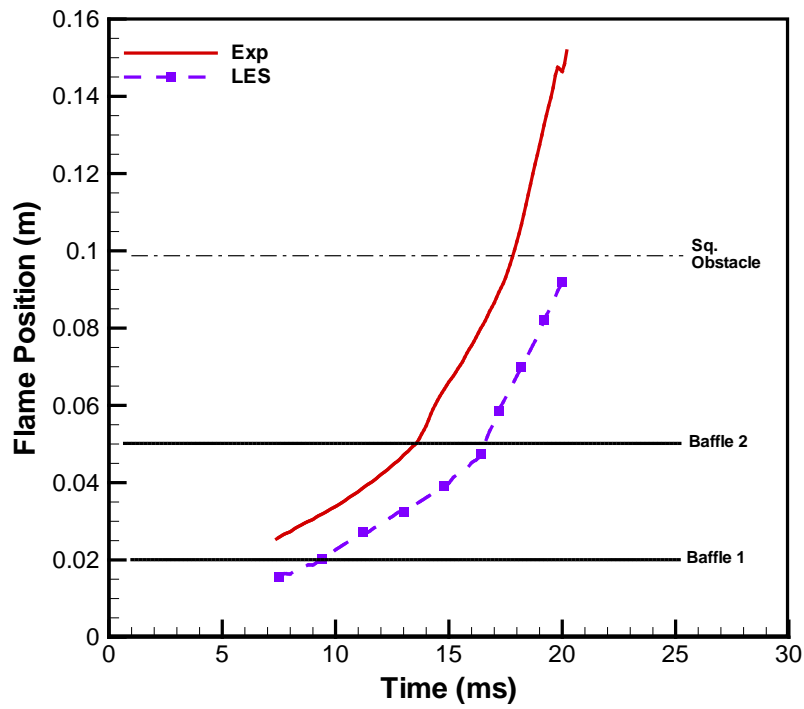


Figure 8.47 Flame position-time histories for CNG-air mixture ($\Phi = 0.8$) and configuration BB0S.

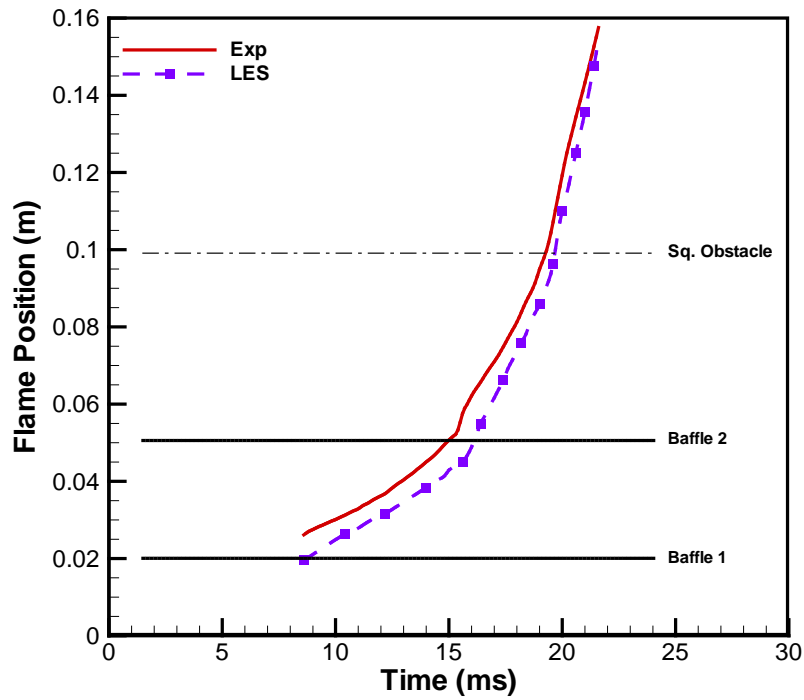


Figure 8.48 Flame position-time histories for LPG-air mixture ($\Phi = 0.8$) and configuration BB0S.

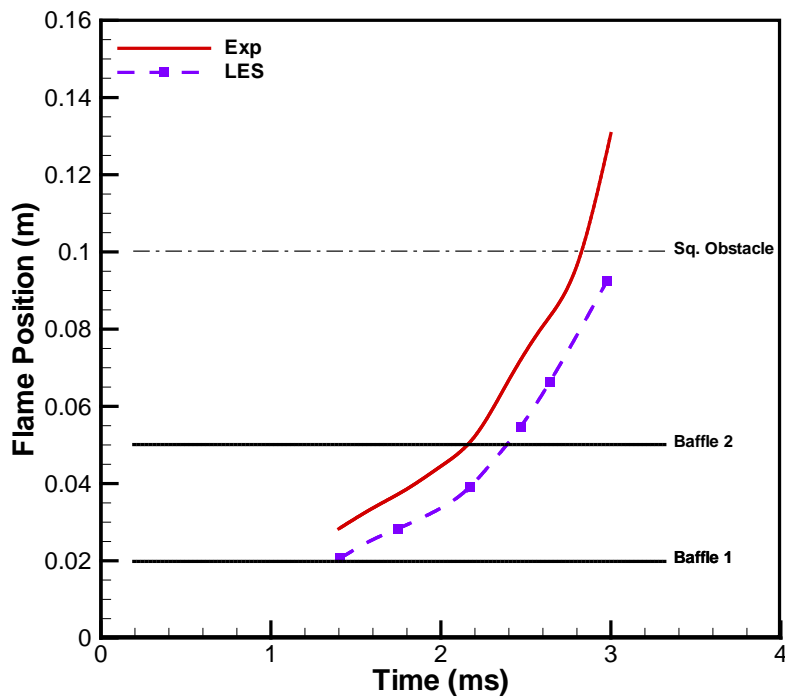


Figure 8.49 Flame position-time histories for hydrogen-air mixture ($\Phi = 0.8$) and configuration BB0S.

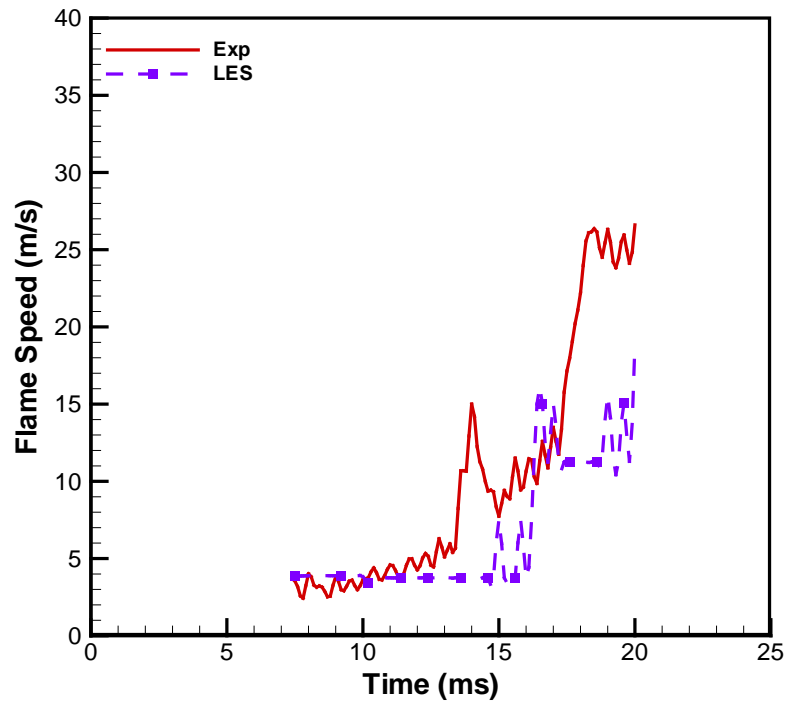


Figure 8.50 Flame speed-time histories for CNG-air mixture ($\Phi = 0.8$) and configuration BB0S.

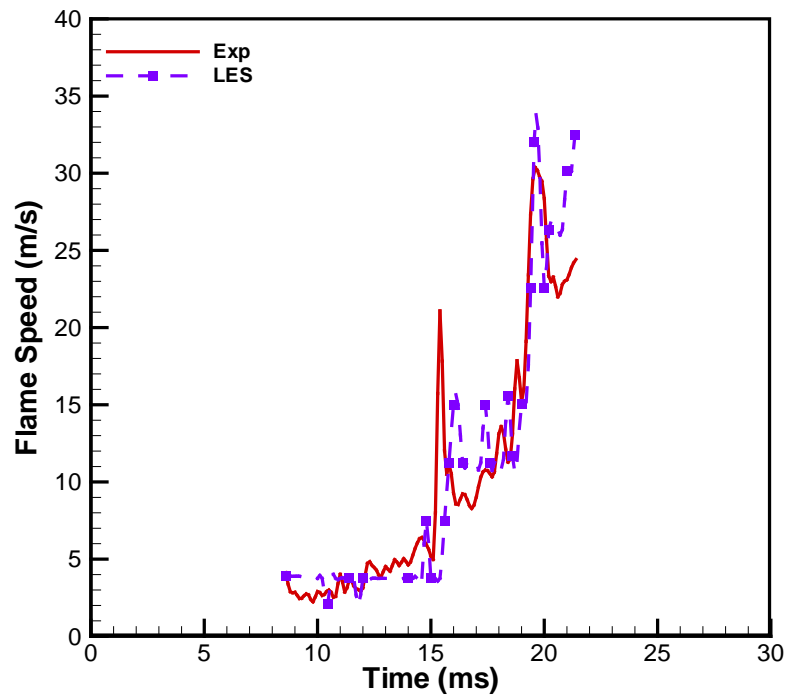


Figure 8.51 Flame speed-time histories for LPG-air mixture ($\Phi = 0.8$) and configuration BB0S.

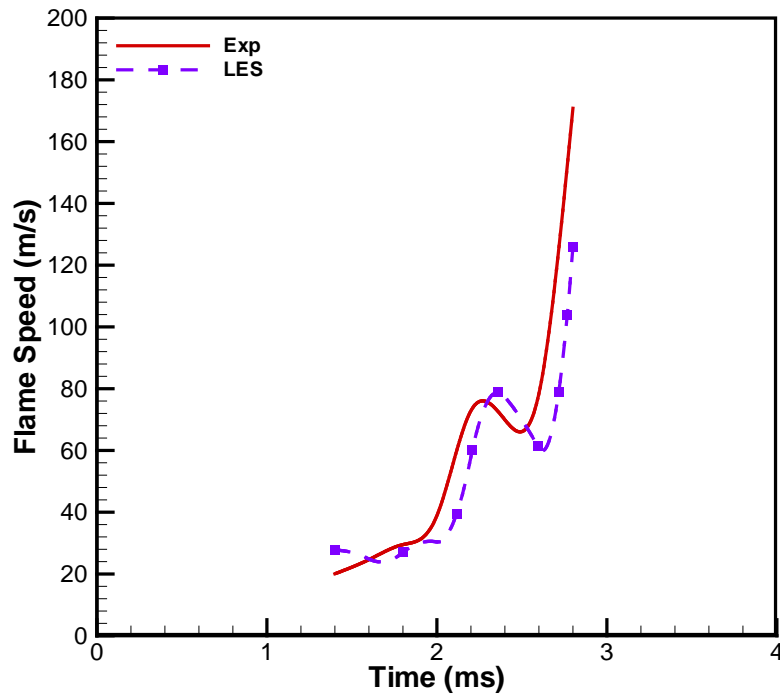


Figure 8.52 Flame speed-time histories for hydrogen-air mixture ($\Phi = 0.8$) and configuration BB0S.

In this configuration BB0S; the effect of adding one more baffle starts to appear in all the figures and for all the three fuels. This is due to the extensive flame-flow interactions which tend to increase the flame speed and generated overpressure. The overpressure, flame position and speed are greater in this case over the previous two cases (000S and BBBS). This shows the effect associated with the addition of baffles.

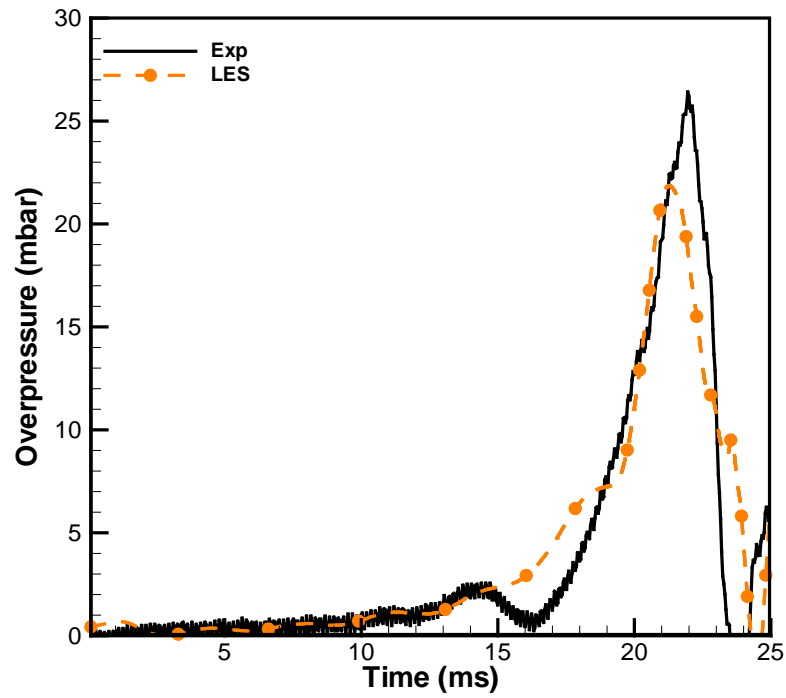


Figure 8.53 Overpressure-time histories for CNG-air mixture ($\Phi = 0.8$) and configuration BBBS.

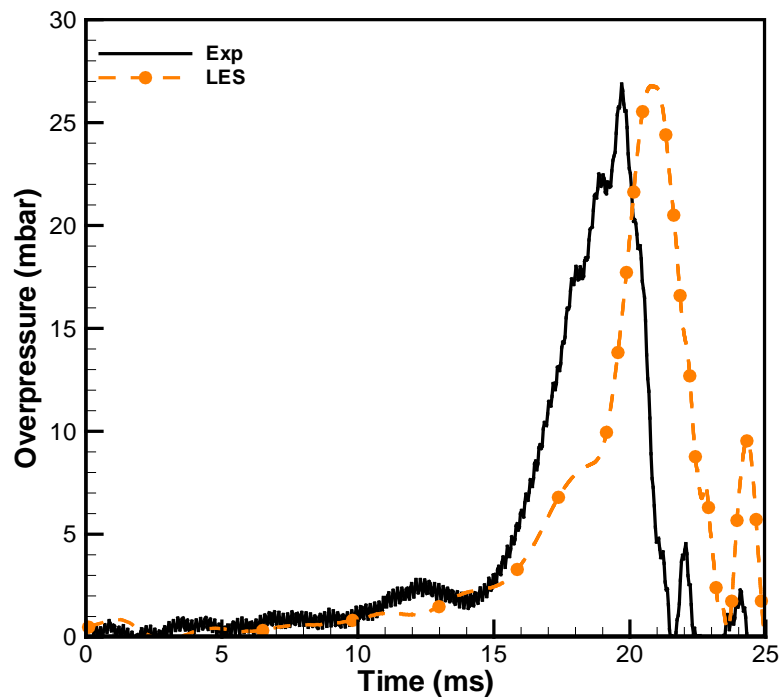


Figure 8.54 Overpressure-time histories for LPG-air mixture ($\Phi = 0.8$) and configuration BBBS.

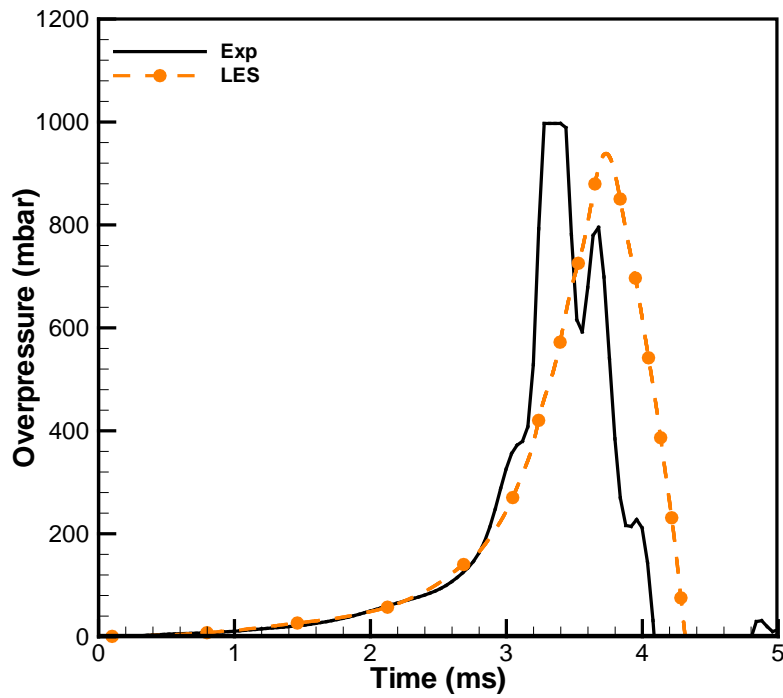


Figure 8.55 Overpressure-time histories for hydrogen-air mixture ($\Phi = 0.8$) and configuration BBBS.

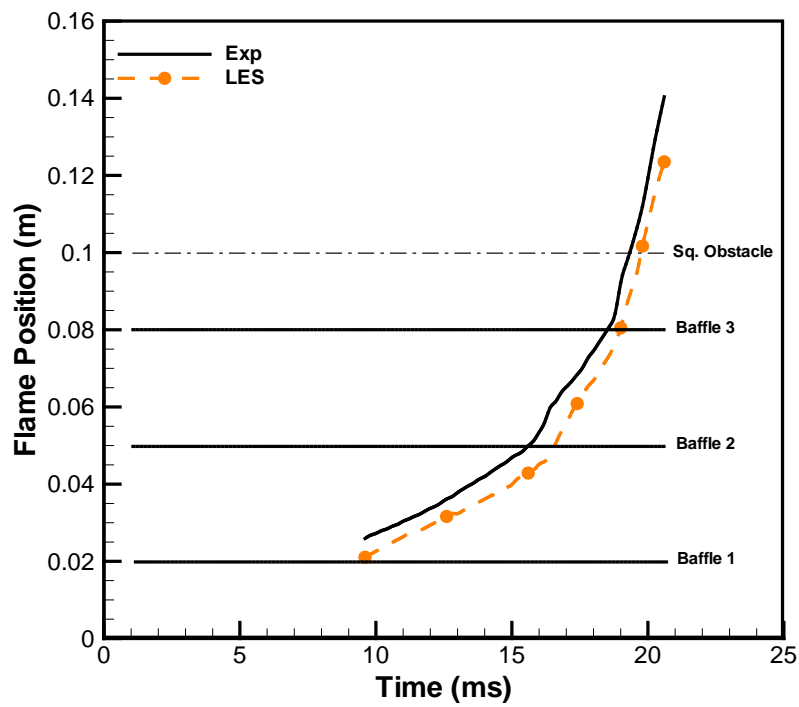


Figure 8.56 Flame position-time histories for CNG-air mixture ($\Phi = 0.8$) and configuration BBBS.

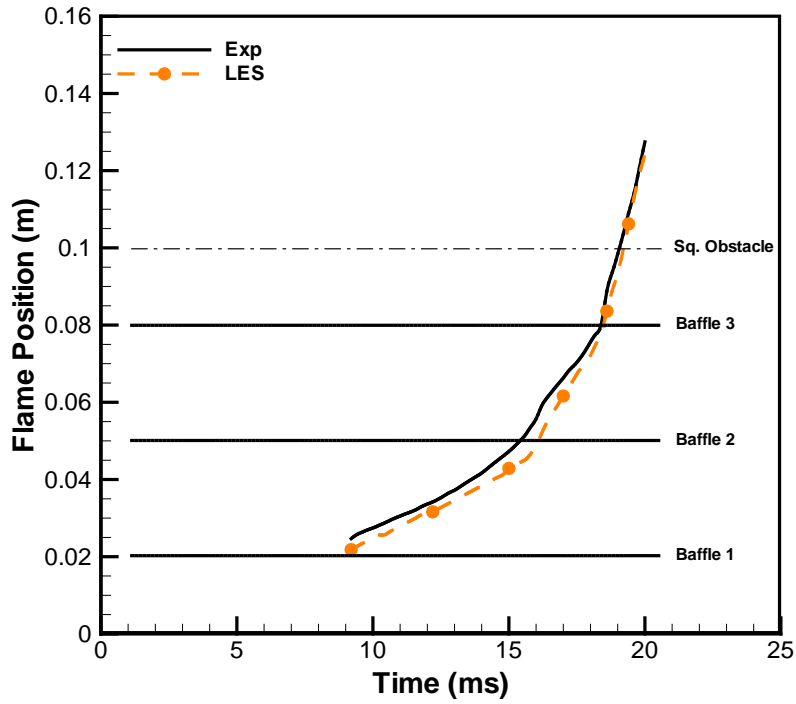


Figure 8.57 Flame position-time histories for LPG-air mixture ($\Phi = 0.8$) and configuration BBBS.

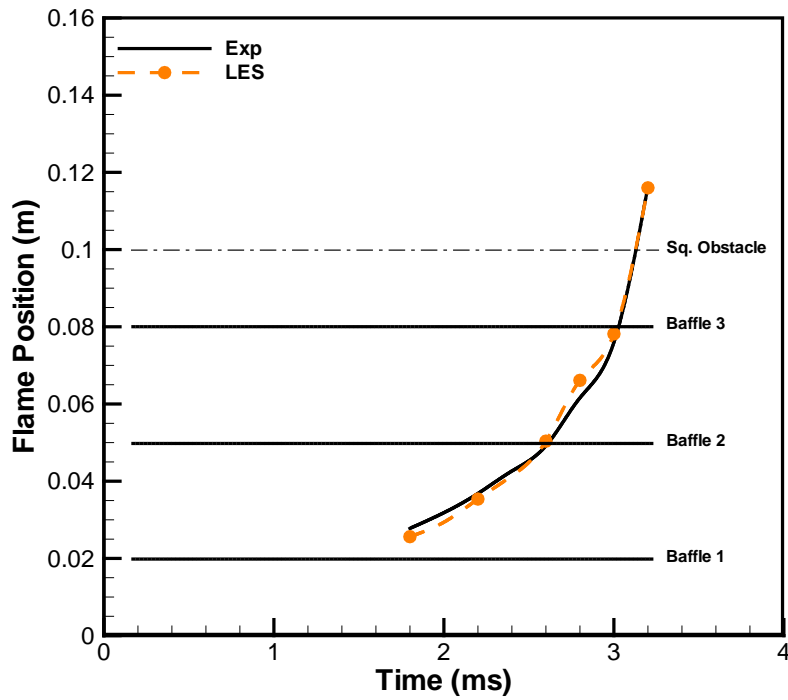


Figure 8.58 Flame position-time histories for hydrogen-air mixture ($\Phi = 0.8$) and configuration BBBS.

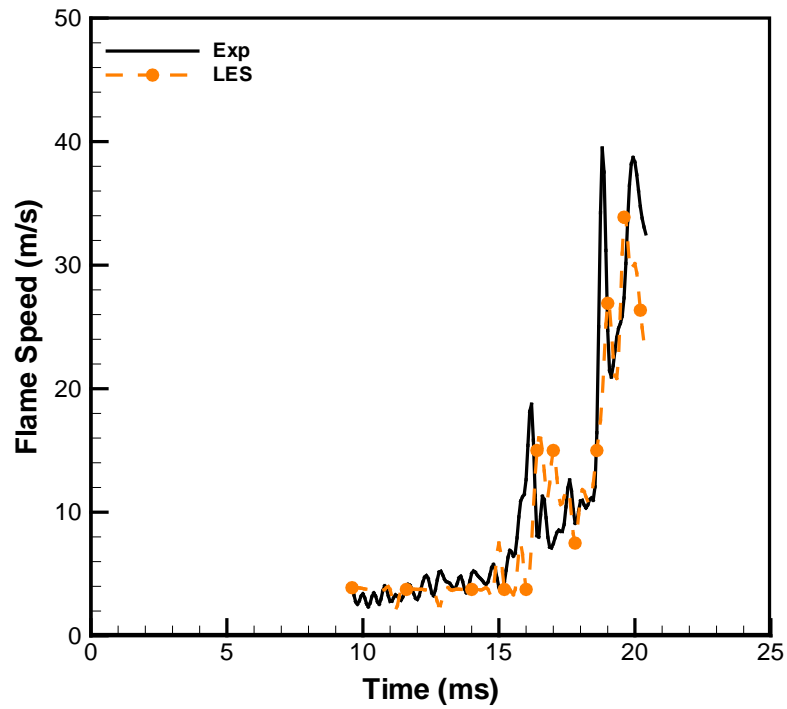


Figure 8.59 Flame speed-time histories for CNG-air mixture ($\Phi = 0.8$) and configuration BBBS.

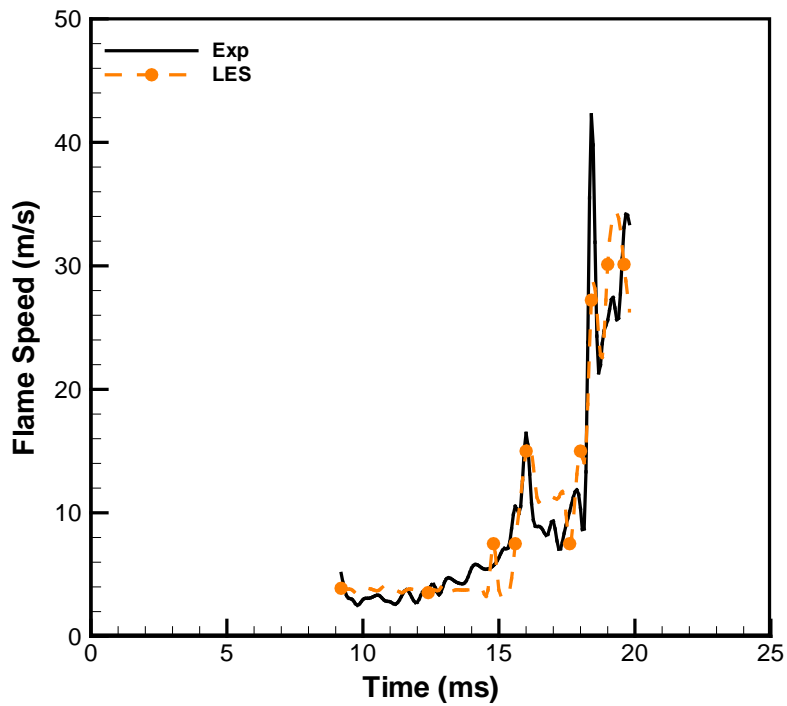


Figure 8.60 Flame speed-time histories for LPG-air mixture ($\Phi = 0.8$) and configuration BBBS.

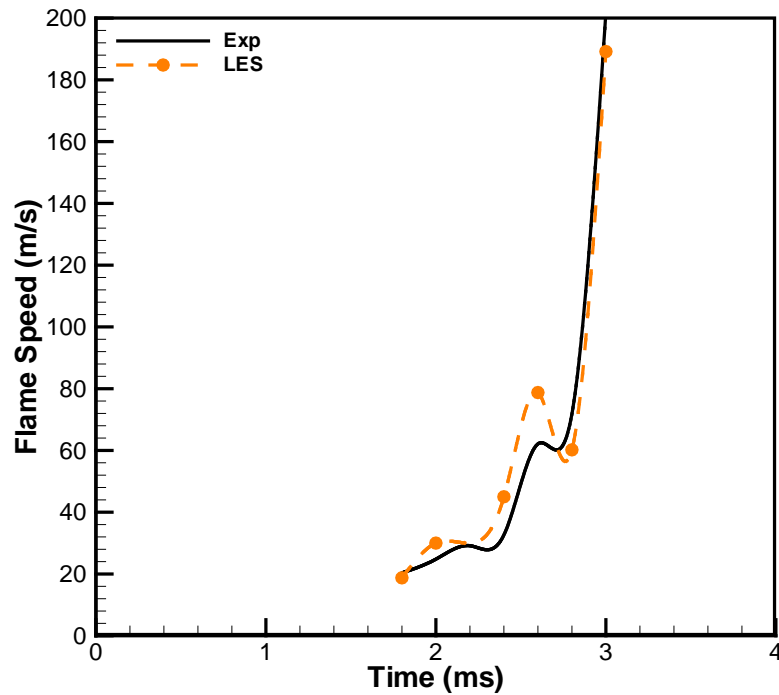


Figure 8.61 Flame speed-time histories for hydrogen-air mixture ($\Phi = 0.8$) and configuration BBBS.

Finally for case BBBS; the experimental and predicted results are higher than all the previous cases due to the addition of one more baffle. Also, a better agreement is observed for the three fuels when compare with the experimental data over all the previous configurations. Generally, the less number of oscillations can be seen in hydrogen when compare to CNG and LPG. This is because of fewer amounts of data extracted for hydrogen, where in reality intense oscillations could be observed due to the explosive nature of hydrogen.

8.7 Regimes of Combustion

Data from LES simulations for the three fuels are used to identify the regimes of combustion in the current chamber. The baffles and the obstacle are used to define the regions as shown in Figure 8.62 and described later. Tables 8.3-8.5 present summary of the extracted data from LES calculations. All controlling parameters in this analysis are evaluated at the leading edge of the flame front. It is worth mentioning here that this regime diagrams are not valid within the vicinity of wall (Gubba et al. (2009)). This is due to the heat loss to the wall which tends to local quenching.

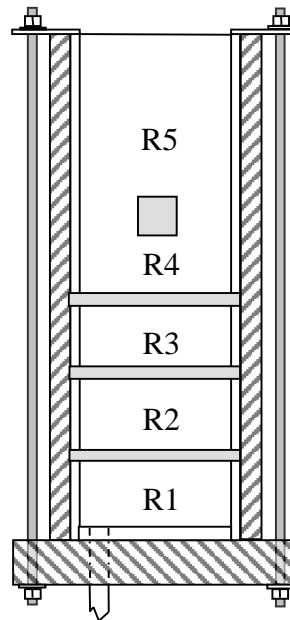


Figure 8.62 Regions used to identify regimes of combustion for the BBBS configurations

Region1 (R1): This region is extended to 20 mm from the ignition end of the chamber. In this region, the flame is quasi laminar and propagates at almost the laminar burning velocity until it starts to approach the first baffle plate. This is confirmed from the numerical image shown in Figure 8.63.

Region 2 (R2): This region extends from 20 to 50 mm (i.e. 1st to 2nd baffles) as shown in Figure 8.62, downstream of the ignition point. Within this region the flame just

emerged from the first baffle plate until hitting the second baffle and traps a small amount of unburnt fuel/air mixture as it evolves from the baffle plates. The flame is then stretched further as it moves from one baffle plate to the other. The entrapment of the flame around the baffles and its evolution through jetting can be noticed from numerical images shown in Figure 8.63.

Region 3 (R3): This region extends from 50 mm to 80 mm downstream from the ignition source (i.e. 2nd to 3rd baffles). As shown in numerical images in Figure 8.63, the flame continues to propagate from the second baffle until reaches the third baffle. The same conclusion from region 2 could be applied in this region but with increase in magnitude as the turbulence level increases as the flame propagates.

Region 4 (R4): This region extends from the third baffle until hitting the square obstacle (80 mm to 96 mm). As shown in numerical images in Figure 8.63, the turbulent flame departed from the third baffle and encounters square obstruction. This has led to have a highly distorted flame as it starts to interact with the solid square obstacle. A rapid rise of overpressure with a steep pressure gradient and a sharp increase in flame propagation speed is observed in this region and observed in the three fuels. This confirms the observations mentioned earlier.

Region 5 (R5): This region may be viewed as start of the blow-down region, where flame starts exiting from the chamber. Due to the presence of square obstacle in this region, a significant amount of unburnt fuel/air mixture is trapped around the obstacle as shown in Figure 8.63. The flame is stretched further and reconnected within the recirculation zone. The reconnected flame has an increase in the surface area, which eventually consumes more unburnt mixture. As a result, the pressure and flame speed are found to increase significantly.

This region covers the remainder of the chamber, where the blow-down phase continues and the flame propagates further to outside of the chamber. In this region flame gets reconnected completely as shown in Figure 8.63. The overpressure is found to increase and achieves its maximum for the three fuels further in this region due to the burning of the remaining fuel/air mixture trapped inside the chamber. Experimentally it is observed

that the maximum overpressure is reached to 26.4, 26.9 and 997.1 mbar for CNG, LPG and hydrogen respectively, by consuming the trapped mixture around the solid obstacles. The generated pressure oscillates while the remaining trapped mixture is burning in the chamber.

Relevant estimates from LES predictions at various instants of flame propagation within the above regions are calculated and presented in Tables 8.3-8.5 for the three fuel-air mixtures, CNG, LPG and hydrogen at equivalence ratio 0.8. Various regimes of combustion are calculated based on non-dimensional groups described below and then plotted on two standard combustion regime diagrams.

The Karlovitz number (Ka) represents the relation between chemical time scale to the time scale of straining (Cant and Mastorakos (2008)). However, significant importance is given while the flame is hitting and evolving from the obstacles. The Karlovitz number (Ka) here is calculated based on the filter width as stated by Pitsch and Duchamp de Lageneste (2002) as follows:

$$Ka_{\bar{\Delta}} = \left[\left(\frac{u'_{\Delta}}{u_L} \right)^3 \cdot \left(\frac{L_F}{\bar{\Delta}} \right) \right]^{\frac{1}{2}} \quad (8.1)$$

where $\bar{\Delta}$ is the filter width, u_L is the laminar flame velocity, and L_F is flame thickness. Also, to verify the Reynolds numbers based on the integral length scale L_I , it is calculated as:

$$Re_{L_I} = \frac{u'_{\Delta} L_I}{\nu} \quad (8.2)$$

The RMS of turbulent velocity, u'_{Δ} is obtained Poinot and Veynante (2012) at the leading edge of the flame front and is calculated from

$$u'_{\Delta} \approx \bar{\Delta} |\tilde{S}| = \bar{\Delta} (|2 \tilde{S}_{ij} \tilde{S}_{ij}|) \quad (8.3)$$

The integral length scale L_I is estimated to be 10% of the chamber width (Quillatre et al. (2013) and Masri et al. (2006)), i.e. L_I is taken to be 5 mm. The different scales and dimensionless numbers estimated at various time steps of the flame propagation are summarized in Tables 8.3-8.5. Results from the LES simulation are fitted in the two regimes of combustion diagrams to get adequate confirmation of the combustion model

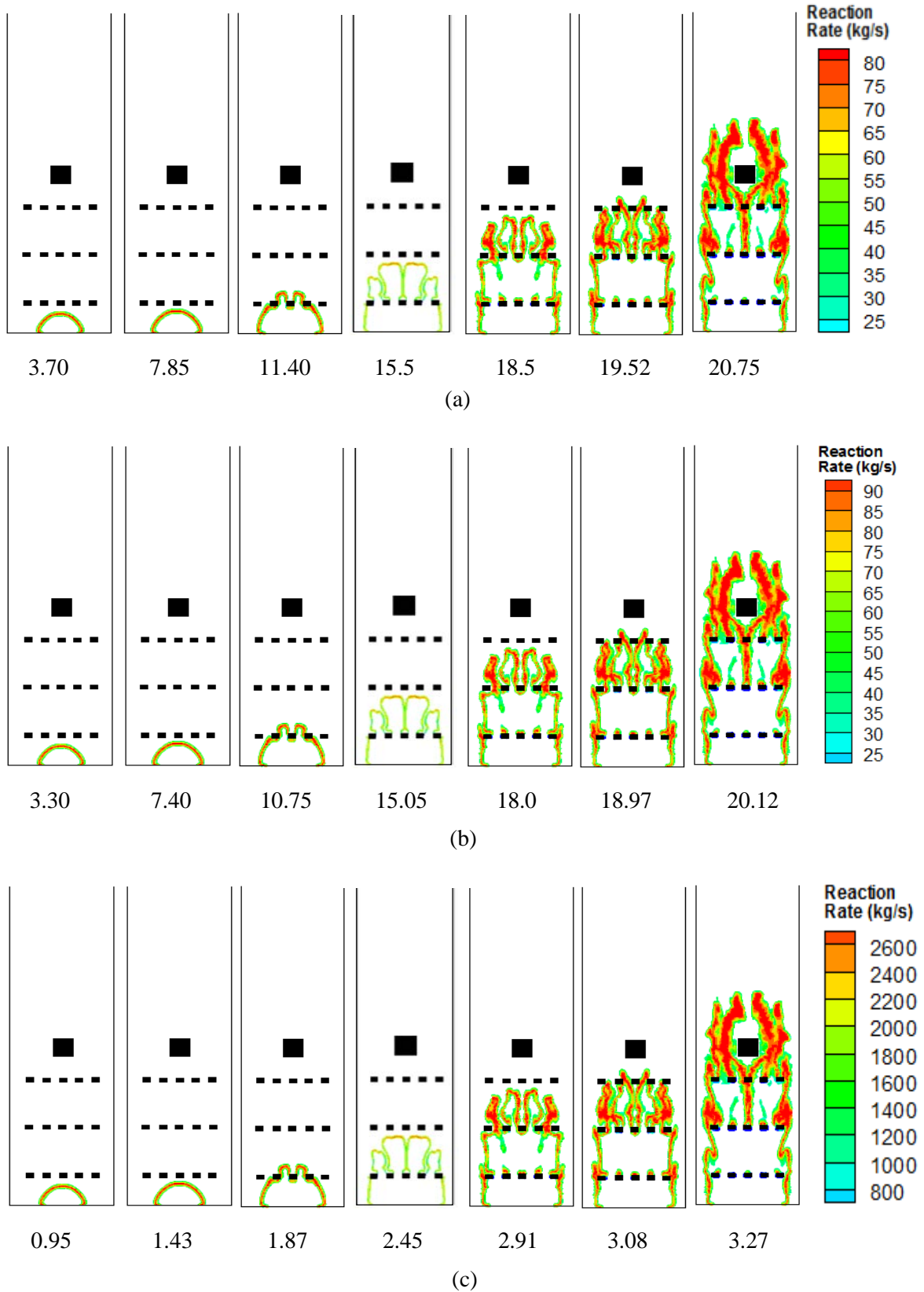


Figure 8.63 Flame structure derived from the LES calculations for the reaction rate contours of the three fuels, showing the flame propagation at different times after ignition with in the five regions. (a) CNG, (b) LPG and (c) Hydrogen. The time mentioned at the bottom of each chamber is in millisecond (ms).

used in the present calculations as shown in Figures 8.64 and 8.65. Both regime diagrams confirm that the leading edge of the flame is always within the thin reaction zone regardless its position and interactions with the solid obstacles.

A rapid increase in the Karlovitz and Reynolds numbers is observed as the flame starts approaching the first solid baffle plate. The same trend of Karlovitz and Reynolds numbers can be observed until the flame starts evolving from the first baffle plate. This feature continues as the flame propagates through the chamber. Also, it is very clear that the effect of first baffle is not that much on turbulence level and this is due to the nearby location to the ignition source and this agrees with the earlier observation. Moreover, a slowdown in the flame can be observed just before hitting the baffles as can be seen before hitting the second baffle and this confirms with AlHarbi et al. (2013) and Abdel-Raheem et al. (2015) observation.

From these tables it is clear that hydrogen generates the highest level of turbulence because of the high laminar burning velocity and mass diffusivity. Also, there is close similarity between CNG and LPG with priority for LPG in terms of Ka number and turbulence velocity.

The calculated results for the three fuels are plotted in the classical regime diagram for turbulent premixed flames of Peters (2004) as shown in Figure 8.64. Also, the LES regime diagram for turbulent premixed flames developed by Pitsch and Duchamp de Lageneste (2002) in terms of Karlovitz number (Ka) and the ratio of $L_F/\bar{\Delta}$ is used to plot the results as shown in Figure 8.65. The current analysis has successfully classified the regimes of the flame at different stages of its propagation while interacting with the solid obstacles.

Table 8.3 Different scale estimates from LES predictions for CNG with equivalence ratio $\Phi = 0.8$, case BBBS. These estimates are plotted in combustion regime diagrams in Figures 8.64 and 8.65.

	Time (ms)	Z (mm)	$\bar{\Delta}$ (mm)	u_L (m/s)	u' (m/s)	L_F (mm)	Re_{L_I}	u'/u_L	Ka	L_I/L_F	$\bar{\Delta}/L_F$
R1	3.70	10.29	1.51	0.28	0.58	0.47	145.8	2.08	1.68	10.64	3.21
	7.85	16.39	1.52	0.28	1.35	0.47	519.2	4.82	5.89	10.64	3.23
R2	11.40	27.13	1.51	0.28	1.63	0.47	1164.3	5.82	7.87	10.64	3.21
	15.5	42.88	1.51	0.28	1.50	0.47	1071.4	5.17	6.50	10.64	3.21
R3	18.5	72.13	1.51	0.28	3.05	0.47	2541.7	10.89	20.12	10.64	3.21
R4	19.52	92.66	1.51	0.28	2.88	0.47	2087.0	10.28	18.45	10.64	3.21
R5	20.75	127.3	1.51	0.28	4.64	0.47	3093.3	16.55	37.68	10.64	3.21

Table 8.4 Different scale estimates from LES predictions for LPG with equivalence ratio $\Phi = 0.8$, case BBBS. These estimates are plotted in combustion regime diagrams in Figures 8.64 and 8.65.

	Time (ms)	Z (mm)	$\bar{\Delta}$ (mm)	u_L (m/s)	u' (m/s)	L_F (mm)	Re_{L_I}	u'/u_L	Ka	L_I/L_F	$\bar{\Delta}/L_F$
R1	3.30	10.29	1.51	0.30	0.65	0.44	161.3	2.15	1.70	11.36	3.43
	7.40	16.39	1.52	0.30	1.49	0.44	573.1	4.97	5.95	11.36	3.45
R2	10.75	27.13	1.51	0.30	1.79	0.44	1278.6	5.97	7.89	11.36	3.43
	15.05	42.88	1.51	0.30	1.67	0.44	1192.9	5.39	6.68	11.36	3.43
R3	18.0	72.13	1.51	0.30	3.85	0.44	2961.5	12.83	24.90	11.36	3.43
R4	18.97	92.66	1.51	0.30	3.34	0.44	2385.7	11.13	20.06	11.36	3.43
R5	20.12	127.3	1.51	0.30	5.28	0.44	3520.0	17.58	39.83	11.36	3.43

Table 8.5 Different scale estimates from LES predictions for hydrogen with equivalence ratio $\Phi = 0.8$, case BBBS. These estimates are plotted in combustion regime diagrams in Figures 8.64 and 8.65.

	Time (ms)	Z (mm)	$\bar{\Delta}$ (mm)	u_L (m/s)	u' (m/s)	L_F (mm)	Re_{L_I}	u'/u_L	Ka	L_I/L_F	$\bar{\Delta}/L_F$
R1	0.95	10.29	1.51	1.65	4.37	0.299	750.09	2.63	1.90	16.72	5.05
	1.43	16.39	1.52	1.68	9.91	0.297	1011.2	5.90	6.31	16.83	5.12
R2	1.87	27.13	1.51	1.69	14.0	0.292	2333.3	8.27	10.47	17.12	5.17
	2.45	42.88	1.51	1.75	12.10	0.282	2086.2	6.90	7.84	17.73	5.35
R3	2.91	72.13	1.51	1.80	29.20	0.275	5959.2	16.22	27.92	18.18	5.49
R4	3.08	92.66	1.51	1.87	27.1	0.269	5037.2	14.49	23.17	18.59	5.61
R5	3.27	127.3	1.51	1.93	44.94	0.249	8642.3	23.28	45.75	20.08	6.06

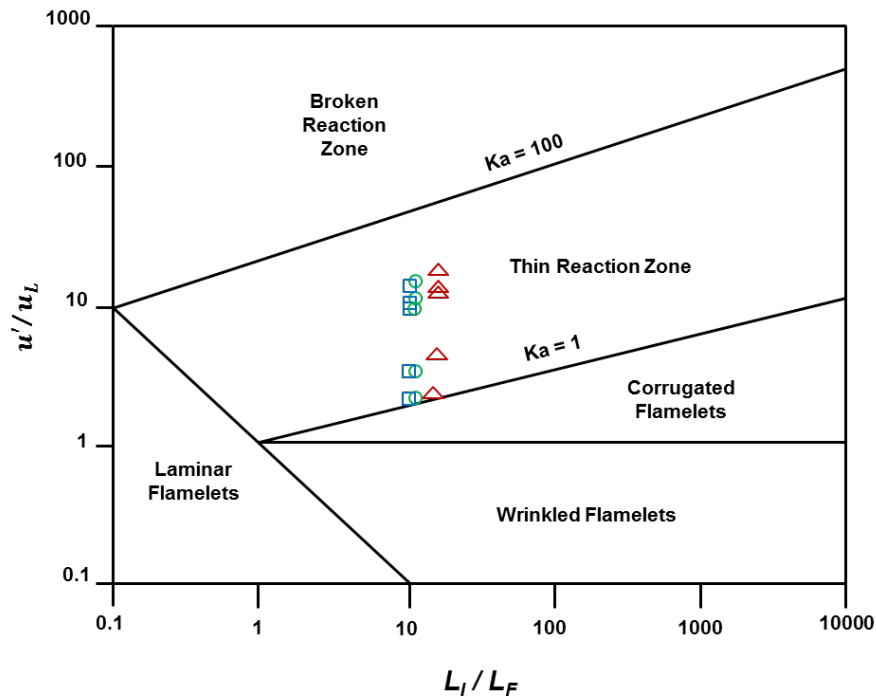


Figure 8.64 Estimates from the three fuels in Tables 8.3-8.5 are fitted into the regimes of turbulent premixed combustion diagram reported by Peters (2004). CNG (\square), LPG (\circ) and Hydrogen (Δ).

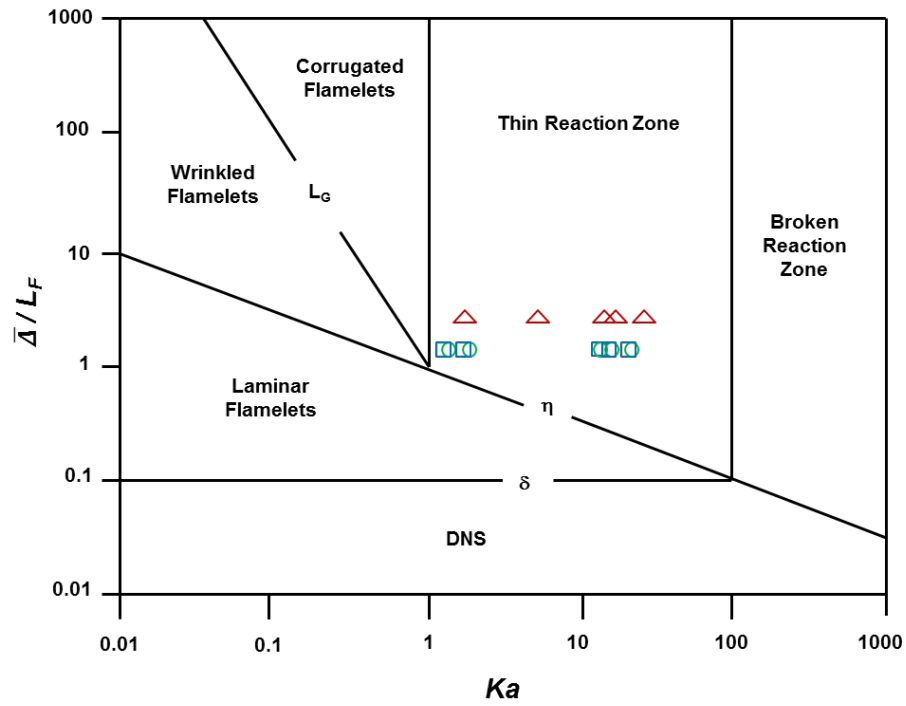


Figure 8.65 Estimates for the three fuels presented in Tables 8.3-8.5 are fitted into the regimes of LES turbulent premixed combustion diagram reported by Pitsch and Duchamp de Lageneste (2002). CNG (\square), LPG (O) and Hydrogen (Δ).

Chapter 9

Conclusions and Recommendations for Future Work

The flame surface density (FSD) models, based on the well-known laminar flamelet concept are well accepted choice in predicting turbulent premixed flames. Although, the application of FSD models in LES is recent and much similar to RANS models. These models are gaining the acceptance in industry to model a variety of turbulent premixed combustion scenarios in complex combustion chambers. However, many issues are exist such as their ability in calculating accurate flame surface density and applicability to a range of combustion regimes need to be clarified. Inspired by the demand for eco-friendly combustion systems and fuel scarcity, advancements in the predictive capability of turbulent premixed combustion are considered to be essential, which enhances the fundamental understanding of the entire combustion process, are the main motivation for the current research.

9.1 The work presented in this thesis has achieved the following objectives:

- Gain confidence in using LES technique for turbulent premixed propagating flames in laboratory scale combustion chamber with solid obstacles using the DFSD model. LES simulations have been carried out employing various grid resolutions to achieve grid-independent solution. The laboratory scale combustion chamber has been divided into five regions of interest and a detailed analysis was carried out to verify the combustion regimes of the turbulent flame inside the chamber.
- A method proposed to account for the effect of no-unity Lewis number by using the actual values for the Schmidt and Prandtl numbers. The LES simulations carried out using above model were identified to improve predictions. For LPG and hydrogen a change in the predicted overpressure is observed compared with the unity Lewis number case. While, for the CNG almost no change in the results due to the small difference in the value of actual Lewis number and the unity Lewis number assumption.

- LES simulations using the developed DFSD model have been performed for a series of simple to complex flow configurations having different number and position of baffles in a laboratory combustion chamber. LES simulations were validated against experimental data to establish the DFSD model for turbulent premixed flames. For these configurations, generated overpressure, flame position and speed were generated and compared to available experimental data. LES predictions using DFSD model showed excellent agreement with experimental measurements for various configurations. However, present research has identified slight under-prediction/over-prediction of peak overpressure, which can be enhanced by accounting for proper modelling of laminar phase.
- This investigation demonstrates the comparison of LES predictions with experimental measurements and the effects of placing multiple obstacles at various locations in the path of the turbulent propagating premixed flames.

9.2 Conclusions

- The grid-independence tests conducted using four different grid resolutions have concluded that the employed grid is independent of the filter width and grid resolution.
- The applicability of the DFSD model using grid-independent results for turbulent premixed propagating flames was examined by validating the generated pressure and other flame characteristics, such as flame position and speed against experimental data. This study concludes that the predictions using DFSD model provide reasonably good results.
- The effect of Lewis number was implemented with the DFSD model. It was found that LES predictions were slightly improved in predicting overpressure, flame position and speed.
- The agreement obtained confirms the applicability of the DFSD model to predict the dynamics of turbulent premixed flames or explosions in any flow configurations in as engineering applications or chemical/fuel process/storage industries.

- It is identified that the overpressure generated in any individual configuration, is directly proportional to the number of baffles plates used in this study. The flame position and speed are clearly dependent on the number of obstacle used and their blockage ratio. Also, higher pressure gradient develops along the length of the chamber with more number of baffles or obstacles.
- Flame-flow interactions occur as the flame propagates past the baffle plate and the solid obstructions leading to the formation of disconnected flame islands with higher burning rates. The flame progressively accelerates as it travels through the various stages of the chamber. However there are no evidences to prove the presence of flame quenching due to elongation and stretching in the present study. This may be due to the small volume of the chamber used in this study.
- Large separation between the solid baffle plates allows sufficient residence time for turbulence decay causing flow re-laminarisation and hence lowering overpressures.
- It is observed that the trapped unburnt mixtures up and down stream of obstacles are consumed once the main flame leaves the chamber leading to subsequent oscillations in pressure.
- The flame stretch extracted from both the experimental and numerical images shows that hydrogen has the highest stretch values over CNG and LPG. This is expected due to the high generated turbulence levels associated with hydrogen flame deflagration and also the thermo-physical properties of hydrogen.
- The regime of combustion identified for the three fuels in the present combustion chamber at various times after ignition at the leading edge of the flame is found to lie within the thin reaction zone, regardless of the classified regions and their interactions with obstacles. This finding supports the use of the laminar flamelet modelling concept that has been in use for the modelling of turbulent premixed flames in practical applications.

9.3 Present Contributions

- A good level of confidence has been established in using large eddy simulation technique for transient turbulent premixed propagating flames in various flow configurations by parameterising various numerical factors.
- Enhancement in the sophistication of sub-grid scale combustion modelling capability has been achieved in the in-house LES code through incorporation of Lewis number effect within the model.
- Influence of ignition radius on LES predictions has been studied using various ignition radii, shape and location. The use of ignition modelling in the present LES code has been substantiated by this analysis in order to achieve the quasi-laminar phase of the early stage of flame propagation.
- A systematic study has been conducted to identify the influence of the number of baffles and their respective positions from ignition bottom.
- The extracted flame stretch for the three fuels has shown that hydrogen has the highest stretch values due to the highest generated turbulence levels. LPG and CNG have close values due to the close properties of both fuels.
- The combustion regime for the three fuels has been calculated and identified that hydrogen has the highest turbulence levels generation among the three fuels. LPG and CNG have close values with priority to LPG.

9.4 Recommendations for Future Work

- The DSD model shows good overall predictions. However, it could be further improved by identifying or developing more rigorous model for the flame stretch.
- The over-prediction/under-prediction of overpressure with DFSD model could possibly further improved by employing a proper ignition model to predict correctly the quasi-laminar phase.

- The current in-house LES code can be further improved by the implementation of simplified chemistry mechanisms or detailed chemistry through look-up table method. As these concepts could enhance the ability of the current model to predict the effect of Lewis number on the results but with a considerable amount of complexity.
- Parallelisation of the LES in-house code is highly recommended, which can utilise the available computational resources more efficiently and could easily be extendable to predict more complex combustion scenarios.

Appendix A

MATLAB Program to Correct the Time Shift in Experimental Data

```
% Locating Maximum Pressure for each curve
Clear AllNewData AveragePeakTime AveragePosition Axis L Max NewData
NewTime PeakTime Positions Time W i j
[L,W]=size(data);
Time=data(:,1);
Pressure=data(:,2:W);
[Max,Positions]=max(Pressure);

% Finding the average
for i=1:length(Positions)
    PeakTime(i)=Time(Positions(i));
end
AveragePeakTime=mean(PeakTime);
AveragePosition=round(mean(Positions))+1;
Axis=AveragePosition;

% Fixing the shift for the pressure
[L,W]=size(Pressure);
for j=1:length(Positions)
    if Positions(j)>=Axis
        for i=1:L-(Positions(j)-Axis)
            NewData(i,j)=Pressure(i+(Positions(j)-Axis),j);
        end
    end
    if Positions(j)<Axis
        for i=1:L
            NewData(i+(Axis-Positions(j)),j)=Pressure(i,j);
        end
    end
end

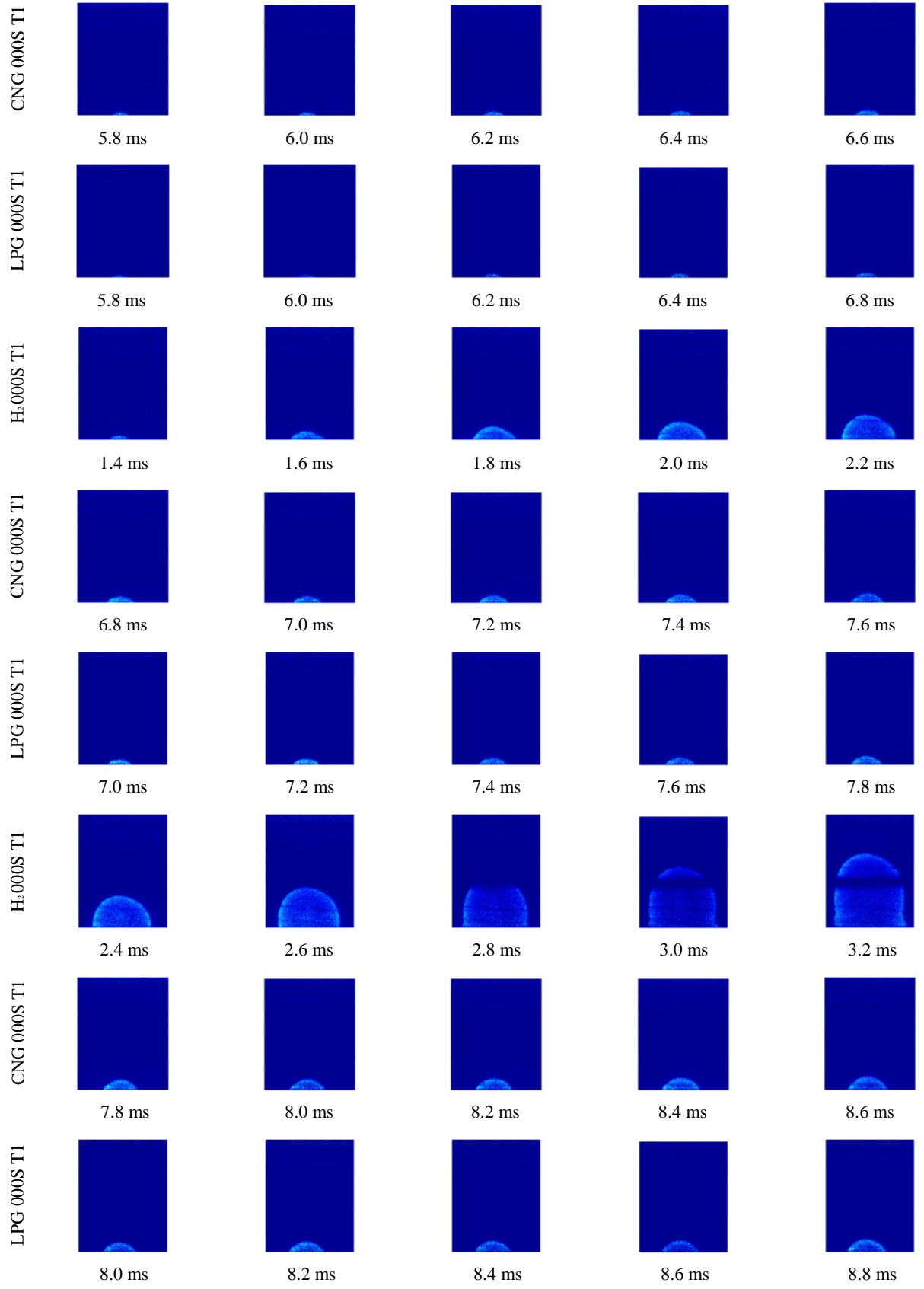
% Adjusting the time to the equivalent pressure
NewTime=zeros(length(NewData),1);
NewTime(Axis)=AveragePeakTime;
for i=1:Axis-1
```

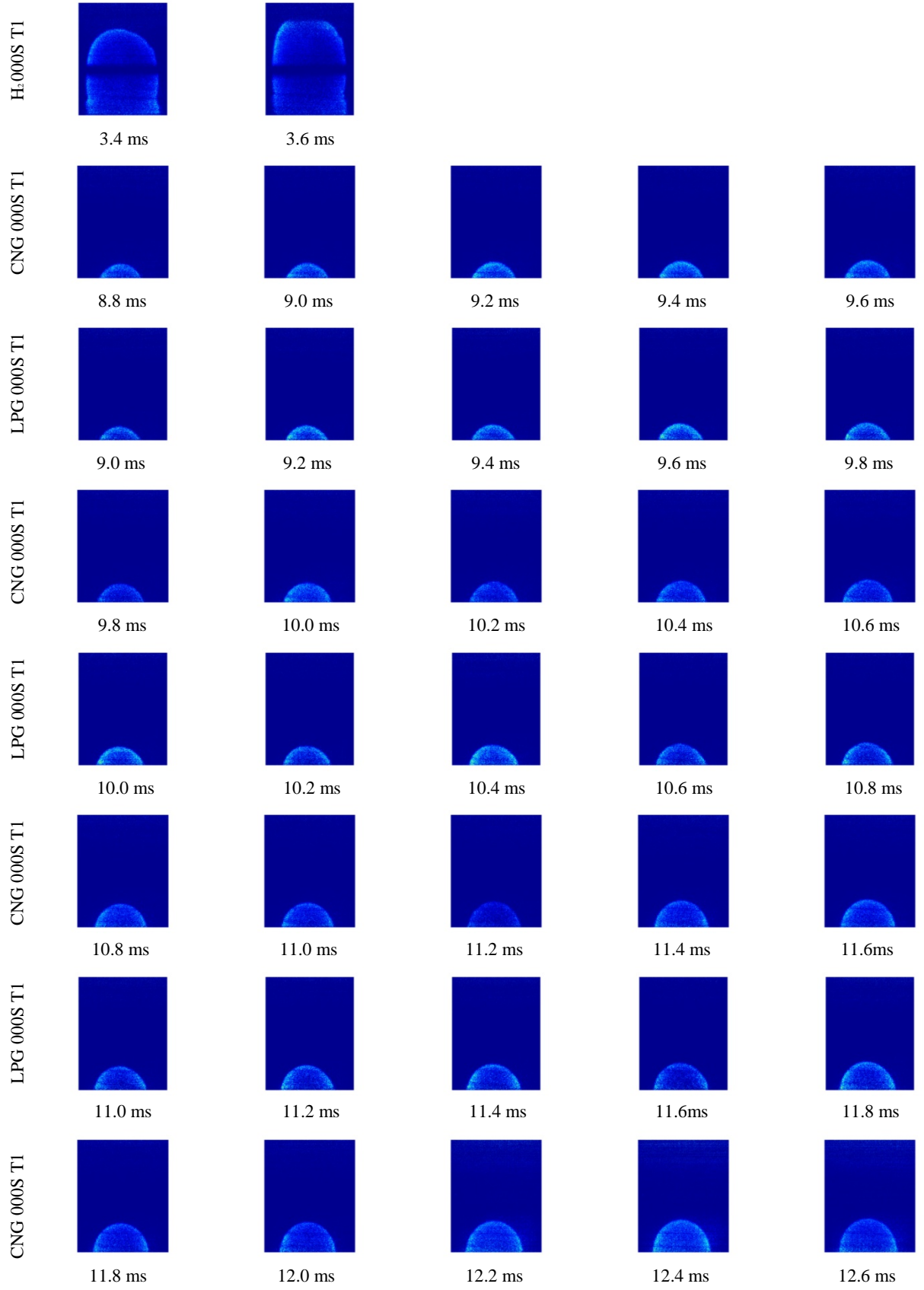
```
    NewTime(i)=NewTime(Axis)-(Axis-i)*(Time(2)-Time(1));  
end  
for i=Axis+1:length(NewData)  
    NewTime(i)=NewTime(Axis)-(Axis-i)*(Time(2)-Time(1));  
end  
  
% Writing the data in the new file  
AllNewData=[NewTime,NewData];  
dlmwrite('NewData.txt',AllNewData,'newline','PC','precision','%8d');
```

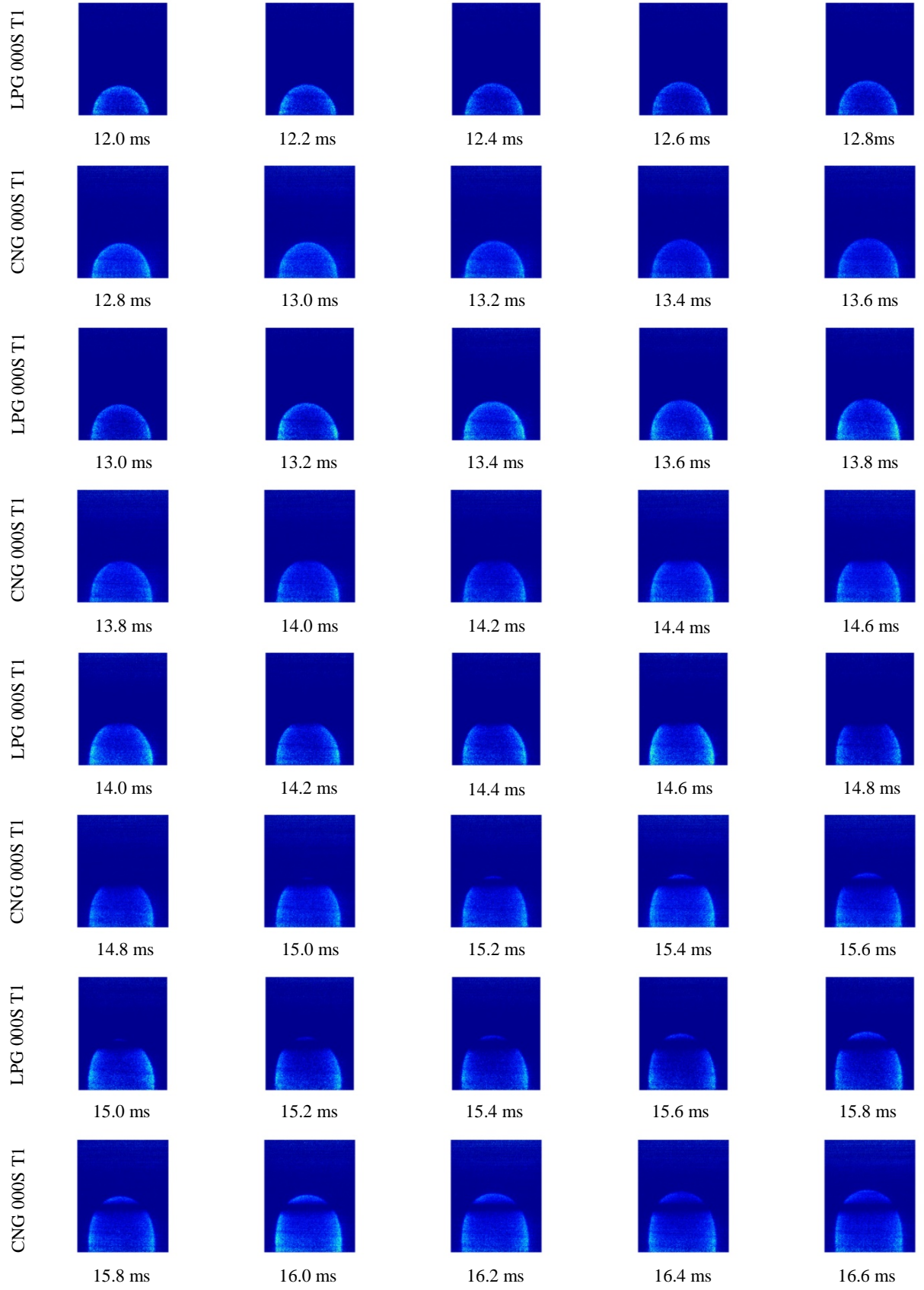

Appendix B

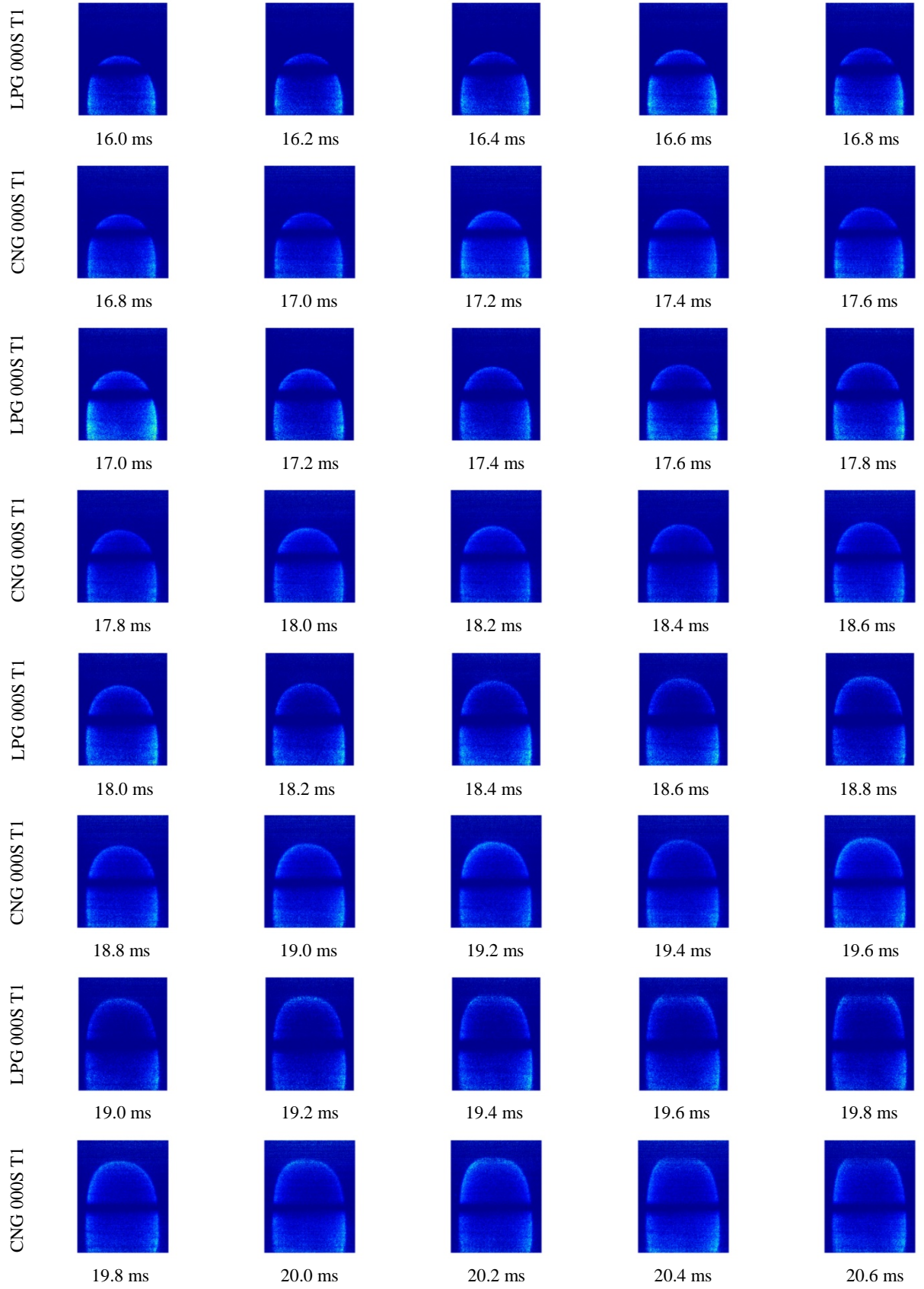
High Speed Imaging of OH-LIF

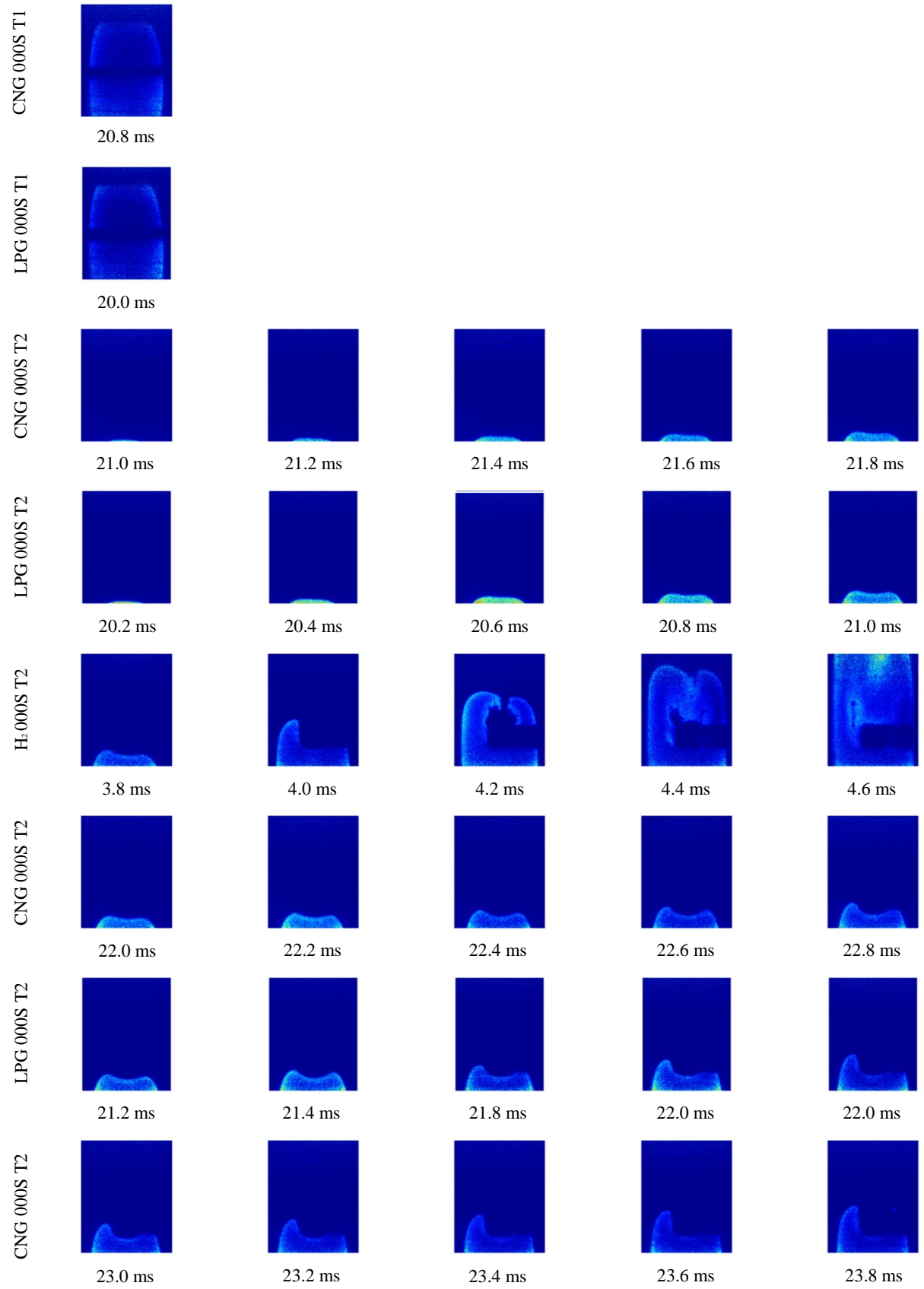
The OH-LIF imaging system was used to record the flame front images (AlHarbi (2013)) for the configurations listed in Table 7.3. The two image tiers mentioned in chapter 6 were used to cover the viewable length of the chamber. The time step used throughout the experiment was 0.2 ms. The images for CNG, LPG, and hydrogen using configurations 000S and BBBS are presented below. The images on Figure B.1 are arranged in such a way that a comparison between the three fuels is clear. The colour scale used here is arbitrary where red corresponds to peak OH and dark blue to zero.

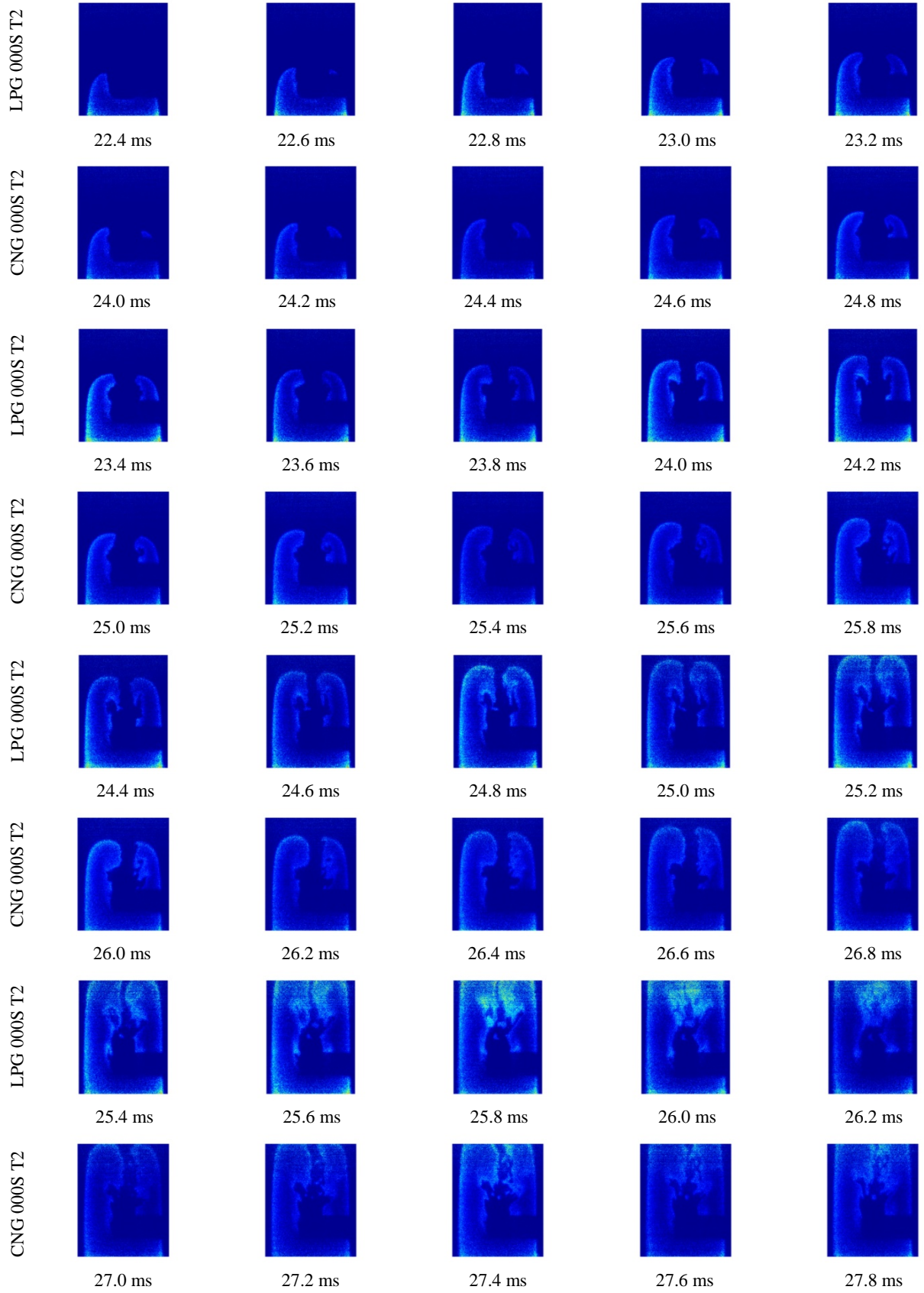


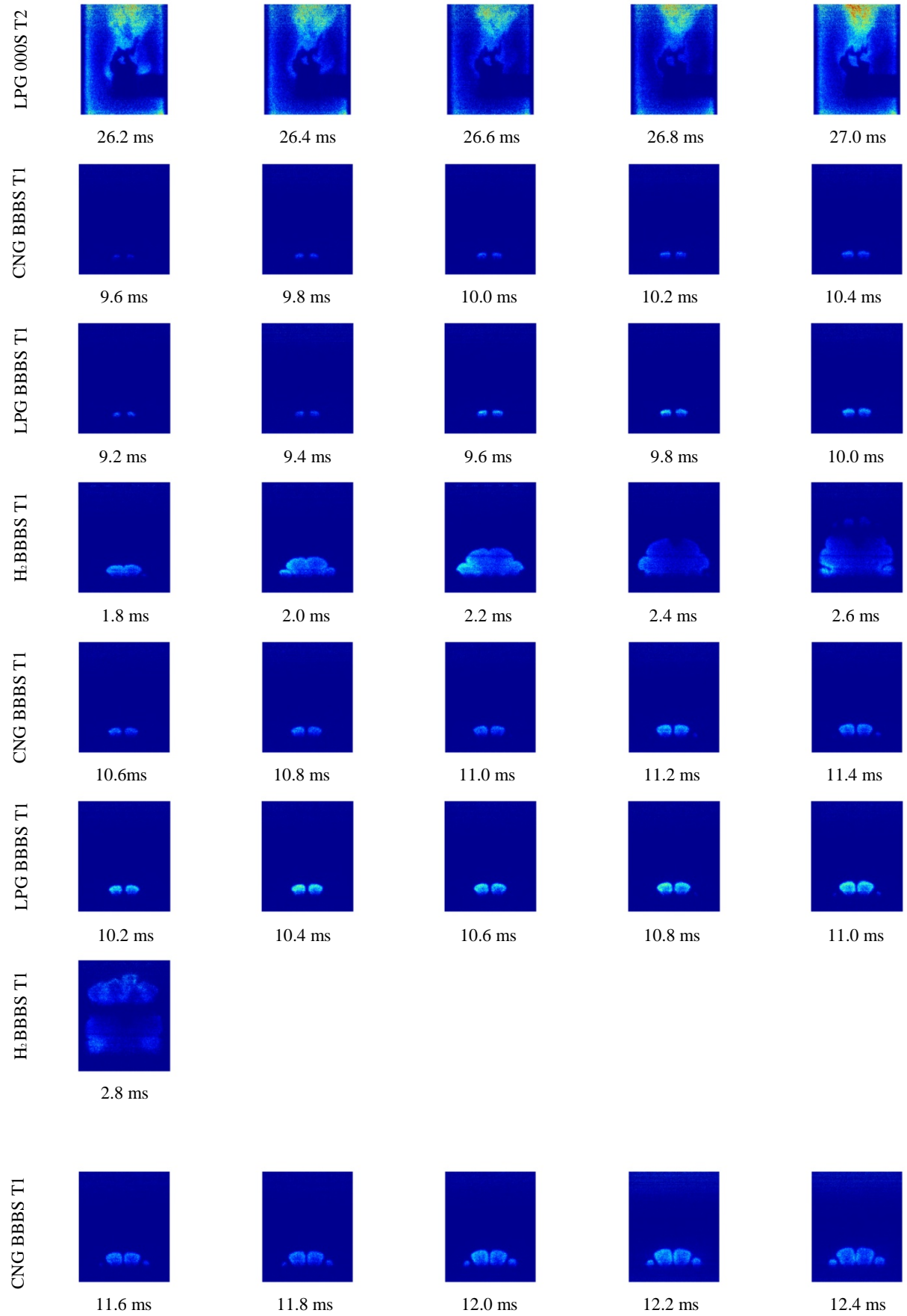


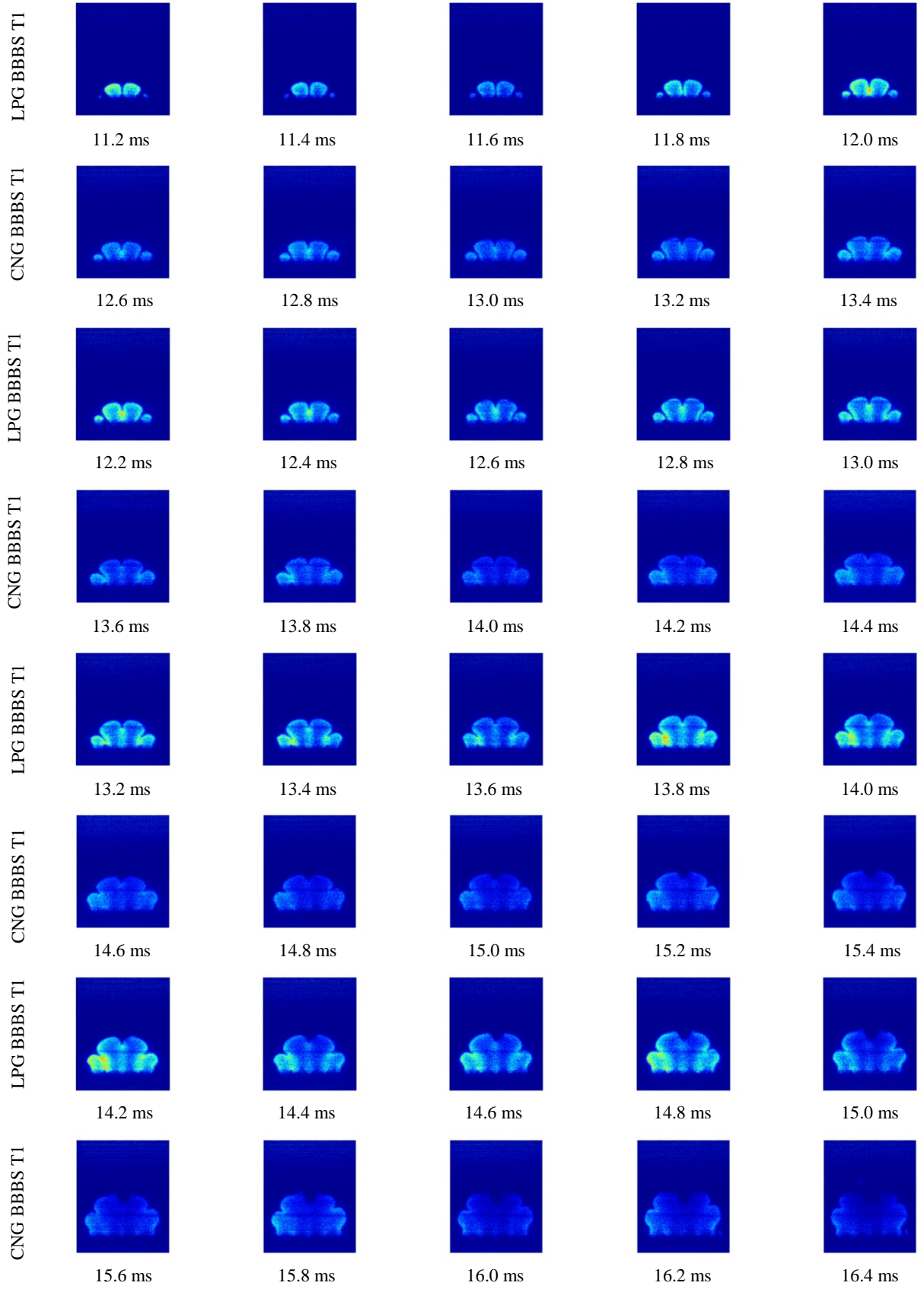


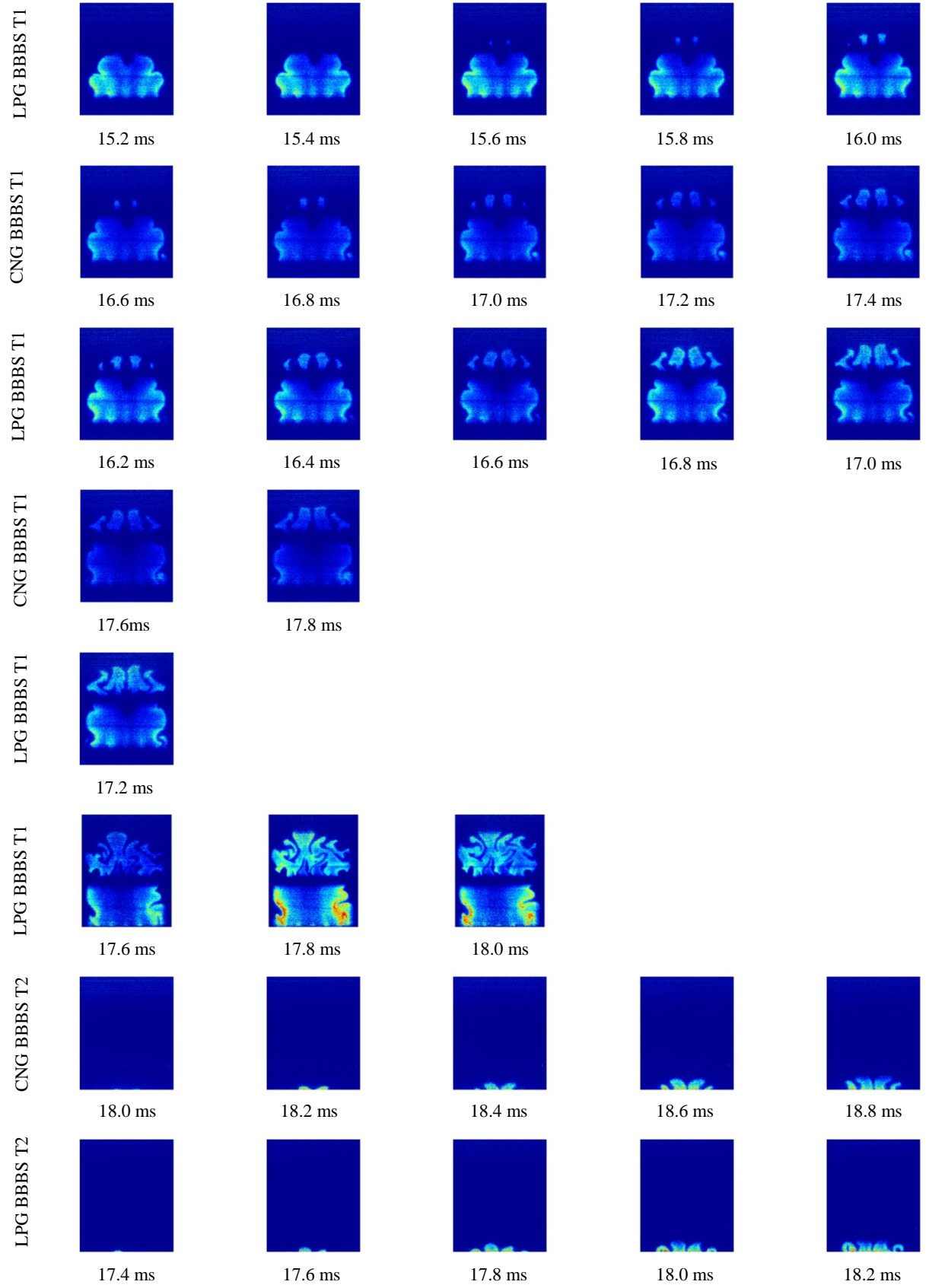












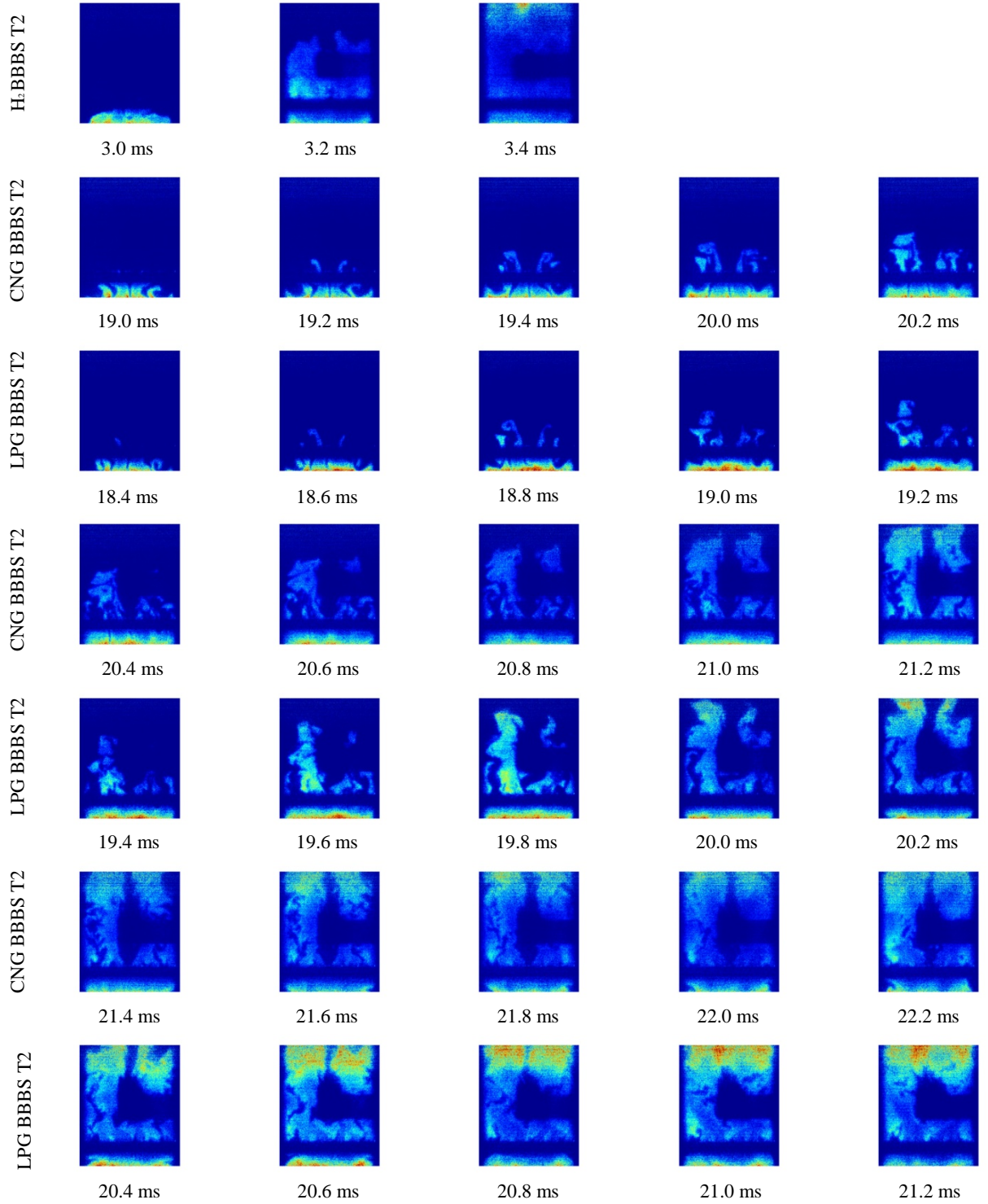


Figure B.1 Time sequences for the three fuels (CNG, LPG and Hydrogen) with time step $t = 0.2$ ms through configurations 000S and BBBS at equivalence ratio $\Phi = 0.8$ (AlHarbi (2013)).

References

- Abdel-Gayed, R. G., Bradley, D. and Lawes, M. (1987). Turbulent burning velocities: A general correlation in terms of straining rates. *Proceedings of the Royal Society of London. Series A, Mathematical and Physical Sciences*, 414, 389-413.
- Abdel-Raheem, M. A., Ibrahim, S. S., Malalasekera, W. and Masri, A. R. (2015). Large Eddy simulation of hydrogen–air premixed flames in a small scale combustion chamber. *International Journal of Hydrogen Energy*, 40 (7), 3098-3109.
- Abu-Gharbieh, R., Hamarneh, G., Gustavsson, T. and Kaminski, C. (2001). Flame front tracking by laser induced fluorescence spectroscopy and advanced image analysis. *Opt. Express*, 8 (5), 278-287.
- Abu-Orf, G. M. and Cant, R. S. (2000). A turbulent reaction rate model for premixed turbulent combustion in spark-ignition engines. *Combustion and Flame*, 122 (3), 233-252.
- Al-Shahrany, A. S., Bradley, D., Lawes, M., Liu, K. and Woolley, R. (2006). Darrieus-landau and thermo-acoustic instabilities in closed vessel explosions. *Combustion Science and Technology*, 178 (10-11), 1771-1802.
- AlHarbi, A. (2013). *Turbulent Premixed Flames Propagating Past Repeated Obstacles*. PhD Thesis, The University of Sydney, Australia.
- AlHarbi, A., Juddoo, M. and Masri, A. R. (2012). High-speed LIF-OH imaging in premixed flames propagating past repeated solid obstacles. *In 18th Australasian Fluid Mechanics Conference*.
- AlHarbi, A., Masri, A. R. and Ibrahim, S. S. (2013). Turbulent premixed flames of CNG, LPG, and H₂ propagating past repeated obstacles. *8th Mediterranean Combustion Symposium, Izmir, Turkey*.
- AlHarbi, A., Masri, A. R. and Ibrahim, S. S. (2014). Turbulent premixed flames of CNG, LPG, and H₂ propagating past repeated obstacles. *Experimental Thermal and Fluid Science*, 56 (0), 2-8.
- Aluri, N. K., Reddy Muppala, S. P. and Dinkelacker, F. (2006). Substantiating a fractal-based algebraic reaction closure of premixed turbulent combustion for high pressure and the Lewis number effects. *Combustion and Flame*, 145 (4), 663-674.
- Angelberger, C., Veynante, D., Egolfopoulos, F. and Poinso, T. (1998). Large eddy simulations of combustion instabilities in premixed flames. *Proceedings of the Summer Program, Center for Turbulence Research, Stanford University*. 61-82.
- Astbury, G. R. (2008). A review of the properties and hazards of some alternative fuels. *Process Safety and Environmental Protection*, 86 (6), 397-414.

- Aung, K. T., Hassan, M. I. and Faeth, G. M. (1997). Flame stretch interactions of laminar premixed hydrogen/air flames at normal temperature and pressure. *Combustion and Flame*, 109 (1-2), 1-24.
- Auzillon, P., Vicquelina, R., Gicquel, O., Darabihaa, N., Veynantea, D. and Fiorinaa, B. (2010). A filtered tabulated chemistry model for Large Eddy Simulation of reactive flows. *48th AIAA Aerospace Sciences Meeting Including the New Horizons Forum and Aerospace*. France.
- Babkin, V. 2003. *RE: Institute of Chemical Kinetics and Combustion, Siberian Branch, Russian Academy of Science, Novosibirsk, Russia*
- Bardina, J., Ferziger, J. and Reynolds, W. (1980). Improved subgrid scales models for large eddy simulations. *13th Fluid and Plasma Dynamics Conference*
- Bell, J. B., Colella, P. and Glaz, H. M. (1989). A second-order projection method for the incompressible navier-stokes equations. *Journal of Computational Physics*, 85 (2), 257-283.
- Bilger, R. W. (2004). Marker fields for turbulent premixed combustion. *Combustion and Flame*, 138 (1-2), 188-194.
- Bilger, R. W., Kim, S. H. and Martin, S. M. (2004). Direct numerical simulation of turbulent premixed flames with a marker field and application to RANS and LES. *Proceedings of the 2004 Summer Program* Center for Turbulence Research Stanford University.
- Bjerketvedt, D., Bakke, J. R. and Van Wingerden, K. (1997). Gas Explosion Handbook. *Journal of Hazardous Materials*, 52 (1), 1-150
- Bjorkhaug, M. (1988). Investigation of the behaviour of louver panels subjected to gas explosions. *CMI, 25110-1*. Bergen, Norway: Chr. Michelsen Institute.
- Boger, M. and Veynante, D. (2000). Large eddy simulation of a turbulent premixed v-shaped flame. *Advances in Turbulence VIII*, 449-452.
- Boger, M., Veynante, D., Boughanem, H. and Trouvé, A. (1998). Direct numerical simulation analysis of flame surface density concept for large eddy simulation of turbulent premixed combustion. *Symposium (International) on Combustion*, 27 (1), 917-925.
- Boughanem, H. and Trouvé, A. (1998). The domain of influence of flame instabilities in turbulent premixed combustion. *Symposium (International) on Combustion*, 27 (1), 971-978.
- Boussinesq, J. (1877). Essai sur la theorie des eaux courantes. *Mem. Acad. Sci. Inst. Fr*, 23 (1), 252-260.
- Bradley, D. (1992). How fast can we burn? *Proceedings of the Combustion Institute*, 24 (1), 247-262.

- Bradley, D., Haq, M. Z., Hicks, R. A., Kitagawa, T., Lawes, M., Sheppard, C. G. W. and Woolley, R. (2003). Turbulent burning velocity, burned gas distribution, and associated flame surface definition. *Combustion and Flame*, 133 (4), 415-430.
- Bradley, D., Lau, A. K. C. and Lawes, M. (1992). Flame stretch rate as a determinant of turbulent burning velocity. *Philosophical Transactions of the Royal Society: Physical and Engineering Sciences*, 338 (1650), 359-387.
- Bradley, D., Lawes, M. and Liu, K. (2008). Turbulent flame speeds in ducts and the deflagration/detonation transition. *Combustion and Flame*, 154 (1-2), 96-108.
- Bradley, D., Lawes, M., Liu, K., Verhelst, S. and Woolley, R. (2007). Laminar burning velocities of lean hydrogen-air mixtures at pressures up to 1.0 MPa. *Combustion and Flame*, 149 (1-2), 162-172.
- Bradley, D. and Lung, F. K. K. (1987). Spark ignition and the early stages of turbulent flame propagation. *Combustion and Flame*, 69 (1), 71-93.
- Bray, K. N. C. (1990). Studies of the turbulent burning velocity. *Proceedings of the Royal Society: Mathematical and Physical Sciences*, A431 (1882), 315-335.
- Bray, K. N. C. and Cant, R. S. (1991). Some applications of Kolmogorov's turbulence research in the field of combustion. *Proceedings of the Royal Society: Mathematical and Physical Sciences*, 434 (1890), 217-240.
- Bray, K. N. C., Chmapión, M. and Libby, P. A. (1989). *Turbulent Reactive Flows*. Berlin, Springer Verlag.
- Bray, K. N. C., Libby, P. A., Masuya, G. and Moss, J. B. (1981). Turbulence production in premixed turbulent flames. *Combustion Science and Technology*, 25 (3), 127-140.
- Bray, K. N. C., Libby, P. A. and Moss, J. B. (1985). Unified modelling approach for premixed turbulent combustion—Part I: General formulation. *Combustion and Flame*, 61 (1), 87-102.
- Bray, K. N. C. and Moss, J. B. (1977). A closure model for the turbulent premixed flame with sequential chemistry. *Combustion and Flame*, 30, 125-131.
- Bray, K. N. C. and Peters, N. (1993). Laminar flamelets in turbulent flames. *Turbulent reaction flows*, eds. P.A. Libby and F.A. Williams, Academic Press, 63-113.
- Breuer, M. and Rodi, W. (1994). Large-Eddy Simulation of Turbulent Flow through a Straight Square Duct and a 180° Bend. In: Voke, P., Kleiser, L. & Chollet, J.-P. (eds.) *Direct and Large-Eddy Simulation I*. Springer Netherlands.
- Buckmaster, J., Clavin, P., Liñán, A., Matalon, M., Peters, N., Sivashinsky, G. and Williams, F. A. (2005). Combustion theory and modeling. *Proceedings of the Combustion Institute*, 30 (1), 1-19.

- Butler, T. D. and O'Rourke, P. J. (1977). A numerical method for two dimensional unsteady reacting flows. *Proceedings of the Combustion Institute*, 16 (1), 1503-1515.
- Cadwallader, L. C. and Herring, J. S. (1999). Safety Issues with Hydrogen as a Vehicle Fuel. Idaho National Engineering and Environmental Laboratory.
- Candel, S. M. and Poinso, T. J. (1990). Flame Stretch and the Balance Equation for the Flame Area. *Combustion Science and Technology*, 70 (1-3), 1-15.
- Cant, R. and Mastorakos, E. (2008). *An introduction to turbulent reacting flows*. London, Imperial College Press.
- Cant, R. S. and Bray, K. N. C. (1989). Strained laminar flamelet calculations of premixed turbulent combustion in a closed vessel. *Proceedings of the Combustion Institute*, 22 (1), 791-799.
- Cant, R. S., Pope, S. B. and Bray, K. N. C. (1991). Modelling of flamelet surface-to-volume ratio in turbulent premixed combustion. *Proceedings of the Combustion Institute*, 23 (1), 809-815.
- Carati, D. and Wray, A. A. (2000). Time filtering in large eddy simulations. *Proceedings of the Summer Program*, , Center for Turbulence Research, Stanford University. 263-270.
- Castro, I. P. and Jones, J. M. (1987). Studies in numerical computations of recirculating flows. *International Journal for Numerical Methods in Fluids*, 7 (8), 793-823.
- Catlin, C. A., Fairweather, M. and Ibraim, S. S. (1995). Predictions of turbulent, premixed flame propagation in explosion tubes. *Combustion and Flame*, 102 (1-2), 115-128.
- Chan, C. K. and Li, X. (2005). Flame surface density in turbulent premixed V-flame with buoyancy. *Flow, Turbulence and Combustion*, 74, 273-289.
- Charlette, F., Meneveau, C. and Veynante, D. (2002). A power-law flame wrinkling model for LES of premixed turbulent combustion Part II: dynamic formulation. *Combustion and Flame*, 131 (1-2), 181-197.
- Charlette, F., Trouvé, A., Boger, M. and Veynante, D. (1999). A flame surface density model for large eddy simulations of turbulent premixed flames. *The Combustion Institute Joint Meeting of the British, German and French Sections*.
- Chow, F. K. and Moin, P. (2003). A further study of numerical errors in large-eddy simulations. *Journal of Computational Physics*, 184 (2), 366-380.
- Christophe, D. and Laszlo, F. (2007). Large eddy simulation of turbulent premixed combustion using a marker field. *Combustion Science and Technology*, 179 (10), 2135-2152.
- Chung, S. H. and Law, C. K. (1984). An invariant derivation of flame stretch. *Combustion and Flame*, 55 (1), 123-125.

- Ciccarelli, G. and Dorofeev, S. (2008). Flame acceleration and transition to detonation in ducts. *Progress in Energy and Combustion Science*, 34 (4), 499-550.
- Colin, O., Ducros, F., Veynante, D. and Poinso, T. (2000). A thickened flame model for large eddy simulations of turbulent premixed combustion. *Physics of Fluids*, 12 (7), 1843-1863.
- Colucci, P. J., Jaber, F. A., Givi, P. and Pope, S. B. (1998). Filtered density function for large eddy simulation of turbulent reacting flows. *Physics of Fluids*, 10 (2), 499-515.
- Cook, A. W. and Riley, J. J. (1994). A subgrid model for equilibrium chemistry in turbulent flows. *Physics of Fluids*, 6 (8), 2868-2870.
- Cook, A. W. and Riley, J. J. (1998). Subgrid-scale modeling for turbulent reacting flows. *Combustion and Flame*, 112 (4), 593-606.
- Cook, A. W., Riley, J. J. and Kosály, G. (1997). A laminar flamelet approach to subgrid-scale chemistry in turbulent flows. *Combustion and Flame*, 109 (3), 332-341.
- Coward, H. F. and Jones, G. W. (1952). Limits of flammability of gases and vapors. Bureau of Mines Bulletin.
- Cronhjort, A. (2005). Optical Studies in a Direct Injected Diesel Engine 5th Symposium Towards Clean Diesel Engines Lund, Sweden.
- Dahoe, A. (2005). Laminar burning velocities of hydrogen–air mixtures from closed vessel gas explosions. *Journal of Loss Prevention in the Process Industries*, 18 (3), 152-166.
- Damköhler, G. Z. (1940). *Elektrochem*, vol. 46, 610.
- Deardorff, J. W. (1970). A numerical study of three-dimensional turbulent channel flow at large Reynolds numbers. *Journal of Fluid Mechanics*, 41 (02), 453-480.
- Debligny, O., Knaepen, B., Carati, D. and Wray, A. A. (2004). Sampling versus filtering in large-eddy simulations. *Proceedings of Summer Program , Center for Turbulence Research, Stanford University*. 133-144.
- Di Sarli, V., Di Benedetto, A., Russo, G., Jarvis, S., Long, E. J. and Hargrave, G. K. (2009). Large Eddy Simulation and PIV Measurements of Unsteady Premixed Flames Accelerated by Obstacles. *Flow, Turbulence and Combustion*, 83 (2), 227-250.
- Dryer, F. L., Chaos, M., Zhao, Z., Stein, J. N., J.Y., A. and Homer, C. J. (2007). Spontaneous ignition of pressurized releases of hydrogen and natural gas into air. *Combustion Science and Technology*, 179, 663-694.
- Duclos, J. M., Veynante, D. and Poinso, T. (1993). A comparison of flamelet models for premixed turbulent combustion. *Combustion and Flame*, 95 (1-2), 101-117.

- Efimenko, A. A. and Dorofeev, S. B. (2001). CREBCOM code system for description of gaseous combustion. *Journal of Loss Prevention in the Process Industries*, 14 (6), 575-581.
- Fairweather, M., Hargrave, G. K., Ibrahim, S. S. and Walker, D. G. (1999a). Studies of premixed flame propagation in explosion tubes. *Combust. Flame*, 116, 504-518.
- Fairweather, M., Hargrave, G. K., Ibrahim, S. S. and Walker, D. G. (1999b). Studies of premixed flame propagation in explosion tubes. *Combustion and Flame*, 116 (4), 504-518.
- Fairweather, M., Ibrahim, S. S., Jagers, H. and Walker, D. G. (1996). Turbulent premixed flame propagation in a cylindrical vessel. *Symposium (International) on Combustion*, 26 (1), 365-371.
- Ferziger, J. H. (1977). Large Eddy Numerical Simulations of Turbulent Flows. *AIAA Journal*, 15 (9), 1261-1267.
- Ferziger, J. H. (1982). *State of the Art in Subgrid-Scale Modeling, Numerical and Physical Aspects of Aerodynamic Flows*. New York, Springer-Verlag.
- Ferziger, J. H. (1993). Subgrid-scale modelling. In: Galperin, B. & Orszag, S. A. (eds.) *Large Eddy Simulation of Complex Engineering and Geophysical Flows*. Cambridge, UK: Cambridge University Press.
- Fiorina, B., Baron, R., Gicquel, O., Thevenin, D., Carpentier, S. and Darabiha, N. (2003). Modelling non-adiabatic partially premixed flames using flame-prolongation of ILDM. *Combustion Theory and Modelling*, 7 (3), 449-470.
- Flohr, P. and Pitsch, H. (2000). A turbulent flame speed closure model for LES of industrial burner flows. *Proceedings of the Summer Program, Center for Turbulence Research, Stanford University*, 169-179.
- Fröhlich, J. and Rodi, W. (2002). Introduction to Large Eddy Simulation of Turbulent Flows. In: Launder, B. E. & Sandham, N. D. (eds.) *Closure Strategies for Turbulent and Transitional Flows*. Cambridge University Press.
- Fureby, C. (1998). Towards Large Eddy Simulation of flows in complex geometries. *29th AIAA, Fluid Dynamics Conference*. American Institute of Aeronautics and Astronautics.
- Fureby, C. (2005). A fractal flame-wrinkling large eddy simulation model for premixed turbulent combustion. *Proceedings of the Combustion Institute*, 30 (1), 593-601.
- Fureby, C. and Löfström, C. (1994). Large-eddy simulations of bluff body stabilized flames. *Proceedings of the Combustion Institute*, 25 (1), 1257-1264.
- Fureby, C. and Möller, S. I. (1995). Large eddy simulation of reacting flows applied to bluff body stabilized flames. *American Institute of Aeronautics and Astronautics*, 33 (12), 2339-2347.

- Fureby, C., Tabor, G., Weller, H. G. and Gosman, A. D. (1997). A comparative study of subgrid scale models in homogeneous isotropic turbulence. *Physics of Fluids*, 9 (5), 1416-1429.
- Gao, F. and O'Brien, E. E. (1993). A large-eddy simulation scheme for turbulent reacting flows. *Physics of Fluids A: Fluid Dynamics*, 5 (6), 1282-1284.
- GASEQ. A Chemical Equilibrium Program. Version 0.79. www.gaseq.co.uk.
- Germano, M., Piomelli, U., Moin, P. and Cabot, W. H. (1991). A dynamic subgrid-scale eddy viscosity model. *Physics of Fluids A: Fluid Dynamics*, 3 (7), 1760-1765.
- Ghosal, S., Lund, T., Moin, P. and Akselvoll, K. (1995). A dynamic localization model for large-eddy simulation of turbulent flows. *Journal of Fluid Mechanics*, 286, 229-255.
- Gicquel, O., Darabiha, N. and Thévenin, D. (2000). Liminar premixed hydrogen/air counterflow flame simulations using flame prolongation of ILDM with differential diffusion. *Proceedings of the Combustion Institute*, 28 (2), 1901-1908.
- Givi, P. (1989). Model-free simulations of turbulent reactive flows. *Progress in Energy and Combustion Science*, 15 (1), 1-107.
- Glassman, I. (1987). *Combustion*, 2nd ed. Orlando, Florida, Academic Press.
- Gouldin, F. C. (1987). An application of fractals to modeling premixed turbulent flames. *Combustion and Flame*, 68 (3), 249-266.
- Gouldin, F. C., Bray, K. N. C. and Chen, J. (1989a). Chemical closure model for fractal flamelets. *Combustion and Flame*, 77 (3-4), 241-259.
- Gouldin, F. C., Hilton, S. M. and Lamb, T. (1989b). Experimental evaluation of the fractal geometry of flamelets. *Proceedings of the Combustion Institute*, 22 (1), 541-550.
- Grant, W. (2008). *Turbulent Premixed Propagation Flames in Obstructed Flow*.
, School of Aerospace, Mechanical and Mechatronic Engineering, University of Sydney.
- Gubba, S. R. (2009). *Development of a dynamic LES model for premixed turbulent flames*. PhD, Loughborough University.
- Gubba, S. R., Ibrahim, S. S., Malalasekera, W. and Masri, A. R. (2007). LES modelling of propagating turbulent premixed flames using a dynamic flame surface density model. 2nd ECCOMAS Thematic Conference on Computational Combustion, Delft, Netherlands.
- Gubba, S. R., Ibrahim, S. S., Malalasekera, W. and Masri, A. R. (2009). An assessment of large eddy simulations of premixed flames propagating past repeated obstacles. *Combustion Theory and Modelling*, 13 (3), 513-540.

- Gubba, S. R., Ibrahim, S. S., Malalasekera, W. and Masri, A. R. (2011). Measurements and LES calculations of turbulent premixed flame propagation past repeated obstacles. *Combustion and Flame*, 158 (12), 2465-2481.
- Hall, R. (2006). *Flow field measurement in transient premixed flames*. BEng Thesis, University of Sydney, Australia.
- Hall, R. (2008). *Influence of obstacle location and frequency on the propagation of premixed flames*. MEng Thesis, University of Sydney, Australia.
- Hamiroune, D., Bishnu, P., Metghalchi, M. and Keck, J. C. (1998). Rate-controlled constrained-equilibrium method using constraint potentials. *Combustion Theory and Modelling*, 2 (1), 81-94.
- Hawkes, E. R. and Cant, R. S. (2000). A flame surface density approach to large-eddy simulation of premixed turbulent combustion. *Proceedings of the Combustion Institute*, 28 (1), 51-58.
- Hawkes, E. R. and Cant, R. S. (2001). Implications of a flame surface density approach to large eddy simulation of premixed turbulent combustion. *Combustion and Flame*, 126 (3), 1617-1629.
- Hentschel, H. and Procaccia, I. (1984). Relative diffusion in turbulent media: the fractal dimension of clouds. *Physical Review A*, 29 (3), 1461.
- Hjertager, B. H., Fuhre, K. and Bjørkhaug, M. (1988). Concentration Effects on Flame Acceleration by Obstacles in Large-Scale Methane-Air and Propane-Air Vented Explosions. *Combustion Science and Technology*, 62 (4-6), 239-256.
- Horiuti, K. (1997). A new dynamic two-parameter mixed model for large-eddy simulation. *Physics of Fluids*, 9 (11), 3443-3464.
- Houf, W. G. and Schefer, R. W. (2007). Predicting radiative heat fluxes and flammability envelopes from unintended releases of hydrogen. *International Journal of Hydrogen Energy* 32, 136-151.
- Huang, Y., Sung, H., Hsieh, S. and Yang, V. (2003). Large-eddy simulation of combustion dynamics of lean-premixed swirl-stabilized combustor. *Journal of Propulsion and Power*, 19 (5), 782-794.
- HySafe (2007). Biennial report on hydrogen safety.
- Ibrahim, S. S., Hargrove, G. K. and Williams, T. C. (2001). Experimental investigation of flame/solid interaction in turbulent premixed combustion. *Experimental Thermal and Fluid Science*, 24, 99-106.
- Ibrahim, S. S. and Masri, A. R. (2001). The effects of obstructions on overpressure resulting from premixed flame deflagration. *Journal of Loss Prevention in the Process Industries*, 14 (3), 213-221.
- Iijima, T. and Takeno, T. (1986). Effects of temperature and pressure on burning velocity. *Combustion and Flame*, 65 (1), 35-43.

- Jackson, T., Macaraeg, M. G. and Hussaini, M. Y. (1993). The role of acoustics in flame/vortex interactions. *Journal of Fluid Mechanics*, 254, 579-603.
- Janbozorgi, M., Ugarte, S., Metghalchi, H. and Keck, J. C. (2009). Combustion modeling of mono-carbon fuels using the rate-controlled constrained-equilibrium method. *Combustion and Flame*, 156 (10), 1871-1885.
- Johansen, C. T. and Ciccarelli, G. (2009). Visualization of the unburned gas flow field ahead of an accelerating flame in an obstructed square channel. *Combust. Flame*, 156, 405-416.
- Jones, W. P. (1993). Turbulence modelling and numerical solution methods for variable density and combusting flows. In: Libby, P. A. & Williams, F. A. (eds.) *Turbulent Reacting Flows*. Academic Press.
- Joulin, G. (1994). On the response of premixed flames to time-dependent stretch and curvature. *Combustion Science and Technology*, 97 (1-3), 219-229.
- Kamardin, K. Z. (2005). *Premixed Flame Propagation Past Solid Obstacles*. School of Aerospace, Mechanical and Mechatronic Engineering, University of Sydney
- Kan, J. v. (1986). A second-order accurate pressure correction scheme for viscous incompressible flow. *SIAM J. Sci. Stat. Comput.*, 7 (3), 870-891.
- Kent, J. E., Masri, A. R. and Starner, S. H. (2005). A new chamber to study premixed flame propagation past repeated obstacles. *5th Asia-Pacific Conference on Combustion*. The University of Adelaide, Australia.
- Kerstein, A. R. (1988). Fractal dimension of turbulent premixed flames. *Combustion Science and Technology*, 60 (4), 441-445.
- Kerstein, A. R. (1991). Linear-eddy modelling of turbulent transport. Part 6. Microstructure of diffusive scalar mixing fields. *Journal of Fluid Mechanics*, 231, 361-394.
- Kim, W., Lienau, J. J., Slooten, P. R. V., Colket III, M. B., Malecki, R. E. and Syed, S. (2006). Towards modeling lean blow out in gas turbine flame holder applications. *Journal of engineering for Gas turbines and power*, 128, 40-48.
- Kim, W. and Menon, S. (2000). Numerical modeling of turbulent premixed flames in the thin-reaction-zones regime. *Combustion Science and Technology*, 160 (1), 119-150.
- Kirkpatrick, M. P. (2002). *A Large Eddy Simulation Code for Industrial and Environmental Flows*. PhD Thesis, The University of Sydney, Australia.
- Kirkpatrick, M. P., Armfield, S. W., Masri, A. R. and Ibrahim, S. S. (2003). Large Eddy Simulation of a Propagating Turbulent Premixed Flame. *Flow, Turbulence and Combustion*, 70 (1-4), 1-19.

- Klein, M. (2005). An Attempt to Assess the Quality of Large Eddy Simulations in the Context of Implicit Filtering. *Flow, Turbulence and Combustion*, 75 (1-4), 131-147.
- Knikker, R., Veynante, D. and Meneveau, C. (2002). A priori testing of a similarity model for large eddy simulations of turbulent premixed combustion. *Proceedings of the Combustion Institute*, 29, 2105-2111.
- Knikker, R., Veynante, D. and Meneveau, C. (2004). A dynamic flame surface density model for large eddy simulation of turbulent premixed combustion. *Physics of Fluids*, 16 (11), L91-L94.
- Kogarko, S. M. and Ryzhkov, D. L. (1961). A study of the amplification of compression waves during combustion. *Sov Phys Tech Phys*, 31, 211-216.
- Kollmann, W. and Schmitt, F. (1981). The PDF of Temperature in Recirculating Flows. *7th Biennial Symposium on Turbulence*
- Kuo, K. K. (2005). *Principles of Combustion*, 2nd ed. Hoboken, New Jersey, John Wiley & Sons.
- Leonard, B. P. (1979). A stable and accurate convective modelling procedure based on quadratic upstream interpolation. *Computer Methods in Applied Mechanics and Engineering*, 19 (1), 59-98.
- Leyer, J. C. and Manson, N. (1971). Development of vibratory flame propagation in short closed tubes and vessels. *Thirteenth Symp. (Intl) on Combustion*, 551-557.
- Libby, P. A. and Bray, K. N. C. (1981). Countergradient diffusion in premixed turbulent flames. *AIAA Journal*, 19 (2), 205-213.
- Lilly, D. K. (1966). The representation of small-scale turbulence in numerical simulation experiments. University Corporation for Atmospheric Research.
- Lilly, D. K. (1992). A proposed modification of the Germano subgrid-scale closure method. *Physics of Fluids A: Fluid Dynamics*, 4 (3), 633-635.
- Lindstedt, R. P. and Sakthitharan, V. (1998). Time resolved velocity and turbulence measurements in turbulent gaseous explosions. *Combust. Flame*, 114, 469-483.
- Lindstedt, R. P. and Váos, E. M. (1999). Modeling of premixed turbulent flames with second moment methods. *Combustion and Flame*, 116 (4), 461-485.
- Liu, X. and Zhang, Q. (2014). Influence of initial pressure and temperature on flammability limits of hydrogen-air. *International Journal of Hydrogen Energy*, 39 (12), 6774-6782.
- Lohrer, C., Drame, C., Schalau, B. and Gratz, R. (2008). Propane/air deflagrations and CTA measurements of turbulence inducing elements in closed pipes. *Journal of Loss Prevention in the Process Industries*, 21, 1-10.

- Lovejoy, S. (1982). Area-perimeter relation for rain and cloud areas. *Science*, 216 (4542), 185-187.
- Lu, T. and Law, C. K. (2008). A criterion based on computational singular perturbation for the identification of quasi steady state species: A reduced mechanism for methane oxidation with NO chemistry. *Combustion and Flame*, 154 (4), 761-774.
- Lund, T. S. and Kaltenbach, H. J. (1995). Experiments with explicit filtering for LES using a finite-difference method. *Proceedings of the Summer Program, , Center for Turbulence Research, Stanford University*. 91-105.
- Madina, C. K. and Givi, P. (1993). Direct and large eddy simulation of reacting homogeneous turbulence. In: Galperin B. & Orszag S.A. (eds.) *Large Eddy Simulations of Complex Engineering and Geophysical Flows*. Cambridge, UK: Cambridge University Press.
- Makarov, D., Verbecke, F., Molkov, V., Kotchourko, A., Lelyakin, A., Yanez, J., Baraldi, D., Heitsch, M., Efimenko, A. and Gavrikov, A. (2010). An intercomparison of CFD models to predict lean and non-uniform hydrogen mixture explosions. *International Journal of Hydrogen Energy*, 35 (11), 5754-5762.
- Malalasekera, W., Ibrahim, S. S., Masri, A. R., Gubba, S. R. and Sadasivuni, S. (2013). Experience with the Large Eddy Simulation (LES) Technique for the Modeling of Premixed and Non-premixed Combustion. *Heat Transfer Engineering*, (just-accepted).
- Mandelbrot, B. B. (1975). On the geometry of homogeneous turbulence, with stress on the fractal dimension of the iso-surfaces of scalars. *Journal of Fluid Mechanics*, 72 (2), 401-416.
- Marble, F. E. and Broadwell, J. E. (1977). The coherent flame model for turbulent chemical reactions. *Project Squid Technical Report, TRW-9-PU*.
- Markstein, G. H. and Somers, L. M. (1953). Cellular flame structure and vibratory flame movement in N-butane-methane mixtures. *Symposium (International) on Combustion*, 4 (1), 527-535.
- Masri, A. R., AlHarbi, A., Meares, S. and Ibrahim, S. S. (2011). A Comparative Study of Turbulent Premixed Flames Propagating Past Repeated Obstacles. *Industrial and Engineering Chemistry Research*, 51 (22), 7690-7703.
- Masri, A. R., Ibrahim, S. S. and Cadwallader, B. J. (2006). Measurements and large eddy simulation of propagating premixed flames. *Experimental Thermal and Fluid Science*, 30 (7), 687-702.
- Masri, A. R., Ibrahim, S. S., Nehzat, N. and Green, A. R. (2000). Experimental study of premixed flame propagation over various solid obstructions. *Experimental Thermal and Fluid Science*, 21 (1-3), 109-116.

- Matalon, M. (2009). Flame dynamics. *Proceedings of the Combustion Institute*, 32 (1), 57-82.
- Matalon, M. and Matkowsky, B. J. (1982). Flames as gasdynamic discontinuities. *Journal of Fluid Mechanics*, 124, 239-259.
- Meneveau, C. and Poinso, T. (1991). Stretching and quenching of flamelets in premixed turbulent combustion. *Combustion and Flame*, 86 (4), 311-332.
- Menon, S. and Jou, W. H. (1991). Large-eddy simulations of combustion instabilities in an axisymmetric ramjet combustor. *Combustion Science and Technology*, 84, 51-79.
- Metghalchi, M. and Keck, J. C. (1980). Laminar burning velocity of propane-air mixtures at high temperature and pressure. *Combustion and Flame*, 38 (0), 143-154.
- Metghalchi, M. and Keck, J. C. (1982). Burning velocities of mixtures of air with methanol, isooctane, and indolene at high pressure and temperature. *Combustion and Flame*, 48 (0), 191-210.
- Middha, P. (2010). *Development, Use, and Validation Of The CFD Tool Flacs For Hydrogen Safety Studies*. PhD, University of Bergen.
- Moen, I. O., Donato, M., Knystautas, R. and Lee, J. H. (1980). Flame acceleration due to turbulence produced by obstacles. *Combustion and Flame*, 39 (1), 21-32.
- Moen, I. O., Lee, J. H. S., Hjertager, B. H., Fuhre, K. and Eckhoff, R. K. (1982). Pressure development due to turbulent flame propagation in large-scale methane-air explosions. *Journal Name: Combust. Flame; (United States); Journal Volume: 47, Medium: X; Size: Pages: 31-52.*
- Moin, P. and Kim, J. (1982). Numerical investigation of turbulent channel flow. *Journal of Fluid Mechanics*, 118, 341-377.
- Moin, P. and Kim, J. (1997). Tackling turbulence with supercomputers. *Scientific American*, 276, 62-68.
- Moin, P., Reynolds, W. and Ferziger, J. (1978). Large eddy simulation of incompressible turbulent channel flow. *NASA STI/Recon Technical Report N*, 78, 31383.
- Moin, P., Squires, K., Cabot, W. and Lee, S. (1991). A dynamic subgrid-scale model for compressible turbulence and scalar transport. *Physics of Fluids A: Fluid Dynamics*, 3 (11), 2746-2757.
- Molkov, V. (2007). HYDROGEN SAFETY RESEARCH: STATE-OF-THE-ART. *5th International Seminar on Fire and Explosion Hazards, Edinburgh, UK.*
- Molkov, V., Makarov, D. and Schneider, H. (2006). LES modelling of an unconfined large-scale hydrogen-air deflagration. *Journal of Physics D: Applied Physics*, 39, 4366-4376.

- Möller, S. I., Lundgren, E. and Fureby, C. (1996). Large eddy simulation of unsteady combustion. *Proceedings of the Combustion Institute*, 26 (1), 241-248.
- Muppala, S. P. R., Aluri, N. K., Dinkelacker, F. and Leipertz, A. (2005). Development of an algebraic reaction rate closure for the numerical calculation of turbulent premixed methane, ethylene, and propane/air flames for pressures up to 1.0 MPa. *Combustion and Flame*, 140 (4), 257-266.
- Naitoh, K., Itoh, T., Takagi, Y. and Kuwahara, K. (1992). Large eddy simulation of premixed-flame in engine based on the multi-level formulation and the renormalization group theory. *SAE Paper*, vol. 920590.
- North, G. L. and Santavicca, D. A. (1990). The fractal nature of premixed turbulent flames. *Combustion Science and Technology*, 72 (4), 215.
- Nottin, C., Knikker, R., Boger, M. and Veynante, D. (2000). Large eddy simulations of an acoustically excited turbulent premixed flame. *Proceedings of the Combustion Institute*, 28 (1), 67-73.
- Oijen, J. v. and Goey, L. D. (2000). Modelling of premixed laminar flames using flamelet-generated manifolds. *Combustion Science and Technology*, 161 (1), 113-137.
- Oran, E. S. and Boris, J. P. (2000). *Numerical Simulation of Reactive Flow*. Cambridge University Press.
- Oran, E. S. and Gardner, J. H. (1985). Chemical-acoustic interactions in combustion systems. *Progress in Energy and Combustion Science*, 11 (4), 253-276.
- Park, D. J., Green, A. R., Lee, Y. S. and Chen, Y. C. (2007). Experimental studies on interactions between a freely propagating flame and single obstacles in a rectangular confinement. *Combust. Flame*, 150, 27-39.
- Park, D. J., Lee, Y. S. and Green, A. R. (2008). Experiments on the effects of multiple obstacles in vented explosion chamber. *Hazardous Materials*, 153, 340-350.
- Patel, S., Ibrahim, S. S., Yehia, M. A. and Hargrave, G. K. (2003). Investigation of premixed turbulent combustion in a semi-confined explosion chamber. *Experimental Thermal and Fluid Science*, 27 (4), 355-361.
- Patel, S. N. D. H., Jarvis, S., Ibrahim, S. S. and Hargrave, G. K. (2002). An experimental and numerical investigation of premixed flame deflagration in a semiconfined explosion chamber. *Proceedings of the Combustion Institute*, 29 (2), 1849-1854.
- Peters, N. (1988). Laminar flamelet concepts in turbulent combustion. *Symposium (International) on Combustion*, 21 (1), 1231-1250.
- Peters, N. (1999). The turbulent burning velocity for large-scale and small-scale turbulence. *Journal of Fluid Mechanics*, 384, 107-132.
- Peters, N. (2004). *Turbulent Combustion*. Cambridge University Press.

- Phylaktou, H. and Andrews, G. E. (1991). The acceleration of flame propagation in a tube by an obstacle. *Combust. Flame*, 85, 363-379.
- Piana, J., Veynante, D., Candel, S. and Poinso, T. (1997). Direct numerical simulation analysis of the G-equation in premixed combustion. In: Chollet J.P. , Vole P.R. & Kleiser L. (eds.) *Direct and Large Eddy simulation II*. Amsterdam: Kluwer Academic Publishers.
- Piomelli, U. and Liu, J. (1995). Large-eddy simulation of rotating channel flows using a localized dynamic model. *Physics of Fluids*, 7 (4), 839-848.
- Piomelli, U., Moin, P. and Ferziger, J. H. (1988). Model consistency in large eddy simulation of turbulent channel flows. *Physics of Fluids*, 31 (7), 1884-1891.
- Piomelli, U., Yu, Y. and Adrian, R. J. (1996). Subgrid-scale energy transfer and near-wall turbulence structure. *Physics of Fluids*, 8 (1), 215-224.
- Piomelli, U., Zang, T. A., Speziale, C. G. and Hussaini, M. Y. (1990). On the large-eddy simulation of transitional wall-bounded flows. *Physics of Fluids A: Fluid Dynamics*, 2 (2), 257-265.
- Pitsch, H. (2006). Large-eddy simulation of turbulent combustion. *Annual Review of Fluid Mechanics*, 38, 453-482.
- Pitsch, H. and Duchamp de Lageneste, L. (2002). Large-eddy simulation of premixed turbulent combustion using a level-set approach. *Proceedings of the Combustion Institute*, 29 (2), 2001-2008.
- Poinso, T., Candel, S. and Trouvé, A. (1995). Applications of direct numerical simulation to premixed turbulent combustion. *Progress in Energy and Combustion Science*, 21 (6), 531-576.
- Poinso, T. and Veynante, D. (2012). *Theoretical and Numerical Combustion*, 3rd ed. Bordeaux, France.
- Poinso, T., Veynante, D. and Candel, S. (1991). Quenching processes and premixed turbulent combustion diagrams. *Journal of Fluid Mechanics*, 228, 561-606.
- Polifke, W., Flohr, P. and Brandt, M. (2000). Modeling of inhomogeneously premixed combustion with an extended TFC model. *Proceedings of ASME TURBO EXPO*, 2000-GT-0135.
- Pope, S. B. (1985). PDF methods for turbulent reactive flows. *Progress in Energy and Combustion Science*, 11 (2), pp. 119-192.
- Pope, S. B. (1988). The evolution of surfaces in turbulence. *International Journal of Engineering Science*, 26 (5), 445-469.
- Pope, S. B. (2004). Ten questions concerning the large-eddy simulation of turbulent flows. *New Journal of Physics*, 6 (1), 35.

- Porumbel, I. and Menon, S. (2006). Large eddy simulation of bluff body stabilized premixed flame *44th AIAA Aerospace Science Meeting and Exhibit*
- Prasad, R. O. S. and Gore, J. P. (1999). An evaluation of flame surface density models for turbulent premixed jet flames. *Combustion and Flame*, 116 (1-2), 1-14.
- Quillatre, P., Vermorel, O., Poinso, T. and Ricoux, P. (2013). Large Eddy Simulation of Vented Deflagration. *Industrial & Engineering Chemistry Research*, 52 (33), 11414-11423.
- Ranasinghe, C. P. (2013). *Development of combustion models for RANS and LES applications in SI engines*. PhD, Loughborough University.
- Ranga-Dinesh, K. K. J. (2007). *Large eddy simulation of turbulent swirling flames*,. PhD Thesis, Loughborough University.
- Ranga Dinesh, K. K. J., Jiang, X., Malalasekera, W. and Odedra, A. (2013). Large eddy simulation of fuel variability and flame dynamics of hydrogen-enriched nonpremixed flames. *Fuel Processing Technology*, 107 (0), 2-13.
- Regele, J. D., Knudsen, E., Pitsch, H. and Blanquart, G. (2013). A two-equation model for non-unity Lewis number differential diffusion in lean premixed laminar flames. *Combustion and Flame*, 160 (2), 240-250.
- Reveillon, J. and Vervisch, L. (1997). Dynamic sub-grid PDF modelling for non-premixed turbulent combustion. In: Cholle J.P., Vole P.R. & Kleiser L. (eds.) *Direct and Large Eddy Simulation II*. Amsterdam: Kluwer Academic Publishers.
- Richard, S., Colin, O., Vermorel, O., Benkenida, A., Angelberger, C. and Veynante, D. (2007). Towards large eddy simulation of combustion in spark ignition engines. *Proceedings of the Combustion Institute*, 31, 3059–3066.
- Richardson, E. S. and Chen, J. H. (2012). Application of PDF mixing models to premixed flames with differential diffusion. *Combustion and Flame*, 159 (7), 2398-2414.
- Rogallo, R. S. and Moin, P. (1984). Numerical Simulation of Turbulent Flows. *Annual Review of Fluid Mechanics*, 16 (1), 99-137.
- Salvetti, M. V. and Banerjee, S. (1995). A priori tests of a new dynamic subgrid-scale model for finite-difference large-eddy simulations. *Physics of Fluids*, 7 (11), 2831-2847.
- Schumann, U. (1975). Subgrid scale model for finite difference simulations of turbulent flows in plane channels and annuli. *Journal of Computational Physics*, 18 (4), 376-404.
- Schumann, U. (1989). Large-eddy simulation of turbulent diffusion with chemical reactions in the convective boundary layer. *Atmospheric Environment* (1967), 23 (8), 1713-1727.

- Searby, G. and Rochwerger, D. (1991). A parametric acoustic instability in premixed flames. *Journal of Fluid Mechanics*, 231, 529-543.
- Smagorinsky, J. (1963). General circulation experiments with the primitive equations. *Monthly Weather Review*, 91 (3), 99-164.
- Spalding, D. B. (1971). Mixing and chemical reaction in steady confined turbulent flames. *Proceedings of the Combustion Institute*, 13 (1), 649-657.
- Sreenivasan, K. and Meneveau, C. (1986). The fractal facets of turbulence. *Journal of Fluid Mechanics*, 173, 357-386.
- Starke, R. and Roth, P. (1986). An experimental investigation of flame behavior during cylindrical vessel explosions. *Combustion and Flame*, 66 (3), 249-259.
- Starke, R. and Roth, P. (1989). An experimental investigation of flame behavior during explosions in cylindrical enclosures with obstacles. *Combustion and Flame*, 75 (2), 111-121.
- Swart, J. M. d., Bastiaans, R. M., van Oijen, J., de Goey, L. P. and Cant, R. S. (2010). Inclusion of Preferential Diffusion in Simulations of Premixed Combustion of Hydrogen/Methane Mixtures with Flamelet Generated Manifolds. *Flow, Turbulence and Combustion*, 85 (3-4), 473-511.
- Tabor, G. and Weller, H. G. (2004). Large Eddy Simulation of Premixed Turbulent Combustion Using Ξ Flame Surface Wrinkling Model. *Flow, Turbulence and Combustion*, 72 (1), 1-27.
- Tamanini, F. and Chaffee, J. L. (1992). Turbulent vented gas explosions with and without acoustically-induced instabilities. *Symposium (International) on Combustion*, 24 (1), 1845-1851.
- Teodorczyk, A. and Lee, J. H. S. (1995). Detonation attenuation by foams and wire meshes lining the walls. *Shock Waves*, 4 (4), 225-236.
- Thibaut, D. and Candel, S. (1998). Numerical study of unsteady turbulent premixed combustion: application to flashback simulation. *Combustion and Flame*, 113 (1-2), 53-65.
- Thomas, G., Bambrey, R. and Brown, C. (2001). Experimental observations of flame acceleration and transition to detonation following shock-flame interaction. *Combustion Theory and Modelling*, 5 (4), 573-594.
- Tomlin, A. S., Pilling, M. J., Turányi, T., Merkin, J. H. and Brindley, J. (1992). Mechanism reduction for the oscillatory oxidation of hydrogen: Sensitivity and quasi-steady-state analyses. *Combustion and Flame*, 91 (2), 107-130.
- Trouvé, A. and Poinso, T. (1994). The evolution equation for the flame surface density in turbulent premixed combustion. *Journal of Fluid Mechanics*, 278 (1), 1-31.
- Turns, S. R. (2011). *An Introduction to Combustion: Concepts and Applications*, 3rd ed., McGraw Hill.

- Van Wingerden, C. J. M. and Zeeuwen, J. P. (1983). On the role of acoustically driven flame instabilities in vented gas explosions and their elimination. *Combustion and Flame*, 51 (C), 109-111.
- Verbecke, F. (2009). *Formation and combustion of non-uniform hydrogen-air mixtures*. PhD Thesis, University of Ulster.
- Versteeg, H. K. and Malalasekera, W. (2007). *An introduction to computational fluid dynamics: the finite volume method*. Prentice Hall.
- Veynante, D., Piana, J., Duclos, J. M. and Martel, C. (1996). Experimental analysis of flame surface density models for premixed turbulent combustion. *Proceedings of the Combustion Institute*, 26 (1), 413-420.
- Veynante, D. and Poinso, T. (1997). Large eddy simulations of the combustion instabilities in turbulent premixed burners *Annual Research Briefs* Centre for Turbulence Research Stanford University
- Veynante, D., Trouvé, A., Bray, K. N. C. and Mantel, T. (1997). Gradient and counter-gradient scalar transport in turbulent premixed flames. *Journal of Fluid Mechanics*, 332, 263-293.
- Veynante, D. and Vervisch, L. (2002). Turbulent combustion modeling. *Progress in Energy and Combustion Science*, 28 (3), 193-266.
- Vianna, S. S. V. and Cant, R. S. (2013). Initial Phase Modelling in Numerical Explosion Applied to Process Safety. *Process Safety and Environmental Protection*, (0).
- Vreman, A., Albrecht, B., Van Oijen, J., De Goey, L. and Bastiaans, R. (2008). Premixed and nonpremixed generated manifolds in large-eddy simulation of Sandia flame D and F. *Combustion and Flame*, 153 (3), 394-416.
- Wang, G., Boileau, M., Veynante, D. and Truffin, K. (2012). Large eddy simulation of a growing turbulent premixed flame kernel using a dynamic flame surface density model. *Combustion and Flame*, 159 (8), 2742-2754.
- Warnatz, J., Maas, U. and Dibble, R. W. (2006). *Combustion: Physical and Chemical Fundamentals, Modeling and Simulation, Experiments, Pollutant Formation*, 4th ed., Springer.
- Weller, H. G., Tabor, G., Gosman, A.D. and Fureby, C. (1998). Application of a flame-wrinkling LES combustion model to a turbulent mixing layer. *Proceedings of the Combustion Institute*, 1, 899-907.
- Werner, H. and Wengle, H. (1991). Large-eddy simulation of turbulent flow over and around a cube in a plate channel. *8th Symposium on Turbulent Shear Flows*
- Williams, F. A. (1985a). *Combustion Theory*. Perseus Books Group.
- Williams, F. A. (1985b). Turbulent Combustion. In: Buckmaster, J. D. (ed.) *The Mathematics of Combustion*. Philadelphia: SIAM.

- Winklhofer, E. (2003). HCCI combustion. *6th international conference on engines in automobiles*
- Winter, C.-J. (2009). Hydrogen energy — Abundant, efficient, clean: A debate over the energy-system-of-change. *International Journal of Hydrogen Energy*, 34 (14, Supplement 1), S1-S52.
- Xiao, H., Duan, Q., Jiang, L. and Sun, J. (2014). Effects of ignition location on premixed hydrogen/air flame propagation in a closed combustion tube. *International Journal of Hydrogen Energy*, 39 (16), 8557-8563.
- Xiao, H., Shen, X. and Sun, J. (2012). Experimental study and three-dimensional simulation of premixed hydrogen/air flame propagation in a closed duct. *International Journal of Hydrogen Energy*, 37 (15), 11466-11473.
- Xu, C., Cong, L., Yu, Z., Song, Z. and Bi, M. (2015). Numerical simulation of premixed methane–air deflagration in a semi-confined obstructed chamber. *Journal of Loss Prevention in the Process Industries*, 34 (0), 218-224.
- Yakhot, V. (1988). Propagation Velocity of Premixed Turbulent Flames. *Combustion Science and Technology*, 60 (1), 191-214.
- Yakhot, V. and Orszag, S. (1986). Renormalization group analysis of turbulence. I. Basic theory. *Journal of Scientific Computing*, 1 (1), 3-51.
- Yakhot, V. and Orszag, S. A. (1987). Renormalization group and local order in strong turbulence. *Nuclear Physics B - Proceedings Supplements*, 2 (0), 417-440.
- Yoshizawa, A. (1986). Statistical theory for compressible turbulent shear flows, with the application to subgrid modeling. *Physics of Fluids*, 29, 2152.
- Zang, Y., Street, R. L. and Koseff, J. R. (1993). A dynamic mixed subgrid-scale model and its application to turbulent recirculating flows. *Physics of Fluids A: Fluid Dynamics*, 5 (12), 3186-3196.
- Zimont, V. L. (2000). Gas premixed combustion at high turbulence - turbulent flame closure combustion model. *Experimental Thermal and Fluid Science*, 21 (1-3), 179-186.
- Zimont, V. L. and Lipatnikov, A. N. (1995). A numerical model of premixed turbulent combustion of gases. *Chemical physics reports*, 14 (7), 993-1025.
- Zimont, V. L., Polifke, W., Bettelini, M. and Weisenstein, W. (1997). An efficient computational model for premixed turbulent combustion at high Reynolds numbers based on a turbulent flame speed closure. *Journal of Engineering for Gas Turbine and Power, Transactions of ASME*, 120, 526-532.